uOttawa

L'Université canadienne
Canada's university

FACULTÉ DES ÉTUDES SUPÉRIEURES ET POSTOCTORALES

uOttawa

L'Université canadienne
Canada's university

FACULTY OF GRADUATE AND POSDOCTORAL STUDIES

Dongil Chang

AUTEUR DE LA THÈSE / AUTHOR OF THESIS

Ph.D. (Mechanical Engineering)

GRADE / DEGREE

Department of Mechanical Engineering

FACULTÉ, ÉCOLE, DÉPARTEMENT / FACULTY, SCHOOL, DEPARTMENT

Numerical simulations of turbulent flow and heat transfer in rod bundles

TITRE DE LA THÈSE / TITLE OF THESIS

Stavros Tavoularis

DIRECTEUR (DIRECTRICE) DE LA THÈSE / THESIS SUPERVISOR

CO-DIRECTEUR (CO-DIRECTRICE) DE LA THÈSE / THESIS CO-SUPERVISOR

EXAMINATEURS (EXAMINATRICES) DE LA THÈSE / THESIS EXAMINERS

Bantwal Rabi Baliga

Yves Bourgault

Dionysius Groeneveld

Junjie Gu

Gary W. Slater

LE DOYEN DE LA FACULTÉ DES ÉTUDES SUPÉRIEURES ET POSTDOCTORALES / DEAN OF THE FACULTY OF GRADUATE AND POSTDOCORAL STUDIES

Numerical simulations of turbulent flow and heat transfer in rod bundles

by

Dongil Chang

A thesis presented to the
Faculty of Graduate and Postdoctoral Studies
in partial fulfillment of the
requirement for the degree of

DOCTOR OF PHILOSOPHY
in
MECHANICAL ENGINEERING

Ottawa-Carleton Institute for Mechanical and Aerospace Engineering
Department of Mechanical Engineering
University of Ottawa
Ottawa, Ontario, Canada
March 2006

Your file Votre référence
ISBN: 978-0-494-15010-8
Our file Notre référence
ISBN: 978-0-494-15010-8

Abstract

The unsteady Reynolds-averaged Navier-Stokes equations, supplemented by a Reynolds stress model, were solved with relatively high spatial and temporal resolutions to determine the time-averaged mean velocity and turbulent stresses in isothermal, single-phase flows in a rectangular duct containing a single rod and in a 37-rod rod bundle. In addition, the time-averaged mean temperature, temperature fluctuation variance and turbulent heat fluxes were computed in the single-rod duct flow in which the rod was heated passively. The computed values were, in general, in fair agreement with available experimental results. The simulations also resolved the formation of coherent structures in the form of counter-rotating vortices with axes alternating on either side of rod-rod and rod-wall gaps. The contributions of these coherent structures on the turbulent and thermal fields and on cross-gap mixing were documented and found to be substantial. The action of coherent structures moderates the mean temperature rise in the gap region but creates substantial local variation of the instantaneous temperature fluctuations at relatively low frequencies. Reduction of the gap size below a critical value resulted in a decrease of the frequency of coherent fluctuations and the cross-channel mixing efficiency, contrary to predictions based on the extrapolation of available empirical correlations. In the case of the 37-rod bundle, the coherent velocity fluctuations were found to be strongly correlated in the entire computational domain.

Acknowledgements

My gratitude to Professor Stavros Tavoularis for becoming such an important part of my life, for giving me insight into every aspect of my research and for being supportive. He has spared his valuable time to check every step of my research and invested his expertise and effort on our four journal articles and two international conference papers. I would not have been successful without him.

I am deeply grateful to Professor Sadok Guellouz who was willing to share his valuable time to discuss various topics in this thesis. I would also like to express my appreciation to my colleagues, including Andrew Cameron, Dr. Bum-Su Kim, Choong-Hi Cho, Hoon-Bin Hong, Matthew Doyle, Pascal Tremblay, Sean Bailey, Dr. Timothy Rennie, Tony Standbridge, Dr. Warren Dunn, and William Stannus, for their friendship and support.

My deep thanks are due to my wife, Young-Youn Choi, and my wonderful kids, Young-Tae and Su-Youn, whose tremendous love and support allowed me to follow my dream.

Contents

Abstract i
Acknowledgements ii
Contents iii
List of Tables vi
List of Figures vii
Nomenclature xv

CHAPTER 1. INTRODUCTION **1**
1.1. Overview on axial flows in complex channels 1
1.2. Thermo-hydraulics of the CANDU nuclear reactor core 3
1.3. Motivation for the present study 7
1.4. Objectives of the thesis 11
1.5. Outline of the thesis 12

CHAPTER 2. LITERATURE REVIEW **13**
2.1. Experimental studies 13
2.2. Analytical models and computational studies 24
2.2.1. Subchannel analyses *24*
2.2.2. CFD simulations *26*

CHAPTER 3. THEORETICAL BACKGROUND **32**
3.1. Unsteady Reynolds Averaged Navier-Stokes approach 32
3.1.1. Two-equation turbulence model *34*
3.1.2. Reynolds stress model *37*
3.1.3. Near-wall modeling *41*
3.2. Energy equation and model 43
3.3. Inter-subchannel mixing 45

CHAPTER 4. NUMERICAL CONDITIONS AND PROCEDURES **47**
4.1. Computational domain and grid generation 47
4.1.1. The single-rod duct *47*
4.1.2. The 37-rod bundle *48*

4.2. Computational conditions 50
4.2.1. The single-rod duct *51*
4.2.2. The 37-rod bundle *53*
4.3. Computational procedures 54
4.3.1. The single-rod duct *55*
4.3.2. The 37-rod bundle *58*
4.4. Numerical schemes 59

CHAPTER 5. COHERENT STRUCTURE IDENTIFICATION 61
5.1. Definition of coherent structures 61
5.2. Identification methods of CS 63
5.3. Contribution of CS on the velocity and temperature fields 65

CHAPTER 6. ISOTHERMAL FLOW IN A SINGLE-ROD DUCT 69
6.1. Time-averaged streamwise velocity 70
6.2. Time-averaged turbulent statistics 71
6.3. Contribution of coherent components on the total turbulent activity 72
6.4. Characteristics of coherent structures 74
6.5. Summary of the isothermal turbulent flow field 75

CHAPTER 7. CONVECTIVE HEAT TRANSFER IN A SINGLE-ROD DUCT 77
7.1. Local temperature differences and fluctuations 78
7.2. Variation of the Nusselt number on the rod 80
7.3. Influence of the coherent structures on the instantaneous temperature fields 80
7.4. Power spectra 81
7.5. Summary of convective heat transfer results 84

CHAPTER 8. EFFECT OF GAP SIZE VARIATION ON THE TURBULENT FLOW AND HEAT TRANSFER IN A SINGLE-ROD DUCT 85
8.1. Time- averaged velocity and turbulent kinetic energy 85
8.2. Resolved temperature and temperature fluctuations 87
8.3. Skin friction coefficient and Nusselt number 89
8.4. Coherent structure characteristics 91
8.5. Inter-subchannel mixing 95
8.6. Summary of the gap size variation effects 98

CHAPTER 9. SIMULATION OF TURBULENT FLOW IN A 37-ROD BUNDLE 100
9.1. Mean velocity and turbulence characteristics 100

9.2. Partition of Reynolds stresses to coherent and non-coherent parts 104
9.3. Wall shear stress 106
9.4. Coherent structures 107
9.5. Summary 109

CHAPTER 10. CONCLUSIONS AND RECOMMENDATIONS FOR FUTURE WORK 111
10.1. Conclusions 111
10.2. Recommendations for future work 115
REFERENCES 117
TABLES 130
FIGURES 140
APPENDIX A DEVELOPING FLOW IN THE SINGLE-ROD DUCT 213

List of Tables

Table 1 - 1 Typical dimensions and operating conditions of CANDU type reactors..... 131
Table 2 - 1 Experimental studies of rod bundles (1).. 132
Table 2 - 2 Experimental studies of rod bundles (2).. 133
Table 2 - 3 Experimental studies of rod bundles (3).. 134
Table 2 - 4 Experimental studies of rod bundles (4).. 135
Table 2 - 5 Computational studies of rod bundles (1) 136
Table 2 - 6 Computational studies of rod bundles (2) 137
Table 2 - 7 Computational studies of rod bundles (3) 138
Table 4 - 1 Cases studied for the selection of grid and time step resolution 139

List of Figures

Figure 1 - 1 Typical rod bundle arrangement in nuclear reactor cores 140

Figure 1 - 2 Examples of complex channels 141

Figure 1 - 3 Sketch of an idealized concentric annular channel flow 141

Figure 1 - 4 Catheter in blood flow through an artery 142

Figure 1 - 5 Train moving in a tunnel 142

Figure 1 - 6 Sketch of a flooded river cross-section 143

Figure 1 - 7 Flow in a typical CANDU rod channel 143

Figure 1 - 8 Fuel bundle types and generated power 144

Figure 4 - 1 Sketches of the single rod duct showing a) the computational geometry and b) the computational mesh on the y-z plane, also showing details in the gap region and near the bottom wall 145

Figure 4 - 2 Cross-section of the computational geometry and mesh details of the 37-rod bundle. 146

Figure 4 - 3 Variation of the time-averaged streamwise velocity at $z/D=1$, $x/D=10$ in the single-rod duct, near the bottom wall (■: case 1 ; —: case 2 ; ♦: case 3 ; ▲: case 4) 147

Figure 6 - 1 a) Isocontours of the time-averaged dimensionless axial velocity in the GT experiments (left) and the present simulations (right) b) vector plots of the time-averaged velocity component (left) and projected streamlines (right) on a cross-sectional plane in the present simulations 148

Figure 6 - 2 Isocontours of time-averaged, non-dimensionalized axial rms velocity fluctuation u'/U_b : GT measurements (left) and present simulations (right) 149

Figure 6 - 3 Isocontours of time-averaged, non-dimensionalized spanwise rms velocity fluctuation w'/U_b : GT measurements (left) and present simulations (right) 150

Figure 6 - 4 Isocontours of time-averaged, non-dimensionalized transverse rms velocity fluctuation v'/U_b : GT measurements (left) and present simulations (right) 151

Figure 6 - 5 Isocontours of time-averaged, non-dimensionalized turbulent kinetic energy unit mass $\bar{k}/U_b^2$: GT measurements (left) and present simulations (right) 152

Figure 6 - 6 Isocontours of time-averaged, non-dimensionalized transverse turbulent shear stress $\overline{uv}/U_b^2$: GT measurements (left) and present simulations (right)..... 153

Figure 6 - 7 Isocontours of time-averaged, non-dimensionalized spanwise turbulent shear stress $\overline{uw}/U_b^2$:GT measurements (left) and present simulations (right)..... 154

Figure 6 - 8 Isocontours of time-averaged, non-dimensionalized axial turbulent shear stress $\overline{vw}/U_b^2$: GT measurements (left) and present simulations (right)..... 155

Figure 6 - 9 Isocontours of time-averaged, non-dimensionalized transverse turbulent shear stress coefficient $\overline{uv}/u'v'$: GT measurements (left) and present simulations (right) 156

Figure 6 - 10 Isocontours of time-averaged, non-dimensionalized spanwise turbulent shear stress coefficient $\overline{uw}/u'w'$: GT measurements (left) and present simulations (right) 157

Figure 6 - 11 Isocontours of time-averaged, non-dimensionalized axial turbulent shear stress coefficient $\overline{vw}/v'w'$: GT measurements (left) and present simulations (right) 158

Figure 6 - 12 Predicted isocontours of the percent ratio of the coherent components to the totals : a) streamwise rms velocity ratio $\overline{u_c'}/\overline{u'}\times 100$; b) spanwise rms velocity ratio $\overline{w_c'}/\overline{w'}\times 100$; c) transverse rms velocity ratio $\overline{v_c'}/\overline{v'}\times 100$; and d) turbulent kinetic energy ratio $\bar{k}_c/\bar{k}\times 100$ 159

Figure 6 - 13 Comparison of present simulations (open symbols) with GT measurements (solid symbols) for total averages (□, ■) and coherent (Δ, ▲) parts on the equidistant plane : a) streamwise normal stress ; b) transverse normal stress ; c) spanwise normal stress ; the simulation results have been connected by solid lines as an aid to the eye 160

Figure 6 - 14 Coherent structures identified by the Q criterion ; the section shown is $20D$ long ; front view also shown for relative locations of coherent structures from the rod 161

Figure 6 - 15 Predicted isocontours on the equidistant plane of : a) the dimensionless instantaneous static pressure $P/(1/2\rho U_b^2)$; b) the dimensionless instantaneous spanwise velocity W/U_b ; coherent structures identified by the Q criterion are also shown in all plots, all plots are $7.2D$ long and $3D$ high 162

Figure 6 - 16 Experimental (a) and simulated (b) surface streamlines of velocity fields as seen by an observer moving with the average convective speed of the coherent structures 163

Figure 6 - 17 a) Representative time histories of the spanwise velocity in the centre of the gap : present simulations (——) and experimental results (----) ; b) the power spectrum, in arbitrary logarithmic scale, of the time history of the simulated spanwise velocity 164

Figure 7 - 1 Predicted isocontours of the dimensionless time-averaged temperature difference $\overline{\Theta} = \left(\overline{T} - \overline{T}_b\right)/\left(\overline{T}_{\mathrm{rod,m}} - \overline{T}_b\right)$; the left-side plots correspond to the uniform rod temperature case and the right-side plots to the uniform rod heat flux case 165

Figure 7 - 2 Predicted isocontours of the standard deviation of the normalized coherent temperature fluctuations $\sqrt{\overline{\vartheta_{co}^2}}\Big/\left(\overline{T}_{\mathrm{rod,m}} - \overline{T}_b\right)$; the left-side plots correspond to the uniform rod temperature case and the right-side plots to the uniform rod heat flux case 166

Figure 7 - 3 Predicted isocontours of the standard deviation of the normalized non-coherent temperature fluctuations $\sqrt{\overline{\vartheta_{nc}^2}}\Big/\left(\overline{T}_{\mathrm{rod,m}} - \overline{T}_b\right)$; the left-side plots correspond to the uniform rod temperature case and the right-side plots to the uniform rod heat flux case 167

Figure 7 - 4 Predicted isocontours of the percent ratio of the variances of coherent and total temperature fluctuations $\overline{\vartheta_{co}^2} / \overline{\vartheta^2} \times 100$; the left-side plots correspond to the uniform rod temperature case and the right-side plots to the uniform rod heat flux case 168

Figure 7 - 5 Spanwise variations of the time-averaged (————) and representative instantaneous (- - -, — — —) dimensionless temperature differences Θ on the bottom wall in the uniform rod temperature case (a) and uniform rod heat flux case (b) 169

Figure 7 - 6 Streamwise variations of the time-averaged (———) and representative instantaneous (- - -, — — —) dimensionless temperature differences Θ on the bottom wall at $z/D = 0$ in the uniform rod temperature case (a) and uniform rod heat flux case (b) 170

Figure 7 - 7 Circumferential variations of the time-averaged (———) and representative instantaneous (- - -, — — —) normalized Nusselt numbers $\mathrm{Nu}/\overline{\mathrm{Nu}}_{\mathrm{rod,m}}$ around the rod in the uniform rod temperature case (a) and uniform rod heat flux case (b) ; the values have been normalized by the corresponding circumferential averages 171

Figure 7 - 8 Streamwise variations of the time-averaged (———) and representative instantaneous (- - -, — — —) normalized Nusselt numbers $\mathrm{Nu}/\overline{\mathrm{Nu}}_{m}$ along the rod on the symmetry plane and facing the bottom wall in the uniform rod temperature case (a) and uniform rod heat flux case (b) ; the values have been normalized by the corresponding streamwise averages 172

Figure 7 - 9 Predicted isocontours of the dimensionless instantaneous temperature difference Θ on the equidistant plane in the uniform rod temperature case (a) and uniform rod heat flux case (b) ; coherent structures identified by the Q criterion are also shown in both plots, which are 7.5D long and 3D high 173

Figure 7 - 10 (a) Smoothened power spectra of the spanwise velocity in the centre of the gap in the present simulations (——) and as measured by Guellouz and Tavoularis (2000a) (.....) ; (b) Smoothened power spectra of the resolved temperature in the centre of the gap in the constant rod temperature case (——) and the constant rod heat flux case (.....) 174

Figure 8 - 1 Isocontours of the dimensionless time-averaged streamwise velocity $\overline{U}/U_b$: (a) $\delta/D = 0.10$, (b) $\delta/D = 0.03$ and (c) $\delta/D = 0.01$; plots on the left are near-gap details of those on the right 175

Figure 8 - 2 Isocontours of the dimensionless time-averaged total turbulent kinetic energy per unit mass $\overline{k}/U_b^2$: (a) $\delta/D = 0.10$, (b) $\delta/D = 0.03$ and (c) $\delta/D = 0.01$; plots on the left are near-gap details of those on the right 176

Figure 8 - 3 Isocontours of the dimensionless time-averaged coherent turbulent kinetic energy per unit mass $\overline{k}_c/U_b^2$: (a) $\delta/D = 0.10$, (b) $\delta/D = 0.03$ and (c) $\delta/D = 0.01$; plots on the left are near-gap details of those on the right 177

Figure 8 - 4 Isocontours of the dimensionless time-averaged non-coherent turbulent kinetic energy per unit mass $\overline{k}_{nc}/U_b^2$: (a) $\delta/D = 0.10$, (b) $\delta/D = 0.03$ and (c) $\delta/D = 0.01$; plots on the left are near-gap details of those on the right 178

Figure 8 - 5 Isocontours of the ratio of coherent component and the total time-averaged turbulent kinetic energy per unit mass $\overline{k}_c/\overline{k}\ \times 100$: (a) $\delta/D = 0.10$ and (b) $\delta/D = 0.03$; plots on the left are near-gap details of those on the right ... 179

Figure 8 - 6 Isocontours of the time-averaged dimensionless temperature difference $\overline{\Theta}$: (a) $\delta/D = 0.10$, (b) $\delta/D = 0.03$ and (c) $\delta/D = 0.01$; plots on the left are near-gap details of those on the right 180

Figure 8 - 7 Circumferential variations of the time-averaged (————) and two representative instantaneous (— · —,········) dimensionless temperature differences Θ : (a) $\delta/D = 0.10$, (b) $\delta/D = 0.03$ and (c) $\delta/D = 0.01$ 181

Figure 8 - 8 Spanwise variations of the time-averaged (————) and two representative instantaneous (— · —, ········) dimensionless temperature differences Θ : (a) $\delta/D = 0.10$, (b) $\delta/D = 0.03$ and (c) $\delta/D = 0.01$ 182

Figure 8 - 9 Isocontours of the normalized standard deviation of the coherent temperature fluctuations $\sqrt{\overline{\vartheta_c^2}}\,/\left(\overline{T}_{\mathrm{rod,m}} - \overline{T}_b\right)$: (a) $\delta/D = 0.10$, (b) $\delta/D = 0.03$ and (c) $\delta/D = 0.01$; plots on the left are near-gap details of those on the right........ 183

Figure 8 - 10 Isocontours of the normalized standard deviation of non-coherent temperature fluctuations $\sqrt{\overline{\vartheta_{nc}^2}}\,/\left(\overline{T}_{\mathrm{rod,m}} - \overline{T}_b\right)$: (a) $\delta/D = 0.10$, (b) $\delta/D = 0.03$ and (c) $\delta/D = 0.01$; plots on the left are near-gap details of those on the right.... 184

Figure 8 - 11 Isocontours of the percent ratio of the variances of coherent and total temperature fluctuations $\overline{\vartheta_c^2}\,/\,\overline{\vartheta^2} \times 100$: (a) $\delta/D = 0.10$, (b) $\delta/D = 0.03$ and (c) $\delta/D = 0.01$; plots on the left are near-gap details of those on the right........ 185

Figure 8 - 12 Circumferential variations of the time-averaged (————) and representative instantaneous (— · —, ········) normalized skin friction coefficient around the rod ; (a) $\delta/D = 0.10$, (b) $\delta/D = 0.03$ and (c) $\delta/D = 0.01$; the values have been normalized by the corresponding circumferential averages, given in the text........ 186

Figure 8 - 13 Variations of the time-averaged (————) and representative instantaneous (— · —, ········) skin friction coefficients across the span of the bottom wall ; (a) $\delta/D = 0.10$, (b) $\delta/D = 0.03$ and (c) $\delta/D = 0.01$; the values have been normalized by corresponding averages across the span, given in the text........ 187

Figure 8 - 14 Circumferential variations of the time-averaged (———) and representative instantaneous (— · —, ·······) Nusselt number around the rod ; (a) $\delta/D = 0.10$, (b) $\delta/D = 0.03$ and (c) $\delta/D = 0.01$; the values have been normalized by the corresponding circumferential averages, given in the text........ 188

Figure 8 - 15 Variation of the minimum time-averaged Nusselt number on the rod, normalized by the circumferential average ; ▲ present simulations ; ——— curve fitted to Guellouz and Tavoularis' measurements (1992) ; – – – Guellouz's correlation (1998) 189

Figure 8 - 16 Power spectra of the spanwise velocity (a) and the temperature (b) in the center of the gap ; ——— $\delta/D = 0.10$; – – – $\delta/D = 0.03$; — · — $\delta/D = 0.01$. 190

Figure 8 - 17 Variation of the peak Strouhal number in the gap centre with gap size; ● present simulations ; ○ Guellouz and Tavoularis' measurements (2000) ; □ Baratto, Sean and Tavoularis' measurements (2006) ; + Wu and Trupp's measurements (1994) ; ——— Möller's correlation (1991) 191

Figure 8 - 18 Variation of the mixing factor Y with gap size ; ● present simulations; ○ Guellouz and Tavoularis' measurements (2000a) ; + Wu and Trupp's measurements (1994) ; ——— Rehme's correlation (1992); ······· Rogers and Tahir's correlation (1975) 192

Figure 9 - 1 (a) Dimensionless time-averaged streamwise velocity $\overline{U}/\overline{U}_{max}$ around the middle outer rod ; —— simulations ; ○ OT experiments ; (b) predicted isocontours of $\overline{U}/U_b$ 193

Figure 9 - 2 (a) Dimensionless standard deviation of axial velocity fluctuations $u'/\overline{U}_{max}$ around the middle outer rod ; —— simulations ; ○ OT experiments ; (b) predicted isocontours of u'/U_b 194

Figure 9 - 3 (a) Dimensionless standard deviation of azimuthal velocity fluctuations $u'_\phi/\overline{U}_{max}$ around the middle outer rod ; —— simulations ; ○ OT experiments ; (b) predicted isocontours of u'_ϕ/U_b in local coordinates..................................... 195

Figure 9 - 4 (a) Dimensionless standard deviation of radial velocity fluctuations $u'_r/\overline{U}_{max}$ around the middle outer rod ; —— simulations ; ○ OT experiments ; (b) predicted isocontours of u'_r/U_b in local coordinates 196

Figure 9 - 5 (a) Dimensionless time-averaged turbulent kinetic energy per unit mass $\overline{k}/\overline{U}_{max}^2$ around the middle outer rod ; —— simulations ; ○ OT experiments ; (b) predicted isocontours of $\overline{k}/U_b^2$ 197

Figure 9 - 6 Dimensionless time-averaged turbulent shear stress $\overline{uu_\phi}/\overline{U}_{\max}^2$ in the azimuthal direction around the middle outer rod ; —— simulations ; ○ OT experiments 198

Figure 9 - 7 Dimensionless time-averaged turbulent shear stress $\overline{uu_r}/\overline{U}_{\max}^2$ in the radial direction around the middle outer rod ; —— simulations ; ○ OT experiments 199

Figure 9 - 8 Dimensionless standard deviations of the predicted (a) coherent u'_c/U_b and (b) non-coherent u'_{nc}/U_b axial velocity fluctuations 200

Figure 9 - 9 Dimensionless standard deviations of the predicted (a) coherent $u'_{\phi c}/U_b$ and (b) non-coherent $u'_{\phi nc}/U_b$ azimuthal velocity fluctuations in local coordinates 201

Figure 9 - 10 Dimensionless standard deviations of the predicted (a) coherent $u'_{r,c}/U_b$ and (b) non-coherent $u'_{r,nc}/U_b$ radial velocity fluctuations in local coordinates.... 202

Figure 9 - 11 Dimensionless kinetic energies of the predicted (a) coherent $\overline{k_c}/U_b^2$ and (b) non-coherent $\overline{k_{nc}}/U_b^2$ velocity fluctuations 203

Figure 9 - 12 Predicted variance ratios of the coherent and total (a) axial velocity fluctuations $\overline{u_c^2}/\overline{u^2}\times 100$ and (b) azimuthal velocity fluctuations $\overline{u_{\phi,c}^2}/\overline{u_\phi^2}\times 100$ in local coordinates 204

Figure 9 - 13 Predicted variance ratios of time-averaged coherent and total (a) radial velocity fluctuations $\overline{u_{r,c}^2}/\overline{u_r^2}\times 100$ in local coordinates and (b) kinetic energies $\overline{k_c}/\overline{k}\times 100$ 205

Figure 9 - 14 Circumferential variations around the middle outer rod of (a) the predicted time-averaged wall shear stress (————) and that measured by OT (– · –) ; (b) the predicted time-averaged wall shear stress (————) and representative instantaneous ones (- - -, – · –) ; the values have been normalized by the corresponding circumferential averages (0.63 Pa for both the simulations and the OT experiments) 206

Figure 9 - 15 Two isometric views of coherent structures identified by the modified Q criterion : (a) square subchannels on a radial plane ; (b) wall subchannels between rods of the third ring and the wall of pressure tube 207

Figure 9 - 16 Inner views of the rod bundle showing coherent structures ; the rod in the center of each view has been made invisible, so that coherent structures in the surrounding subchannels can be seen 208

Figure 9 - 17 Smoothened power spectra of the azimuthal velocity in local coordinates in selected gap centers ; each spectrum has been shifted by a different distance along the logarithmic axis to prevent overlapping (arbitrary scale) 209

Figure 9 - 18 Auto-correlation coefficients of the azimuthal velocity in the centers of selected gaps ; each curve has been shifted by a different distance along its axis to prevent overlapping (see Fig. 9-17 for nomenclature) 210

Figure 9 - 19 Cross-correlation coefficients between the azimuthal velocity fluctuations in the center of gap 3M-O and those in other selected gaps ; each curve has been shifted by a different distance along its axis to prevent overlapping (see Fig. 9-17 for nomenclature) 211

Figure 9 - 20 Cross-correlation coefficients between the azimuthal velocity fluctuations in the center of the gap 3M-O and the velocity fluctuations tangential to the maximum velocity line; each curve has been shifted by a different distance along its axis to prevent overlapping 212

Figure A 1 Isocontours of the time-averaged dimensionless axial velocity in the GT experiments (left) and the developing flow simulations (right) 214

Nomenclature

A	=	cross sectional area
C_w	=	wall reflection coefficient
c_f	=	skin friction coefficient, $\frac{\tau_w}{1/2\,\rho U_b^2}$
c_p	=	specific heat at constant pressure
c_q	=	empirical factor in modified Q criterion
D	=	rod diameter
D_h	=	hydraulic diameter, $\frac{4A}{P_m}$
D_{ij}	=	turbulent diffusion tensor
f	=	frequency of flow pulsations
f_p	=	peak frequency of flow pulsations in power spectrum

f_{tube} = friction factor for smooth circular tubes

h = local heat transfer coefficient

k = turbulent kinetic energy per unit mass

L = streamwise length of the duct

$\dot{m}$ = mass flow rate

Nu = Nusselt number, $\dfrac{hD_h}{\kappa}$

P = static pressure; also, pitch (distance between adjacent rod centers in a rod bundle)

P_m = wet perimeter

Pr = Prandtl number, $\dfrac{\mu c_p}{\kappa}$

p = non-coherent static pressure fluctuation

$\dot{Q}$ = convective heat transfer rate between subchannels

$\dot{q}$ = local heat flux

Re = Reynolds number, $\dfrac{\rho U_b D_h}{\mu}$

Re_T	=	turbulent Reynolds number, $\mathrm{Re}_T = \dfrac{\rho k_{nc}^2}{\mu \varepsilon_{nc}}$
r	=	normal wall distance
S_{ij}	=	strain rate tensor, $\dfrac{1}{2}\left(\dfrac{\partial U_i}{\partial x_j} + \dfrac{\partial U_j}{\partial x_i}\right)$
St	=	Strouhal number, $\dfrac{f\,D}{U_b}$
T	=	temperature
T_b	=	bulk temperature
t	=	time
t_c	=	average flow turn-over time, L/U_b
t_f	=	characteristic time of temperature fluctuations
U, V, W	=	time dependent velocity components
U_b	=	bulk velocity
U_c	=	convective velocity of coherent structure
U_i, i=1,2,3	=	resolved, time dependent "coherent" velocity tensor
u^*	=	friction velocity, $\sqrt{\dfrac{\tau_w}{\rho}}$

u_i, i=1,2,3 = non-coherent velocity fluctuation tensor

u, u_r, u_ϕ, v, w = time dependent velocity fluctuation components

$u', u'_r, u'_\phi, v', w'$ = rms velocity fluctuation components

$\overline{uv}, \overline{uu_r}, \overline{uu_\phi}, \overline{uw}, \overline{vw}$ =time-averaged turbulent shear stress components

W = sum of the rod diameter and gap width

w_{eff} = effective mixing velocity across the gap

x, r, ϕ = streamwise, radial and azimuthal coordinates, respectively

x, y, z = streamwise, transverse and spanwise coordinates, respectively

x_i, i=1,2,3 = coordinate tensor

Y = empirical mixing factor

Y_R = Reheme's empirical mixing factor

y^+ = dimensionless distance from the wall, $\dfrac{\rho u^* y}{\mu}$

Greek symbols

α_{ij} = Reynolds-stress anisotropy tensor, $\dfrac{\tau_{ij-nc} - 2/3\, k_{nc}\delta_{ij}}{k_{nc}}$

Γ_{ij}	=	production tensor
γ	=	thermal diffusivity coefficient
δ	=	gap between the rod wall and the adjacent plane wall
δ_{ij}	=	Kronecker delta
δ_{12}	=	mixing distance between two subchannels
ε	=	local turbulent kinetic energy dissipation rate
η	=	Kolmogorov microscale
η_k	=	x_k component of the unit normal to the wall
Θ	=	dimensionless temperature difference
ϑ	=	temperature fluctuation
κ	=	von Kármán constant ; also, thermal conductivity of the fluid
λ	=	Taylor microscale
λ_{cs}	=	streamwise spacing between two consecutive coherent structures
μ	=	dynamic viscosity of the fluid
μ_T	=	dynamic eddy viscosity of the fluid

ν = kinematic viscosity, $\frac{\mu}{\rho}$

ν_T = kinematic eddy viscosity

ν_{tube} = kinematic eddy viscosity for circular tube

Π_{ij} = pressure-strain rate tensor, $p\left(\frac{\partial u_i}{\partial x_j}+\frac{\partial u_j}{\partial x_i}\right)$

$\Pi_{ij,f}$ = fast term of pressure-strain rate tensor

$\Pi_{ij,s}$ = slow term of pressure-strain rate tensor

$\Pi_{ij,w}$ = wall-reflection term of pressure-strain rate tensor

ρ = density

σ_T = turbulent Prandtl number

τ = time difference

τ_{ij-nc} = non-coherent, time-dependent Reynolds stress tensor, $\left(u_i u_j\right)_{nc}$

τ_w = wall shear stress

χ = normal distance from the wall

Ω_{ij}	=	rotation tensor, $\frac{1}{2}\left(\frac{\partial U_i}{\partial x_j}-\frac{\partial U_j}{\partial x_i}\right)$

Subscripts

b	=	bulk quantity
c	=	coherent quantity
cr	=	critical value
m	=	averaged quantity in streamwise direction
max	=	maximum quantity
nc	=	non-coherent quantity
rb	=	quantity for the rod bundle simulation
rod	=	rod surface
rod,m	=	circumferentially-averaged quantity
sr	=	quantity for the single-rod duct simulation
T	=	turbulent quantity
tube	=	quantity for circular tube

Superscripts

+	=	quantity non-dimensionalized by wall scales

Other notation

$\overline{(\ )}$	=	time-averaged quantity
$(\ )'$	=	root mean square fluctuation

Chapter 1. Introduction

1.1. Overview on axial flows in complex channels

Axial flows in complex channels with narrow axial subchannels can be found in a wide range of industrial and environmental systems. Common examples are rod bundle flows in nuclear reactors, annular flows in heat exchangers and mixers, and river flows in channels composed of a deep main channel and shallow flood plains.

The cores of most nuclear reactors consist of rod bundles with coolant or moderator flowing axially through the subchannels formed between the rods. Examples of rod bundles employed in current nuclear reactors are shown in **Figure 1 - 1**. Some conventional heat exchangers also encompass clusters of tubes cooled by axial, turbulent flow through the subchannels, as seen in **Figure 1 - 2**. The same figure also shows a typical CPU cooling fin system, on which a fan is installed to blow air through the fins. Of particular interest is the coolant flow through gap regions between adjacent subchannels. It is well known that turbulent flows in rod bundles exhibit patterns not present in pipe flows.

Other examples of axial flows commonly encountered in engineering applications are the eccentric or concentric annular flows (**Figure 1 - 3**). Concentric annular flows formed by two immiscible liquids like water and oil are one application of axial flows to lift heavy oil in oil wells. This flow can be obtained through the lateral injection of small quantities of water, in order to lubricate the oil core along the pipe (Prada and Bannwart, 2000). For long-distance transportation of heavy oil inside horizontal pipes, the advantage of using water as a lubricant, thus creating eccentric annular flow, has been explored by the petroleum industry. An application of annular flows of medical interest is the blood flow in an artery containing a catheter inserted for diagnostic purposes (**Figure 1 - 4**) or a stent whose function is to dilate a clogged section. One additional example of axial flows in nearly annular channels is air flow caused by a train moving inside a tunnel (**Figure 1 - 5**). Finally, a flooded river is another example of axial flows with narrow subchannels, as it is composed of shallow flood plains adjacent to a much deeper main channel (**Figure 1 - 6**).

During the last three decades, numerous experiments have been conducted in such channels and various physical models to explain the complex flow distribution near the gap region have been suggested. The unusual transporting mechanisms in gap regions adjacent to relatively wide open flow regions have attracted great interest in many engineering applications, and there is much controversy among researchers on how and why gap regions affect single-phase and two-phase flows. It has been recognized that the flow characteristics and the heat and mass transfer in such channels depend greatly upon the properties of strong coherent structures that form in the gap regions. These structures are of main interest to the present research.

1.2. Thermo-hydraulics of the CANDU nuclear reactor core

Nuclear reactors provide 48 % of Ontario's electricity, while, in Canada, about 14% of the total electricity supply is nuclear (source: Electric Power in Canada 1997, Natural Resources Canada). Ontario's power outage of 14 August 2003 and the ratification of the Kyoto Protocol on climate change have intensified interest in safety and operation of nuclear power plants. A study by Deutch and Moniz (2003) noted that a global tripling of nuclear power generation could eliminate nearly two billion tones of carbon emissions annually. This study mentions that four critical problems, including relatively high cost compared to natural gas and coal cost, safety, radioactive waste, and nuclear weapon proliferation, must be overcome for commercial nuclear power plants to become competitive (Dawson, 2003). Before dealing with characteristics of nuclear reactor core flows, it is worth to explain briefly the operating concept of nuclear reactors in Canada.

In contrast to the long vertical fuel assemblies of a pressurized water reactor (PWR), the core of a CANDU (CANada Deuterium Uranium) reactor, as a type of pressurized heavy water reactor (PHWR), holds a horizontal array of fuel channels, each of which typically contains 12 fuel bundles. A fuel channel consists of a Zirconium-Niobium alloy pressure tube containing fuel rods, kept apart by spacers and cooled by heavy water (deuterium oxide, D_2O) for CANDU-6 or light water (H_2O) for ACR (Advanced CANDU Reactor) under a high pressure of 10 MPa. The coolant flows parallel to the rod axes in the complex channels among adjacent rods and between rods and the pressure tube. The pressurized coolant from the fuel channels is taken to the steam generators, where it produces steam to drive turbines, which are coupled to electric generators for the production of electricity. **Figure 1 - 7** shows a typical fuel bundle of the CANDU reactor.

A horizontal, cylindrical vessel (the calandria tube) surrounds the pressure tube array and contains heavy water moderator.

AECL (Atomic Energy of Canada Limited), along with KAERI (Korea Atomic Energy Research Institute), have recently developed the 43-element CANFLEX bundles (CANDU FLEXible fuelling) for the ACR (Advanced CANDU Reactor)-700 (http://www.aecl.ca). The CANFLEX fuel bundle has nearly the same dimensions as the standard 37-element bundle used in a CANDU 6 reactor. A single rod bundle of ACR-700 is 50 cm long, with a diameter of 10 cm. The water is at nearly 312 °C at the exit of a channel and develops a pressure about one hundred times the normal atmospheric pressure (Robertson, 1990). Typical operating conditions and dimensions of the two reactors are summarized in **Table 1 - 1**. The tighter packing of the CANFLEX rod bundle, compared to that of CANDU 6, results in narrower gaps between rods and between rods and the pressure tube (**Figure 1 - 8**).

The mixing mechanism between subchannels of rod bundles is quite complex and difficult to analyze. **Figure 1 - 8** shows the relationship between element numbers of fuel bundles and the power of the reactor. For an advanced nuclear design, higher conversion ratios, defined as the ratio of produced power to heat generated from the fuel bundle, are preferable in most cases. To ensure high power density, rod bundles are tightly packed, forming narrow gaps among adjacent rods or an outer rod and the containing duct wall. The size of these gaps may be distorted as a result of thermally induced rod deformation or flow induced vibrations. Potentially, this could lead to local overheating of the coolant and, in the case of a liquid coolant, boiling and dryout, which could catastrophically affect the operation of the system. Increased mixing across the gap would have a beneficial effect, tending to reduce the local maximum temperature. Three transport mechanisms, which can contribute to the mixing process in fully developed turbulent flow near gap regions, have been identified: convection by mean motion, turbulent convection, and turbulent diffusion (Wu, 1995). The first mechanism represents secondary flows of the second kind, generated by non-uniformity of turbulent stresses. Turbulent convection is associated with large-scale eddies comparable in size to the geometric characteristic length and is of non-gradient type. Turbulent diffusion is caused by small-scale turbulence, which is compatible with the gradient transport concept. There is consensus that, for narrow gaps, turbulent convection, caused by quasi-periodic, large-scale, coherent, vortical structures, is the dominant inter-subchannel mixing mechanism (Guellouz and Tavoularis, 2000a,b; Chang and Tavoularis, 2005a,2006; Row *et al.*, 1974; Möller ,1992; Rehme, 1992; Wu, 1995).

It is also well known that the local heat transfer coefficient in the gap region is weakly dependent on the gap size, except for extremely narrow gaps (Guellouz and Tavoularis, 1992; Groeneveld, 1973), whereas the turbulent kinetic energy in the gap region increases strongly with decreasing rod spacing within the examined ranges (Wu, 1995; Guellouz and Tavoularis, 2000a; Row *et al.*, 1974; Möller ,1992; Rehme, 1992).

Inter-subchannel mixing mechanisms may be classified into the following four categories (Lahey and Moody, 1984).

- Turbulent mixing across a subchannel boundary. This is due to turbulent stochastic pressure and flow fluctuations between subchannels, which cause momentum and heat transfer between the subchannels without mass transfer. In two-phase flow, there is also mass transfer, called void diffusion, in addition to existing momentum and heat transfer between the subchannels. The transport mechanisms which contribute to the mixing process in fully developed turbulent flow may be divided into three different phenomena:

convection by mean motion, turbulent convection, and turbulent diffusion (Wu, 1995). Convection by mean motion is the transport by secondary flows of the second kind, which are caused by inhomogeneity of near-wall turbulence. Turbulence convection is due to large-scale eddies, comparable in size to the geometric characteristic length and is of non-gradient type. Turbulent diffusion is caused by small-scale turbulence of the order of magnitude of the dissipation scale.

- Void drift. This is caused by cross flows resulting from the tendency of a two-phase flow to attain hydrodynamic equilibrium state. This cross flow can occur even in the absence of a lateral pressure gradient between subchannels and can cause net transport of the fluids from one subchannel to an adjacent one. This accounts for the tendency of the vapor phase to shift to channels where the flow velocity is higher.
- Diversion cross flow. This is flow caused by pressure gradients normal to the main flow direction. Pressure gradients may be induced by the subchannel geometry, the variation of heat flux and the onset of boiling between subchannels, or by flow area variation caused by blockage from spacers.
- Buoyancy drift. This occurs due to density gradients in horizontal channels.

The combined effects of inter-subchannel mixing mechanisms may influence the detailed flow features inside fuel channels. In single-phase rod bundle flows, it is the turbulent mixing mechanisms that are most significant.

1.3. Motivation for the present study

Of particular interest to the present research is the phenomenon of strong momentum, heat and mass transfer across narrow gaps formed between fuel-containing rods or between such a rod and the surrounding pressure tube in nuclear reactor cores. It has been long established that flow in the gap region is dominated by quasi-periodic, large-scale, flow pulsations across the gap (Rowe, *et al.*, 1974). During the last three decades, the origin of these flow pulsation across gap regions between adjacent subchannels has been of considerable debate among researchers. Early speculations attributing them to secondary flows generated by Reynolds stress anisotropy were contradicted by direct measurements (Trupp and Azad, 1975; Carajilescov and Todreas, 1976; Seale, 1979; Hooper, 1980; Hooper and Wood, 1984; Hooper and Rehme, 1984). Nevertheless, it is now widely accepted that the flow pulsations near the gap regions are associated with large-scale, quasi-periodic, coherent structures.

Among the documented effects of cross-gap flow pulsations is a reduction in the azimuthal variation of both the skin friction coefficient and the heat transfer coefficient on the rod surface (Hooper and Wood, 1984; Hooper and Rehme, 1984; Guellouz and Tavoularis, 1992; Guellouz, 1998), whereas the turbulent kinetic energy in the gap region increases strongly with decreasing rod spacing within the examined ranges (Rowe, *et al.*, 1974; Möller, 1992; Rehme, 1992; Wu, 1995; Guellouz and Tavoularis, 2000a). Moreover, flow pulsations generate large axial and azimuthal turbulence intensities as well as large turbulent shear stress in the gap region (Hooper, 1980; Hooper and Rehme, 1984; Rehme, 1987; Wu and Trupp, 1993; Wu, 1995; Krauss and Meyer, 1998; Guellouz and Tavoularis, 2000a). The characteristic frequency of these pulsations was found to depend on the gap size and the Reynolds number (Rehme, 1987; Wu and Trupp, 1993; Möller, 1991; Möller, 1992; Rehme, 1992; Meyer and Rehme, 1994).

A thorough understanding of these coherent structures and their role in affecting inter-subchannel mixing (or flow pulsation) and the other mixing mechanisms would be of benefit to safety analyses of nuclear reactors and to the design of future, improved rod bundles.

The majority of studies of flow and heat transfer in rod bundles have been experimental, mostly using drastically simplified geometrical models under conditions that are far less complex than those in operating nuclear reactors. The measurement of the flow properties was in most cases restricted to several line traverses or measurements on a single plane. For these reasons, numerical simulations would make an attractive alternative or supplement to experiments.

In the nuclear industry, because of the need for relatively low computational resources, flow and heat transfer in rod bundles have been mostly analyzed with subchannel codes (Rehme, 1992; Carlucci *et al.*, 2004), considering each subchannel as a unit and employing empirical correlations to reference the flow and heat transfer in each subchannel to those in circular tubes (Carlucci *et al.*, 2004). These codes essentially solve one-dimensional conservation equations of mass, axial momentum and energy and take into account turbulent interactions between subchannels by using empirical inter-subchannel mixing coefficients (Rogers and Tahir, 1975). Previous correlations have been based on a diverse database, including experiments with different geometries, levels of flow development, disturbance levels and measurement accuracies (Rogers and Tahir, 1975; Rehme, 1978; Möller, 1991; Wu and Trupp, 1994; Sadatomi *et al.*, 1996). The accuracy of calculated cladding temperature distributions by subchannel analysis is limited by the significant uncertainty of empirical correlations (Rehme, 1978). For example, Sadatomi *et al.* (1996) concluded that a popular correlation by Rehme (1992) gave a 100% overestimation in cross-subchannel mixing for triangular rod bundles and suggested a different correlation, which also deviated by $\pm 35\%$ from the measurements. Another limitation of the available experimental database is that it does not include cases with very small gaps (roughly smaller than 2% of the rod diameter), reflecting the difficulties in conducting measurements under such conditions. Considering that the practice of using subchannel codes will likely continue in nuclear reactor analysis and design, it seems worthwhile to expand the database on which related correlations are based as well as to enhance our understanding of the limitations of such correlations by comparison to reliable numerical simulations.

In general, previous simulations of turbulent flows in rod bundles have assumed that the flow field is stationary and solved the Reynolds averaged Navier Stokes equations (RANS) using conventional gradient-transport-type turbulence models (e.g., Rapley and Gosman, 1986; Baglietto and Ninokata, 2005). Such simulations have achieved a limited agreement with experiments only by the direct use of empirical information applicable to the specific geometry (Wu, 1994; Baglietto and Ninokata, 2005). The use of RANS (Reynolds-averaged Navier-Stokes equations) with general-purpose turbulence models without specific adjustments has provided poor predictions.

For example, Lee and Jang (1997) performed numerical simulations for a rod bundle flow using a nonlinear $k-\varepsilon$ model without any adjustments to conclude that this approach strongly underestimated the strong azimuthal turbulence intensity measured by Hooper (1980). Yadigaroglu *et al.* (2003) conducted an in-depth review of rod bundle numerical simulations, identifying the needs of light water reactor safety analyses. They summarized the numerical simulations of Tzanos (2001) in a square-lattice rod bundle and concluded that gradient-transport models, like the $k-\varepsilon$ model, are not adequate to predict turbulent flow in the narrow gap regions.

Most previous simulations of rod bundles have considered periodic arrays of rods, only solving the flow in elementary sections of such arrays and assuming symmetry across the boundaries (Rapley and Gosman, 1986; Lee and Jang, 1997; Baglietto and Ninokata, 2005). This approach greatly restricts the solution, because, although the geometric configuration may be symmetric, the flow itself may not be so, particularly as it is known to oscillate across gaps. Moreover, most numerical studies have been conducted for either triangular or square subchannels, which may not be representative of entire rod bundles. For example, the 37-rod bundle of the CANDU reactor has three different kinds of subchannels, triangular, square and wall subchannels. Full bundle simulations are required to capture possible interactions among different types of subchannels.

1.4. Objectives of the thesis

The primary objective of this research is to simulate numerically turbulent flow and heat transfer characteristics in a single-rod duct and turbulent flow in a 37-rod bundle. In particular, the research will be focused on the identification of coherent structures forming in the gap regions of such channels and the documentation of their effects on the structure of turbulence, the heat transfer and the mixing process.

To achieve the general objective, this study is divided into four steps. As a first step, the simulations will be restricted to isothermal, single-phase flow in a rectangular duct containing a single cylindrical rod and will be validated by comparison to measurements (Guellouz and Tavoularis, 2005a,b). The second step is an extension of the first one, in which the rod is passively heated to document the effect of coherent structures on the temperature field. The third step focuses on the effect of gap size variation on the velocity and temperature fields near gap region and reassesses the accuracy of previous inter-subchannel mixing estimates. As a fourth and final step, simulations of the time-averaged flow and turbulence characteristics and the unsteady evolution of coherent structures in a 37-rod bundle have been conducted and the predictions have been validated by comparison to available measurements (Ouma and Tavoularis, 1991a,b; Baratto *et al.*, 2006). Overall, the present work is expected to demonstrate the usefulness of the suggested numerical approach in the operation and safety analyses of current nuclear reactors and in the design of future ones.

1.5. Outline of the thesis

Chapter 2 presents a review of the relevant literature, which is mainly related to experimental and computational studies on turbulent structures, turbulent transporting mechanisms, heat transfer and inter-subchannel mixing in rod bundle flows. This is followed by Chapter 3, which introduces relevant turbulence models, and describes inter-subchannel mixing analysis procedures. Chapter 4 introduces the numerical procedures and conditions employed in this study, including mesh generation, boundary conditions and numerical schemes. Chapter 5 focuses on identification methods of coherent structures. The results of the simulations are presented in Chapters 6 to 9. Chapter 6 shows the results of isothermal computations, followed by heated flow computations results in Chapter 7. Results on the gap size effect are presented in Chapter 8 and Chapter 9 presents computations of isothermal flow in a 37-rod bundle. Finally, the main conclusions and recommendations for future research are summarized in Chapter 10.

Chapter 2. Literature review

2.1. Experimental studies

A large number of experimental studies of rod bundle flows have been conducted during the past few decades. The following review will focus on those references which have historical significance and the ones which are most relevant to the present objectives. Conditions of each experimental study are summarized in **Table 2 - 1** to **Table 2 - 4**.

Due to the narrow gaps between adjacent fuel rods in rod bundles, turbulent characteristics of coolant flowing axially through the subchannels are different from those in pipe flows. A phenomenon of particular interest in experimental studies is flow pulsation near the gap region, which enhances mass, momentum and heat transfer between subchannels.

Rowe *et al.* (1974) first revealed the existence of quasi-periodic flow pulsations in a rod bundle, and concluded that they were responsible for the increase of axial turbulence intensities with decreasing gap spacing. They used a Laser Doppler Anemometer to measure velocity of water flow through a square-pitch rod bundle with pitch–to-diameter ratios of 1.25 and 1.125. They found that the flow pulsations became stronger when the rod spacing was decreased and observed relative minima of the turbulence intensity in the subchannel center and in the rod gap center, with values higher than typical values in pipe flow. They also found that the effect of Reynolds number was weak for the larger rod spacing within their Reynolds number range from 50,000 to 200,000. They speculated that turbulent transport would be both diffusive and convective in the regions adjacent to the gaps, whereas turbulent transport in the subchannel centers and rod gaps would be mostly diffusive. They also observed the insensitivity of turbulent mixing to the gap width variation for gap widths larger than 1.12.

Rehme (1978) measured the mean velocity by Pitot tubes, the turbulent shear stresses and turbulent intensities by hot-wire anemometry and the wall shear stress by Preston tubes in a rectangular duct containing a single array of four rods with a pitch to diameter ratio of 1.071. He observed the bulging of isotachs of velocity toward the gap region as well as highly anisotropic turbulence structure in the gap region.

Seale (1979a) conducted measurements in rod arrays with pitch-to-diameter ratios of 1.100, 1.375 and 1.833. He confirmed the previously observed insensitivity of the mixing rate to gap spacing and the failure of numerical prediction methods to reproduce measured characteristics. Seale measured the axial velocity, temperature, inter-subchannel mixing rates and eddy diffusivities under fully developed thermal conditions. He confirmed the high anisotropy of the turbulence in the gap region that was observed by Rehme (1978), and noticed that the anisotropy increased when the gap width was decreased. However, unlike Rehme (1978), Seale did not observe secondary flows in his measurements. In his consequent work, Seale (1979b) attempted to predict the detailed velocity and temperature distributions using the $k-\varepsilon$ turbulence model and concluded that the failure of predictions using turbulent diffusion theory was partially due to the high anisotropy in the gap region.

Hooper (1980) measured the six Reynolds stresses with hot-wire anemometers in a six-rod square bundle with pitch-to-diameter ratios of 1.107 and 1.194 and Reynolds numbers in the range 48,000 to 156,000. He noticed a marked departure of the turbulent flow structure from that in circular pipe flow and its dependence on gap size.

Hooper and Rehme (1984) measured Reynolds shear stresses with hot-wire anemometers in air flow through a rectangular duct containing four rods and another containing six rods. They found that the axial and azimuthal turbulence intensities in the gap region increased strongly with decreasing rod spacing. The azimuthal intensity was higher than that in pipe flow and independent of the wall distance. Using cross-correlation measurements, they confirmed the findings of Rowe *et al.* (1974) that an energetic large-scale and almost periodic flow pulsation exists through the gaps between rods and between rods and duct walls. This flow pulsation reduced the azimuthal variation of both the skin friction coefficient and the heat transfer coefficient. They also found that the frequency of this pulsation was proportional to the Reynolds number and speculated that turbulent flows through rod bundles are dominated by azimuthal turbulent velocity fluctuations which are not associated with mean secondary flows driven by Reynolds-stress gradients, but are generated by a parallel-channel instability. The magnitude of the azimuthal velocity fluctuations was comparable to that of the axial velocity fluctuations. From autocorrelation measurements, both components of the fluctuating velocity were found to be nearly periodic, with the same frequency. Both velocity components had substantial cross-correlation values over a considerable distance from the gap. Hooper and Rehme speculated that the channel instability was the result of pressure differences in adjacent subchannels.

Hooper and Wood (1984) measured mean axial velocity, wall shear stress and all six Reynolds stresses in fully developed square-pitched rod bundle flow with a pitch to diameter ratio of 1.107 in the range of Reynolds numbers from 22,600 to 207,600. They concluded that there was no detectable effect of secondary flow, based on the symmetric distribution of wall shear stress and the existence of logarithmic law of the wall for the mean axial velocity. They also indicated that the circumferential gradient of the azimuthal Reynolds stress tended to equalize the wall shear stress.

Tahir and Rogers (1986) measured Reynolds stresses using a hot-wire anemometer in a triangular rod bundle with a pitch-to-diameter ratio of 1.06 and a Reynolds number of 36000. They found that their velocity measurements were in good agreement with the universal law of the wall on smooth surfaces. They found high turbulence anisotropy near gap regions, which showed trends similar to those in Rehme's (1978) experiment, and attributed the failure of computational analyses based on eddy viscosities to this anisotropy.

Abdelghany and Eichhorn (1986) used a hot film probe to measure the distribution of the wall shear stress and a hot wire anemometer to measure the axial turbulence intensity in a rectangular 3 x 6 rod bundle with a pitch to diameter ratio of 1.33. They detected the existence of secondary flows from distortions of the turbulence intensity contours and wall shear stress distributions but did not measure secondary flows directly. With respect to Rehme's (1978) hypothesis of inter-subchannel instability, they could not observe regularity in the hot wire measurements that would support this hypothesis.

Rehme (1987b) used hot wire techniques to measure axial and azimuthal turbulence intensities in a rectangular channel containing a four-rod bundle. He pointed out that the high and almost uniform values of the axial turbulence intensity cannot not be associated with the normal wall-shear turbulence generating mechanism. The levels of the azimuthal turbulence intensity away from the wall were higher than those close to the rod surface, which implies that they cannot be due to secondary flows. He found that the azimuthal turbulence intensity in the open flow region increased from a value comparable to the one for pipe flow near its centre to a relative maximum in the rod-rod gap and an absolute maximum at the centre of the rod-wall gap. He also observed that the maximum of the azimuthal turbulence intensity increased as the gap width decreased. His cross correlation measurements confirmed that the cyclic momentum exchange by a pulsating flow between subchannels is the reason for the increased levels of axial and azimuthal turbulence intensities in the open gap areas of rod bundle flow and for high levels of the Reynolds stress parallel to the walls. The turbulent mixing between subchannels was insensitive to the gap variation because of the inter-subchannel flow pulsation. He finally proposed that the generating mechanism for the inter-subchannel flow pulsations might be static pressure instability between the subchannels, which is the transverse pressure difference between subchannels when the local axial pressure gradient decreased due to a decrease of mass flow in one subchannel.

Rehme (1987c) measured the mean velocity, wall shear stresses, and turbulent stresses in the same rod bundle as the one used by Rehme (1987b), having a pitch-to-diameter ratio of 1.30. He found that the highest kinetic energy and axial turbulence intensity were located on the lines of maximum distance from the walls, even though the rod spacing was relatively large. He concluded that a periodic momentum transport across the gaps of the rod bundle existed. However, he reminded that flow was not fully developed at the measuring section. In his consequent work, Rehme (1992) developed a simple correlation of a mixing factor applicable to any gap geometry.

Tavoularis *et al.* (1988) measured mean and turbulent velocity and wall shear stress done in a model of a 60° circular sector of a 37-rod bundle of the CANDU reactor with a pitch-to-diameter ratio of 1.40 and Reynolds number based on hydraulic diameter and bulk subchannel velocity of 50,000. They assessed the effect of flow obstruction by rod spacers and the effect of relative orientation of rod bundles in tandem. They found that the presence of endplates and an upstream rod enhanced the early development of the flow.

By measuring turbulent characteristics in the same test rig as Rehme (1987b), Möller (1991) suggested an empirical correlation for the Strouhal number (dimensionless frequency), which was inversely proportional to the gap width and independent of the Reynolds number. The spectra of the pressure difference measured with two microphones placed symmetrically on the two sides of the gap showed a pronounced peak at the same frequency as the peak in the velocity fluctuation spectra. He confirmed the presence of large-scale coherent structures propagating on either side of the rod by looking at the cross correlation functions of fluctuating velocities. He formulated a phenomenological model that represented these structures as pairs of vortices that were responsible for the mass exchange between the subchannels of rod bundles.

Ouma and Tavoularis (1991a; 1991b) investigated single-phase, isothermal turbulent flow in a model of 60° section of a 37-rod CANDU reactor bundle as a function of the rod-wall gap size at a Reynolds number of 48,000. The results showed that wall shear stress in open regions of the subchannel increased while wall shear stress in gap regions decreased with decreasing gap size. They also found that the averaged wall shear stress was insensitive to the gap size, but that the local wall shear stress near the gap region decreased appreciably, especially for values of gap-to-diameter ratios less than 0.05. They measured the transverse mean velocities, which were less than 1% of the bulk velocity, and attributed the bulging of contours of kinetic energy to transport by secondary flows.

Möller (1992) proposed a correlation for the mixing factor as a function of the dimensionless gap size. He demonstrated that large-scale coherent structures were the main reason for the high mixing rates between adjacent sub-channels. He concluded that the frequency of those structures was determined by the geometry of the gap, it increased with decreasing gap size and was proportional to the bulk velocity.

Rehme (1992) confirmed that cyclic and periodic flow pulsations through the gaps are the reason for the observed mixing rates, which are relatively independent of the gap width. He reviewed previous experiments in detail and suggested that secondary flows do not contribute significantly to the mixing between subchannels of rod bundles because secondary flow vortices do not cross the gaps between the subchannels.

Guellouz and Tavoularis (1992) measured heat transfer characteristics around an outer rod of a 5-rod bundle which was a scaled model of an outer segment of the 37 rod bundles for CANDU. A heating block made of copper and embedded in a cast cement shroud was used to simulate the local effect of heating on the rod's surface. The geometry of the facility and the Reynolds number were the same as those in the Ouma and Tavoularis (1991) experiments. Their measurement showed that the local heat transfer coefficient was minimum near the gap and maximum in open flow regions and had a similar trend with the skin friction coefficient. The average coefficient of heat transfer was less sensitive to gap size variation than the local one was. They provided a comparison for local heat transfer coefficient based on the variation of gap sizes with the data available from open literature and concluded that local heat transfer coefficient would become highly sensitive to gap size only at very narrow gaps.

Wu and Trupp (1993) measured the turbulence intensity distribution formed by a single rod in a trapezoidal duct with a hot-wire anemometer at four different wall-to-diameter ratios. The existence of large scale coherent structure was confirmed from the location of regions of high turbulence kinetic energy near the gap. The axial turbulence intensity distributions showed a dependence on the relative gap size variation similar to those observed by Rehme (1992) and Möller (1992). Wu and Trupp (1993) further concluded that secondary flows affected the wall shear distribution within a subchannel but did not appear to have a dominant effect on inter-subchannel mixing across the gap. They also confirmed the existence of large-scale coherent structures from power spectra measurements.

Meyer (1994) measured turbulence characteristics and heat flux in a heated flow through a fuel bundle of 37 parallel rods, and compared his results with data in isothermal flow in the same apparatus and in heated flow in pipes. He explained the measured wall shear stress and wall temperature distributions by the presence of periodic flow fluctuation near the gap region.

Meyer and Rehme (1994) used hot-wire anemometry to measure flow characteristics in two channels connected by a gap and a channel with a slot. They observed quasi-periodic large-scale coherent structures in any longitudinal slot or groove in a wall or connecting gaps between two flow channels. The frequency of those structures was determined by the geometry of the slot, increased with decreasing length and width of the gap and was linearly dependent on the bulk velocity. They proposed a physical model assuming that the higher velocities outside the gap drove two vortices and rotated them in opposition directions. Then, these vortices were transported axially within the gap. They also concluded that momentum and heat transfer processes in the rod-gap area for turbulent flow through closely spaced rod arrays are governed by a low-frequency quasi-periodic fluctuation of the velocity component crossing the gap regions.

Wu (1995) carried out hot-wire measurements to investigate the turbulent flow characteristics and large-scale coherent structure in rod-to-wall gap regions, formed by a single rod asymmetrically mounted in a trapezoidal duct, which were an extension of the extensive symmetric rod bundle subchannel measurements by Wu and Trupp (1993). Based on the wall shear stress distribution, secondary flow from each duct corner was shown to carry momentum from the subchannel centre to the corner region. He also found a local maximum on the wall shear stress distribution, which he explained by strong flow pulsations across the gap, whose amplitude depended on the subchannel geometry. Regions of high turbulent kinetic energy were located near the narrow gap region confirming the existence of large-scale eddy motions.

Krauss and Meyer (1996) measured the detailed turbulent characteristics in a central channel of a heated 37-rod bundle with a pitch-to-diameter ratio of 1.12 and a wall gap-to-diameter ratio of 1.06. They observed no measurable difference in isocontours of mean velocity between the isothermal and heated case. The slopes of logarithmic plots for the law of the wall at different locations were compared, with the highest slope found in the rod-to-wall gap and the lowest slope in the rod-to-rod gap region.

Krauss and Meyer (1998) studied air flow in a central channel of heated 37-rod bundles with triangular rod arrays at two different pitch-to-diameter ratios (P/D=1.12 and P/D=1.06) and different heat fluxes. They measured time averaged flow velocities, temperatures, wall shear stresses and wall temperatures, as well as turbulent characteristics including the turbulent kinetic energy, Reynolds stresses and turbulent heat flux. They suggested that large-scale periodic coherent structures in the gap region of two adjacent rods were responsible for the high values of the axial intensity even at large distances from the surrounding wall. They observed that the wall shear stress, the wall temperature distribution and the intensity of large-scale pulsations depended on the gap size. They confirmed the linear dependence of the frequency of the pulsations on the Reynolds number, as was also observed by Möller (1991, 1992). They also measured the coherence function between velocities at two points to investigate the relationship between coherent motions in adjacent gaps.

Guellouz and Tavoularis (2000a) measured the variations of the Reynolds-averaged mean velocity, wall shear stress and turbulent stresses in a rectangular channel containing a single-cylindrical rod, which is perceived to be an elementary rod bundle. They observed the bulging of mean axial velocity contours towards the corners of the rectangular duct and the symmetry plane of the duct. Secondary flows of second kind could possibly contribute to the mean axial velocity bulging towards the corners of the duct but not to the bulging towards the symmetry plane, because the increases of axial and azimuthal turbulence intensities in the gap region increased from the wall to a local maximum, a phenomenon that is not compatible with the anticipated effect of secondary flows. They found that the azimuthal variation of the mean skin friction coefficient was only weakly dependent on the change of the gap-to-diameter ratio in the range between 0.15 and 0.25, but further decrease of this ratio led to an increase of the variation of this coefficient. They used spectral analyses and space-time correlation measurements to investigate the presence of large-scale, quasi-periodic coherent structures in the vicinity of the gap and proposed a correlation for the spacing of the coherent structures, which is in agreement with the results of Möller (1991). They identified these large-scale, quasi-periodic coherent structures as an array of vortices across the gap region. In a companion article, Guellouz and Tavoularis (2000b) further characterized these large-scale coherent structures by conducting conditional sampling measurements. They also explained the relative insensitivity of the local friction factor and heat transfer coefficient to the gap size of rod bundles by considering the combined effects of the strength, spacing, convection speed and lateral extent of the coherent vortices on the inter-subchannel mixing. They concluded that viscous effects would hinder the coherent structures from crossing the gap if the gap size were less than the value for which the heat transfer and the mixing start to effectively decrease is the gap width. Isocontours of the three coherent velocity components in a frame traveling with the averaging convection speed visualized the streamwise spacing of the coherent structures and the presence of a street of pairs of counter-rotating vortices with axes alternating on either side of the gap.

Barratto *et al.* (2006) used cross-wire anemometry to identify the flow pulsations around an outer rod of 5-rod bundle which was a scaled model of an outer segment of the 37 rod bundles for CANDU. Their measurements showed that the peak frequency of velocity fluctuations in the gap region was indeed decreased with decreasing gap size in the range $1.015 \leq W/D \leq 1.250$, in sharp contrast to Möller's correlation (1992).

Most recently, Gosset and Tavoularis (2006) conducted an experimental study on laminar instability in a rectangular channel with a cylindrical rod. The instability occurred in the laminar regime in the form of weak flow pulsations across the gap between the rod and the channel wall when the Reynolds number reached a critical value which increased as the gap diminished. As the Reynolds number was increased, the pulsations became stronger and developed, first into hairpin-shaped patterns, then into laminar vortices on either side of the gap. Eventually, the flow became turbulent, albeit preserving a quasi-periodic vortical structure. The Strouhal number of the pulsations increased with increasing Reynolds number.

In summary, most recent measurements have shown that the effect of secondary flows on cross-gap flow pulsations was far less significant than that of coherent structures. These flow pulsations reduce the azimuthal variation of both the skin friction coefficient and the heat transfer coefficient, but also introduce high levels of azimuthal Reynolds stresses in the gap region. Both coefficients reach local minima at rod-wall and rod-rod gaps and local maxima in the open flow regions. The local minima are sensitive to gap size only for very narrow gaps. From previous studies, it appears that the most significant parameter affecting the flow structure is the gap size.

2.2. Analytical models and computational studies

Numerical analyses in rod bundle flows and other complex channel flows can be categorized into analyses of turbulent mixing and simulations using turbulence models. A number of computational studies were summarized in **Table 2 - 5** to **Table 2 - 7**.

2.2.1. Subchannel analyses

Numerical simulations known as subchannel codes approximate the rod bundle as a set of parallel, radially interconnected channels. These analyses need empirical correlations to represent the effect of cross-flow mixing between subchannels and ignores the fine structure of velocity and temperature within the control volumes. The most important models in this approach are the crossflow models and the turbulent mixing models. The three-dimensional nature of fuel bundles may be partially modelled by lumping crossflow effects as source terms in the one dimensional conservation equations of mass, axial momentum and energy, and by the addition of a transverse momentum equation. The codes RELAP5 and CATHARE are programs using subchannel techniques which have been commonly used in industry (Yadigaroglu *et al.*, 2003). The meshing used in these codes is too coarse to account for the three dimensional flow nature such as natural circulation and mixing in containment volumes. Other subchannel analysis codes such as COBRA (Hwang *et al.*, 2000) and ASSERT (Carlucci *et al.*, 2004) use many empirical constants and correlations to simplify the complex interaction processes between subchannels. Rehme (1987b) mentioned that the accuracy of calculated cladding temperature distributions by subchannel analysis might be low, compared with three-dimensional CFD code predictions of fully developed flow, due to the low resolution in the azimuthal direction and the limited capability of empirical correlations for the Nusselt number. The turbulent interactions between subchannels assumed to act as independent parallel channels are taken into account by mixing coefficients, which increase the overall uncertainty (Rehme, 1992).

Teyssedou *et al.* (1992) simulated partially blocked flow subchannels using the time integral of the local instantaneous conservation law and the assumption of a stationary process for their subchannel analysis code and compared two sets of experimental data under single-phase flow condition. They observed inaccuracies downstream of the blockage due to the three-dimensional nature of the wake zone.

Kim and Park (1997) conducted a lumped parameter analysis using the scale analysis method to derive the scale relations of the anisotropic turbulent diffusion factor and the turbulent mixing rate. By comparing their result with the experimental data, they concluded that the flow pulsations is the significant factor that generates the high anisotropy in rod bundle flows and not turbulent diffusion and secondary flows.

Krauss and Meyer (1998) mentioned that the distributed parameter analysis depends on the accuracy of empirical information used on momentum and energy transport.

Su and Freire (2002) presented methods for the prediction of the friction factor and the Nusselt number of fully developed turbulent forced convection in infinite rod bundles arranged in square or hexagonal arrays at pitch-to-diameter ratios lower than 1.2. These methods were based on the law of the wall for velocity and temperature and an empirical expression for the azimuthal variation of the wall shear stress along the rod periphery.

2.2.2. CFD simulations

Rod bundle channel flows have been mostly simulated using conventional gradient transport type turbulence models (RANS) with some exceptions which used large eddy simulations (LES).

Meyder (1975) solved the turbulent flow in a square type rod bundle by introducing a zero-equation model employing an anisotropic eddy diffusivity determined by Prandtl's mixing length hypothesis to improve the isotropic eddy diffusivity model. The anisotropic eddy viscosity was determined by matching experimental and predicted wall shear stress distributions.

Carajilescov and Todreas (1976) predicted fully developed incompressible turbulent flow using an one-equation turbulence model in a triangular rod bundle and compared the results with their experimental study using Laser Doppler Anemometry. They transformed the Navier-Stokes equation and continuity equation to the axial momentum, vorticity, and streamfunction equations to solve the flow fields using a relationship between the turbulent viscosity and the turbulent kinetic energy per unit mass. Comparison between experimental and analytical axial velocity distributions showed good agreement. They observed a pair of counter-rotating secondary flows and found that the secondary vortex in the gap region became larger by reducing the pitch to diameter ratio from 1.217 to 1.123.

Rehme (1978) used the VELASCO code, which used a zero equation model, to compare against his experimental results for rod bundle flow. He speculated that the considerable difference between his experimental results and results using VELASCO may be influenced by the anisotropy factor, which strongly depended on position. He showed that the highest values of the anisotropy factor were found in the gaps of the rod bundle. He did not achieve an agreement between calculated and experimental shear stresses even though he adjusted the circumferential eddy viscosity as a function of the position. He concluded that turbulent mixing phenomena should be considered in the subchannel analysis.

Trupp and Aly (1979) used an one-equation turbulence model to predict secondary flows in fully developed flow through infinite equilateral triangular arrays of parallel rods at pitch-to-diameter ratios between 1.12 and 1.35 over a Reynolds number range between 27000 and 250000. They focused on the effects of secondary flows and the variations of Reynolds number and spacing on the mean axial velocity, turbulent kinetic energy and shear stress distributions. They concluded that secondary flows became weaker with increasing gap width and vanished for sufficiently large gap widths. They also observed an increased penetration of the secondary flow streamlines into the gap region as the gap width was increased. Their prediction of wall stress showed a large deviation from their experiments (Aly *et al.*, 1978). They attributed these discrepancies to a combination of finite array effects on the experimental data, and error from the assumption of local isotropy in eddy viscosities. They speculated that a prediction using isotropic eddy diffusivity overestimated the secondary flow.

Seale (1979b) applied the $k-\varepsilon$ turbulence model to predict inter-subchannel mixing in rod bundle flow and compared the results with his experiment (1979a). His prediction was in relatively good agreement with the experimental results for a bundle flow with large pitch-to-diameter ratio ($P/D \geq 1.3$). He observed that a computation with anisotropic diffusivity partially reproduced the features of the experimental results and concluded that his results did not support of secondary flow contribution on the inter-subchannel mixing.

Seale (1982) used the empirical stress distribution and the axial vorticity equation in combination with the axial-momentum equation to calculate the secondary velocities. He expressed the differential transport equations for the streamfunction, vorticity, turbulent kinetic energy and its dissipation, and axial velocity in elliptic forms and solved them using an upwind finite-difference method. He suspected that, if the secondary flows were not included in his computation, his prediction would not be compatible with his measurements. He also mentioned the equalizing effect of secondary flows on the wall shear stress variation around the walls of the duct. However, this secondary effect may not be conclusive because of its relative wide gap spacing ($P/D = 1.2$).

Rapley and Gosman (1986) applied a finite-volume method using a simplified algebraic turbulence model of the Reynolds stress transport equation to predict the secondary flow in a triangular rod array with pitch-to-diameter ratios of 1.06 and 1.123. Their predicted results were compared against the measurements of Tahir and Rogers (1979). They concluded that the decrease of secondary flow strength with increase of pitch-to-diameter ratio was consistent.

Kaiser and Zeggel (1987) used a finite element method with an algebraic turbulence model based on the anisotropic eddy viscosity using empirically established mixing length and turbulent kinetic energy distributions. They compared their results with those from VELASCO code for the experiment data of Rehme (1980). Some cases showed more discrepancy from the measurements than VELASCO predictions.

Slagter (1988) conducted a numerical simulation using an one-equation turbulence model and an algebraic stress transport model to predict the velocity distribution for the experimental configuration of Vonka (1988a). The predictions confirmed the main features of the experiments, including the existence of secondary flow.

Mohanty and Sahoo (1988) used an algebraic eddy diffusivity and an one-equation (*k*-*l*) turbulence model to investigate turbulent flow and heat transfer in the subchannels of square and triangular rod bundles with varied pitch-to-diameter ratios. They carried out a heat transfer simulation using a Prandtl number value of 0.7 and the Wassel-Cantton model for the turbulent Prandtl number, as,

$$\mathrm{Pr}_T = \frac{C_3}{C_1 \,\mathrm{Pr}} \frac{\left[1-\exp\left(-C_4/(\nu_T/\nu)\right)\right]}{\left[1-\exp\left(-C_2/\mathrm{Pr}(\nu_T/\nu)\right)\right]}$$

where C_1, C_2, C_3 and C_4 were respectively 0.21, 5.25, 0.2 and 5.0, ν_T is the eddy viscosity for momentum and ν is the kinematic viscosity. Overall, they concluded that the algebraic eddy diffusivity model was preferable to the one-equation model because the average Nusselt number by the one-equation model was found to be substantially lower than the calculation by the 2-D eddy diffusivity. However, their pitch-to-diameter ratios were relatively large (1.2 and 1.3), which caused weak effects on the inter-subchannel mixing across the gap regions. The trend of friction factor variation with variation of Reynolds number was in good agreement with the predictions of Trupp and Aly (1979).

Monir and Tavoularis (1991) applied the VELASCO code to predict wall shear stress distribution and secondary flows in the outer subchannel of a 37-rod bundle with varying gap region size. They concluded that the assumption of secondary flows was necessary to compute the velocity field and the wall shear stress for a comparison with the results obtained by Ouma and Tavoularis (1991).

More recently, Wu (1994) conducted numerical simulations of flow in a trapezoidal channel containing a rod and compared them with the experimental results of Wu and Trupp (1993). He employed the algebraic stress model along with two-equation $k-\varepsilon$ turbulence model. The predicted axial mean velocity contours and normalized turbulent kinetic energy contours were in good agreement with measurements. He acknowledged the limited capability of the conventional $k-\varepsilon$ model for the simulation of the transport mechanism near the gap region, where large-scale coherent structures were evident. To overcome that limitation, he introduced an anisotropic factor based on the results of his experiment.

Biemüller *et al.* (1996) performed a large eddy simulation of turbulent flow in two rectangular channels connected by a gap to identify the presence of large-scale periodic vortices. They used a modified version of the TURBIT-code with a Schumann subgrid scale model, in combination with a wall function. Their predictions of turbulence intensities were in qualitative agreement with their experiment. They noted that their simulation showed one pair of vortices rotating in opposite directions, in agreement with the model proposed by Meyer and Rehme (1994).

Lee and Jang (1997) performed numerical simulations of a rod bundle flow using a nonlinear $k-\varepsilon$ model. They concluded that gradient type turbulence models might not properly predict the large-scale flow pulsations across the gap by eddies comparable in size to the geometric characteristic length in the gap region, as evidenced by a large azimuthal turbulence intensity underestimation, compared to the experimental results of Hooper (1980).

In (2001) studied numerically the effect of four different types of flow deflectors of the grid spacers on the turbulence characteristics in a fuel bundle of a PWR (Pressurized

Water Reactor). He modeled a single subchannel of one grid span using flow symmetry and computed the flow using the commercial CFD code CFX, and the standard $k-\varepsilon$ turbulence model. The predictions showed significant deviations from experimental axial velocity profiles near the spacer.

Tavoularis *et al.* (2002) performed unsteady RANS (Reynolds-averaged Navier-Stokes) simulations with the use of a renormalized group (RNG) $k-\varepsilon$ turbulence model and relatively coarse LES (Large Eddy Simulations) using the Smagorinsky subgrid scale model. They concluded that the flow patterns predicted both by unsteady RANS and LES were qualitatively compatible with the experiments of Guellouz and Tavoularis (2000a). Quantitative comparisons of the periods of flow oscillations across the gap, the streamwise spacings of the coherent structures and their streamwise convection velocities showed significant discrepancies from the experimental values.

Yadigaroglu *et al.* (2003) conducted an in-depth review of rod bundle numerical simulations, identifying the needs of light water reactor safety analyses. They summarized the numerical simulations of Tzanos (2001) in a square-lattice rod bundle and concluded that gradient-transport models, like the $k-\varepsilon$ model, are not adequate to predict turbulent flow in the narrow gap regions.

Most recently, Baglietto and Ninokata (2005) evaluated various turbulence models for a fully developed turbulent flow in a triangular channel. They concluded that a quadratic $k-\varepsilon$ model was promising with some adjustment of model coefficients. But those adjustments were not of universal applicability, because the numerical results were not in good agreement with the experimental results at different Reynolds numbers.

Chapter 3. Theoretical background

3.1. Unsteady Reynolds Averaged Navier-Stokes approach

Among the most popular turbulence models are gradient transport models, such as the $k-\varepsilon$ model. Previous studies with such models have been unable to predict the large-scale flow pulsation across the gap by eddies comparable in size to the geometric characteristic length in the gap region (Lee and Jang, 1997; Wu, 1994). RANS generally produce steady solutions for the mean flow. More recently, time dependent large-scale phenomena have been successfully simulated with the use of unsteady RANS (URANS) simulations, in which the time step and the mesh size are sufficiently small (Lomax and Mehta, 1984; Orszag *et al.* 1996; Hanjalić, 2002; Pasinato *et al.* 2004). In this research, we will undertake unsteady RANS simulations using both $k-\varepsilon$ models and Reynolds Stress Models (RSM). The latter are expected to simulate more realistically the strong turbulence anisotropy in the gap region.

To capture large-scale coherent motion in the unsteady flow, short-time Reynolds averaging is introduced (Wilcox, 2000) as

$$U_i(t) = \frac{1}{\Delta t}\int_{t_0}^{t_0+\Delta t} U_i'\,dt$$

where $U_i' = U_i + u_i$, Δt is larger than the time scale of the random fluctuations and smaller than the time scale of large-scale coherent structures U_i. Short-time averaging acts as a low-pass filter. As pointed out by Wegner *et al.* (2004), URANS can be applied to simulate unsteady flow when the spectral ranges of coherent structures and non-coherent turbulence are separated. If the flow has a narrow spectral peak in the midst of a broadband spectrum of non-coherent turbulence, the short-time Reynolds averaging can be interpreted as ensemble or phase averaging.

The URANS equations are obtained by ensemble averaging or short-time averaging the time dependent three-dimensional Navier-Stokes equations. A resolved, time dependent, "coherent" velocity U_i is computed by solving the following URANS equations for incompressible flow of air:

$$\frac{\partial U_i}{\partial x_i} = 0 \tag{3.1}$$

$$\frac{\partial U_i}{\partial t} + U_j \frac{\partial U_i}{\partial x_j} = -\frac{1}{\rho}\frac{\partial P}{\partial x_i} + \nu \frac{\partial^2 U_i}{\partial x_j \partial x_j} - \frac{\partial \tau_{ij-nc}}{\partial x_j}. \tag{3.2}$$

This process introduces additional unknowns, namely the non-coherent Reynolds stresses, $\tau_{ij-nc} = \left(u_i u_j\right)_{nc}$, which may be treated as extra stresses that arise from the randomness of the flow. Solution of the URANS equations requires the use of turbulence models for the non-coherent Reynolds stresses, which may be given in the form of algebraic or differential equations. No RANS model can be used to solve all types of turbulent flows, because there is a need to adjust the empirical coefficients in the model to get the optimized prediction by direct measurement or by trial-and-error adjustment (Bradshaw, 1997). Such models have found successful applications in engineering design and analysis even though there is no universal RANS model for all applications. RANS simulations have the advantage of lower computing time and computer resource requirements than large eddy simulation (LES) and direct numerical simulation (DNS).

URANS models have been developed to incorporate non-local and flow history effects in the eddy viscosity. The simplest turbulence models introduce a single additional relationship for the turbulent kinetic energy per unit mass k_{nc} as

$$\frac{\partial k_{nc}}{\partial t}+U_j\frac{\partial k_{nc}}{\partial x_j}=\tau_{ij-nc}\frac{\partial U_i}{\partial x_j}-\varepsilon_{nc}+\frac{\partial}{\partial x_j}\left[\left(\nu+\frac{\nu_T}{\sigma_k}\right)\frac{\partial k_{nc}}{\partial x_j}\right]. \tag{3.3}$$

To complete the closure of the turbulent kinetic energy equation, turbulence models can be classified into two categories. The first one includes the turbulent viscosity models employing the gradient transport assumption, proposed by Boussinesq in 1877. The other one includes the Reynolds Stress Models (RSM), which determine the turbulent shear stresses by solving transport equations for each stress component: 4 equations in a two-dimensional isothermal flow and 6 equations in a three-dimensional isothermal flow.

3.1.1. Two-equation turbulence model

The two-equation turbulence models have been the most commonly used in industrial applications. The most popular one is the standard $k-\varepsilon$ turbulence model (Launder and Spalding, 1974). This model utilizes the following relationships.

Kinematic eddy viscosity:

$$\nu_T=C_\mu\frac{k_{nc}^2}{\varepsilon_{nc}}, \tag{3.4}$$

Dissipation rate:

$$\frac{\partial \varepsilon_{nc}}{\partial t}+U_j\frac{\partial \varepsilon_{nc}}{\partial x_j}=C_{\varepsilon 1}\frac{\varepsilon_{nc}}{k_{nc}}\tau_{ij-nc}\frac{\partial U_i}{\partial x_j}-C_{\varepsilon 2}\frac{\varepsilon_{nc}^2}{k_{nc}}+\frac{\partial}{\partial x_j}\left[\left(\nu+\frac{\nu_T}{\sigma_\varepsilon}\right)\frac{\partial \varepsilon_{nc}}{\partial x_j}\right] \tag{3.5}$$

Closure coefficients and auxiliary relations

$$C_{\varepsilon 1}=1.44\,,\; C_{\varepsilon 2}=1.92\,,\; C_\mu=0.09\,,\; \sigma_k=1.0\,,\; \sigma_\varepsilon=1.3 \tag{3.6}$$

This model provides the eddy viscosity ν_T in terms of the turbulent kinetic energy per unit mass k_{nc} and its dissipation rate ε_{nc}. It is well known that the standard $k-\varepsilon$ turbulence model has shown low accuracy for the simulation of boundary layers in adverse pressure gradients (Bradshaw, 1997). The standard $k-\varepsilon$ turbulence model has also difficulty in integrating through the viscous sublayer and requires a viscous correction to reproduce the law of the wall for incompressible flat-plate boundary layers (Wilcox, 2000).

The performance of standard two-equation turbulence models is fairly good at high Reynolds number flows in which turbulence is nearly homogeneous and the turbulence production is nearly balanced by dissipation. At low Reynolds number, the difference between turbulent kinetic energy production and dissipation rates may depart from their equilibrium value of zero, thus the ad hoc adjustment of each empirical coefficient in the standard $k-\varepsilon$ turbulence model is inevitable. The RNG (Renormalization group theory) $k-\varepsilon$ turbulence model was introduced to avoid that adjustment (Yakhot and Orszag, 1986). The RNG $k-\varepsilon$ turbulence model uses the same equations for the kinematic eddy viscosity, turbulent kinetic energy per unit mass and dissipation rate, but modified coefficients, as

$$C_{\varepsilon 2}=\widetilde{C}_{\varepsilon 2}+\frac{C_\mu \lambda^3(1-\lambda/\lambda_o)}{1+\beta\lambda^3}\,,\; \lambda=\frac{k_{nc}}{\varepsilon_{nc}}\sqrt{2S_{ij}S_{ji}} \tag{3.7}$$

The closure coefficients for the RNG $k-\varepsilon$ turbulence model are

$$C_{\varepsilon 1}=1.42\,,\ \widetilde{C}_{\varepsilon 2}=1.68\,,\ C_{\mu}=0.085\,,\ \sigma_{k}=0.72\,,\ \sigma_{\varepsilon}=0.72 \tag{3.8}$$

$$\beta=0.012\,,\ \lambda_{o}=4.38$$

The RNG $k-\varepsilon$ turbulence model deduces the behaviour of the large-scale eddies from that of the smaller ones using the scale-similarity inherent in the energy cascade (Bradshaw, 1997). However, Bradshaw (1997) pointed out that it is not quite clear where the proper physics enters the process, which makes this approach similar to dimensional analysis in this respect.

The isotropic (Boussinesq) eddy viscosity model is based on the assumption that the principal axes of the stress tensor are aligned with the axes of the mean-strain rate tensor, as

$$-\tau_{ij-nc}=\nu_{T}\left(\frac{\partial U_{i}}{\partial x_{j}}+\frac{\partial U_{j}}{\partial x_{i}}\right)-\frac{2}{3}\delta_{ij}k_{nc}\,.$$

Two-equation turbulence models, including the RNG $k-\varepsilon$ turbulence model, can not predict the secondary flows of the second kind driven by small normal Reynolds stress differences near corners of rectangular ducts.

To permit inequality of the normal stresses, there are two models available: one is the non-linear eddy viscosity model and the other one is the Reynolds Stress Model. The latter was dealt in detail in section 3.1.2, while the former can be expressed in the following form

$$-\tau_{ij-nc} = \nu_T\left(\frac{\partial U_i}{\partial x_j} + \frac{\partial U_j}{\partial x_i}\right) - \frac{2}{3}\delta_{ij}k_{nc} + \frac{\delta_{ij}}{3}\sum_{m=1}^{3} C_{km}\left(\frac{k^3}{\varepsilon^2}\right)_{nc} S_{mll} - \sum_{m=1}^{3} C_{km}\left(\frac{k^3}{\varepsilon^2}\right)_{nc} S_{mij}$$

where $S_{1ij} = \frac{\partial U_i}{\partial x_l}\frac{\partial U_j}{\partial x_l}$, $S_{2ij} = \frac{1}{3}\left(\frac{\partial U_i}{\partial x_l}\frac{\partial U_l}{\partial x_j} + \frac{\partial U_j}{\partial x_l}\frac{\partial U_l}{\partial x_i}\right)$, $S_{3ij} = 7\frac{\partial U_l}{\partial x_i}\frac{\partial U_l}{\partial x_j}$.

The values for C_{k1}, C_{k2} and C_{k3} can be found in Speziale (1987).

According to Chen and Jaw (1998), the non-linear eddy viscosity model is not able to consider the transport effects in convection and diffusion so that the application of this model is limited to those flows in which production and dissipation of turbulence are balanced. For this reason, our study utilized the best available model, RSM, to resolve highly anisotropic flow near the gap regions and the corners of the duct.

3.1.2. Reynolds stress model

The Reynolds stress models (RSM) determine the turbulent stresses by solving a transport equation for each stress component, without the need to rely on the Boussinesq eddy-viscosity approximation. These equations are

$$\begin{aligned} \rho\left[\frac{\partial \tau_{ij-nc}}{\partial t} + \frac{\partial}{\partial x_k}\left(U_k \tau_{ij-nc}\right)\right] &= -\rho\left(\tau_{ik-nc}\frac{\partial U_j}{\partial x_k} + \tau_{jk-nc}\frac{\partial U_i}{\partial x_k}\right) - 2\mu\left(\frac{\partial u_i}{\partial x_k}\frac{\partial u_j}{\partial x_k}\right)_{nc} \\ &+ \left[p\left(\frac{\partial u_i}{\partial x_j} + \frac{\partial u_j}{\partial x_i}\right)\right]_{nc} + \mu\frac{\partial}{\partial x_k}\left(\frac{\partial \tau_{ij-nc}}{\partial x_k}\right) - \frac{\partial}{\partial x_k}\left[\rho\left(u_i u_j u_k\right)_{nc} + p\left(u_i\delta_{kj} + u_j\delta_{ik}\right)_{nc}\right]. \end{aligned} \tag{3.9}$$

Unlike two-equation and one-equation models, the RSM account for the effect of flow history due to terms representing the convection (second term on the left hand side of equation (3.9)) and diffusion (last term on the right hand side of equation (3.9)) of the shear stress tensor. The effects of streamline curvature, system rotation and stratification can be taken into account through the convection and production terms (first term on the right hand side of equation (3.9)) (Wilcox, 2000).

In equation (3.9), several terms are modeled using a standard Reynolds Stress Model (RSM). In particular, the pressure-strain tensor (third term on the right hand side of equation (3.9)) plays an important role in determining the structure of turbulent flows, partitioning turbulent energy among the Reynolds stress components and accounting for flow anisotropy. The pressure-strain rate tensor $\Pi_{ij} = p\left(\frac{\partial u_i}{\partial x_j} + \frac{\partial u_j}{\partial x_i}\right)$ is modeled using a low-Reynolds version of the linear pressure-strain model with coefficient values as suggested by Launder (1989) and Launder and Shima (1989).

$$\Pi_{ij} = \Pi_{ij,s} + \Pi_{ij,f} + \Pi_{ij,w} \tag{3.10}$$

where $\Pi_{ij,s} = -c_1 \frac{\rho\varepsilon_{nc}}{k_{nc}}\left(\tau_{ij-nc} - \frac{2}{3}k_{nc}\delta_{ij}\right)$ is the slow pressure-strain term and

$$\Pi_{ij,f} = -c_2\left(-\rho\left(\tau_{ik-nc}\frac{\partial U_j}{\partial x_k} + \tau_{jk-nc}\frac{\partial U_i}{\partial x_k}\right) - \frac{\partial}{\partial x_k}\left(\rho U_k \tau_{ij-nc}\right)\right.$$

$$\left. -\frac{1}{3}\delta_{ij}\left(-\rho\left(\tau_{kk-nc}\frac{\partial U_k}{\partial x_k} + \tau_{kk-nc}\frac{\partial U_k}{\partial x_k}\right) - \frac{\partial}{\partial x_k}\left(\rho U_k \tau_{kk-nc}\right)\right)\right)$$

is the fast pressure-strain term.

The third term of Eq. (3.10) is decomposed into:

$$\Pi_{ij,w} = \Pi_{ij,w,1} + \Pi_{ij,w,2} \tag{3.11}$$

where

$$\Pi_{ij,w,1} = c_3 \frac{\varepsilon_{nc}}{k_{nc}} \left(\tau_{km-nc} \eta_k \eta_m \delta_{ij} - \frac{3}{2} \tau_{ik-nc} \eta_j \eta_k - \frac{3}{2} \tau_{jk-nc} \eta_i \eta_k \right) \frac{k_{nc}^{3/2}}{C_w \varepsilon_{nc} \chi} \text{ and}$$

$$\Pi_{ij,w,2} = c_4 \left(\Pi_{km,f} \eta_k \eta_m \delta_{ij} - \frac{3}{2} \Pi_{ik,f} \eta_j \eta_k - \frac{3}{2} \Pi_{jk,f} \eta_i \eta_k \right) \frac{k_{nc}^{3/2}}{C_w \varepsilon_{nc} \chi},$$

where η_k is the x_k component of the unit normal to the wall and χ is the normal distance from the wall.

For turbulent core flows, the following default coefficients were assigned, as follows: $c_1 = 1.8$, $c_2 = 0.6$, $c_3 = 0.5$, $c_4 = 0.3$.

$C_w = \dfrac{(C_\mu)^{3/4}}{\kappa}$ is the wall reflection coefficient, with the von Kármán constant $\kappa = 0.4187$ and $C_\mu = 0.09$.

For flow near the wall, the low-Reynolds version of pressure-strain term was employed, by replacing the values of above default coefficients with following equations as function of Reynolds stress invariant and turbulent Reynolds number (Launder and Shima, 1989):

$$c_1 = 1.00 + 2.58\xi\sqrt{\xi_1}\left(1 - \exp\left(-(0.0067\,\mathrm{Re}_T)^2\right)\right),\ c_2 = 0.75\sqrt{\xi},\ c_3 = 1.67 - \frac{2}{3}c_1$$

and $c_4 = \max\left[\left(\frac{2}{3} - \frac{1}{6c_2}\right), 0\right]$.

where the turbulent Reynolds number was defined as $\mathrm{Re}_T = \dfrac{\rho k_{nc}^2}{\mu \varepsilon_{nc}}$,

$\xi = 1 - \dfrac{9}{8}\left(\alpha_{ik}\alpha_{ki} - \alpha_{ik}\alpha_{kj}\alpha_{ji}\right)$ and $\xi_1 = \alpha_{ik}\alpha_{ki}$

where $\alpha_{ij} = \left(\dfrac{\tau_{ij-nc} - 2/3\, k_{nc}\delta_{ij}}{k_{nc}}\right)$ is the Reynolds-stress anisotropy tensor.

The dissipation rate tensor (second term on the right hand side of equation (3.9)) was assumed to be isotropic, and described by means of a scalar dissipation rate ε_{nc}, which was determined by solving the following modeled transport equation

$$\rho\left[\frac{\partial \varepsilon_{nc}}{\partial t} + \frac{\partial (U_i \varepsilon_{nc})}{\partial x_i}\right] = \frac{\partial}{\partial x_j}\left[(\mu + \mu_T)\frac{\partial \varepsilon_{nc}}{\partial x_j}\right] \frac{0.72\ \Gamma_{ii}\varepsilon_{nc}}{k_{nc}} - 1.92\rho\frac{\varepsilon_{nc}^2}{k_{nc}} \tag{3.12}$$

where k_{nc} is the non-coherent turbulent kinetic energy per unit mass, Γ_{ij} is the production tensor (first term on the right hand side of equation (3.9)), and the turbulent viscosity is modeled as $\mu_T = \rho C_\mu \dfrac{k_{nc}^2}{\varepsilon_{nc}}$, with $C_\mu = 0.09$. Finally, as a means to enhance solution stability (Lien and Leschziner, 1994), the turbulent diffusion tensor (last term on the right hand side of equation (3.9)) was modeled in terms of a scalar diffusivity as

$$D_{ij} = \frac{\partial}{\partial x_k}\left(\frac{\mu_T}{\sigma_T}\frac{\partial \tau_{ij-nc}}{\partial x_k}\right) \tag{3.13}$$

where the turbulent Prandtl number was fixed at $\sigma_T = 0.82$.

The complex Reynolds stress models are known to give superior results to one- and two-equation turbulence models for flows with streamline curvature, sudden change in strain rate and secondary motions of second kind, although at the cost of increased computing time (Bradshaw, 1997).

3.1.3. Near-wall modeling

All RANS models except the $k-\omega$ model have two ways to model the near-wall layer: the wall function approach and the two-layer model. The wall function has an empirical form under the assumption that, in pipe or channel flow, there exists a logarithmic layer where the eddy viscosity can be fairly well approximated as

$$\nu_T = \kappa u^* r \tag{3.14}$$

with a velocity profile as

$$\frac{u}{u^*} = \frac{1}{\kappa} \log \frac{u^* r}{\nu} + c$$

where the constant c, as well as the von Kármán constant κ, vary slightly with the Reynolds number but may be approximated as $c = 5$; $\kappa = 0.4$. r is the normal distance from the wall. With these assumptions, the equations for the $k-\varepsilon$ model are reduced to:

$$k_{nc} = \frac{u^{*2}}{\sqrt{C_\mu}}, \; \varepsilon_{nc} = \frac{u^{*2}}{\kappa r} \tag{3.15}$$

For flow near a narrow gap, which would be expected to have strong cross flow pulsations, the reliability of the wall function approach is reduced. Thus, the two-layer wall treatment was used rather than using a wall function (Eq. (3.14)). In the two-layer model, the computational domain is divided into the near-wall region and the turbulent core flow region, depending on the Reynolds number based on wall distance. To smoothly bridge the turbulent viscosity and dissipation in the near-wall region to the corresponding values in turbulent core flows, the two-layer model was employed by solving algebraic mixing-length equations for the turbulent viscosity and dissipation in the near-wall region. For the calculation of Reynolds stresses in the near-wall region, the low-Reynolds version of RSM as outlined by Launder and Shima (1989) was used.

In the two-layer model, the turbulent viscosity was modeled in the form of the one-equation model to avoid the inconsistency of dissipation equation in the near-wall layer (Chen and Jaw, 1998).

$$\nu_T = C_\mu \sqrt{k_{nc}}\, l_\mu \tag{3.16}$$

where the length scale l_μ is calculated from the following equation:

$$l_\mu = r\, C_l \left(1 - \exp\left(-\mathrm{Re}_r / A_\mu\right)\right)$$

with $\mathrm{Re}_r = \dfrac{r\sqrt{k_{nc}}}{\nu}$ and r being the normal distance from the wall. Equation (3.16) is effective in the near-wall region where Re_r is below 200. The constant A_μ was taken as $A_\mu = 20$, as suggested by Chen and Patel (1988), while C_l is as follows:

$$C_l = \kappa\, C_\mu^{-3/4}$$

where κ is the von Kármán constant.

In the near-wall region, the turbulent dissipation was modelled as

$$\varepsilon_{nc} = \frac{k_{nc}^{3/2}}{l_\varepsilon} \tag{3.17}$$

where $l_\varepsilon = r\,C_l\left(1-\exp\left(-\mathrm{Re}_r / A_\varepsilon\right)\right)$. Here the model constant A_ε is equal to 5.08, as suggested by Chen and Patel (1988). This two-layer model requires special care in the grid distribution near the wall region.

3.2. Energy equation and model

The instantaneous local flow temperature T was computed by solving the following Reynolds-averaged energy equation for incompressible, single-phase flow

$$\frac{\partial T}{\partial t}+\frac{\partial (UT)}{\partial x}+\frac{\partial (VT)}{\partial y}+\frac{\partial (WT)}{\partial z}=$$

$$\gamma\left(\frac{\partial^2 T}{\partial x^2}+\frac{\partial^2 T}{\partial y^2}+\frac{\partial^2 T}{\partial z^2}\right)-\left(\frac{\partial (u\vartheta)_{nc}}{\partial x}+\frac{\partial (v\vartheta)_{nc}}{\partial y}+\frac{\partial (w\vartheta)_{nc}}{\partial z}\right) \tag{3.18}$$

In this equation, the isotropic turbulent heat flux model in the form of Fourier-Fick Law is based on Reynolds analogy between momentum and heat transfer (Murthy and Mathur, 1997) as

$$-(u\vartheta)_{nc}=\frac{\mu_T}{\sigma_T}\frac{\partial T}{\partial x},\quad -(v\vartheta)_{nc}=\frac{\mu_T}{\sigma_T}\frac{\partial T}{\partial y}\quad \text{and}\quad -(w\vartheta)_{nc}=\frac{\mu_T}{\sigma_T}\frac{\partial T}{\partial z} \tag{3.19}$$

where the turbulent Prandtl number was taken as $\sigma_T = 0.85$. The isotopic turbulent heat flux model was chosen because it has shown better convergence rate of the anisotropic heat flux models (Rokni and Sundén, 2003).

The resolved eddy viscosity μ_T was computed in terms of the resolved, non-coherent local turbulent kinetic energy k_{nc} and its dissipation rate ε_{nc} as

$$\mu_T = C_\mu \rho \frac{k_{nc}^2}{\varepsilon_{nc}} \tag{3.20}$$

where $C_\mu = 0.09$.

The non-coherent temperature fluctuations cannot be determined precisely, because the present solution procedure does not solve turbulence equations for the temperature field. In order to compare approximately the magnitudes of the coherent and non-coherent temperature contributions, we have estimated the variance of the non-coherent temperature fluctuations using the following expression (Chen and Jaw, 1998)

$$\overline{\vartheta_{nc}^2} = \overline{-\frac{k_{nc}}{C_\vartheta \varepsilon_{nc}}\left((u\vartheta)_{nc}\frac{\partial T}{\partial x} + (v\vartheta)_{nc}\frac{\partial T}{\partial y} + (w\vartheta)_{nc}\frac{\partial T}{\partial z} \right)} \tag{3.21}$$

This expression is an algebraic model of the balance equation for the non-coherent temperature fluctuation variance, in which convection and diffusion terms were ignored, an assumption that seems appropriate for the present flow. The local, time-dependent resolved heat fluxes $(u\vartheta)_{nc}, (v\vartheta)_{nc}, (w\vartheta)_{nc}$ were determined from the resolved temperature using equation (3.19), and the value of the coefficient C_ϑ was taken as 0.62, as suggested by Launder (1975).

For the uniform temperature case, the time-averaged local heat flux $\dot{q}$ from the rod surface was computed as

$$\dot{q} = \kappa \frac{\partial \overline{T}}{\partial r} \tag{3.22}$$

where κ is the thermal conductivity of the fluid and r is the radial direction. Then, the time averaged local heat transfer coefficient on the surface of the rod was calculated as

$$\bar{h} = \frac{\dot{q}}{\overline{T}_{\mathrm{rod,m}} - \overline{T}_b} \tag{3.23}$$

This coefficient will be presented in dimensionless form as the time-averaged local Nusselt number

$$\overline{\mathrm{Nu}} = \frac{\bar{h} D_h}{\kappa} \tag{3.24}$$

3.3. Inter-subchannel mixing

Inter-subchannel mixing in single-phase rod bundle flows has been described in terms of turbulent diffusion and turbulent convection between subchannels (Möller, 1992; Rehme, 1992). The determination of the inter-subchannel mixing and their dependence on the rod bundle shape have been simplified by the use of a lump parameter approach. For a rod bundle, let us denote the two subchannels adjacent to the gap as 1 and 2, and assume that the bulk temperatures in the two subchannels are T_{b1} and T_{b2}, respectively. Following Rehme (1992), the convective heat transfer rate between these subchannels can be expressed as

$$\dot{Q} = \rho\, c_{\mathrm{p}} w_{eff} \delta_{12}\, L\left(T_{b1} - T_{b2}\right) \tag{3.25}$$

where w_{eff} is an effective mixing velocity across the gap. The latter may be expressed in terms of an eddy viscosity ν_{tube} for circular tubes, a mixing distance δ_{12} between the two subchannels, and an empirical mixing factor Y, which accounts for the subchannel shape, as

$$w_{eff} = Y\frac{\nu_{\text{tube}}}{\delta_{12}} \tag{3.26}$$

Further utilizing the empirical relationship (Rehme, 1992)

$$\nu_{\text{tube}} = 0.0177\nu\,\text{Re}\sqrt{f_{\text{tube}}} \tag{3.27}$$

where ν is the kinematic viscosity of the fluid, Re is the Reynolds number of the circular tube and $f_{\text{tube}} = 0.18\,\text{Re}^{-0.20}$ is the friction factor for smooth circular tubes, and specifying δ_{12} by geometrical reasoning, one needs only to determine Y from available empirical information. The objective of this exercise is to evaluate the applicability of previous empirical correlations for Y to the present configuration. Rehme (1992) summarizes several such correlations and suggests an all-encompassing one as

$$Y_R = \frac{0.7}{\delta / D} \tag{3.28}$$

Chapter 4. Numerical conditions and procedures

4.1. Computational domain and grid generation

4.1.1. The single-rod duct

The computational domain consisted of a rectangular channel containing a rod with a diameter D_{sr}=0.101m, as shown in **Figure 4 - 1**. The height, width and length of the computational section were, respectively, $2D_{sr}$, $3D_{sr}$ and L_{sr} = $20D_{sr}$. The fluid, dimensions and flow rate were chosen to match those in the experimental setup used by Guellouz and Tavoularis (2000a, 2000b). The gap size δ_{sr} between the rod and the adjacent bottom wall was set to $0.10D_{sr}$ for the isothermal turbulent flow simulations, to be described in Chapter 6, and for the convective heat transfer simulations, to be described in Chapter 7. In addition, the effect of the gap size variation was examined in Chapter 8, for which simulations were performed for the values $\delta_{sr} / D_{sr} = 0.10$, 0.03 and 0.01. In all cases, the equidistant plane was defined by $y_{sr} = ½\delta_{sr}$.

A Cartesian coordinate system was defined with its origin at the middle of the bottom wall in the inlet plane, with the x-axis pointing streamwise, the y-axis pointing upwards (transverse direction) and the z-axis pointing towards one side (spanwise direction).

Hexahedral and quadrilateral elements were used for volume and face grid elements, respectively. To permit application of the periodic boundary condition, the meshes at the inlet and outlet were matched by linking both faces. To resolve the steep velocity gradient in the near wall region without using wall functions, five grid elements were placed in the region with $y^+ < 10$, with the first grid element located at $y^+ = 1$.

The presently used main grid (i.e. not including the boundary layers) for $\delta_{sr} / D_{sr} = 0.10$ has elements with dimensions roughly equal to $0.025D_{sr}$ in the transverse direction and $0.099D_{sr}$ in the streamwise direction, which were fine enough to resolve the typical experimental spacing between consecutive pairs of coherent structures of about 4 to $5D_{sr}$ (GT), whereas those grid elements were not deemed to resolve typical measured values of the Taylor microscale $\lambda_{sr} = 0.05D_{sr}$ and Kolmogorov microscale $\eta_{sr} = 0.0017D_{sr}$ (Guellouz, 1998). A direct numerical simulation (DNS) of this flow, capable of resolving motions with scales of the order of the Kolmogorov microscale, would require a mesh with roughly 2×10^{10} grid elements, whereas a large eddy simulation (LES) would typically be required to resolve 2% of the streamwise integral length scale (away from walls and gaps) $0.19D_{sr}$, which corresponds roughly to 2×10^{9} grid elements. Neither approach would be possible to implement with the available resources.

4.1.2. The 37-rod bundle

The computational geometry of the simulations described in Chapter 9 consisted of an idealized model of the 37-rod bundle of the CANDU nuclear reactor. The fluid, dimensions and flow rate were chosen to match those in the experimental setup used by Ouma and Tavoularis (1991a, 1991b) and Baratto *et al.* (2006). Each rod had a diameter

D_{rb} = 0.168 m, which is about 12.8 times larger than the diameter of the CANDU reactor rods. The bundle was contained in a cylindrical tube with an inner diameter equal to $7.9D_{rb}$ and a length of $L_{rb} = 20.0D_{rb}$. Only a 60° sector of the circular cross section, shown in **Figure 4 - 2**, was considered, as the full bundle cross section has azimuthal periodicity. Multiple cylindrical coordinate systems (x,r,ϕ) were defined, each of which had its origin on the axis of a rod; an example for an outer rod is illustrated in **Figure 4 - 2**. The gap size δ_{rb} between an outer rod and the wall of the containing tube was approximately $0.15D_{rb}$. The gaps between adjacent rods positioned at equal distances from the bundle axis were also approximately $0.15D_{rb}$.

As rough estimates of the requirements for meshing, we consider that the typical spacing between consecutive pairs of coherent structures (see section 9.4) was very roughly $4D_{rb}$, whereas typical measured values of the Taylor and Kolmogorov microscales were, respectively, $\lambda_{rb} = 0.014D_{rb}$ and $\eta_{rb} = 0.005D_{rb}$ (Ouma and Tavoularis, 1991b). To perform DNS of this problem, one would require to resolve motions of scales at least equal to η_{rb}, which would require roughly 5×10^8 grid elements. To perform a large eddy simulation LES of the same problem, one would probably need to resolve motions of scale equal to λ_{rb}, which would require roughly 3×10^7 grid elements in the open subchannels, and possibly many more additional elements to resolve the boundary layers. Both of these meshes were impossible to accommodate in the available facilities, so that a more economical approach, based on conventional turbulence models, was employed.

An unstructured hybrid mesh composed of prismatic elements for the core region and hexahedral elements for the boundary layer region was used; its cross section is shown in **Figure 4 - 2**. The streamwise spacing of all elements was $0.222D_{rb}$, deemed to be sufficiently small for resolving the coherent structures. The maximum grid size in the cross section was $0.042D_{rb}$, which, although larger than λ_{rb} and η_{rb}, was also sufficiently fine to resolve motions associated with coherent structures. The elements closest to the walls extended to a dimensionless distance of $y^+ = 1$.

4.2. Computational conditions

The computations were carried out using a specified mass flow rate and a periodic boundary condition in the streamwise direction, by which the velocity field on the outlet plane was inserted back on the inlet plane. The use of this periodic boundary condition permitted the attainment of fully developed conditions in a relatively short flow domain, thus reducing the computational requirements. The length of the domain was sufficiently large to permit complete spatial decorrelation of turbulent statistics available from the Guellouz and Tavoularis (2000a) experiments for the single rod duct and from the Ouma and Tavoularis (1991a, 1991b) experiments for the 37-rod bundle.

In this approach, the velocity distribution on the exit plane was re-introduced on the inlet plane and the local pressure P was set as the sum of a pressure on the inlet plane and a term varying linearly in the streamwise direction as

$$P(0,y,z,t) = P(x,y,z,t) - \frac{\partial P}{\partial x}x \tag{4.1}$$

The required pressure gradient was obtained iteratively such that the resulting mass flow rate $\dot{m}$ matched the value that produced the specified Reynolds number.

No-slip conditions were applied at all solid walls, while body forces were neglected for all studies.

4.2.1. The single-rod duct

For the convective heat transfer and the effect of gap size variation, the periodic temperature boundary condition was applied such that the temperature on the inlet plane was given in terms of the temperature at the corresponding position on the outlet plane as

$$T(0,y,z,t) = T(L,y,z,t) - \frac{\dot{q}}{\dot{m}c_{\mathrm{p}}}L \tag{4.2}$$

where c_{p} is the specific heat under constant pressure. Application of this periodic boundary condition ensures full development of the temperature fluctuation field while keeping the temperature rise within bounds even as heat enters continuously into the system. At all locations, the time average temperature increases linearly with streamwise distance at the rate of $\dot{q}/\left(\dot{m}c_{\mathrm{p}}\right)$. For normalization purposes, we shall define the cross-section-averaged (bulk) temperature $T_b(x)$ as

$$T_b(x,t) = \frac{\int_A \rho U T\, dA}{\rho U_b A} \tag{4.3}$$

and the circumferentially-averaged rod surface temperature $T_{\mathrm{rod,m}}(x,t)$ as

$$T_{\mathrm{rod,m}}(x,t) = \frac{1}{2\pi}\int_0^{2\pi} T_{\mathrm{rod}}(x,\phi,t)\,d\phi \tag{4.4}$$

The time averages of both these temperatures also grow linearly with streamwise position x, at the rate of $\dot{q}/\left(\dot{m}c_{\mathrm{p}}\right)$, whereas the statistical properties of the dimensionless temperature difference

$$\Theta(x,y,z,t) = \frac{T(x,y,z) - \overline{T}_b(x)}{\overline{T}_{\mathrm{rod,m}}(x) - \overline{T}_b(x)} \tag{4.5}$$

are independent of streamwise location. An additional requirement of the solution is the specification of the bulk temperature $\overline{T}_b$ at the inlet, time-averaged and mass-weighted over the entire cross section. In the present analysis, we specified $\overline{T}_b$ = 300 K, which was equal to the temperature used in the isothermal simulations. The values of $\overline{T}_{\mathrm{rod,m}}$ and $\overline{T}_b$ are immaterial, as long as they are sufficiently close to each other for the heating to have a negligible effect on the velocity field.

Two heating modes were considered in Chapter 7 for the heat transfer study: one in which the rod surface temperature T_{rod} was kept to the uniform value 305 K (mode A) and a second one in which the heat flux $\dot{q}$ from the rod surface was kept uniform and equal to $\dot{q}$ =100 W/m^2 (mode B). Mode B applies to nuclear reactors. In both cases, the heat flux on all plane walls was set to zero, corresponding to a thermally insulated duct.

The mode B was only considered for the gap size variation in Chapter 8. The buoyancy force was negligible, as evidenced by the fact that the Richardson number, which represents the ratio of buoyancy and inertia forces, was less than 0.0003 (Burmeister, 1983). The physical and thermodynamic properties of the fluid, taken to be air, were assumed to be constant and equal to those in the reference isothermal case. In turn, the heat was introduced at sufficiently small amounts for the temperature to be essentially a passive scalar and not to affect in any way the fluid properties of the velocity and pressure fields. This was a requirement for using periodic boundary conditions for the temperature (Murthy and Mathur, 1997).

The Reynolds number, based on the bulk velocity $U_{b\text{-}sr}$ and the hydraulic diameter $D_{h-sr} = 1.59 D_{sr}$, was 108,000, nearly matching the available experimental value (Guellouz and Tavoularis, 2000a; 2000b).

4.2.2. The 37-rod bundle

In addition to applying streamwise periodic boundary conditions on the inflow and outflow planes, the rotational periodic boundary condition was applied on the two side boundaries, based on the assumption that, like the geometry, the velocity distribution was also azimuthally periodic. No-slip conditions were applied on the surfaces of the rods and the surrounding tube.

The Ouma and Tavoularis (1991a, 1991b) experimental model was a 5-rod section of a 37-rod bundle, with the same relative gap size, but a length to rod-diameter ratio of 37.

In contrast to the computational geometry which has periodic side boundaries, the experimental model had side walls on which four of its five rods were attached. This difference renders the use of the overall hydraulic diameter and the overall bulk velocity inapplicable in matching the Reynolds number in the two systems. Instead, it is more appropriate to use a local hydraulic diameter and local bulk velocity, characterizing the flow in a subchannel bounded by the middle outer rod and the line of maximum velocity around that rod. This provides a local hydraulic diameter $D_{h-rb} = 0.29 D_{rb}$ and a local bulk velocity $U_{b-rb} = 13$ m/s for the experiments, from which the local Reynolds number can be calculated as $\mathrm{Re}_{rb} = D_{h-rb} U_{b-rb} / \nu = 42{,}000$. The local Reynolds number for the simulations was estimated as 40,309, essentially matching the experimental value. An alternative Reynolds number, based on the hydraulic diameter of the 37-rod bundle, which was $0.57 D_{rb}$, and the same bulk velocity $U_{b-rb} = 13$ m/s was 84,800. The Reynolds number for a typical operating CANDU rod bundle was estimated as about 0.48×10^6 (Page, 1972).

4.3. Computational procedures

The simulations were performed using the commercial CFD code FLUENT (version 6.2.16), which solves the governing equations by the finite volume approach. Computations were conducted in the SunFire cluster at HPCVL (High Performance Computing Virtual Laboratory, a consortium of four Universities in Eastern Ontario), configured with 24 × 1.05 GHz UltraSPARC-III processors and 96 Gb of RAM memory. The SunGrid Engine in the SunFire cluster was used with 10 nodes.

4.3.1. The single-rod duct

For the case of $\delta_{sr} / D_{sr} = 0.10$, grid independence studies were conducted using 404×160×160, 202×80×80 and 101×40×40 elements (see **Table 4 - 1**, cases 1, 2 and 3). As an example of the effect of grid choice on our computations, **Figure 4 - 3** shows computed velocity profiles at a representative location. It can be seen that the velocity variation predicted by the 202×80×80 grid was in good agreement with the universal law of the wall within the viscous and logarithmic sublayers and was fairly close to the one predicted by the 404×160×160 grid, whereas the 101×40×40 grid predictions displayed significant discrepancies. The 202×80×80 element grid was, therefore, adopted for further computations, as the use of finer grids required excessive computational times. The adopted grid is the finest possible that would produce an accurate solution of the problem in a reasonably timely manner. The effect of abrupt changes in mesh size near the wall is not expected to have a significant effect on the solution (Schröder and Gelbe (1999).

Similar studies for the other gap sizes were not deemed to be necessary, because the meshes for these cases were more refined than that for the $\delta_{sr} / D_{sr} = 0.10$ case. The streamwise lengths of all mesh elements were the same for all cases studied, whereas the total number of nodes was increased from 1.2×10^6 for $\delta_{sr}/D_{sr}=0.10$, to 1.4×10^6 for $\delta_{sr}/D_{sr}=0.03$ and 1.5×10^6 for $\delta_{sr}/D_{sr}=0.01$. The two-layer model and the low-Reynolds RSM need proper grid resolution in gap region. Thus, more nodes in smaller gap-size cases were required to resolve the higher local velocity gradients.

Time-step dependence was tested by repeating the computations with two time steps Δt, equal to $1.9\times10^{-2}t_{c\text{-}sr}$ and $1.9\times10^{-3}t_{c\text{-}sr}$, where $t_{c-sr}=L_{sr}/U_{b-sr}$ is the average flow turn-over time, namely the average time that it takes for the fluid to pass through the computational domain. As shown in **Figure 4 - 3** by a representative example, the time-averaged velocity variations were essentially the same for these two time steps. Both time steps also resolved fairly well the coherent structures over some time, however, the larger time step led to distorted patterns for longer computations (Chang and Tavoularis, 2004). Furthermore, it turned out that computations with the smaller time step were faster than those with the larger one, because the former required far fewer iterations for the solution at each time step to converge. For the larger time step (case 4) the CPU time was about 4 min per time step and the real computing time was 5 hrs per time step, while for the smaller one (case 2) these times were, respectively, 5.6 s and 12.6 min. This means that flow computation over one turn-over time took 11 days for the larger time step but only 4.6 days for the smaller one. Thus, the smaller time step, equal to $(1/526)t_{c\text{-}sr}$, was adopted for the main computations. Time discretization was achieved by a second-order implicit method (second-order backward Euler scheme). Although implicit methods are not restricted by the CFL (Courant-Friedrichs-Levy number) limit $\mathrm{CFL}=U_{\max}\Delta t/\Delta x<1$, it may be noted that the time step size may affect the accuracy of solutions because of truncation error increase. For the smaller time step case (case 2), CFL was equal to 0.456, which is deemed to be sufficiently low.

For the study of gap size effect in Chapter 8, the average number of iterations per time step required for convergence was 15, 11 and 3 for the three gap sizes, respectively. The drastic reduction in the number of required iterations for the narrowest gap is attributed partly to mesh refinement and mainly to the extreme weakness of coherent structures in that case, as will be shown later.

It was verified that the RSM model was successful in resolving the turbulence anisotropy and the secondary flows near the corners of a rectangular duct. However, to avoid possible divergence, the computations were initiated using the more stable RNG (Renormalization Group) $k-\varepsilon$ model. These preliminary computations extended over a time equal to $5.7t_{c\text{-}sr}$ (2923 time steps) which was sufficient to allow full development of the flow. The velocity field at the end of the preliminary computations was used as starting condition for the main simulations with the RSM. The development of the flow patterns was checked by monitoring the fluctuations of the spanwise velocity in the gap center, which are known to be sensitive indicators of coherent structure effects. Full development of such patterns was achieved following computational times of $7.6t_{c\text{-}sr}$ (3897 time steps), $22.1t_{c\text{-}sr}$ (11333 time steps) and $95t_{c\text{-}sr}$ (48718 time steps) for the larger, middle and smaller gap sizes, respectively. Following full development, flow parameters were collected for statistical processing over $3.9t_{c\text{-}sr}$ (2000 time steps) for $\delta_{sr}/D_{sr} = 0.10$ and $9.2t_{c\text{-}sr}$ (4718 time steps) for $\delta_{sr}/D_{sr} = 0.03$, which correspond to 11 cycles of spanwise velocity fluctuations. For the $\delta_{sr}/D_{sr} = 0.01$ case, statistics have been collected over $26.2t_{c\text{-}sr}$ (13436 time steps), which corresponds to 6 cycles of spanwise velocity fluctuation, as justified by the long computational time required and the absence of significant variation in turbulent statistics. The convergence of the solution was verified by comparing the time averaged local velocity and time averaged kinetic energy across the gap region averaging over different time duration after achieving fully development flow. It was found that the differences between the values of these parameters over $2t_{c\text{-}sr}$ (1000 time steps) and $2.9t_{c\text{-}sr}$ (1500 time steps) were 0.2% and 8.6%, respectively, while the differences between the values of the same parameters over $2.9t_{c\text{-}sr}$ (1500 time steps) and $3.9t_{c\text{-}sr}$ (2000 time steps) were 0.2% and 0.6%, respectively.

The partial differential equations that govern conservation of mass, momentum, and energy are integrated over each discrete control volume to form algebraic equations. The algebraic equations are then solved iteratively until the conservation laws are satisfied to an acceptable degree of imbalance, called a residual, which is computed as the difference between the value of a variable in a cell and the value that would be expected based on what is flowing into and out of that cell via adjacent cells. A global measure of the imbalance, called normalized residual, is equal to the residuals summed over all computational cells and scaled by a factor representative of the flow rate of the variable through the domain (the sum of the variables in all the cells). The solution at each time step was considered to converge when all normalized residuals became less than 10^{-4}, except for the temperature, for which the value 10^{-6} was used instead.

4.3.2. The 37-rod bundle

The possible dependence of the solution on mesh size was examined by comparing simulations using three different meshes with 0.2×10^6, 0.8×10^6 and 2.2×10^6 elements, respectively. In all cases, the time step was fixed at $3.9\times10^{-4}\,t_{c\text{-}rb}$, where $t_{c-rb} = L_{rb} / U_{b-rb}$ is the average flow turn-over time. This ensured a relatively low value of the Courant-Friedrichs-Levy number (CFL= 0.4), although the presently used implicit method is not subjected to such restriction. The main computations were conducted using the 0.8×10^6

elements mesh, which gave solutions that differed by less than 5% in the local maximum velocity compared to those using the finer mesh. Flow convergence at each time step was considered to be achieved when the normalized residuals for all flow variables reached values lower than 10^{-3}.

The development of the flow patterns was checked by monitoring the fluctuations of the azimuthal velocity in the gap center, which are known to be sensitive indicators of coherent structure effects (Guellouz and Tavoularis, 2000a; Chang and Tavoularis, 2005a). Full development of such patterns was achieved following computational times of $3t_{c\text{-}rb}$ (7693 time steps). Following full development, flow parameters were collected for statistical processing over $2.6t_{c\text{-}rb}$ (6667 time steps), which corresponds to 12 periods of azimuthal velocity fluctuations. The simulations were performed in a SunFire cluster, using 10 parallel processors. A typical run using 0.8×10^6 nodes and 6667 time steps took about 350 hr of running time.

4.4. Numerical schemes

For high accuracy, the second-order upwind scheme with a linear reconstruction procedure, similar to that of Barth and Jesperson (1989), was chosen for deriving the face values of different variables for space discretization. The pressure was interpolated at the cell faces using the Rhie-Chow scheme (Rhie and Chow, 1983) to avoid pressure oscillations (checkerboarding) under the constraint of mass conservation. The second-order implicit Euler scheme was employed for temporal discretization (Gresho *et al.*, 1980).

The combination of high-aspect ratio grid cells and highly-clustered near-wall spacing, as required for turbulence modeling, often causes numerical instability, The SIMPLEC (Semi-Implicit Pressure Linked Equations – Consistent) algorithm, which achieves better convergence rate by using a consistent approximation to the momentum equation, was used for the treatment of pressure-velocity coupling (Van Doormal and Raithby, 1984).

Chapter 5. Coherent structure identification

5.1. Definition of coherent structures

Although there is no consensus on the definition of coherent structures (CS), the following definitions would help one understand the general concept. Hussain (1983, 1986) referred to CS as "connected turbulent mass with instantaneous phase-correlated vorticity over its spatial extent". Robinson (1991) defined CS as "a three-dimensional region of the flow over which at least one fundamental flow variable exhibits significant correlation with itself or with another variable over a range of space and/or time that is significantly larger than the smallest local scales of the flow". Mogens *et al.* (1991) defined CS as "a large-scale motion with instantaneous phase correlated (i.e. coherent) vorticity over its spatial extent in turbulent flow". Jeong and Hussain (1995) indicated CS as "spatially coherent, temporally evolving vortical structures". Robinson (1991) had a more broad view of CS than Hussain (1986) by indicating that CS as "a three-dimensional region of the flow over which at least one fundamental flow variable exhibits significant correlation with itself or with another variable over a range of space and/or time that is significantly larger than the smallest local scales of the flow".

Vortices are among the most common types of coherent structures in turbulent flows and tend to be persistent in the absence of destructive instabilities (Robinson, 1991). Hussain (1986) emphasized that coherent vorticity is the primary identifier of coherent structures, which have distinct boundaries and independent territories.

It has been known from experiments employing conditional sampling that coherent structures in turbulent shear flows account for a significant fraction of the turbulent kinetic energy, and of the Reynolds stresses and fluxes (Libby, 1996). According to Robinson (1991), flow visualization between 1960 and 1971 revealed that coherent motions play a major role in production of turbulence near the wall, in the transport of momentum across the mean velocity gradient in both directions, and in the growth of the boundary layer through entrainment. However, conventional averaging of the governing equations does not preserve information concerning coherent structures. Experimental studies of the statistical features of coherent structures involve conditional averaging, but are subjected to uncertainty as to the appropriate trigger for conditional sampling as well as a difficulty in distinguishing essential from inessential fluctuations (Hussain, 1986; Jeong and Hussain, 1995). Vortex dynamics, which govern the evolution, interaction and coupling of coherent structures with background turbulence, are important in understanding turbulence phenomena such as entrainment, mixing, heat, mass transfer, chemical reactions, combustion, drag, and aerodynamic noise generation as well as in modeling of turbulence and devising active/passive control techniques for boundary layers (Cucitore *et al.*, 1999).

5.2. Identification methods of CS

Identification of CS in highly turbulent shear flows is subject to considerable difficulties, as they can be easily confused with non-coherent turbulence and mean vorticity patterns. Such identification can only be based on an unambiguous quantitative criterion.

Methods for the identification of CS can be roughly classified as vortex eduction methods (Jeong and Hussain, 1995) and filtering methods (Bonnet and Delville, 2001). The present research will focus on the vortex eduction methods. The simplest procedures used to identify vortices are mostly based on a search for regions of the flow field characterized by some appropriate property, intuitively related to a vortical motion. These include a local pressure minimum, iso-vorticity surfaces and closed streamlines.

More recently, two quantitative criteria for coherent structure identification were proposed. They are known as the Q criterion, proposed by Hunt *et al.* (1988), and the λ_2 criterion, proposed by Jeong and Hussain (1995). Both methods are based on analysis of properties of the velocity gradient tensor $\dfrac{\partial U_i}{\partial x_j}$ and less intuitive physical considerations. The present study will focus on the Q criterion, which has been used more widely than the λ_2 criterion, because of its simplicity and applicability.

According to Hussain (1986), the purpose of eduction is to separate the coherent and incoherent parts of instantaneous flow fields. Eduction methods are based on the analysis of the velocity gradient tensor $\partial U_i / \partial x_j$. In the vicinity of an arbitrary point in a coordinate system, the velocity field can be approximated by:

$$U_i \approx \frac{\partial U_i}{\partial x_j} x_j \tag{5.1}$$

Chong *et al.* (1990) proposed that a vortex core is a region with complex eigenvalues of $\partial U_i / \partial x_j$; complex eigenvalues imply that the local streamline pattern is closed or spiral in a reference frame. Its characteristic equation is given by:

$$\lambda^3 + P\lambda^2 + Q\lambda + R = 0 \tag{5.2}$$

where $P = -\partial U_i / \partial x_i$ is an invariant of the velocity gradient tensor, which is identically zero for incompressible flows.

$$Q = -\frac{1}{2}\frac{\partial U_i}{\partial x_j}\frac{\partial U_j}{\partial x_i} = -\frac{1}{2}\left(S_{ij}S_{ji} + \Omega_{ij}\Omega_{ji}\right) \tag{5.3}$$

$$R = -\frac{1}{3}\frac{\partial U_i}{\partial x_j}\frac{\partial U_j}{\partial x_k}\frac{\partial U_k}{\partial x_i} = \frac{1}{3}\left(S_{ij}S_{jk}S_{ki} + 3\Omega_{ij}\Omega_{jk}\Omega_{ki}\right) \tag{5.4}$$

are the second and third invariants of $\frac{\partial U_i}{\partial x_j}$, respectively, where $S_{ij} = \frac{1}{2}\left(\frac{\partial U_i}{\partial x_j} + \frac{\partial U_j}{\partial x_i}\right)$ and $\Omega_{ij} = \frac{1}{2}\left(\frac{\partial U_i}{\partial x_j} - \frac{\partial U_j}{\partial x_i}\right)$ are the symmetric and anti-symmetric parts of the velocity gradient tensor, respectively.

The criterion Q can be rewritten as

$$Q = \frac{1}{2}\left(\Omega_{ij}\Omega_{ij} - S_{ij}S_{ij}\right) \tag{5.5}$$

Positive Q indicates regions where vorticity overcomes strain, thus distinguishing vortical activity from high-strain activity. Unlike iso-vorticity surfaces, which cannot identify CS near a wall where the magnitudes of vorticity and strain are almost the same, Q can, because it is not influenced by near-wall vorticity.

In previous studies (da Silva and Métais, 2002; Dubief and Delcayre, 2000) coherent structures have been identified as surfaces on which Q maintains a constant positive value, called the threshold. The Q criterion with a threshold value of 1 was adequate in identifying realistic coherent structures in the present single-rod simulations, but failed in the 37-rod simulations, although various thresholds between 0.001 and 1 were tried. To overcome this difficulty, a modified Q-criterion was introduced as

$$Q_m = \frac{1}{2}\left(\Omega_{ij}\Omega_{ij} - c_q\, S_{ij}S_{ij}\right) \tag{5.6}$$

where $c_q < 1$ is an empirical factor which reduces the rate of strain effect on the coherent structure identification. By selecting $c_q = 0.55$ and a threshold of 1, it became possible to identify the surfaces of realistic coherent structures whose locations coincided with low static pressure regions.

5.3. Contribution of CS on the velocity and temperature fields

Unlike RANS, which provide a steady-state solution, URANS resolves a time-dependent velocity field as well as, through the RSM, time-dependent modeled Reynolds stresses. The instantaneous resolved velocity can be decomposed to two parts: the time averaged local velocity and the resolved velocity fluctuation. This decomposition is different from Reynolds decomposition, which decomposes the instantaneous values into means and fluctuations, with the latter including both the resolved velocity fluctuations and modeled turbulent stresses. This triple decomposition is based on the assumption that cross-correlation terms are negligible (Hussain, 1983; Wilcox, 2000; Bonnet and Delville, 2001), which is justified in our case because the length and time scales of the resolved velocity fluctuations are considerably larger than those of modeled turbulent stresses. Then, one may identify the resolved velocity fluctuations as coherent and the solutions of the Reynolds stress equations as non-coherent.

The time-dependent resolved fields are coupled with the modeled fields through the momentum and energy equations. The solution of the modeled, "non-coherent" parameters is not obtained by directly computing time-dependent non-coherent fluctuations of velocity or temperature, but rather time-dependent Reynolds stresses and heat fluxes, which take into account the variation of the resolved variables through the corresponding turbulence models. Therefore, we believe that there is no need to include additional cross-correlation terms, which, in any case, would be impossible to determine. However, this assumption can not be sufficient anymore in the case of strong disequilibrium caused by unsteady large scale coherent motion. In that case, it may be necessary to incorporate the spectral information into turbulence models (Wegner *et al.*, 2004).

In order to compare the results of the present computations with experimental, time-averaged turbulence statistics, one needs to consider both time-averaged coherent and non-coherent parts. Both contributions have to be time-averaged (to be indicated by overbars) over a time interval that is sufficiently long to capture a significant number of coherent structures. The kinetic energy of the coherent velocity fluctuations is obtained by time averaging the sum of the squares of the resolved velocity component fluctuations as

$$\overline{k_c} = \frac{1}{2}\left\{\overline{(U-\overline{U})^2} + \overline{(V-\overline{V})^2} + \overline{(W-\overline{W})^2}\right\} \tag{5.7}$$

The non-coherent turbulent kinetic energy is obtained by time averaging the sum of the normal Reynolds stresses provided by the solutions of the Reynolds stress equations as

$$\overline{k_{nc}} = \frac{1}{2}\left(\overline{u_{nc}^2} + \overline{v_{nc}^2} + \overline{w_{nc}^2}\right) \tag{5.8}$$

And the total time-averaged turbulent kinetic energy per unit mass is determined as the sum of the above terms, i.e. as

$$\overline{k} = \overline{k_c} + \overline{k_{nc}} \tag{5.9}$$

In a similar manner, the local variance of the temperature fluctuation is determined as the sum of the coherent and non-coherent components, as

$$\overline{\vartheta^2} = \overline{\vartheta_c^2} + \overline{\vartheta_{nc}^2} \tag{5.10}$$

The coherent component $\overline{\vartheta_c^2}$ is the variance of the resolved temperature T, given by

$$\overline{\vartheta_c^2} = \overline{\left(T - \overline{T}\right)^2} \tag{5.11}.$$

where $\overline{T}$ is the resolved local temperature, time averaged over a time interval that is sufficiently long to capture a significant number of coherent structures. The non-coherent temperature fluctuations cannot be determined precisely, because the present solution procedure does not solve turbulence equations for the temperature field. In order to compare approximately the magnitudes of the coherent and non-coherent temperature contributions, we have estimated the variance of the non-coherent temperature fluctuations through an algebraic model (Chen and Jaw, 1998), as described in section (3.2).

Chapter 6. Isothermal flow in a single-rod duct*

The present work is focused on the application of the unsteady RANS (URANS) approach to simulate the simplified rod-bundle-like flows by capturing coherent structure effects. The most detailed relevant experimental studies are by Guellouz and Tavoularis (2000a,b), hereafter to be referred to as GT, who studied isothermal flow in a rectangular channel containing a cylindrical rod. They identified the formation of large-scale coherent structures in the gap region between a cylindrical rod and the wall of a rectangular channel using conditional sampling and phase averaging. GT concluded that the coherent structures formed a street of pairs of counter-rotating vortices with axes alternating on either side of the gap.

Some preliminary results in the same geometry have been presented by Tavoularis *et al.* (2002) and Chang and Tavoularis (2004). An essential objective of the present simulations is to accurately predict the unsteady evolution of the large-scale structures and to provide a thorough understanding of the influence of coherent structures on flow characteristics in a rod-bundle-like configuration, which may lead to improved modeling of such processes.

---

* Material in this Chapter has also been discussed by Chang and Tavoularis (2005a).

6.1. Time-averaged streamwise velocity

The present simulations were partially validated by a comparison with available measurements by GT. **Figure 6 - 1**(a) compares the simulated and experimental time-averaged streamwise velocity variations on a cross plane, while computed time-averaged streamline projections and velocity vectors on the same plane are shown in **Figure 6 - 1**(b). When comparing the values of the velocity at corresponding locations, it becomes evident that the two "core" regions in which the velocity maintains relatively large values are larger in the experimental case than in the simulations. In other words, the wall regions appear to be somewhat thicker in the simulations than in the experiments. Although the simulations reproduced quite well the bulging of the experimental velocity contours in the gap region and in the corners of a duct, they also presented a notable difference from the experiments in that the predicted maximum velocity was on the symmetry plane above the rod, while in the experiments two maxima were observed in the two open subchannels, half way between the symmetry plane and the side walls. This difference is associated with secondary flows near the corners of the duct, but is not very disconcerting, because the velocity variation in the core region was only of the order of a small percent in both the simulations and the experiments. We have performed a number of additional simulations, not discussed here, showing some sensitivity of the maximum velocity location on the type of turbulence model used, on the grid size and on the type of boundary condition employed (see Appendix A). Furthermore, part of the difference can be attributed to differences in flow development: unlike the present computations which represent fully developed flow, the experimental results correspond to a flow in which the turbulence structure was still evolving, albeit slowly.

6.2. Time-averaged turbulent statistics

In **Figure 6 - 2** to **Figure 6 - 5**, the predicted rms turbulent velocity components and the turbulent kinetic energy are compared with the corresponding experimental values, with all values normalized by the bulk velocity. Fairly good qualitative agreement can be observed in all cases, while the quantitative agreement may also be considered as at least fair, in view of the differences in the numerical and experimental conditions and the uncertainties involved in both. The axial rms turbulent velocity reached minimum values in the core region above the rod and maximum values in the gap region (**Figure 6 - 2**). The spanwise rms turbulent velocity had a distribution that was comparable to that of the axial one (**Figure 6 - 3**), while the transverse rms-turbulent velocity was maximum on the sides of the rod (**Figure 6 - 4**). All these trends can be observed both in the experimental and the numerical results.

The variations of the three turbulent shear stresses and the corresponding correlation coefficients in the simulations are compared to the experimental ones in **Figure 6 - 6** to **Figure 6 - 11**. Once more, the qualitative agreement is reasonably good and the corresponding magnitudes of the local stresses are, in most cases, not too far from each other, considering the differences in the two sets of conditions and the main objective of the present study, which is to identify the effect of coherent structures. A general observation that can be made by comparing the magnitudes of turbulent stresses with the corresponding local mean velocity gradients is that gradient transport seems to describe approximately the time-averaged turbulence structure in much of the cross-section but fails to do so in the core region.

In the gap region, the time-averaged mean velocity reaches a minimum and gradient transport would imply that turbulence activity should be minimum there as well. On the contrary, the axial and spanwise turbulent stresses as well as the turbulent kinetic energy reach their maxima in the centre of the gap, which are trends observed in both the experimental and the numerical results.

6.3. Contribution of coherent components on the total turbulent activity

To assess the importance of the coherent components on the turbulent activity, we have plotted, in **Figure 6 - 12**, the ratios of the coherent and total values of the three normal rms turbulent velocities and the turbulent kinetic energy. This figure clearly demonstrates that the coherent contributions to the streamwise and spanwise components are very significant, and indeed dominant, in the gap region, where they account for up to 70% and 80%, respectively, of the total activity. The coherent contribution to the transverse stress is insignificant in the gap region and takes a maximum value of 20% on the sides of the rod, indicating that the flow pulsations follow the rod contour. About 60% of the total turbulent kinetic energy in the gap region is due to the coherent activity, while such activity is negligible away from the gap.

GT have provided some rough estimates of the contributions of the coherent stresses on the total turbulent activity along the spanwise direction on the equidistant plane. Their results are compared to the present simulations in **Figure 6 - 13**. Although agreement is not perfect, it may be considered as remarkably good, both qualitatively and, in most cases, quantitatively, considering the differences in flow conditions and the uncertainties of both experiment and simulations. The experimental trends and the orders of magnitude of the different stresses are captured realistically by the simulations. Both experiments and simulations show that the maximum coherent streamwise stress occurs at an intermediate position between the gap and the side wall of the channel, while the maximum coherent spanwise stress occurs on the symmetry plane and the transverse coherent stress is negligible on the entire equidistant plane.

From the above discussion, it is evident that the resolved velocity fields are strongly time-dependent. This time dependence is intimately associated with the convection of large-scale, quasi-periodic, vortical coherent structures, which appear in pairs on either side of the gap between the rod and the channel plane wall. Such structures, captured using the Q criterion, are shown in **Figure 6 - 14**. Their appearance is consistent with the heuristic model presented by GT.

To illustrate the influence of the coherent structure location on the instantaneous pressure and velocity fields, **Figure 6 - 15** shows isocontours of the instantaneous resolved static pressure and spanwise velocity. The main structures coincide with low static pressure regions. This confirms their vortical character, demonstrated by cores with high vorticity and low pressure. The spanwise velocity at the gap alternates in direction with streamwise location and seems to be an excellent indicator of coherent structure passage near the gap, in conformity with experimental observations (Guellouz and Tavoularis, 2000a).

Figure 6 - 16 shows surface streamlines on the equidistant plane for both the experimental and the numerical studies from the velocity vector projections on the equidistant plane using the graphics package Tecplot (Amtec Engineering, Inc.). Besides the striking agreement between the two sets of streamlines, one may observe without doubt that the coherent structures are counter-rotating vortices with axes alternating on

either side of the gap causing large-scale transport of fluid across the gap. The sense of rotation of the vortices is the same as the sense of rotation of coherent structures in mixing layers, if one considers the subchannel core to be the high-speed stream and the gap region to be the low-speed stream. It is also clear that these vortices transport fluid across the gap and deeply into the opposite subchannel. The spanwise spacing of the axes of vortices obtained by the numerical study was comparable to that in the experimental study, within the expected uncertainty due to differences in the imposed conditions and cycle-to-cycle variations.

6.4. Characteristics of coherent structures

To characterize the coherence structures, we have determined their frequency, streamwise spacing (wavelength) and convection speed. There was substantial variability from one structure to the next and the averages reported below were based on statistical samples which, although quite small, are considered to be sufficient for the present purposes. **Figure 6 - 17**a shows representative time histories of the spanwise velocity in the centre of the gap in the experimental and numerical studies. Both time histories show a quasi-periodic character, with a zero average and a nearly constant amplitude of about $0.17U_b$, which demonstrates the significant strength of flow pulsations across the gap. The dimensionless spacing between pairs of structures, based on 4 structure pairs, was $\lambda_{cs} / D = 4.9 \pm 1.2$, also compatible with the experimental value of 4.2. **Figure 6 - 17**b shows power spectra of the spanwise velocity in the centre of the gap. The frequency f was presented in dimensionless form as a Strouhal number

$$\mathrm{St} = \frac{fD}{U_b} \tag{6.1}$$

The Strouhal number at the peak frequency of the velocity spectrum was about 0.17, which was comparable to the experimental value of 0.18. Finally, the dimensionless convection speed of the structures, averaged over 8 structures and measured from animated sequences of images similar to **Figure 6 - 14**, was $U_c / U_b \approx 0.62$, which is not too far from the experimental value of 0.78. Overall, the above results show that velocity fluctuations in the gap region are of sufficiently large wavelength and low frequency for local conditions to potentially prevail in wall heating and possible phase change.

6.5. Summary of the isothermal turbulent flow field

The present simulations have clearly documented the significance of coherent vortical structures in turbulent flow near a rod-wall gap region. The use of the Q criterion has identified the formation of such coherent structures, with features comparable to those found experimentally (Guellouz and Tavoularis, 2000b). The time-averaged mean velocities and turbulent stresses in the simulations were also in fair agreement with their experimental counterparts. It is, therefore, concluded that the present approach is sufficiently accurate for the conduction of parametric studies of the effects of gap size, geometry and Reynolds number on the variation of flow and heat transfer characteristics in rod bundles.

It is also observed that the coherent components were very significant in the gap region, where they accounted for 60% of the total kinetic energy. The coherent contribution to the transverse stress was much lower than the coherent contributions to the spanwise and streamwise stresses. It is evident that the time dependent velocity fields in the gap region are mainly associated with the convection of large-scale, quasi-periodic, vortical coherent structures, which appear in pairs of counter-rotating vortices with axes alternating on either side of the gap and transporting fluid far across the gap. Velocity fluctuations in the gap region are of sufficiently large wavelength and low frequency for local conditions to potentially prevail in wall heating and possible phase change.

Chapter 7. Convective heat transfer in a single-rod duct*

Forced convective heat transfer in complex channels with narrow gap regions between solid walls flanked by wider subchannels occurs commonly in thermal equipment, particularly in nuclear reactor rod bundles. The fluid in gap regions is more likely to overheat than fluid in the adjacent subchannels, especially if the gap size diminishes, due to vibrations or thermally induced strains. Such conditions may lead to reduced thermal efficiency and have the potential of causing accidents, if local overheating causes dryout in a device designed for liquid-phase operation. It is well known that axial flow near narrow gaps, and the associated heat and mass transfer across the gap, are dominated by strong, large-scale, quasi-periodic, flow pulsations, which have been characterized as coherent structures (Rowe *et al.*, 1974; Hooper and Rehme, 1984; Möller, 1992; Wu, 1995; Krauss and Meyer, 1996; Guellouz and Tavoularis, 2000a,b). Cross-gap motions enhance inter-subchannel mixing and heat transfer in the gap region. This is evidenced by the fact that the local heat transfer coefficient in the gap is insensitive to the gap size, except for extremely narrow gaps (Groeneveld, 1973; Guellouz and Tavoularis, 1992).

---

* Material in this Chapter has also been discussed by Chang and Tavoularis (2006).

In the previous Chapter we have described isothermal simulations in a rectangular duct containing a single rod by using the unsteady Reynolds averaged Navier-Stokes equations (URANS) approach and a Reynolds stress model. These simulations reproduced most experimental observations in a similar system. The present Chapter describes an extension of this study, in the same geometry but with the rod heated to introduce a thermal field. The main objective of this study is to provide a thorough understanding of the influence of coherent structures on heat transfer characteristics in a simplified rod-bundle-like configuration, which may lead to improved modeling of such processes. It is hoped that the present results would be of benefit to safety analyses of nuclear reactors and to the design of improved rod bundles and other heat exchangers.

7.1. Local temperature differences and fluctuations

The cross-sectional variations of the time-averaged dimensionless local temperature difference $\overline{\Theta}$ for the two heating modes examined are shown in **Figure 7 - 1**. It can be seen that relatively high temperature regions were restricted around the rod and across the gap and that the wall facing the gap was far warmer than any of the other walls. The isocontours of $\overline{\Theta}$ were slightly closer to the rod for mode B than for mode A, but had comparable shapes for both modes. The apparent inclination of some isotherms to the wall is an artifact of the near-wall mesh refinement; unlike the appearance in this figure, in reality, all computed isotherms approached the wall perpendicularly. **Figure 7 - 2** and **Figure 7 - 3** show, respectively, isocontours of the normalized standard deviations of the coherent and non-coherent temperature fluctuations. Both sets of isocontours had similar shapes for the two modes and their corresponding values were also comparable. The coherent temperature fluctuations were mostly confined in the gap region, while non-coherent fluctuations, modeled by Eq. (3.21), were distributed nearly uniformly around the rod with strong values near the rod. Coherent temperature fluctuations accounted for up to 50% of the estimated total temperature variance for both modes A and B (**Figure 7 - 4)**), dominating the temperature field in the gap region, much like coherent fluctuations dominated the velocity fluctuations in the same region, as demonstrated by Chapter 6.

The spanwise variations of the time-averaged dimensionless temperature differences $\overline{\Theta}$ and two representative profiles of instantaneous resolved dimensionless temperature differences Θ across the bottom wall are plotted for the two heating modes in **Figure 7 - 5**. It may be seen that, although the maximum time-averaged temperature was on the symmetry plane, the locations of instantaneous temperature maxima fluctuated within the approximate range $-0.5 < z/D < 0.5$ for both heating modes.

The streamwise variation of the time-averaged temperature difference $\overline{\Theta}$ on the bottom wall is depicted in **Figure 7 - 6**, in which two representative plots of instantaneous resolved temperature differences have also been shown for comparison. It is observed that, although the local time-averaged temperature difference on the wall was essentially independent of streamwise distance for both heating modes, its instantaneous value fluctuated by as much as 57% for mode A and 69% for the mode B. These instantaneous temperature fluctuations are associated with cross-gap motions caused by the passage of coherent structures.

7.2. Variation of the Nusselt number on the rod

Figure 7 - 7 shows the variation of the Nusselt number around the rod, whereas **Figure 7 - 8** shows the corresponding variation along the rod, on the symmetry plane and facing the gap. Both figures show time-averaged values and two representative instantaneous variations. Averaged in time and around the rod, the Nusselt number was about 190 for both heating modes. Local instantaneous values of the Nusselt number were significantly lower than the corresponding averages around the rod (as much as 38% lower for mode A and 20% lower for mode B). The minimum time-averaged Nusselt number was located on the symmetry plane towards the gap, while instantaneous minima spanned an angular range as wide as possibly ±60° around the symmetry plane. The maximum Nusselt number was not on the symmetry plane facing the top wall, but on either side of it, at about ±30° from this plane. The time-averaged Nusselt number was essentially constant along the bottom of the rod, approximately equal to 165 for both heating modes. In contrast, the instantaneous local Nusselt number along the same line reached values lower than the time-average by as much as about 30% for both modes.

7.3. Influence of the coherent structures on the instantaneous temperature fields

From the above discussion, it is evident that the resolved velocity fields and temperature fields are strongly time-dependent. This time dependence is intimately associated with the convection of large-scale, quasi-periodic, vortical coherent structures, which appear in pairs on either side of the gap between the rod and the channel plane wall. To illustrate the influence of the coherent structures on the instantaneous temperature fields, **Figure 7 - 9** shows isocontours of the instantaneous resolved temperature difference on the equidistant plane, together with the locations of coherent structures, captured using the Q criterion. The characteristics of these structures, based on phase-averaged measurements, have been presented by Guellouz and Tavoularis (2000a), while their numerical identification and detailed features were discussed in previous Chapters. Briefly, these structures consist of pairs of counter-rotating vortices with axes alternating on either side of the gap and transporting fluid far across the gap. This transport has the beneficial effect of moderating the time-averaged temperature rise in the gap region, which otherwise would have been significantly higher. The highest local instantaneous temperatures occur in the gap region between structures, occurring at streamwise locations at which there is little cross flow across the gap.

7.4. Power spectra

Figure 7 - 10 shows power spectra of the spanwise velocity and the temperature in the centre of the gap. The Strouhal number at the peak frequency of the velocity spectrum was about 0.17, which was comparable to the experimental value 0.18 (Guellouz and Tavoularis, 2000a). The Strouhal number at the peak frequency of the temperature

spectrum for both heating modes was approximately twice as large. This is perfectly consistent with the symmetry of the channel and the balanced strengths of the two vortices in each pair: while the spanwise velocity alternates *once* across the gap during each cycle, cool fluid from the two subchannels flanking the gap region is swept across the gap *twice* in each cycle.

Figure 7 - 10a also shows a comparison of the computed and experimental (total) spectra of the azimuthal velocity in the gap center, which demonstrates that the URANS approach acts like a band-pass filter, separating the coherent fluctuations from the non-coherent ones. The present approach produces comparable spectral effects to those generated by adaptive filters and the proper orthogonal decomposition (POD), as described by Bonnet and Delville (2001). A note of explanation seems useful when comparing the experimental and numerical frequency spectra shown in Fig. 7-10a. The peak in the experimental spectrum, although detectable, is not nearly as prominent as the peak in the numerical spectrum. This is due to the inability of Fourier analysis to account for phase shifts and missing cycles in the signals. Such phenomena, which can clearly be seen in the corresponding velocity signals (see Fig. 9 of Guellouz and Tavoularis (2000a) and Fig. 11 of Chang and Tavoularis (2005a)), reflect lateral and streamwise jitter of the coherent structures, occasional merging of them, and other distortions and broaden the spectral peaks. The measured spectral peaks become more distinct when the gap is reduced (see Fig. 10 of Guellouz and Tavoularis (2000a)), which indicates not only the strengthening, but also the tighter organization of the coherent structures at narrower gaps.

Sharp peaks in measured spectra of the azimuthal velocity component in rod-bundle gaps have also been presented by several other researchers (e.g., Möller, 1992; Krauss and Meyer, 1996; Wu and Trupp, 1994; Baratto *et al.* 2006). In the present simulations, the spectral energy is concentrated at a peak because the fine structure and most of the non-coherent turbulence are filtered by the algorithm; moreover, the periodic boundary condition and the limited streamwise length of the domain effectively filter fluctuations with scales much larger than the dominant structure scales and plausibly tend to organize the dominant structures spatially to reduce spatial scatter and phase shifts. As discussed by CT, the strength of the predicted coherent fluctuations in the gap center was essentially the same as the corresponding experimental value, computed by phase averaging of the measured signals (Guellouz and Tavoularis, 2000b), irrespectively of the differences in the appearances of the experimental and numerical spectra.

An important question of concern to designers of thermal equipment using liquids as coolants is whether the local fluctuations in rod and channel wall temperatures would be of sufficiently long durations to permit overheating and possible phase change, which may lead to dryout. The time scale t_f for the duration of such fluctuations can be estimated as the inverse of the peak frequency of the temperature spectrum. For the present configuration, the corresponding Strouhal number was about 0.35, which gives the "period" of temperature fluctuations as

$$t_f \approx 3\frac{D}{U_b} \tag{7.1}$$

There is ample experimental evidence (Möller, 1991) that the Strouhal number of coherent structures in rod bundles is insensitive to the Reynolds number. Consequently, expression (7.1) is expected to be approximately applicable to a wide range of flow conditions. On the other hand, because the temperature spectral peak is wideband, one should consider that parts of the wall would be exposed to local high temperatures over periods which may be several times longer than t_f.

7.5. Summary of convective heat transfer results

The present simulations have clearly documented the significance of coherent vortical structures in heat transfer in a rod-wall gap region. These structures transport fluid across the gap, moderating the time-averaged temperature rise in the gap region but also creating substantial local variations of the instantaneous temperature and heat transfer coefficient. These fluctuations are at relatively low frequencies and may have to be taken into consideration in safety analyses.

Chapter 8. Effect of gap size variation on the turbulent flow and heat transfer in a single-rod duct*

The present Chapter describes unsteady numerical simulations to determine the effect of diminishing gap size on local flow and heat transfer. It also investigates the degree by which coherent structures persist as the gap diminishes and determines their relative importance in the mixing process. Moreover, the present results are used to reassess the accuracy of previous correlations describing inter-subchannel mixing.

8.1. Time- averaged velocity and turbulent kinetic energy

Predicted isocontours of the local time-averaged dimensionless streamwise velocity $\overline{U}/U_b$ for three different gap sizes are shown in **Figure 8 - 1**, with detail views of the gap region shown on the left side of each figure. Away from the gap, the local velocity was

* Material in this Chapter has also been discussed by Chang and Tavoularis (2005b).

nearly insensitive to the gap size, however, in the gap region, it was dramatically reduced in magnitude with decreasing gap size, reflecting the increasing influence of viscous friction in this region.

Predicted isocontours of the local time-averaged total dimensionless kinetic energy per unit mass $\bar{k}/U_b^2$ are plotted in **Figure 8 - 2**, and **Figure 8 - 3**, **Figure 8 - 4** and **Figure 8 - 5** show contours of the local time-averaged coherent turbulent kinetic energy $\bar{k}_c/U_b^2$, the non-coherent turbulent kinetic energy $\bar{k}_{nc}/U_b^2$ and the ratio $\bar{k}_c/\bar{k}$, respectively. For $\delta/D = 0.10$, the boundary layer around the rod was separated from the boundary layer on the bottom wall, as evidenced by the fact that the total kinetic energy on the symmetry plane had two maxima located on either side of the gap middle (**Figure 8 - 2a**). The coherent component, however, had a single maximum near the gap middle (**Figure 8 - 3a**) and its relative contribution to the total kinetic energy achieved its maximum of 72% at the same location (**Figure 8 - 5a**). The non-coherent component had two maxima near the surface of the rod and the bottom wall and a single minimum near the gap middle (**Figure 8 - 4a**). It is also interesting to notice that two secondary weak local maxima of the coherent kinetic energy also occurred at $\pm 30^\circ$ on either side of the symmetry plane, towards the adjacent subchannels; these maxima are due to axial velocity fluctuations, while the main maximum on the symmetry plane represents mostly spanwise velocity fluctuations (**Figure 8 - 3a**). **Figure 8 - 2b** and **Figure 8 - 3b**, for $\delta/D = 0.03$, show that the coherent fluctuations dominated boundary layer turbulence, so that a single main turbulent kinetic energy maximum occurred on the symmetry, together with two weak local maxima on either side of this plane. The non-coherent component for $\delta / D = 0.03$ decreased slightly from two local maxima near the surface of the rod and the bottom wall near the gap middle, while two strong local maxima of the non-coherent kinetic energy were located at $\pm 45°$ on either side of the symmetry plane (**Figure 8 - 4**b). The mid-gap total turbulent kinetic energy increased slightly with decreasing gap (**Figure 8 - 2**b), whereas its coherent component increased significantly to reach 91% of the total for the smaller of the two gaps (**Figure 8 - 5**b). With further decrease in gap size to $\delta / D = 0.01$, evidence for the formation of coherent structures is barely visible (**Figure 8 - 3**c). As **Figure 8 - 2**c shows, the total turbulent kinetic energy in the gap region became several orders of magnitude smaller than its values for the two larger gaps, pointing to the extremely large viscous actions under such conditions.

8.2. Resolved temperature and temperature fluctuations

The cross-sectional variations of the time-averaged dimensionless local temperature difference for different gap sizes are shown in **Figure 8 - 6**. It is noted that the bulk temperature and the circumferentially-averaged rod temperature are fairly insensitive to gap size variations, because most of the heat transfer occurs away from the gap region. Moreover, the contours shown in **Figure 8 - 6** apply to all streamwise cross sections, because all time averaged temperatures grow with streamwise distance at the same rate. As expected, the temperature in the gap region increases with decreasing δ / D, and becomes much higher than $\overline{T}_{\mathrm{rod,m}}$ for $\delta / D = 0.01$ due to lack of mixing with the outer flow.

The variations of the time-averaged temperature differences $\overline{\Theta}$ around the rod surface and across the bottom wall are shown in **Figure 8 - 7** and **Figure 8 - 8**, respectively. In all cases, the maximum time-averaged temperature difference occurred on the symmetry plane facing the gap, and its value increased dramatically as the gap size decreased. **Figure 8 - 7** and **Figure 8 - 8** also present two representative plots of instantaneous resolved surface temperature differences Θ. These temperature differences varied significantly for the larger two gap size cases (more significantly for the $\delta / D = 0.03$ case than for the $\delta / D = 0.10$ case), but almost not at all for the $\delta / D = 0.01$ case. To allow determination of actual temperature values, we note that the bulk temperature at the inlet was always kept at 300 K, whereas the circumferentially averaged rod temperature at the inlet was found to be 303, 304 and 311 K, for $\delta / D = 0.10$, 0.03 and 0.01, respectively.

Figure 8 - 9 shows predicted isocontours of the standard deviation of coherent temperature fluctuations $\sqrt{\overline{\vartheta_c^2}} / \left(\overline{T}_{\mathrm{rod,m}} - \overline{T}_b\right)$ for the three gap sizes examined. It can be seen that these fluctuations increased by nearly four-fold as the relative gap size δ / D decreased from 0.10 to 0.03, pointing to increased coherent activity. In contrast, as the gap size further decreased to $\delta / D = 0.01$, the temperature fluctuations in the gap diminished. One may note that, in the latter case, local temperature differences from the bulk temperature were much larger than those in the other cases, so that coherent

temperature fluctuations would have appeared to be even smaller if they were normalized by the local flow temperature difference. The intensity of the non-coherent temperature fluctuations (**Figure 8 - 10**) monotonically decreased with decreasing gap size, as a result of a corresponding decrease in the local mean temperature gradient. The ratio $\overline{\vartheta_c^2} / \overline{\vartheta^2}$ of the coherent and total temperature fluctuations is shown in **Figure 8 - 11**. In all cases, the contribution of coherent fluctuations diminished with increasing distance from the gap, however, the distance at which this contribution became insignificant decreased with decreasing gap size. One may further observe that, for $\delta / D = 0.10$, coherent fluctuations were dominant only near the two walls, whereas for the other two gap sizes they were overwhelming in the entire gap region.

8.3. Skin friction coefficient and Nusselt number

The variation of the time-averaged local skin friction coefficient $\bar{c}_f = \dfrac{\bar{\tau}_w}{1/2\,\rho U_b^2}$ (τ_w is the local wall shear stress) around the rod is depicted in **Figure 8 - 12**, in which two representative plots of the instantaneous resolved skin friction coefficient are also shown for comparison and to indicate the level of local skin friction fluctuations. All values have been normalized by the corresponding circumferentially averaged skin friction coefficients, which were 0.0048, 0.0047 and 0.0053 for $\delta / D = 0.10$, 0.03 and 0.01, respectively, thus only weakly sensitive to gap size. Similar variations across the span of the bottom wall are shown in **Figure 8 - 13**, in which all values have been normalized by the corresponding spanwise averaged skin friction coefficients, which were 0.0030, 0.0036 and 0.0034 for $\delta / D = 0.10$, 0.03 and 0.01, respectively. It may be observed that skin friction fluctuations in the gap region were quite large for $\delta / D = 0.10$, they maintained significant values for $\delta / D = 0.03$ and vanish altogether for $\delta / D = 0.01$. These results are compatible with experimental evidence (Meyer and Rehme, 1994; Krauss and Meyer, 1998; Guellouz and Tavoularis, 2000a).

The Nusselt number variation around the rod, shown in **Figure 8 - 14**, was comparable with that of the skin friction coefficient. The presented values have been normalized by corresponding circumferential averages, which were 191, 185 and 166 for $\delta / D = 0.10$, 0.03 and 0.01, respectively; this indicates that heat flux was more sensitive to gap size than skin friction was. Nusselt number fluctuations were significant for the larger two gaps and disappeared for $\delta / D = 0.01$. The present results support the conclusion that local and temporal variations of both skin friction and heat transfer coefficient were strongly associated with cross-gap motions caused by coherent structures (Guellouz and Tavoularis, 2000a).

Figure 8 - 15 plots the predicted minimum time-averaged normalized Nusselt number on the rod surface vs. gap size. The value of this parameter dropped only slightly as the gap width decreased from $\delta / D = 0.10$ to $\delta / D = 0.03$, but very dramatically when the latter further decreased to $\delta / D = 0.01$. The present results are in excellent agreement with direct experimental observations (Guellouz and Tavoularis, 1992) and an empirical

correlation that was fitted to a large number of experimental results in a variety of rod bundle geometries and for a wide range of Reynolds numbers (Guellouz, 1998).

8.4. Coherent structure characteristics

Considering the importance of the coherent structures on the performance of rod bundles, it is worthwhile to document their macroscopic characteristics, particularly their frequency and streamwise spacing. For comparisons with other flow configurations, the frequency must be non-dimensionalized in the form of a Strouhal number, using appropriate length and velocity scales. Because, for the present geometry, the hydraulic diameter of the entire duct is determined mostly from parts of the duct away from the gap, it is the rod diameter D which seems to be the most appropriate length scale. Previous investigators have suggested the use of the bulk velocity U_b, the average friction velocity $u^* = \sqrt{\tau_w/\rho}$ (Wu and Trupp, 1994; Sadatomi *et al.* 1996), and a coherent structure convection speed represented by an average velocity within the gap (Krauss and Meyer, 1998), as a velocity scale. When considering turbulent flow at sufficiently large Reynolds numbers in a duct of fixed geometry, all three scales would be proportional to each other and it is immaterial which one is chosen for normalizing the frequency, as such choice would only affect only the numerical value of the Strouhal number and not its sensitivity to other flow parameters. In such cases, the coherent structure frequency would be proportional to the velocity scale and therefore the Strouhal number would be independent of the Reynolds number (Möller,1991). However, matters are complicated when attempting to correlate results in different rod bundle geometries, particularly when evaluating the effect of gap size on the coherent structure frequency. In a single-rod configuration, like the present one and the one used by Wu and Trupp (1994), rod displacement towards a wall would cause negligible changes on the bulk velocity and the overall streamwise pressure drop, but a significant change on the near-gap velocity field. On the other hand, when considering a rod bundle with fixed rod diameters, like the one used by Möller (1991), changing all rod spacings as well as the size of the surrounding duct to modify the (uniform) gap width would have profound effects on all velocity scales. The point of the previous statements is that one must use extreme care when trying to predict coherent structure characteristics in one configuration using correlations developed from measurements in another.

Representative smoothened spectra for the three gap sizes examined are shown in **Figure 8 - 16**a. It may be seen that all spectra have very distinct peaks and that the peak Strouhal number decreased measurably as the gap size was reduced.

Although periodicity was detected at an extremely low frequency for the $\delta / D = 0.01$ case (as explained in section 4.3.1, particularly long sets of results were used for this purpose: data were collected over a time of $26.2t_c$, after waiting for full development of flow over $95t_c$), one is reminded that the coherent structures were also extremely weak in this case, so that their effects on inter-subchannel mixing would be negligible. The observed trend, also illustrated in **Figure 8 - 17**, is in agreement with the GT1 experimental results in the same geometry (Guellouz and Tavoularis, 2000a), as well as with recent measurements in an outer subchannel of a five-rod bundle in which only one of the outer rods was displaced towards the wall (Baratto *et al.*, 2006).

The present findings contradict a widely used correlation by Möller (1991). This correlation was based on a large number of measurements in a four-rod bundle in which all gaps were changed at the same time and predicts that the Strouhal number would increase with decreasing gap size. Möller's correlation, with the Strouhal number adjusted to conform with Eq. (6-1), has also been plotted in **Figure 8 - 17**. It is clear that this correlation does not describe the present results in either level or trend. Wu and Trupp (1994) presented measurements of Strouhal number in different gaps between a single rod and the walls of a surrounding trapezoidal duct. They concluded that Möller's correlation was applicable to their results in a qualitative sense and proposed a slightly different correlation that would, presumably, account for differences in the two geometries. Wu and Trupp's measurements include a wide range of gap sizes and gaps with very different adjacent subchannels. In **Figure 8 - 17,** we present only those measurements taken in a symmetric configuration, in the gap between the rod and the longer one of the parallel walls in the trapezoidal duct, and only for the range of relative gap sizes that is close to the present one. The trend in these measurements is evidently in agreement with the present findings and contrasts both Möller's and Wu and Trupp's correlations. Careful observation of all available measurements and logical reasoning lead to the following conclusion: for each given geometry and Reynolds number, there is a critical relative gap size $(\delta/D)_{cr}$ for which the coherent structure frequency reaches a maximum. For $\delta/D > (\delta/D)_{cr}$, the frequency decreases with increasing δ/D, in conformity with Möller's correlation. However, as $(\delta/D) \rightarrow 0$, the frequency decreases again and eventually the coherent structures cease to exist. The latter statement can be justified by considering that viscous damping is accentuated in extremely narrow gaps, slowing down both the velocity of cross-gap pulsations and their rate of occurrence. One may further speculate that the value of $(\delta/D)_{cr}$ for a given geometry would decrease as the Reynolds number increases, because viscous effects would become of lesser importance in comparison to inertial effects.

The average convection speed U_c of coherent structures was estimated from the convection speed of spanwise velocity isocontours in the gap centre. This approach is considered somewhat more accurate than the approach adopted in Chapter 6, using coherent structures identified by the Q criterion, which depended on the identification threshold. The present estimate for $\delta / D = 0.10$ was $U_c/U_b = 0.71$, which is closer to the experimental value 0.78 (Guellouz and Tavoularis, 2000a), than the estimate of 0.62 in Chapter 6. For $\delta / D = 0.03$, the present estimate was 0.38, which was also not too far from the experimental value of 0.48 (Guellouz and Tavoularis, 2000a). In conclusion, the present simulations confirm the experimental finding of Guellouz and Tavoularis (2000a) that the convection speed of coherent structures decreases with diminishing gap size.

The average normalized streamwise spacing λ_c / D between two consequent coherent structures was found to be 4.0 for $\delta / D = 0.10$ and 3.5 for $\delta / D = 0.03$, in reasonable agreement in level and trend with the corresponding experimental values of 4.3 and 3.0 (Guellouz and Tavoularis, 2000a).

Power spectra of the temperature fluctuations in the gap center are shown in **Figure 8 - 16b**. In the $\delta / D = 0.10$ case, the temperature spectrum has a sharp peak at a frequency that is approximately twice the peak frequency of the velocity spectrum. This has been explained in Chapter 7, who pointed out that the temperature field is transported across the gap twice during each coherent structure cycle. Curiously, in the $\delta / D = 0.03$ case, the temperature spectrum has no peak, although one may observe a change in slope at a frequency that is roughly twice the peak frequency of the corresponding velocity spectrum. In the case with $\delta / D = 0.01$, the temperature spectrum increases monotonically and without slope discontinuities with decreasing frequency. A plausible explanation for the lack of peaks in the temperature spectra near very narrow gaps is that heat transport by coherent structures is smeared by heat conduction, accentuated by the low levels of local convection velocity and the low frequency of flow pulsations across the gap.

8.5. Inter-subchannel mixing

In closing, it seems worthwhile to apply the present findings to a problem of practical importance, namely the prediction of mixing across narrow gaps by the lump parameter approach, described in section 3.3.

Equation (3.28) and all other similar correlations are fitted to measurements within wide ranges of δ/D, which, however, do not include values lower than 0.011 (Rehme, 1992); they all predict an increase of Y with decreasing δ/D. If extrapolated towards the zero gap, this trend would lead to an obvious fallacy because it implies that, as the gap vanishes, cross-gap mixing would increase without bounds, rather than also vanish, as common sense dictates.

Möller (1992) proposes to use the distance between the centroids of the two subchannels as the mixing distance δ_{12} for Eq. (3.26). This choice may be appropriate for tightly packed rod bundles, but, for the present geometry, it seems more suitable to use a length that describes the distance over which the effects of coherent structures are significant. From **Figure 8 - 3**, one may verify that this length is comparable to the rod diameter D for the two cases with $\delta / D = 0.10$ and $\delta / D = 0.03$, while it would be far smaller for the $\delta / D = 0.01$ case. For simplicity, we shall take $\delta_{12} = D$, for the two larger-gap cases (the $\delta / D = 0.01$ need not be considered in view of the extremely low turbulence activity in the gap). Among the previously suggested approaches to estimate w_{eff}, most appropriate appears to be Rehme's (1992) suggestion to use the half-width integral of the power spectral density of the full-band azimuthal velocity at a spanwise location that is $0.2\delta_{12}$ away from the center of the gap. This approach separates, to some degree, the coherent from the non-coherent fluctuations, while also accounting for the wide-band nature of coherent pulsations and roughly averaging their varying strength across the gap. For consistency, we followed this approach for the experimental results of

GT1 and Wu and Trupp (1994) (the case of symmetrically placed rod near the longer of the two parallel walls) as well as for the present URANS simulations, for which the resolved velocity mainly represents coherent fluctuations. It is noted that, in the present simulations, the estimates of w_{eff} from the half-width spectral integral were lower than the full-band estimates by 19% for $\delta / D = 0.10$ and by 28% for $\delta / D = 0.03$. As GT1 provide spectra in the gap center only, off-center values w_{eff} were computed using a correlation suggested by Rehme (1992). To account for differences in Reynolds numbers, all results have been referenced to Re=50000, assuming that the friction coefficient is proportional to $\mathrm{Re}^{0.9}$ (Rehme, 1992).

Figure 8 - 18 presents estimates of the mixing factor Y estimated as described in Chapter 3 for the present simulations and the experiments of GT1 and Wu and Trupp (1994). Both sets of experimental results show a weak trend of decreasing Y with decreasing δ / D, but they do not extend to values of δ / D lower than 0.02, due to difficulties in using hot-wire probes in extremely narrow gaps. The present simulations show a strong trend of decreasing Y with decreasing δ / D, and include the case with $\delta / D = 0.01$, for which cross-gap mixing was found to be negligible. The same figure also plots the correlations suggested by Rehme (1992) and Rogers and Tahir's (1975). Whereas the value of Y predicted by either correlation for $\delta / D = 0.10$ is in fair agreement with the present simulation and previous experimental values, both correlations predict an unbounded increase of Y as $\delta / D \rightarrow 0$. The method of Sadatomi *et al.* (1996) also predicts that $Y \rightarrow \infty$ as $\delta / D \rightarrow 0$. Thus, none of the available

correlations is capable of predicting that Y will become negligible for relative gap widths δ / D smaller than a critical value. For the relatively low Reynolds number of the present simulations, this critical value seems to be somewhat larger than 0.01, however, it is expected that this value would become smaller as the Reynolds number increases, due to the diminishing significance of viscous actions in the gap. Heat transfer measurements in rod bundles (Guellouz, 1998; Groeneveld, 1973) also support the postulate that the critical gap size depends on the Reynolds number. The practical significance of this postulate is that the critical relative gap size δ / D for the obliteration of cross-subchannel mixing in operating nuclear reactors is expected to be smaller than those observed in low Reynolds number rod bundle models.

8.6. Summary of the gap size variation effects

In the present study, the unsteady Reynolds averaged Navier-Stokes and energy equations, supplemented by the Reynolds stress model and a gradient transport-type model for the turbulent heat fluxes, were solved to determine the effect of diminishing gap size on local flow and heat transfer in a simplified rod-bundle-like geometry. It was shown that the coherent parts of the turbulent kinetic energy and the temperature fluctuations dramatically increased as the gap size decreased from $\delta / D = 0.10$ to $\delta / D = 0.03$, but, with further decrease in gap size to $\delta / D = 0.01$, coherent fluctuations essentially disappeared, presumably due to dominating viscous actions in the gap region.

It was further concluded that, for each given geometry and Reynolds number, there is a critical relative gap size $(\delta/D)_{cr}$ for which the coherent structure frequency would reach a maximum. For $\delta/D > (\delta/D)_{cr}$, the frequency decreases with increasing δ/D, in conformity with available correlations, however, as $\delta/D \rightarrow 0$, the frequency decreases again until the coherent structures cease to exist. This trend, which contradicts all available empirical correlations, is also attributed to accentuated viscous damping, which slows down both the velocity of cross-gap pulsations and their rate of occurrence. The present simulations are in fair agreement with measurements of the convection speed of coherent structures and their average streamwise spacing. Both were found to decrease with diminishing gap size. Finally, the present simulations imply that cross-gap mixing would tend to vanish as the gap size decreases below a certain value. This observation is supported by experimental evidence in very narrow gaps but contradicts predictions obtained by extrapolating available correlations.

Chapter 9. Simulation of turbulent flow in a 37-rod bundle*

Based on the single-rod simulations described in previous Chapters, we have built considerable confidence in the applicability of the URANS approach to rod bundles, and we now proceed to simulate the flow in the more realistic geometry of a sector of a 37-rod bundle, for which experimental results are available (Ouma and Tavoularis, 1991a, 1991b, hereafter referred to as OT; Baratto *et al.*, 2006).

9.1. Mean velocity and turbulence characteristics

The present simulations were validated by comparison to the experimental results of OT in the subchannels surrounding the middle outer rod, in which the effects of differences between the computational and experimental geometries are expected to be small. Considering the differences in bulk velocity definitions in the two setups, comparisons are made by normalizing all velocities by the corresponding maximum time-average velocities in the subchannels surrounding the middle outer rod. In both cases, the maximum velocities occurred in the center of the subchannel towards the interior of the

* Material in this Chapter has also been discussed by Chang and Tavoularis (2005c).

bundle and differed by only 3% from each other; their values were 16.8 m/s for the OT experiments and 16.3 m/s for the present simulations.

As shown in **Figure 9 - 1a**, computed time-averaged axial velocity variations along different radial directions surrounding the middle outer rod were in excellent agreement with OT measurements, both in trends and actual values. Predicted isocontours of the local time-averaged dimensionless streamwise velocity $\overline{U}/U_b$ are shown in **Figure 9 - 1b**. The self-consistency of the simulations is evidenced by the symmetry of the contours about a radial centerplane that includes the middle outer rod axis, the formation of local maxima in the centers of all subchannels, and the bulging of the contours towards the gaps, in agreement with experimental findings (OT; Trupp and Azad, 1975). Contour bulging tends to increase the local velocity in the gap region. In an operating reactor, this would help remove heat from the rods. While comparing the local velocity maxima, it may be observed that the highest one ($\overline{U}/U_b = 1.35$) occurred in the square subchannels between rods in the second and third rings, followed by those in the square subchannels between rods in the first and second rings ($\overline{U}/U_b = 1.32$), the triangular subchannel between two rods in the second ring and one rod in the third ring ($\overline{U}/U_b = 1.25$), the subchannels between rods in the third ring and the outer tube ($\overline{U}/U_b = 1.19$) and the triangular subchannel between one rod in the first ring and two rods in the second ring ($\overline{U}/U_b = 1.00$). The local maxima surrounding the central rod were relatively low ($\overline{U}/U_b = 0.96$). Local velocity minima occurred in all gap centers, with the lowest one

($\overline{U}/U_b = 0.76$) also occurring in the gaps surrounding the central rod. Excluding boundary layers, the variation of the local time-averaged velocity was relatively mild, spanning the range between 76% and 132% of U_b.

The variations of the time-averaged normal and shear turbulent stresses and the turbulent kinetic energy, together with comparisons to corresponding measurements by OT, are shown in **Figure 9 - 2** to **Figure 9 - 7**. When necessary, these parameters are plotted in local cylindrical coordinates having origins on the axes of the corresponding rods. With minor exceptions, all predictions are in good agreement with the experimental results, a fact that creates high confidence in the use of the present approach for rod-bundle flow simulations. Moreover, all contours were found to be essentially symmetric about the radial centerplane, which adds to the evidence that the turbulence structure was fully developed in the present simulations.

As **Figure 9 - 2**b shows, local minima of the axial velocity fluctuations occurred in the centers of all open subchannels. In addition, local minima also occurred in the centers of most, but not all, of the gaps, while local maxima were found in regions flanking the gap centers, in agreement with previous experimental findings (Krauss and Meyer, 1996). The highest levels of axial velocity fluctuations ($u'/U_b = 0.12$) were found in the space between rods in the first and second rings. In agreement with previous measurements in similar rod bundles (OT; Trupp and Azad, 1975; Tavoularis *et al.*, 1988), the axial velocity fluctuations took values that were substantially larger than those observed in the core region of fully developed pipe flows (Laufer, 1956).

The azimuthal velocity fluctuations had a more complex distribution (**Figure 9 - 3**b). Although they presented some local maxima near several of the gap centers, they also presented stronger local maxima at positions intermediate between adjacent gaps. Radial velocity fluctuations were, in general, weaker than axial and azimuthal ones and presented no strong local maxima and minima (**Figure 9 - 4**b). The present distributions of azimuthal and radial fluctuation levels were comparable to earlier measurements in wall subchannels (Krauss and Meyer, 1996) and inner subchannels (Krauss and Meyer, 1998).

The total time-averaged turbulent kinetic energy variation (**Figure 9 - 5**b) resembled that of the axial fluctuations. It presented local minima both in the open subchannel centers and the gap centers and local maxima at positions intermediate between these two. Finally, the predicted turbulent shear stresses in the azimuthal and the radial directions (**Figure 9 - 6** and **Figure 9 - 7**, respectively) were much weaker than the normal stresses, in agreement with OT measurements. In summary, the current simulation approach was found to be successful in predicting the turbulence structure that is peculiar to rod bundles, as documented by previous experimental studies (OT; Krauss and Meyer, 1996; Krauss and Meyer, 1998).

9.2. Partition of Reynolds stresses to coherent and non-coherent parts

The time averaged stresses presented in the previous section certainly display effects of coherent structures, but these effects are often obscured by the superposition of non-coherent fluctuation effects. A more clear understanding of the complex structure of this flow can be obtained by examining separately the coherent (i.e. those computed from the resolved velocity fluctuations) and non-coherent (i.e. those computed from the resolved Reynolds stresses) parts of the normal Reynolds stresses and turbulent kinetic energy, shown in **Figure 9 - 8** to **Figure 9 - 11**. Contours of these parameters, especially of the coherent parts, have much more pronounced maxima and minima than those of the corresponding total parameters. All contours are qualitatively symmetric about the radial centrerplane, although some small quantitative asymmetry can be observed in the coherent contours; this asymmetry is attributed to the relatively small statistical populations from which coherent averages have been computed (see next section).

While comparing the distributions of the coherent and non-coherent axial velocity fluctuations (**Figure 9 - 8**a and b, respectively), it is interesting to observe that the locations of many local maxima of the coherent part (on the flanks of gap centers) nearly coincide with locations of local minima of the non-coherent part. This is a phenomenon that results in smoothing the total axial fluctuation distribution. In contrast, the local maxima of the coherent azimuthal velocity fluctuations clearly occurred in gap centers

(**Figure 9 - 9**a), which, in general, had relatively low levels of non-coherent velocity fluctuations (**Figure 9 - 9**b).

The variations of the radial turbulence intensities (**Figure 9 - 10**) were rather difficult to interpret. The coherent radial velocity fluctuations (**Figure 9 - 10**a) had levels that were much lower than those of the axial and radial ones and their distribution did not exhibit any distinct features. The non-coherent fluctuations also had a relatively even distribution but presented extended local maxima near the surface of the rods in each subchannel at about $\pm 120°$ (**Figure 9 - 10**b). Overall, the distributions of both the coherent (**Figure 9 - 11**a) and non-coherent (**Figure 9 - 11**b) kinetic energy parts resembled largely those of the corresponding axial fluctuations.

To help in assessing the relative significance of the coherent structures on the turbulent activity, **Figure 9 - 12** and **Figure 9 - 13** show the distributions of the ratios of the coherent and total normal stresses and turbulent kinetic energies. Both the axial (**Figure 9 - 12**a) and the azimuthal (**Figure 9 - 12**b) coherent components were dominant in the gap regions, with maximum values of 70% and 55%, respectively, and weak in the open subchannel regions. The radial coherent component (**Figure 9 - 13**a) was relatively weak throughout rod bundle, although it reached values near 40% in some gap regions. The contribution of coherent fluctuations to the total turbulent kinetic energy reached local maxima of between 50 and 55%, slightly off gap centers (**Figure 9 - 13**b). An interesting observation is the apparent suppression of coherent fluctuations in the space between the central rod and the rods of the first ring.

9.3. Wall shear stress

Figure 9 - 14a shows the circumferential variation of the time averaged, normalized wall shear stress around the middle outer rod in the present simulations and the OT experiments. The circumferential averages of the wall shear stress in both the simulations and the experiments were about 0.63 Pa. Some differences can be observed in the locations of local maxima and minima, with the predictions being below measured values for $90° < \phi < 130°$, and above the latter for $40° < \phi < 80°$, with similar observations made for the negative ϕ range. In the simulations, local maxima of the shear stress occurred at $\phi \approx \pm 60°$ and 180°, i.e., facing the open subchannels, whereas the gap regions ($\phi \approx 0°$ and $\pm 98°$) were characterized by local shear stress minima. The present observations, although partially deviating from the OT measurements, are in qualitative agreement with measurements by Krauss and Meyer (1996). **Figure 9 - 14b** indicates that instantaneous distributions of the wall shear stress could be visibly distinct from the time-averaged wall shear stress distribution; this phenomenon is attributed to the passage of coherent structures, in agreement with the observations in Chapter 6.

9.4. Coherent structures

Figure 9 - 15 and **Figure 9 - 16** show typical coherent structures identified using the modified Q criterion, as described in Chapter 5. Coherent structures appeared clearly in organized pairs on either side of each gap between the outer rods and the tube wall. The average spacing between these pairs was roughly $4D$, corresponding to 5 pairs along the computational domain. They also appeared in all other parts of the bundle, except in the space between the central rod and the rods of the first ring. It is evident from these plots that coherent structures are important features of the rod bundle flow and they appear regularly at specific locations in the subchannels. The average frequencies f_p of appearance of the structures at different locations were essentially the same, as shown by the nearly matching frequencies of peaks of the power spectra of the azimuthal velocity in different gaps (**Figure 9 - 17**). The average Strouhal number (dimensionless frequency) $\mathrm{St} = f_p D / U_b$ was about 0.27, which is nearly twice the experimental value of 0.14 (Baratto *et al.*, 2006). Although the reason for such significant difference is not entirely clear, it may be hypothesized that the side and bottom walls in the experimental section impede the formation of coherent structures, which therefore appear at lower rates than those in the computational section, which does not have such walls. In support of this hypothesis, it is worth mentioning that measurements of the Strouhal number in wall subchannels of a 37-rod bundle with $\delta / D = 0.06$ and a hexagonal outer tube ranged from 0.36 to 0.43 (Krauss and Meyer, 1996).

The near periodicity of the coherent structure formation, and resulting cross-gap flow pulsations, is also illustrated by the strong oscillatory character of the autocorrelation coefficients of the azimuthal velocity fluctuations at all gap centres, even including the one between the central rod and the rods in the first ring (**Figure 9 - 18**). In all cases, the streamwise wavelength of oscillations was about $4D$.

To explore the possible coordination among coherent structures and transverse flow pulsations in different parts of the rod bundle, we have computed the two-point space-time cross-correlation coefficient between the azimuthal velocity fluctuations in the center of the gap between the middle outer rod (denoted as 3M) and the surrounding wall (denoted as O) and azimuthal velocity fluctuations in other gap centers (**Figure 9 - 19**). All these cross-correlations had positive and negative peaks with amplitudes as high as ± 0.5. This indicates that coherent structures were not scattered randomly throughout the rod bundle, but were connected to each other forming a network of vortices, each of which passed near multiple rods. The fact that correlation peaks appeared in many cases with considerable time delay (phase shift) may be explained by assuming that each vortex has different sections, each of which appeared near different gaps at different streamwise positions. The reason for not seeing intermediate connections among the coherent structures that were identified in **Figure 9 - 15** and **Figure 9 - 16** may be that these connections were too weak to be captured by the present identification criterion.

Finally, the strength of spatial coherence in velocity fluctuations around the middle outer rod was examined by plotting the cross-correlation coefficient between the azimuthal velocity fluctuations in the center of the rod-wall gap and the velocity fluctuations tangent to the maximum velocity line (**Figure 9 - 20**). In agreement with measurements by Baratto *et al.* (2006), this cross-correlation coefficient maintained strong peak amplitudes (well exceeding ±0.5) in the entire examined range. It is also interesting to note that the primary peaks occurred following a time delay that increased with increasing separation.

9.5. Summary

The present study reports the first known realistic simulations of fully developed isothermal turbulent flow in a 37-rod bundle, using standard CFD procedures and without any empirical adjustments accounting for specific features of this configuration. Having demonstrated that the proper use of direct numerical simulation (DNS) and large eddy simulation (LES) approaches would require computer resources far larger than those presently available, we used conventional methods to solve the unsteady Reynolds averaged Navier Stokes (URANS) equations, supplemented by the Reynolds Stress Model. This approach separates the velocity fluctuations into coherent fluctuations, whose time dependence is resolved by the solution method, and non-coherent fluctuations, which are resolved only as time dependent modeled Reynolds stresses. The time averaged mean velocity and time averaged Reynolds stresses were found to be in good agreement with experimental results in a similar channel (OT). Detailed distributions of the partition of the total turbulent kinetic energy to coherent and non-coherent parts and to axial, azimuthal and radial components have been presented in isocontour forms, permitting an in-depth understanding of the turbulence structure and proving that coherent fluctuations are an indispensable feature of this flow. A novel modified Q criterion was successful in identifying coherent structures in the form of pairs of vortices forming on either side of gaps between adjacent rods or outer rods and the tube wall. The streamwise spacing between successive pairs of coherent structures was roughly equal to four rod diameters and the Strouhal number (frequency of transverse flow pulsations non-dimensionalized by the rod diameter and the bulk Reynolds number) was about 0.27. Measurements of two-point space time correlations demonstrate that coherent velocity fluctuations were strongly correlated in the entire rod bundle. Moreover, they imply that coherent structures were not spaced randomly, but were connected to each other forming a network of vortices that surrounded all rods in the bundle. The present results have important implications that deserve consideration in analyses of nuclear reactor operation and safety.

Chapter 10. Conclusions and recommendations for future work

10.1. Conclusions

The objective of this research was to simulate numerically turbulent flow and heat transfer characteristics in a duct containing a single rod and a 37-rod bundle, with emphasis given to the identification of coherent structures forming in the gap regions and the documentation of their effects on the structure of turbulence, the heat transfer and the mixing process. This study has reproduced the main findings of experimental observations by using the unsteady Reynolds-averaged Navier-Stokes equation with fine spatial and temporal resolutions; it has also successfully identified the coherent structures using the Q criterion for the single-rod duct and a modified Q criterion for the 37-rod bundle. The results of this study have been applied to a reassessment of previous intersubchannel mixing estimates.

More specifically, the present simulations have confirmed the following important experimental findings.

<u>Single-rod duct simulations:</u>

- In the gap centre, the time-averaged mean velocity reaches a minimum, whereas the axial and spanwise turbulent stresses as well as the turbulent kinetic energy reach maxima, in sharp contrast to gradient transport theory predictions.
- The maximum coherent streamwise stress occurs at an intermediate position between the gap centre and the open subchannel centre, while the maximum coherent azimuthal stress occurs in the gap centre.
- The dominant coherent structures are counter-rotating vortices with axes alternating on either side of the gap causing large-scale transport of fluid across the gap.
- Velocity fluctuations in the gap region are of sufficiently large wavelength and low frequency for local conditions to potentially prevail in wall heating and possible phase change.
- The Strouhal number at the peak frequency of the temperature spectrum for a heated rod was approximately twice as large as the Strouhal number at the peak frequency of the velocity spectrum.
- Coherent structures transport fluid across the gap, moderating the time-averaged temperature rise in the gap region but also creating substantial local variations of the instantaneous temperature and heat transfer coefficient.
- Coherent parts of the turbulent kinetic energy and the temperature fluctuations dramatically increased as the relative gap size decreased from $\delta / D = 0.10$ to $\delta / D = 0.03$, but, with further decrease in gap size to $\delta / D = 0.01$, coherent fluctuations essentially disappeared, presumably due to dominating viscous actions in the gap region.

- Skin friction fluctuations in the gap region were quite large for $\delta / D = 0.10$, they maintained significant values for $\delta / D = 0.03$ and vanished altogether for $\delta / D = 0.01$.
- Local and temporal variations of both the skin friction coefficient and the heat transfer coefficient were strongly associated with cross-gap motions caused by coherent structures.
- For each given geometry and Reynolds number, there is a critical relative gap size $(\delta/D)_{cr}$ for which the coherent structure frequency reaches a maximum. For the case of $\delta/D > (\delta/D)_{cr}$, the frequency decreases with increasing δ/D, in conformity with a popular correlation. However, as (δ/D) approaches zero, the frequency decreases again and eventually the coherent structures cease to exist.
- Experimental results show a weak trend of decreasing mixing factor Y with decreasing δ / D, but they do not extend to values of δ / D lower than 0.02, due to difficulties in using hot-wire probes in extremely narrow gaps. The present simulations show a strong trend of decreasing Y with decreasing δ / D, and include the case with $\delta / D = 0.01$, for which cross-gap mixing was found to be negligible.
- Whereas the values of Y predicted by previous correlations for $\delta / D = 0.10$ are in fair agreement with the present simulation and previous experimental values, none of the available correlations is capable of predicting that Y will become negligible for relative gap widths δ / D smaller than a critical value. For the relatively low Reynolds number of the present simulations, this critical value seems to be somewhat larger than 0.01, however, it is expected that this value would become smaller as the Reynolds number increases, due to the diminishing

significance of viscous actions in the gap. The practical significance of this postulate is that the critical relative gap size δ / D for the obliteration of cross-subchannel mixing in operating nuclear reactors is expected to be smaller than those observed in low Reynolds number rod bundle models.

37-rod bundle simulations:

- Local maxima of the axial velocity fluctuations were found in regions flanking the gap centers. The highest levels of axial velocity fluctuations were found in the space between rods in the first and second rings. The axial velocity fluctuations were substantially larger than those observed in the core region of fully developed pipe flows.
- Both the axial and the azimuthal coherent components were dominant in the gap regions, with maximum values of 70% and 55%, respectively, and weak in the open subchannel regions. The radial coherent component was relatively weak throughout the rod bundle, although it reached values near 40% in some gap regions. The contribution of coherent fluctuations to the total turbulent kinetic energy reached local maxima of between 50 and 55%, slightly off gap centers.
- In the simulations, local maxima of the shear stress occurred at locations facing the open subchannels, whereas the gap regions were characterized by local shear stress minima.
- The near periodicity of the coherent structure formation, and resulting cross-gap flow pulsations, is also illustrated by the strong oscillatory character of the autocorrelation coefficients of the azimuthal velocity fluctuations at all gap centres. In all cases, the streamwise wavelength of oscillations was about $4D$.

- Cross-correlations between azimuthal velocity fluctuations in different gaps had positive and negative peaks with relatively high amplitudes. This indicates that coherent structures were not scattered randomly throughout the rod bundle, but were connected to each other forming a network of vortices, each of which passed near multiple rods.
- A novel modified Q criterion was successful in identifying coherent structures in the form of pairs of vortices forming on either side of gaps between adjacent rods or outer rods and the tube wall.

10.2. Recommendations for future work

Based on the previous conclusions, the following recommendations for future work can be suggested.

- Most accident scenarios for nuclear power plants involve two-phase flows. In forced convective boiling flow, it is likely that the maximum heat flux on the fuel element would be limited by dryout or CHF, which is defined as the breakdown of the water film on the surface of a heated fuel element. Once the CHF is exceeded, failure of the heated surface may occur due to formation of a stable vapor layer on the surface of fuel element causing sharp increase in sheath temperature. To understand boiling phenomena and the effect of gap conditions on CHF and dryout, numerical simulations need to be conducted with various gap sizes at atmospheric pressure for the simulation of loss of coolant accidents (LOCA) as well as at the higher, operating pressure. It is noted that most available correlations are empirical, and thus sensitive to the experimental conditions. The accurate prediction of temperature fields and CHF characteristics under normal and LOCA conditions is crucial to the safe operation of nuclear reactors.

- Further assessment of the ability of various turbulence models and large-eddy simulations to simulate realistically rod-bundle flows should be targeted towards substantially reducing the computational time and memory required, so that this approach can become an effective tool for the nuclear industry.
- The present approach may be extended to assess the effects of grid spacers, end plates and upstream rod-bundle orientation, to produce more realistic simulations of actual rod bundles.

References

Abdelghany, M. and Eichhorn, R., 1986, "Measurements of wall shear stress in axial flow in a square lattice rectangular rod bundle," Trans. ASME, J. Fluids Engrg., **108**, 165-173.

Aly, A.M.M., Trupp, A.C. and Gerrard, A.D., 1978, "Measurements and prediction of fully developed turbulent flow in an equilateral triangular duct," J. Fluid Mech., **85**, 57-83.

Baglietto, E. and Ninokata, H., 2005, "A turbulence model study for simulating flow inside tight lattice rod bundles," Nucl. Eng. Des. **235**, 773-784.

Baratto, F., Bailey, S.C.C. and Tavoularis, S., 2006, "Measurements of frequencies and spatial correlations of coherent structures in rod bundle flows," Nucl. Engrg. Des., in press.

Barth, T. J. and Jespersen, D. C., 1989, "The design and application of upwind schemes on unstructured meshes," AIAA Paper 89-0366, *AIAA 27th Aerospace Sciences Meeting*, Reno, Nevada, USA.

Biemüller, M., Meyer, L. and Rehme, K., 1996, "Large eddy simulation and measurement of the structure of turbulence in two rectangular channels connected by a gap," Engineering Turbulence Modelling and Experiments, (eds. W. Rodi and G. Bergeles), **3**, 249-258.

Bonnet, J. and Delville, J., 2001, "Review of coherent structures in turbulent free shear flows and their possible influence on computational methods," Flow, Turbulence and Combustion, **66**, 333-353.

Bradshaw, P., 1997, "Understanding and prediction of turbulent flow-1996," Int. J. Heat Fluid Flow, **18**, 45-54.

Burmeister, L.C., 1983. "Convective Heat Transfer," John Wiley & Sons, Inc., New York, USA.

Carajilescov, P. and Todreas, N.E., 1976, "Experimental and analytical study of axial turbulent flows in an interior subchannel of a bare rod bundle," Trans. ASME, J. Heat Transfer, **98**, 262-268.

Carlucci, L.N., Hammouda, N. and Rowe, D.S. 2004, "Two-phase turbulent mixing and buoyancy drift in rod bundles," Nucl. Engrg. Des., **227**, 65-84.

Chang, D. and Tavoularis, S., 2004, "Identification of coherent Structures in axial flow in a rectangular channel containing a rod," *Proc. 12th Ann. Conf. CFD Society of Canada*, May 9-11, Ottawa, Ontario, Canada, 303-309.

Chang, D. and Tavoularis, S., 2005a, "Unsteady numerical simulations of turbulence and coherent structures in axial flow near a narrow gap", Trans. ASME, J. Fluids Eng., 127, 458-466.

Chang, D. and Tavoularis, S., 2005b, "Turbulent flow and heat transfer in axial flow near a gap with diminishing size", Int. J. Heat Mass Transfer, submitted.

Chang, D. and Tavoularis, S. 2005c, "Simulation of turbulent flow in a rod bundle", Nucl. Engrg. Des., submitted.

Chang, D. and Tavoularis, S., 2006, "Convective heat transfer in turbulent flow near a gap", Trans. ASME, J. Heat Transfer, in press.

Chen, C.J. and Jaw, S.Y. 1998, "Fundamentals of Turbulence Modeling," Taylor & Francis, Washington DC, USA.

Chen, H. C., and Patel, V. C., 1988, "Near-wall turbulence models for complex flows including separation," AIAA J. **26**(6), 641-648.

Chong, M.S., Perry, A.E. and Cantwell, B.J., 1990, "A general classification of three-dimensional flow field," Phys. Fluids A, **2**, 765-777.

Cucitore, R., Quadrio, M. and Baron A., 1999, "On the effectiveness and limitations of local criteria for the identification of a vortex," Eur. J. Mech. B, **18**, 261-282.

da Silva, C.B. and Métais, O., 2002, "On the influence of coherent structures upon interscale interactions in turbulent plane jets," J. Fluid Mech., **473**, 103-145.

Dawson, J., 2003, "MIT study sees nuclear power as green weapon against global warming," Physics Today, December, p. 34, http://www.physicstoday.org.

Dubief, Y. and Delcayre, F., 2000, "On coherent-vortex identification in turbulence," J. Turbulence **1**, 1-22.

Deutch, J. and Moniz, E., 2003, "MIT study on the future of nuclear power", Massachusetts Institute of Technology Report, ISBN 0-615-12420-8 http://www.mit.edu/afs/athena/org/n/nuclearpower.

Eifler, W. and Nijsing, R., 1967, "Experimental investigation of velocity distribution and flow resistance in a triangular array of parallel rods," Nucl. Engrg. Des., **5**, 22-42.

Fakory, M. and Todreas, N., 1979, "Experimental investigation of flow resistance and wall shear stress in the interior subchannel of a triangular array of parallel rods," Trans. ASME, J. Fluids Engrg., **101**, 429-435.

Gosset, A. and Tavoularis, S., 2006, "Laminar flow instability in a rectangular channel with a cylindrical core," Phys. Fluids, in press.

Gresho, P. M., Lee, R. L. and Sani, R. L., 1980, "On the time-dependent solution of the incompressible Navier-Stokes equations in two and three dimensions," Recent Advances in Numerical Methods in Fluids, (eds. C. Taylor and K. Morgan), Pineridge Press, Swansea, UK.

Groeneveld, D.C., 1973, "Forced convective heat transfer to superheated steam in rod bundles," AECL-4450, Atomic Energy of Canada Ltd., Chalk River, Ontario, Canada.

Guellouz, M.S., 1998, "Turbulent Flow and Heat transfer in Rod Bundles," Ph.D. Thesis, Department of Mechanical Engineering, University of Ottawa, Ottawa, Ontario, Canada.

Guellouz, M.S. and Tavoularis, S., 1992, "Heat transfer in rod bundle subchannels with varying rod-wall proximity," Nucl. Engrg. Des., **132**, 351-366.

Guellouz, M.S. and Tavoularis, S., 2000a, "The structure of turbulent flow in a rectangular channel containing a cylindrical rod – Part1: Reynolds-averaged measurements," Exp. Thermal Fluid Sci., **23**, 59-73.

Guellouz, M.S. and Tavoularis, S., 2000b, "The structure of turbulent flow in a rectangular channel containing a cylindrical rod – Part 2: Phase-averaged measurements," Exp. Thermal Fluid Sci., **23**, 75-91.

Hanjalić, K., 2002, "One-point closure models for buoyancy-driven turbulent flows," Annu. Rev. Fluid Mech., **34**, 321-347.

Hooper, J.D., 1980, "Developed single phase turbulent flow through a square-pitch rod cluster," Nucl. Engrg. Des., **60**, 365-379.

Hooper, J.D. and Rehme, K., 1984, "Large-scale structural effects in developed turbulent flow through closely-spaced rod arrays," J. Fluid Mech., **145**, 305-337.

Hooper, J.D. and Wood, D.H., 1984, "Fully developed rod bundle flow over a large range of Reynolds number," Nucl. Engrg. Des., **83**, 31-46.

Hunt, J.C.R., Wray, A.A. and Moin, P., 1988, "Eddies, streams, and convergence zones in turbulent flows," Center for Turbulence Research Report CTR-S88, Stanford University, 193-207.

Hussain, A.K.M.F., 1983, "Coherent structures – reality and myth," Phys. Fluids, **26**, 2816-2850.

Hussain, A.K.M.F., 1986, "Coherent structures and turbulence," J. Fluid Mech., **173**, 303-356.

Hwang, D.H., Yoo, Y.J., In, W.K., and Zee, S.Q., 2000, "Assessment of the interchannel mixing model with a subchannel analysis code for BWR and PWR conditions," Nucl. Engrg. Des., **199**, 257-272.

In, W.K., 2001, "Numerical study of coolant mixing caused by the flow deflectors in a nuclear fuel bundle," Nucl. Technol., **134**, 187-195.

Jeong, J. and Hussain, F., 1995, "On the identification of a vortex," J. Fluid Mech., **285,** 69–94.

Kaiser, H.G. and Zeggel, W., 1987, "Turbulent flows in complex rod bundle geometries numerically predicted by the use of FEM and a basic turbulence model," Nucl. Engrg. Des., **99**, 351-363.

Kim, S. and EL-Genk, M.S., 1989, "Heat transfer experiments for low flow of water in rod bundles," Int. J. Heat Mass Transfer, **32**, 1321-1336.

Kim, S. and Park, G., 1997, "Estimation of anisotropic factor and turbulent mixing rate in rod bundles based on the flow pulsation phenomenon," Nucl. Technol., **117**, 340-352.

Krauss, T. and Meyer, L., 1996, "Characteristics of turbulent velocity and temperature in a wall channel of a heated rod bundle," Exper. Therm. Fluid Sci., **12**, 75-86.

Krauss, T. and Meyer, L., 1998, "Experimental investigation of turbulent transport of momentum and energy in a heated rod bundle," Nucl. Engrg. Des., **180**, 185-206.

Lahey, R.T. and Moody, F.J., 1984, "The thermal-hydraulics of a boiling water nuclear reactor," American Nuclear Society, USA.

Laufer, J. 1956, "The structure of turbulence in fully developed pipe flow," NACA Report 1174.

Launder, B.E. 1975, "Prediction methods for turbulent flows," Lecture Series 76, von Kármán Institute for Fluid Dynamics, Rhode-St-Gense, Belgium.

Launder, B.E., 1989, "Second-moment closure and its use in modeling turbulent industrial flows," Int. J. Numer. Methods Fluids, **9**, 963-985.

Launder, B. E. and Shima, N., 1989, "Second-moment closure for the near-wall sublayer: Development and application," AIAA J., **27**(10), 1319-1325.

Launder, B.E. and Spalding, D.B., 1974, "The numerical computation of turbulent flow," Comp. Meth. in Appl. Mech. and Engng., **3**, 269-289.

Lee, K.B. and Jang, H.G., 1997, "A numerical prediction on the turbulent flow in closely spaced bare rod arrays by a nonlinear $k-\varepsilon$ model," Nucl. Engrg. Des., **172**, 351-357.

Libby, P.A., 1996, "Introduction to Turbulence," Taylor & Francis, Washington, DC, USA.

Lien, F.S. and Leschziner, M.A., 1994, "Assessment of turbulent transport models including non-linear RNG eddy-viscosity formulation and second-moment closure," Comput. Fluids, **23** (8), 983-1004.

Lomax H. and U.B. Mehta, 1984, "Some physical and numerical aspects of computing the effects of viscosity on fluid flow," Computational Methods in Viscous Flows (ed. Habashi, W.G.), **3**, pp. 1-50, Pineridge Press Ltd, Swansea, U.K.

Marek, J., Mauback, K. and Rehme, K., 1973, "Heat transfer and pressure drop performance of rod bundles arranged in square arrays," Int. J. Heat Mass Transfer, **16,** 2215-2228.

Meyder, R., 1975, "Turbulent velocity and temperature distribution in the central subchannel of rod bundles," Nucl. Engrg. Des., **35,** 181-189.

Meyer, L, 1994, "Measurements of turbulent velocity and temperature in axial flow through a heated rod bundle," Nucl. Engrg. Des., **146,** 71-82.

Meyer, L. and Rehme, K., 1994, "Large-scale turbulence phenomena in compound rectangular channels," Exp. Thermal Fluid Sci., **8,** 286-304.

Mogens, V.M., Hussain, H.S. and Hussain, F., 1991, "The complementary roles of experiments and simulation in coherent structure studies," New Perspectives in Turbulence (ed. Sirovich, L.), Springer-Verlag, New York, USA.

Mohanty, A.K. and Sahoo, K.M., 1988, "Turbulent flow and heat transfer in rod-bundle subchannel," Nucl. Engrg. Des., **106**, 327-344.

Möller, S. V., 1991, "On phenomena of turbulent flow through rod bundles," Exp. Thermal Fluid Sci., **4**, 25-35.

Möller, S. V., 1992, "Single-phase turbulent mixing in rod bundles," Exp. Therm. Fluid Sci., **5**, 26-33.

Monir, C. and Tavoularis, S., 1991, "Computations of subchannel flows in a 37-rod bundle," Technical Report UOME-BF-91-09, University of Ottawa, Canada.

Murthy, J.Y. and Mathur, S. 1997, "Periodic flow and heat transfer using unstructured meshes," Int. J. Numer. Meth. Fluids, **25**, 659-677.

Orszag, S., Meyer, L. and Rehme, K., 1996, "Introduction to renormalization group modeling of turbulence," Simulation and Modeling of Turbulent Flow (eds. Gatski, T., Hussaini, M. and Lumley, J..), pp. 155-182, Oxford University Press, Inc., New York, USA.

Ouma, B.H. and Tavoularis, S., 1991a, "Turbulence structure in triangular subchannels of a reactor bundle model," Nucl. Engrg. Des., **128**, 271-287.

Ouma, B.H. and Tavoularis, S., 1991b, "Flow measurements in rod bundle subchannels with varying rod-wall proximity," Nucl. Engrg. Des., **131**, 193-208.

Page, R.D., 1972, "Canadian power reactor fuel," Lecture 5, *Nuclear power symposium*, Atomic Energy of Canada Ltd, Sheridan Park, Ontario, Canada.

Pasinato, H.D., Squires, K.D. and Roy, R.P., 2004, "Assessment of Reynolds-averaged turbulence models for prediction of the flow and heat transfer in an inlet vane-endwall passage," Trans. ASME, J. Fluids Engrg., **126**, 305-315.

Prada, J.W.V. and Bannwart, A.C., 2000, "Modeling of vertical core annular flows and application to heavy oil production," *Proceedings of ETCE/OMAE 2000*, Energy for the New Millenium, New Orleans, LA, USA.

Rapley, C.W. and Gosman, A.D., 1986, "The prediction of fully developed axial turbulent flow in rod bundles," Nucl. Engrg. Des., **97**, 313-325.

Rehme, K., 1978, "The structure of turbulent flow through a wall subchannel of a rod bundle," Nucl. Engrg. Des., **45**, 311-323.

Rehme, K., 1980, "Turbulent momentum transport in rod bundles," Nucl. Engrg. Des., **62**, 137-146.

Rehme, K., 1987a, "On the development of turbulent flow in wall subchannels of a rod bundle," Nucl. Technol., **77**, 331-342.

Rehme, K., 1987b, "The structure of turbulent flow through rod bundles," Nucl. Engrg. Des., **99**, 141-154.

Rehme, K., 1987c, "The structure of turbulence in wall subchannels of a rod bundle," Atomkernenergie Kerntechnik, **49**, 145-150.

Rehme, K., 1992, "The structure of turbulence in rod bundles and the implications on natural mixing between the subchannels," Int. J. Heat Mass Transfer, **35**, 567-581.

Rhie, C. M. and Chow, W. L., 1983, "Numerical study of the turbulent flow past an airfoil with trailing edge separation," AIAA J., **21**, 1523-1532.

Robertson, J.A.L., 1990, "Nuclear power in Canada: The CANDU System," AECL-6328, Atomic Energy of Canada Limited, Chalk River, Ontario, Canada.

Robinson, S.K., 1991, "Coherent motions in the turbulent boundary layer," Annu. Rev. Fluid Mech., **23**, 601-639.

Rogers, J.T. and Tahir, A.E.E., 1975, "Turbulent interchange mixing in rod bundles and the role of secondary flows," ASME paper 75-HT-31.

Rokni, M. and Sundén, B., 2003, "Calculation of turbulent fluid flow and heat transfer in ducts by a full Reynolds stress model," Int. J. Numer. Meth. Fluids, **42**, 147-162.

Rowe, D.S., Johnson, B.M. and Knudsen, J.G., 1974, "Implications concerning rod bundle crossflow mixing based on measurements of turbulent flow structure," Int. J. Heat Mass Transfer, **17**, 407-419.

Sadatomi, M., Kawahara, A. and Sato, Y., 1996, "Prediction of the single-phase turbulent mixing rate between two parallel subchannels using a subchannel geometry factor," Nucl. Engrg. Des., **162**, 245-256.

Schröder, K. and Gelbe, H., 1999, "Two- and Three-Dimensional CFD-Simulation of Flow-Induced Vibration Excitation in Tube Bundles," Chemical Eng. Proc., **38**, 621-629.

Seale, W. J., 1979a, "Turbulent diffusion of heat between connected flow passages, Part1 : outline of problem and experimental Investigation," Nucl. Engrg. Des., **54**, 183-195.

Seale, W.J., 1979b, "Turbulent diffusion of heat between connected flow passages," Nucl. Engrg. Des., **54**, 197-209.

Seale, W.J., 1981, "The effect of subchannel shape on heat transfer in rod bundles with axial flow," Int. J. Heat Mass Transfer, **24**, 768-770.

Seale, W.J., 1982, "Measurements and predictions of fully developed turbulent flow in a simulated rod bundle," J. Fluid Mech., **123**, 399-423.

Slagter, W., 1988, "Finite element, stream function-vorticity solution of secondary flow in the channels of a rod bundle," Int J. Numer Methods Fluids, **8**, 687-704.

Spalart, P.R., 2000, "Strategies for Turbulence Modeling and Simulation", Int. J. Heat Fluid Flow, **21**, 252-263.

Speziale, C.G., 1987, "On nonlinear *k-l* and *k-ε* models of turbulence," J. Fluids Mech., **178**, 459-475.

Speziale, C., 1998, "Turbulence modeling for time-dependent RANS and VLES:A review," AIAA J., **36**, 173-184.

Su, J. and Freire, A.P.S., 2002, "Analytical prediction of friction factors and Nusselt numbers of turbulent forced convection in rod bundles with smooth and rough surfaces," Nucl. Engrg. Des., **217**, 111-127.

Sutherland, W.A. and Kays, W.M., 1966, "Heat transfer in parallel rod arrays," Trans ASME, J. Heat Transfer, 117-124.

Tahir, A. and Rogers, J.T. 1979, "The mechanism of secondary flows in turbulent interchange in rod bundles," *7th Canadian Congress of Applied Mechanics*, Sherbrooke, Canada.

Tahir, A.E.E. and Rogers, J.T., 1986, "Turbulent flow structure in a closely-spaced triangular-array rod bundle," *Proc. 8th Intern. Heat Transfer Conference*, San Francisco, USA.

Tavoularis, S., Sitaraman, S. and Prinos, P., 1988, "Measurement of turbulent flow in rod bundle subchannels," Int. J. Eng. Fluid Mech., **1**, .471-494.

Tavoularis, S., Madrane, A. and Vaillancourt, R., 2002, "Numerical simulation of coherent structures in axial flow through a rectangular channel containing a cylindrical rod," *Proc. 10th Ann. Conf. CFD Society of Canada*, June 9-11, Windsor, Ontario, Canada.

Teyssedou, A., Tapucu, A. and Camarero, R., 1992, "Blocked flow subchannel simulation comparison with single-phase flow data," Trans. ASME, J. Fluids Engrg., **114**, 205-213.

Trupp, A.C. and Aly, A.M.M., 1979, "Predicted secondary flow in triangular array rod bundles," Trans. ASME, J. Fluids Engrg, **101**, 354-363.

Trupp, A.C. and Azad, R.S., 1975, "The structure of turbulent flow in triangular array rod bundles," Nucl. Engrg. Des., **32**, 47-84.

Tzanos, C., 2001, "Performance of $k-\varepsilon$ turbulence models in the simulation of LWR fuel-bundle flows," Trans. ANS, **84**, 197-199.

Van Doormal, J. P. and Raithby, G. D., 1984, "Enhancements of the SIMPLE method for predicting incompressible fluid flows," Numer. Heat Transfer, **7**, 147-163.

Vonka, V., 1988a, "Measurement of secondary flow vortices in a rod bundle," Nucl. Engrg. Des., **106**, 191-207.

Vonka, V., 1988b, "Measurement of secondary flow vortices in a rod bundle," Nucl. Engrg. Des., **106**, 209-220.

Wegner, B., Maltsev, A., Schneider, C., Sadiki, A., Dreizler, A., Janicka, J., 2004, "Assessment of unsteady RANS in predicting swirling flow instability based on LES and experiments," Int. J. Heat Fluid Flow, **25** 528-536.

Wilcox, D. C., 2000, "Turbulence Modelling for CFD," DCW Industries, Inc., La Canada, California, USA.

Wu, X., 1994, "Numerical study on the turbulence structures in closely spaced rod bundle subchannels," Numer. Heat Transfer, Part A, **25**, 649-670.

Wu, X., 1995, "On the transport mechanisms in simulated heterogeneous rod bundle subchannels," Nucl. Engrg. Des., **158**, 125-134.

Wu, X. and Trupp, A.C., 1993, "Experimental study on the unusual turbulence intensity distributions in rod-to-wall gap regions," Exp. Thermal Fluid Sci., **6**, 360-370.

Wu, X. and Trupp, A.C., 1994, "Spectral measurements and mixing correlation in simulated rod bundle subchannels, Int. J. Heat Mass Transfer, **37**, 1277-1281.

Yadigaroglu, G., Andreani, M., Dreier, J. and Coddington, P., 2003, "Trends and needs in experimentation and numerical simulation for LWR safety," Nucl. Engrg. Des., **221**, 205-223.

Yakhot, V., Orszag, S. A., 1986, "Renormalization Group Analysis of Turbulence: I. Basic Theory," J. Sci. Comp., **1**, 3-51.

Tables

Table 1 - 1 Typical dimensions and operating conditions of CANDU type reactors

		Pickering[1]	CANDU-6[2]	ACR-700[3]
Number of elements per bundle		28	37	43
Coolant		Heavy water	Heavy water	Light water
Moderator		Heavy water	Heavy water	Heavy water
Inner diameter of Calandria	(m)	N/A	7.6	5.2
Number of fuel channel in a Calandria		N/A	380	284
Elements				
Outside Diameter	(mm)	15.23	13.8	N/A
Min. Cladding Thickness	(mm)	0.38	0.38	N/A
Bundles				
Length	(mm)	495	495	495
Outer Diameter	(mm)	102.4	112	112
Spacing between Elements	(mm)	1.27	1.02	N/A
Number per Channel		12	12	12
Pressure Tube				
Inside diameter	(mm)	103.4	132	156
Operating Condition				
Nominal inlet pressure	(MPA)	9.8	10.5***	13
Pressure Drop/Channel*	(KN/m^2)	565	738	N/A
Operating Pressure (exit)	(MPA)	N/A	10***	13
Inlet Temperature	(°C)	249	266***	N/A
Outlet Temperature	(°C)	293	312***	327.7
Exit Steam Quality	(%)	N/A	0/3.5**	N/A
Max. Mass Flow / Channel	(kg/s)	23.8	23.8	N/A
Max. Sheath Temperature	(°C)	304	302	N/A
Max. Heat Rating $\int \lambda \, d\theta$	(kW/m)	4.2	3.7	4.1
Max. Linear Element Power	(kW/m)	52.8	46.5	51
Max. Linear Bundle Power	(kW/m)	1325	1472	N/A
Average Burnup ± 10	(%)	168	204	N/A
Maximum Surface Heat Flux	(W/m^2)	1150	1090	N/A

* measured with fresh bundles ** inner zone/outer zone 1, 2: (Page, 1971)

***, 3: http://canteach.candu.org

Table 2 - 1 Experimental studies of rod bundles (1)

authors	year	characteristics			comments
		$Re_b[10^{-4}]$	*P/D*	L/D_h	
Sutherland and Kays	1966	0.7~20	1.15 1.25	122.2	turbulent flow and heat transfer in triangular pitched array of rods with air flow (Pr=0.7)
Eifler and Nijsing	1967	1.5, 3, 5	1.05 1.1 1.15	139 90 65.5	turbulent flow through the triangular array of rods
Marek *et al.*	1973	1~30	1.283	80 for 9 rods 65 for 16 rods	turbulent flow and heat transfer in square array of rod bundles. (9 rods and 16 rods) heat flux 160 W/cm, wall temperature 700°C
Rowe *et al.*	1974	5~20	1.125~1.25	105	turbulent water flow in rod bundles Laser Doppler Anemometry
Trupp & Azad	1975	2.4~8.4 1.2~7.2 1.2~6.0	1.2 1.35 1.5	20 30 51.5	turbulent air flow in triangular array rod bundle hot wire anemometry, pitot tube
Carajilescov & Todreas	1976	2.7	1.123	77	turbulent air flow in triangular array rod bundle Laser Doppler Anemometry
Rehme	1978	8.7 based on the average velocity	1.07	143	turbulent air flow in a rectangular channel with 4 square array rods hot wire measurements
Fakory & Todreas	1979	0.4~3.6	1.1	182	turbulent air flow in a simulated triangular rod array Preston tube for wall shear stress
Seale	1979a	3.4~29.9 for 3 rods 4.5~18.9 for 4 rods 4.6~9.1 for 5 rods	1.833 1.357 1.1	216 469 996	turbulent heat transfer in simulated rod arrays in a wind tunnel for the case of three-rod, four-rod duct and five-rod duct *L*: heated length, Pitot-temperature probe heat input electric power to the heater plate (W/m^2) 106~1014 for the 3-rod duct, 709~1522.6 for the 4-rod duct and 746~1511 for the 5-rod duct
Hooper	1980	4.8~15.6	1.194 1.107	95 128	turbulent air flow through a square array rod bundle Pitot probes for the mean velocity, Preston tubes for wall shear stress, hot-wire for six Reynolds stresses

Table 2 - 2 Experimental studies of rod bundles (2)

authors	year	characteristics			comments
		Re_b [10^{-4}]	P/D	L/D_h	
Rehme	1980	8.73 12.3 19.4	1.071 1.148 1.401	133 97 60	turbulent air flow in a simulated rod bundle channel containing 4 rods Pitot tube for mean velocity, hot-wire for turbulence intensities and kinetic energy Preston tubes for the wall shear stresses
Seale	1981	90	1.1 1.375 1.83	N/A	turbulent air flow and heat transfer in a simulated interconnected subchannels Pitot tube, hot-wire anemometry
Seale	1982	8,28~34.67	1.2	120	turbulent air flow in a simulated interconnected subchannels Pitot tube, hot-wire anemometry
Hooper & Rehme	1984	7.6 for 4 rods 13.3 for 6 rods	1.036 for 4 rods 1.107 for 6 rods	128 for 6 rods	turbulent air flow through two different square array rod clusters, 4 rods in wall bounded array and 6 rods in square array rod cluster Pitot tube, hot-wire measurement
Hooper & Wood	1984	2.26~20.76	1.107	128	turbulent air flow in a square array rod bundle Pitot tube, hot-wire measurement
Tahir & Rogers	1986	3.6	1.06	160	turbulent air flow in a triangular array rod bundle, hot-wire measurement
Abdelghany & Eichhorn	1986	6.7~7.9	1.33	62	turbulent air flow in a square lattice rectangular rod bundle hot film probe measurement for wall shear stress
Rehme	1987 a	11.7	1.148	48.7 73 97.4	turbulent air flow in a simulated rod bundle channel containing 4 rods flow development, hot-wire measurement
Rehme	1987 b	7.89	1.148	97	turbulent air flow in a simulated rod bundle channel containing 4 rods cross-correlation, inter-subchannel turbulent mixing
Rehme	1987 c	16.7	1.3	68.6	turbulent air flow in a simulated rod bundle channel containing 4 rods hot-wire measurement

Table 2 - 3 Experimental studies of rod bundles (3)

authors	year	characteristics			comments
		Re_b [10^{-4}]	P/D	L/D_h	
Tavoulairs *et al.*	1988	5.0	1.14	138	turbulent water flow in a 60° sector of a 37-rod horizontal bundle, focusing on an inner square subchannel for the cases of single bundle and two bundles in tandem aligned and mis-aligned by 15 and 30° and the case of the effect of rod spacers pressure tube for mean axial velocity Preston tube for wall shear stress cross-film anemometer for turbulence quantities
Kim and El-Genk	1989	Forced 0.008~5 Natural 0.026~0.2	1.25 1.38 1.5	71.21 for L/D	heat transfer for fully developed forced and natural water flow through seven uniformly heated triangular rod bundle, Pr: 3~8.5 for forced flow, Ra: 8×10^6~2.5×10^8
Ouma and Tavoularis	1991	4.8	1.15	65	turbulent air flow in a five-rod outer sector of a CANDU (12.9:1 scaled) cases with the central rod displaced towards the external tube wall and/or towards a neighboring rod, cases with rod-wall and rod-rod contact hot wire measurement
Möller	1991 1992	8.5	1.036~ 1.148	148~ 165	turbulent air flow in a square duct containing 4 rods, Preston tube for wall shear stress Pitot tube for axial velocity const. Temp. Anemometer for Reynolds stress Hot wire and microphone for power spectra and correlation and fluctuating velocity
Guellouz & Tavoularis	1992	4.8	1.0~ 1.16 for W/D	65	turbulent air flow and heat transfer in a five-rod outer sector of a CANDU (12.9:1 scaled model) electric cartridge heater, with a length of 381 mm and a diameter of 9.5 mm, thermistor probe for flow temperature, Resistance thermometer for fluctuating temperature
Wu and Trupp	1993	2.1~5.3	1.02~ 1.22	154	turbulent air flow in a trapezoidal duct containing a rod, Hot-wire measurement
Meyer	1994	6.65	1.12	128	heat transfer with the wall heat flux 1.37 kW/m
Meyer & Rehme	1994	25	1.7~15	40	turbulent air flow in complex channel with longitudinal slots, X-wire probe for turbulence quantities and autocorrelation
Meyer & Rehme	1995	0.23-10 for water 4-20 for air	1.66~ 10*	47~ 142	turbulent flow through channels with longitudinal slots (air, water/glycol)

Table 2 - 4 Experimental studies of rod bundles (4)

authors	year	characteristics			comments
		Re_b [10^{-4}]	P/D	L/D_h	
Wu	1995	2.6	1.079 for *W/D*	77.6	turbulent air flow through a trapezoidal duct containing a rod asymmetrically Preston tube, Pitot tube, Hot wire measurement
Krauss & Meyer	1996	6.5	1.12	86 for un-heated 129 for heated (P/D= 1.12)	turbulent air flow with heat transfer in an hexagonal symmetric wall channel of a heated 37 triangular array rod bundle rod-wall heat flux 1.39 (kW m^{-2}) for P/D=1.12 hot wire anemometry for turbulence quantities Preston tube for wall shear stress
Krauss & Meyer	1998	6.5 3.9	1.12	86 for un-heated 129 for heated (P/D= 1.12)	turbulent air flow with heat transfer in an hexagonal symmetric wall channel of a heated 37 triangular array rod bundle heat flux 1.39 (kW m^{-2}) for P/D=1.12 heat flux 0.98 (kW m^{-2}) for P/D=1.06
Guellouz & Tavoularis	2000	10.8	1.05~ 1.25 for *W/D*	54	turbulent air flow in a rectangular channel containing a rod Preston tube for the mean wall sear stress around the rod, Hot-film probe for the mean and fluctuating wall shear stress on the channel base hot wire measurement for the turbulence quantities smoke injection for flow visualization phase average measurement using VITA (Variable interval time averaging) technique
Baratto, Bailey and Tavoularis	2006	4.8	1.15	65	turbulent air flow in a five-rod outer sector of a CANDU (12.9:1 scaled) cross-wire anemometry

Table 2 - 5 Computational studies of rod bundles (1)

authors	year	characteristics			comments
		Re_b [10^{-4}]	P/D	L/D_h	
Meyder	1975	27 for isothermal case 10 for heat transfer	1.57	N/A	turbulent flow with heat transfer in a hexagonal rod bundle VERA code for velocity distribution steady state problem zero-equation turbulence model employing an anisotropic eddy diffusivity curvilinear orthogonal mesh TERA code for heat transfer Pe=494, q_w=234 W cm^{-2}
Carajilescov and Todreas	1976	2.7	1.123	77	turbulent flow in triangular array rod bundle steady state problem solving the axial momentum, vorticity and stream function equations one equation turbulence model
Rehme	1978	8.7 based on the average velocity	1.07	143	turbulent air flow in a rectangular channel with 4 square array rods zero equation turbulence model
Trupp and Aly	1979	2.7~25	1.12~ 1.35	N/A	turbulent flow in triangular array rod bundle steady state problem solving the axial momentum, vorticity and stream function equations one equation turbulence model
Seale	1979b	3.4~29.9 for 3 rods 4.5~18.9 for 4 rods 4.6~9.1 for 5 rods	1.1 1.375 1.833	216 469 996	turbulent heat transfer in simulated rod arrays for the case of three-rod, four-rod duct and five-rod duct steady state problem solving the axial momentum, vorticity and stream function equations $k-\varepsilon$ turbulence model with an algebraic model for the normal Reynolds stress term in an axial vorticity equation
	1982	8.28~34.6	1.2	120	turbulent heat transfer in two interconnected subchannels of a rod bundle steady state problem solving the axial momentum, vorticity and stream function equations $k-\varepsilon$ turbulence model with an algebraic model for the normal Reynolds stress term in an axial vorticity equation

Table 2 - 6 Computational studies of rod bundles (2)

authors	year	characteristics			comments
		Re_b [10^{-4}]	P/D	L/D_h	
Rapley and Gosman	1986	N/A	1.06 1.123	N/A	turbulent flow in triangular array rod bundle steady state problem algebraic turbulence model compared to the experiment (Tahir and Rogers, 1979)
Kaiser and Zeggel	1987	12.3	1.148	97	isothermal turbulent flow in a wall bounded seven triangular array rod bundle steady state problem using Finite Element Method (FEM) algebraic turbulence model compared to the experiment (Rehme, 1980)
Slagter	1988	N/A	N/A	N/A	isothermal turbulent flow steady state problem algebraic stress turbulence model compared to the experiment (Vonka, 1988a)
Mohanty and Sahoo	1988	3~10.5	1.1~ 1.5	N/A	turbulent flow with heat transfer (Prandtl number 0.7) in 30° and 45° subchannels for triangular and square rods steady state problem for the comparison of two-dimensional diffusion eddy model and one equation (*k-l*) turbulence model
Monir and Tavoularis	1991	4.8~ 48	1.137 1.0	65	turbulent air flow in a five-rod outer sector of a CANDU VELASCO-TUBS code cylindrical coordinates zero-equation turbulence model
Teyssedou *et al.*	1992	N/A	N/A	N/A	vertical isothermal flow subchannel analysis drift-flux model for a gas mixing equation

Table 2 - 7 Computational studies of rod bundles (3)

authors	year	characteristics			comments
		Re_b [10^{-4}]	P/D	L/D_h	
Wu	1994	5.3 5.4 5.5	1.22	N/A	fully developed turbulent flow through a trapezoidal duct containing a rod coordinate transformation from an orthogonal cylindrical system to a nonorthogonal curvilinear system algebraic stress model
Biemüller *et al.*	1996	0.33~58	4 for D/g	42.1	turbulent flow in two rectangular vertical channels connected by a gap wall function, periodic boundary condition LES with Schumann subgrid scale model compared to the experimental result (Meyer and Rehme, 1994)
Kim and Park	1997	N/A	N/A	N/A	turbulent flow in rod bundle lumped parameter analysis relationship of the anisotropic turbulent diffusion factor and the turbulent mixing
Lee and Jang	1997	2.7	1.123	N/A	two dimensional turbulent flow compared to the experimental result (Carajilescov and Todreas, 1976) nonlinear $k-\varepsilon$ model
In	2001	6.5	N/A	40	turbulent flow for the effect of vane types $k-\varepsilon$ model with CFX4.2
Baglietto and Ninokata	2005	6.4 10.9	1.17	N/A	turbulent flow, infinite triangular array rod bundle quadratic $k-\varepsilon$ model and realizable Reynolds stress algebraic equation model compared to the experimental result (Trupp and Azad, 1976)

Table 4 - 1 Cases studied for the selection of grid and time step resolution

Case	Grid element size			Number of grid elements	Total number of elements	Time step size
	x/D	y/D	z/D			
1	0.05	0.015	0.02	404×160×160	10,217,362	$1.9\times10^{-3}\ t_c$
2	0.1	0.03	0.04	202×80×80	1,278,054	$1.9\times10^{-3}\ t_c$
3	0.2	0.06	0.08	101×40×40	281,588	$1.9\times10^{-3}\ t_c$
4	0.1	0.03	0.04	202×80×80	1,278,054	$1.9\times10^{-2}\ t_c$

Figures

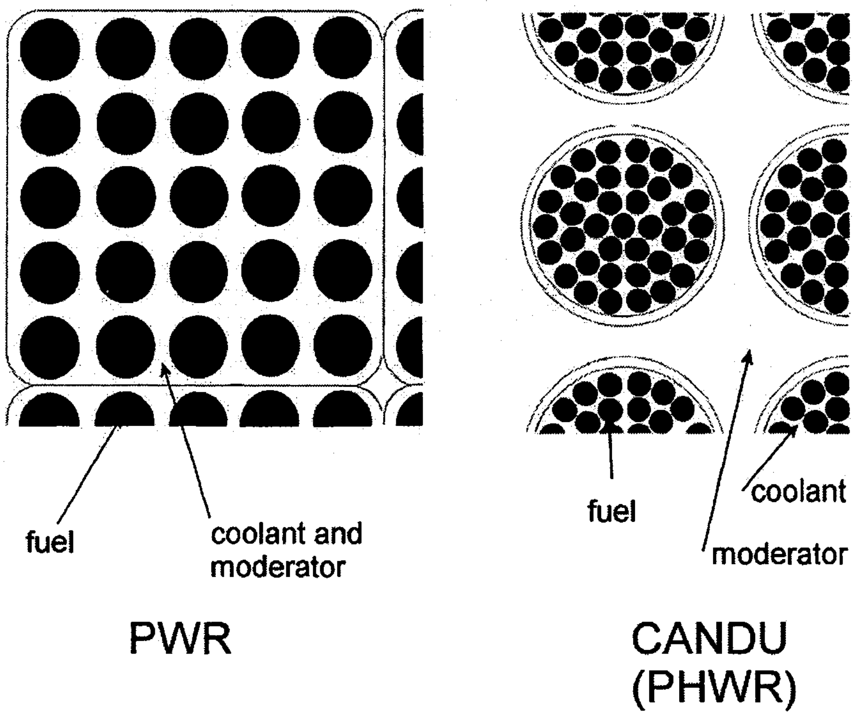

Figure 1 - 1 Typical rod bundle arrangement in nuclear reactor cores

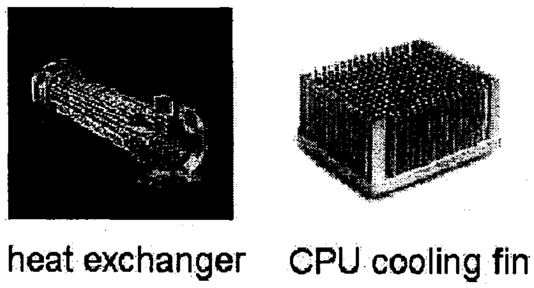

Figure 1 - 2 Examples of complex channels

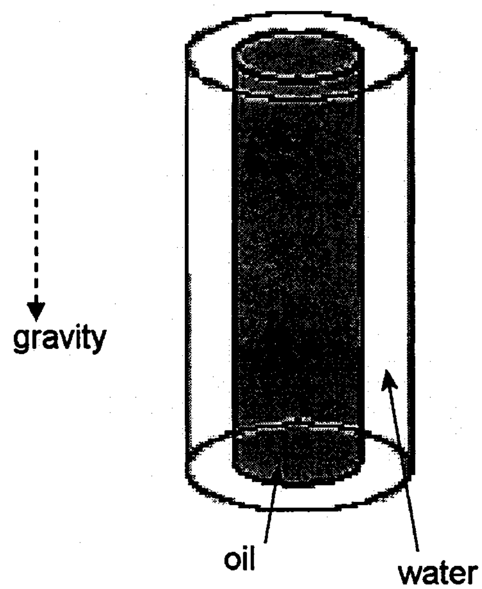

Figure 1 - 3 Sketch of an idealized concentric annular channel flow

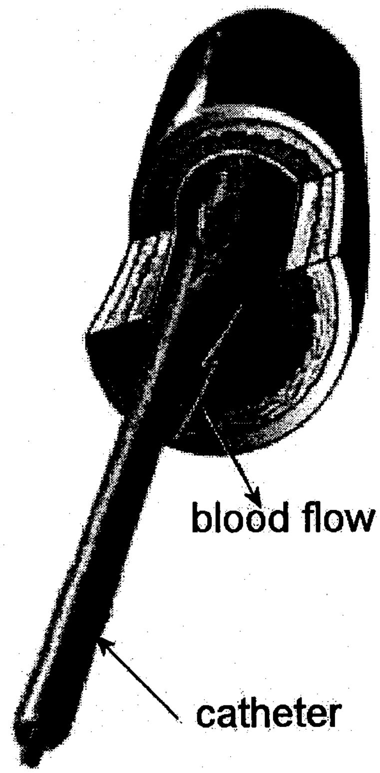

Figure 1 - 4 Catheter in blood flow through an artery

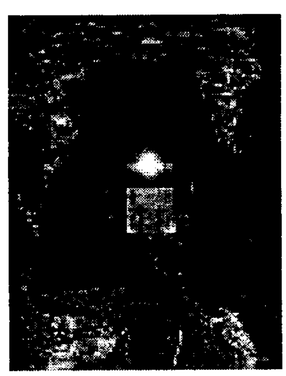

Figure 1 - 5 Train moving in a tunnel

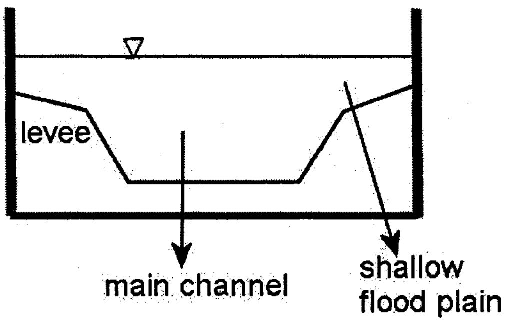

Figure 1 - 6 Sketch of a flooded river cross-section

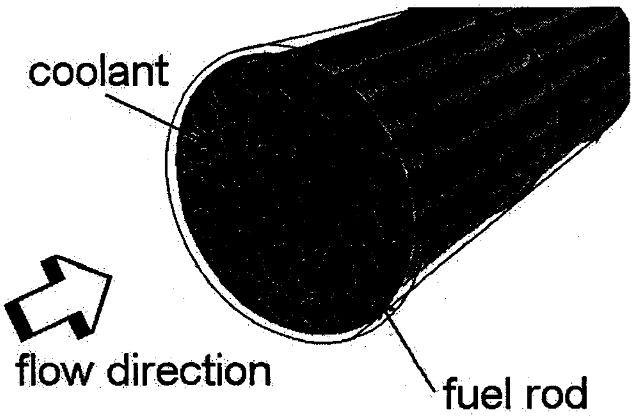

Figure 1 - 7 Flow in a typical CANDU rod channel

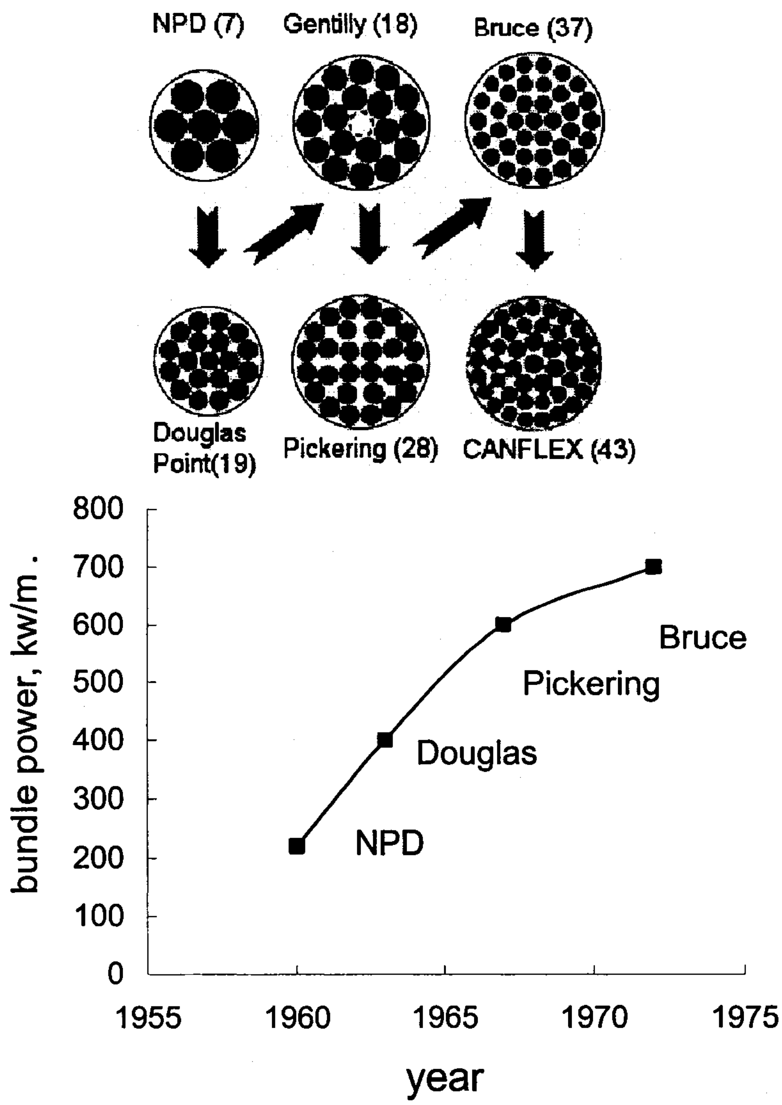

Figure 1 - 8 Fuel bundle types and generated power

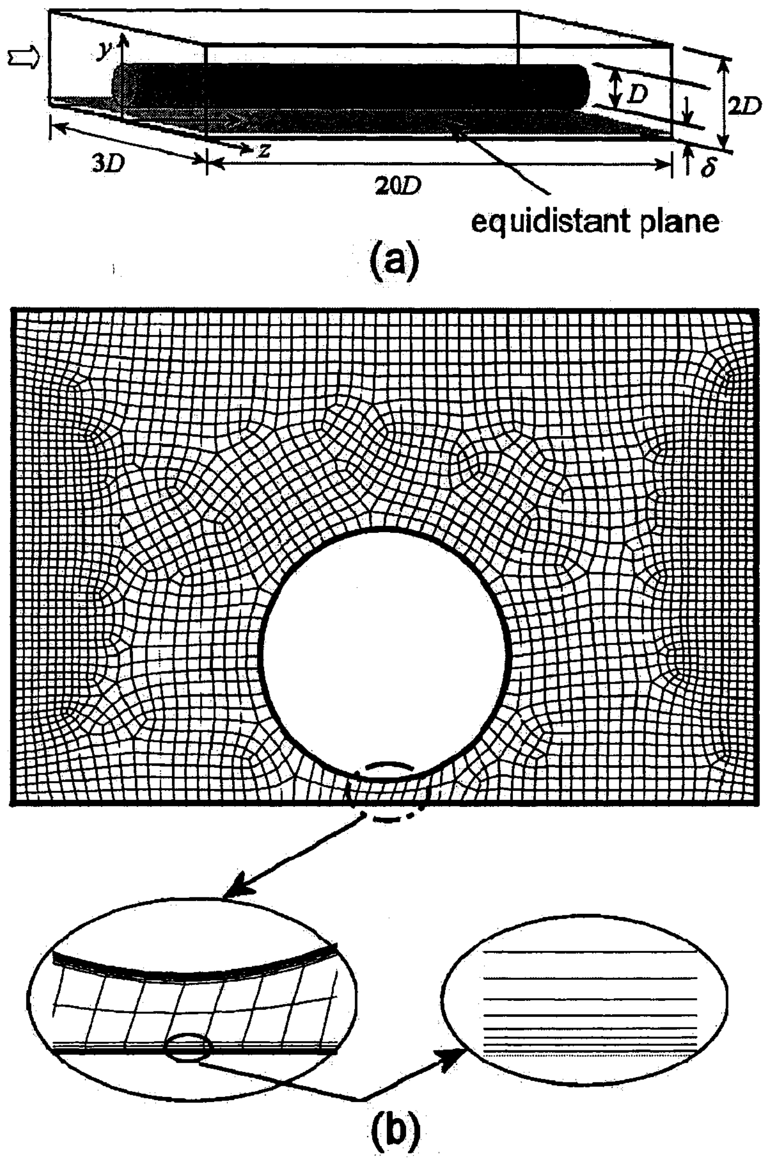

Figure 4 - 1 Sketches of the single rod duct showing a) the computational geometry and b) the computational mesh on the y-z plane, also showing details in the gap region and near the bottom wall

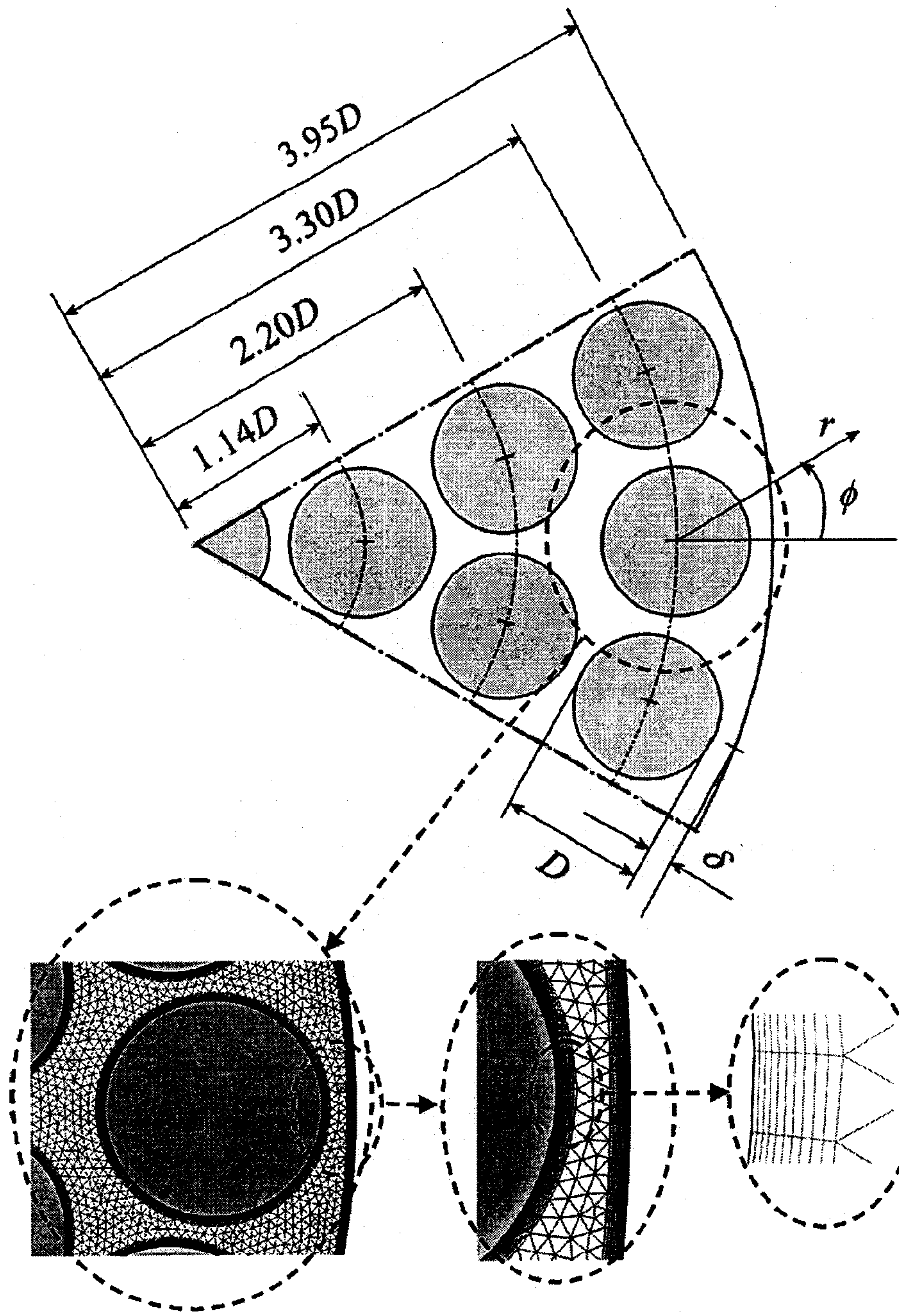

Figure 4 - 2 Cross-section of the computational geometry and mesh details of the 37-rod bundle.

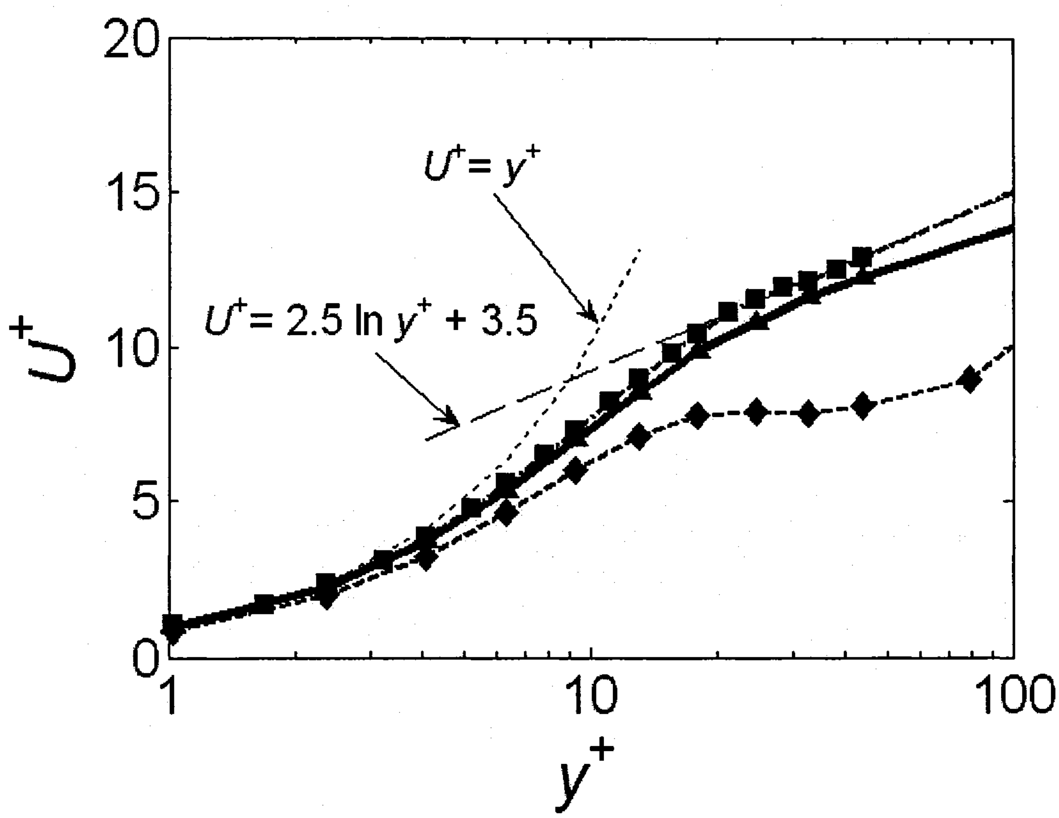

Figure 4 - 3 Variation of the time-averaged streamwise velocity at $z/D = 1$, $x/D = 10$ in the single-rod duct, near the bottom wall (■: case 1 ; ▬: case 2 ; ♦: case 3 ; ▲: case 4)

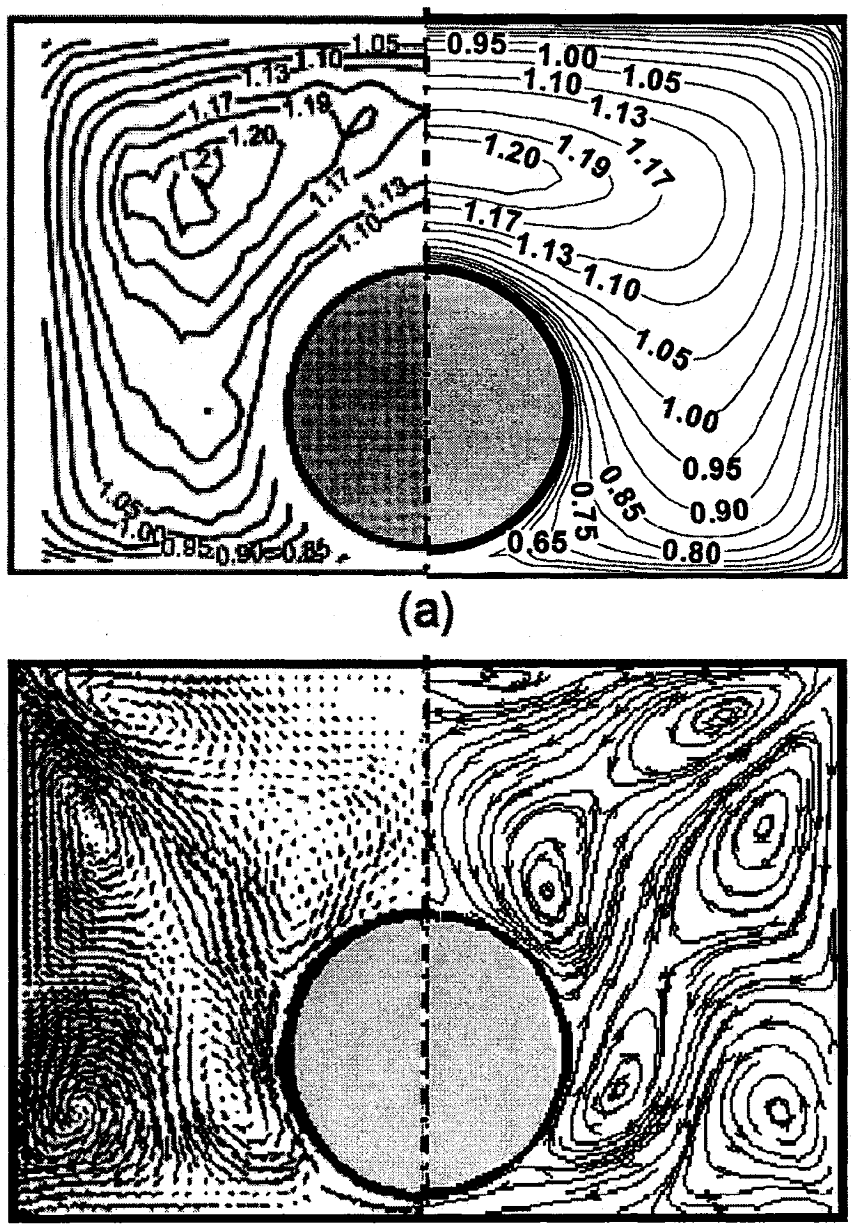

Figure 6 - 1 a) Isocontours of the time-averaged dimensionless axial velocity in the GT experiments (left) and the present simulations (right) b) vector plots of the time-averaged velocity component (left) and projected streamlines (right) on a cross-sectional plane in the present simulations

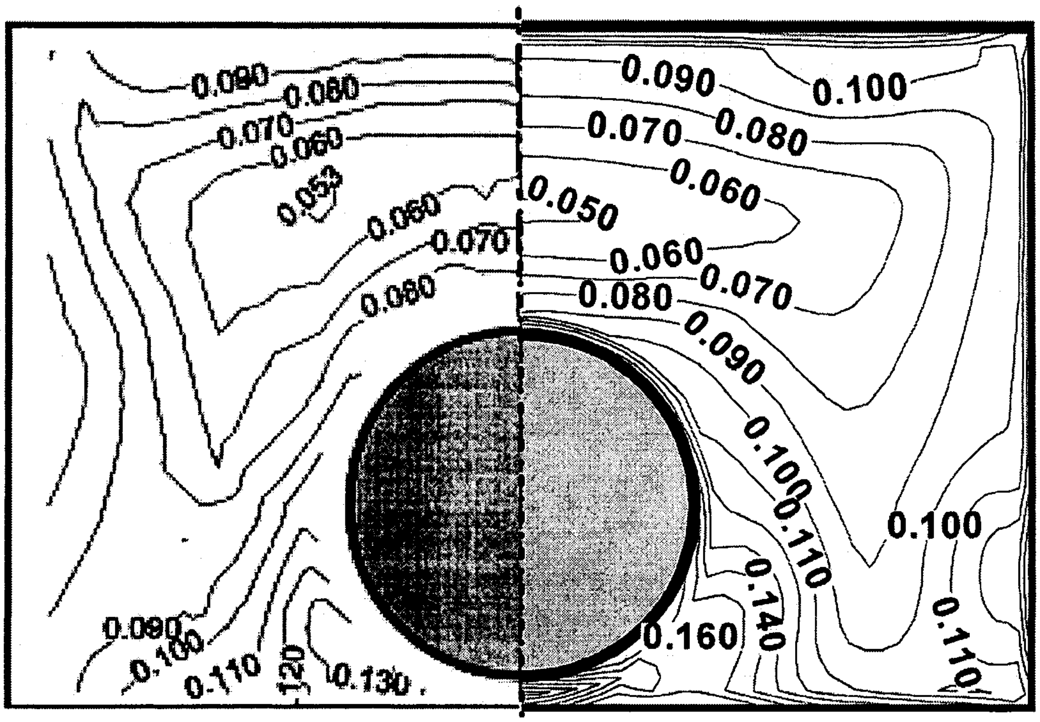

Figure 6 - 2 Isocontours of time-averaged, non-dimensionalized axial rms velocity fluctuation u'/U_b : GT measurements (left) and present simulations (right)

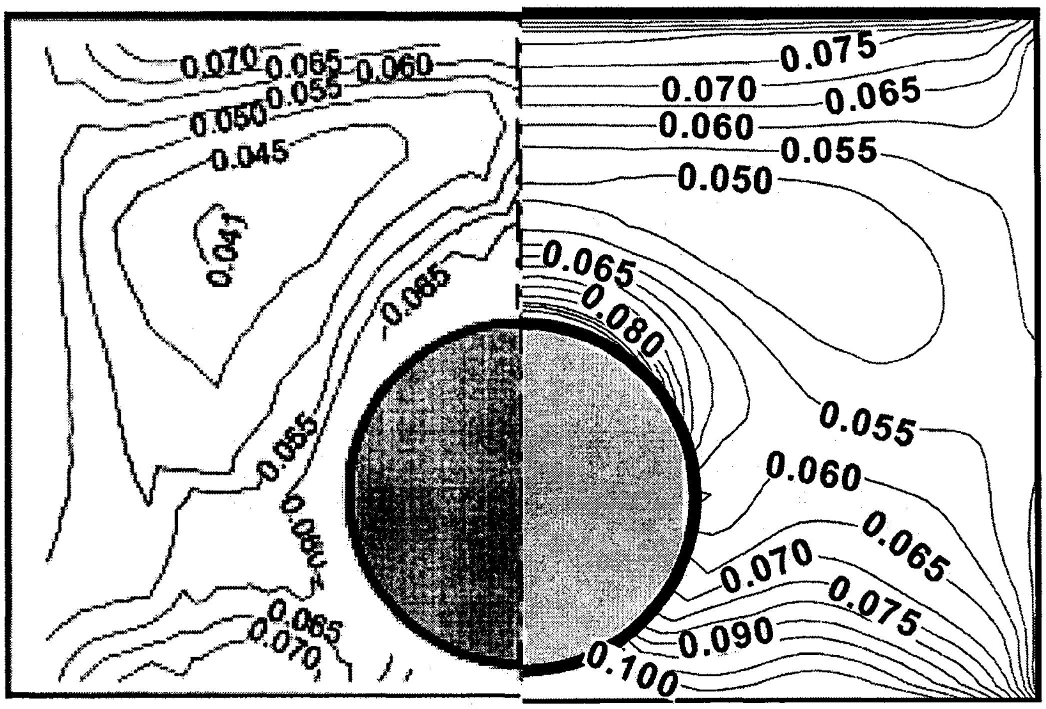

Figure 6 - 3 Isocontours of time-averaged, non-dimensionalized spanwise rms velocity fluctuation w'/U_b : GT measurements (left) and present simulations (right)

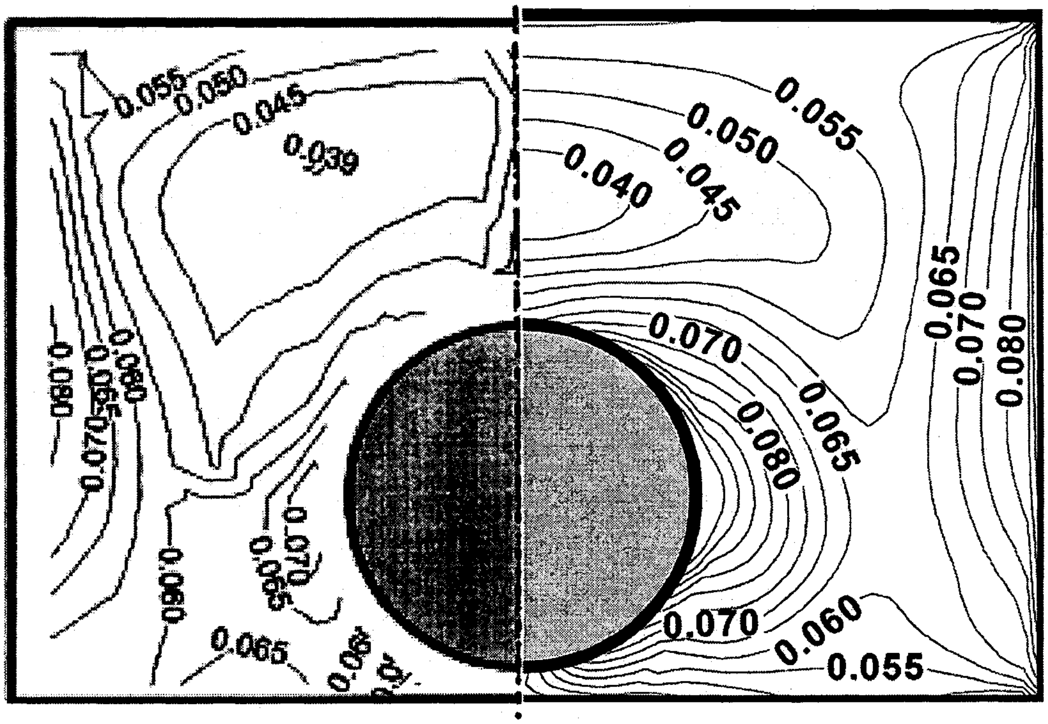

Figure 6 - 4 Isocontours of time-averaged, non-dimensionalized transverse rms velocity fluctuation v'/U_b : GT measurements (left) and present simulations (right)

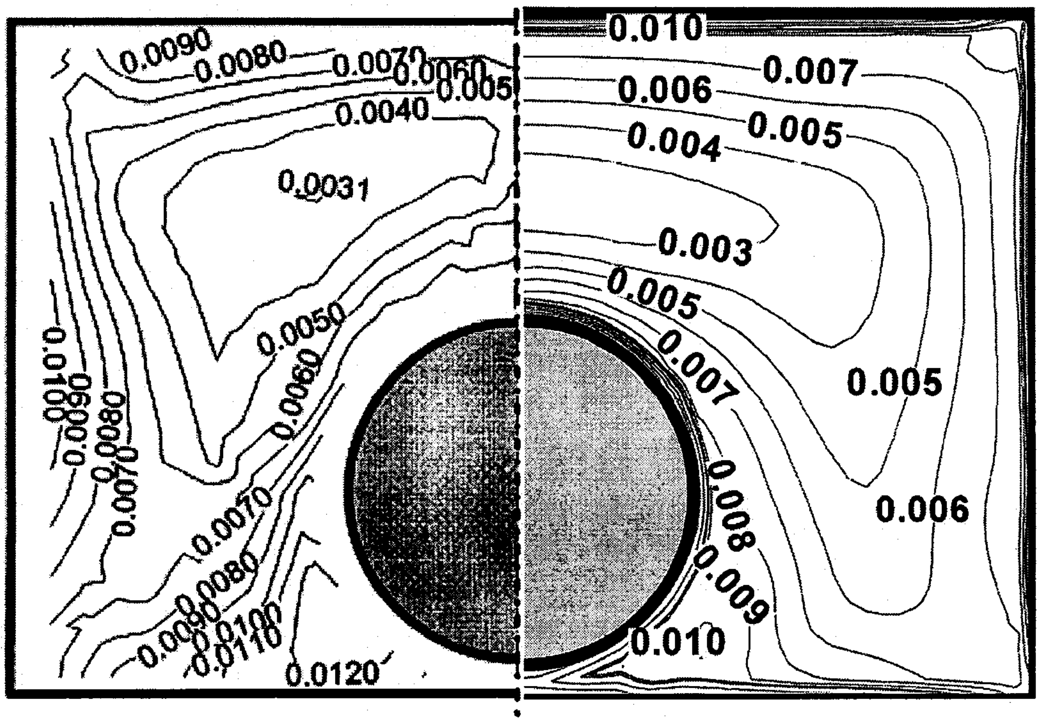

Figure 6 - 5 Isocontours of time-averaged, non-dimensionalized turbulent kinetic energy unit mass $\bar{k}/U_b^2$: GT measurements (left) and present simulations (right)

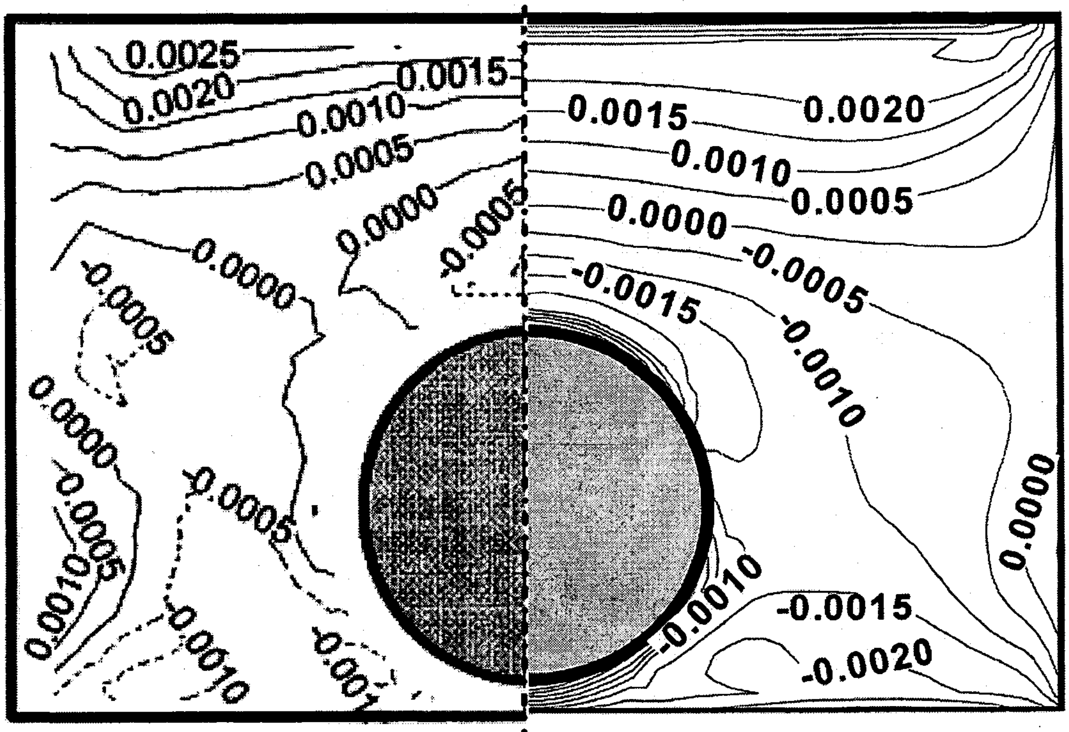

Figure 6 - 6 Isocontours of time-averaged, non-dimensionalized transverse turbulent shear stress $\overline{uv}/U_b^2$: GT measurements (left) and present simulations (right)

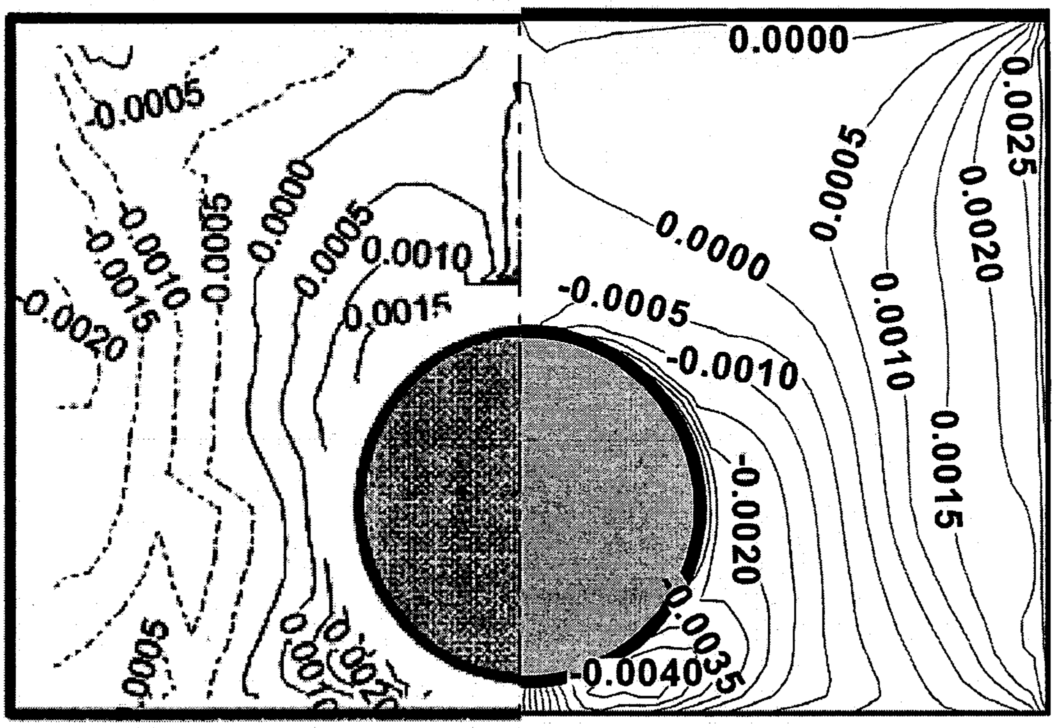

Figure 6 - 7 Isocontours of time-averaged, non-dimensionalized spanwise turbulent shear stress $\overline{uw}/U_b^2$:GT measurements (left) and present simulations (right)

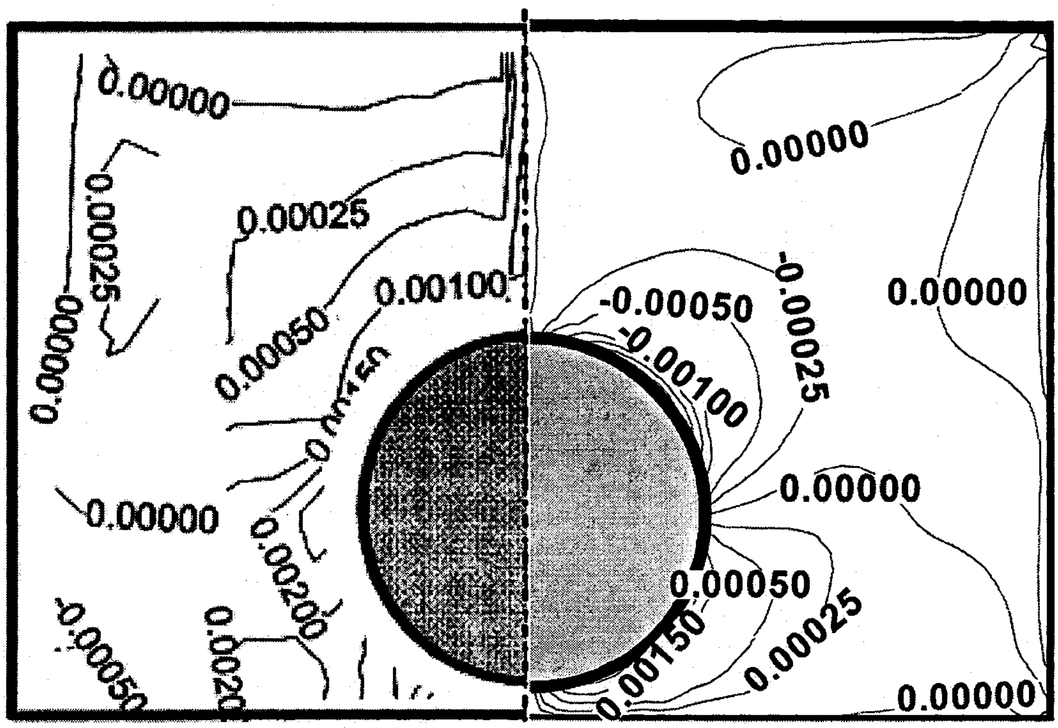

Figure 6 - 8 Isocontours of time-averaged, non-dimensionalized axial turbulent shear stress $\overline{vw}/U_b^2$: GT measurements (left) and present simulations (right)

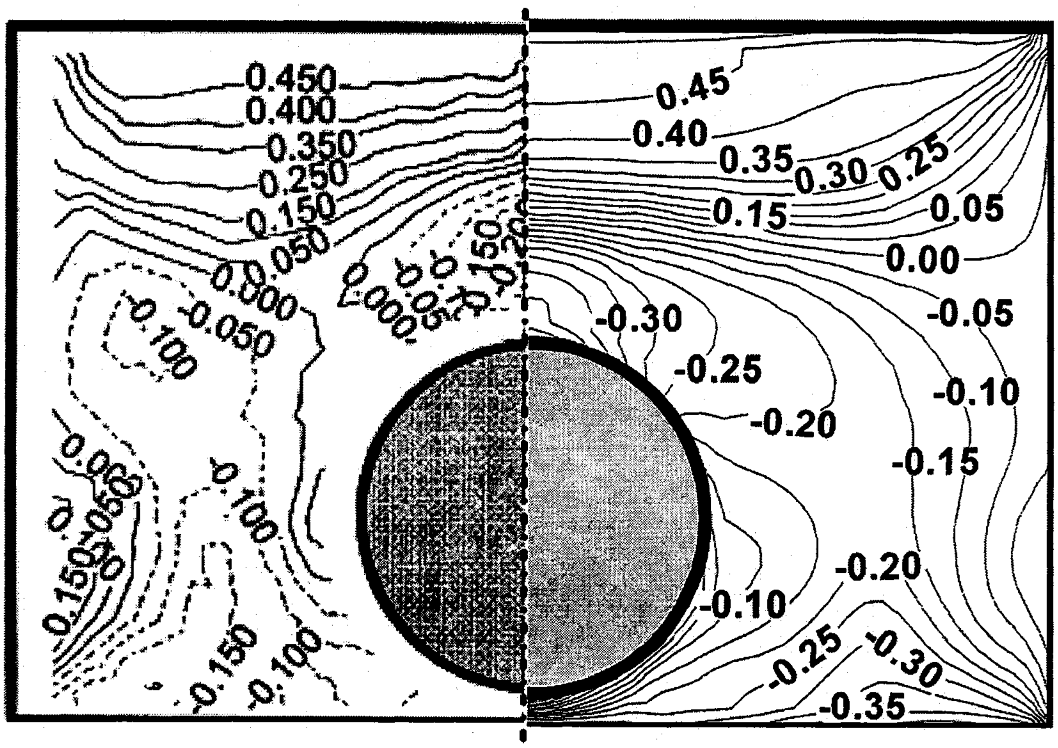

Figure 6 - 9 Isocontours of time-averaged, non-dimensionalized transverse turbulent shear stress coefficient $\overline{uv}/u'v'$: GT measurements (left) and present simulations (right)

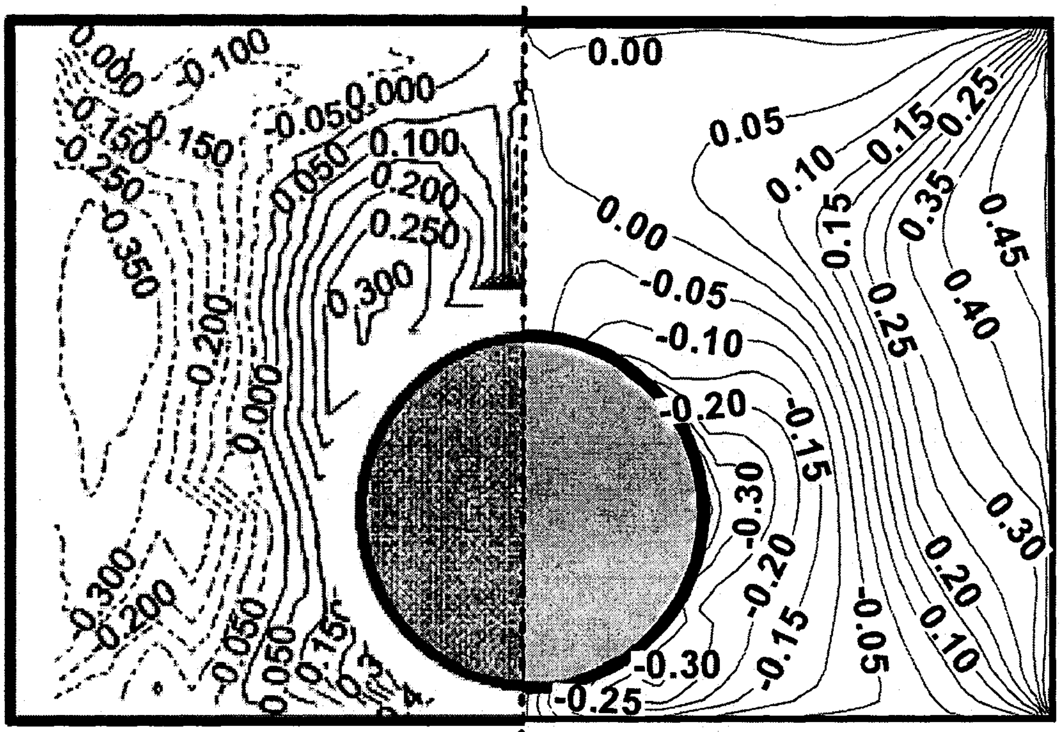

Figure 6 - 10 Isocontours of time-averaged, non-dimensionalized spanwise turbulent shear stress coefficient $\overline{uw}/u'w'$: GT measurements (left) and present simulations (right)

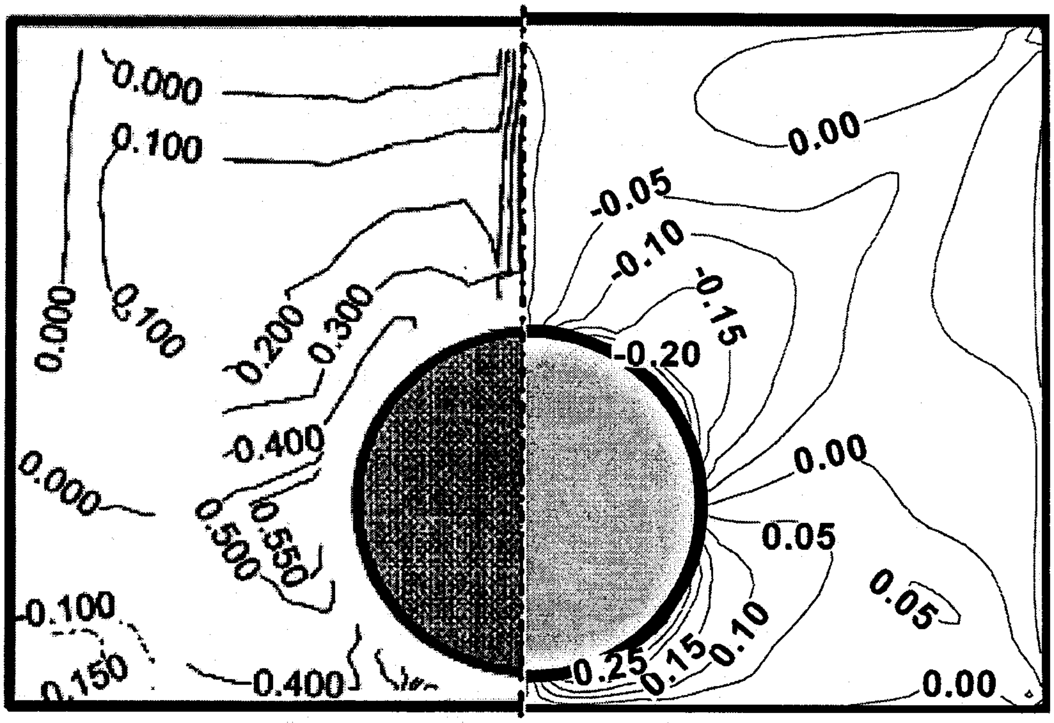

Figure 6 - 11 Isocontours of time-averaged, non-dimensionalized axial turbulent shear stress coefficient $\overline{vw}/v'w'$: GT measurements (left) and present simulations (right)

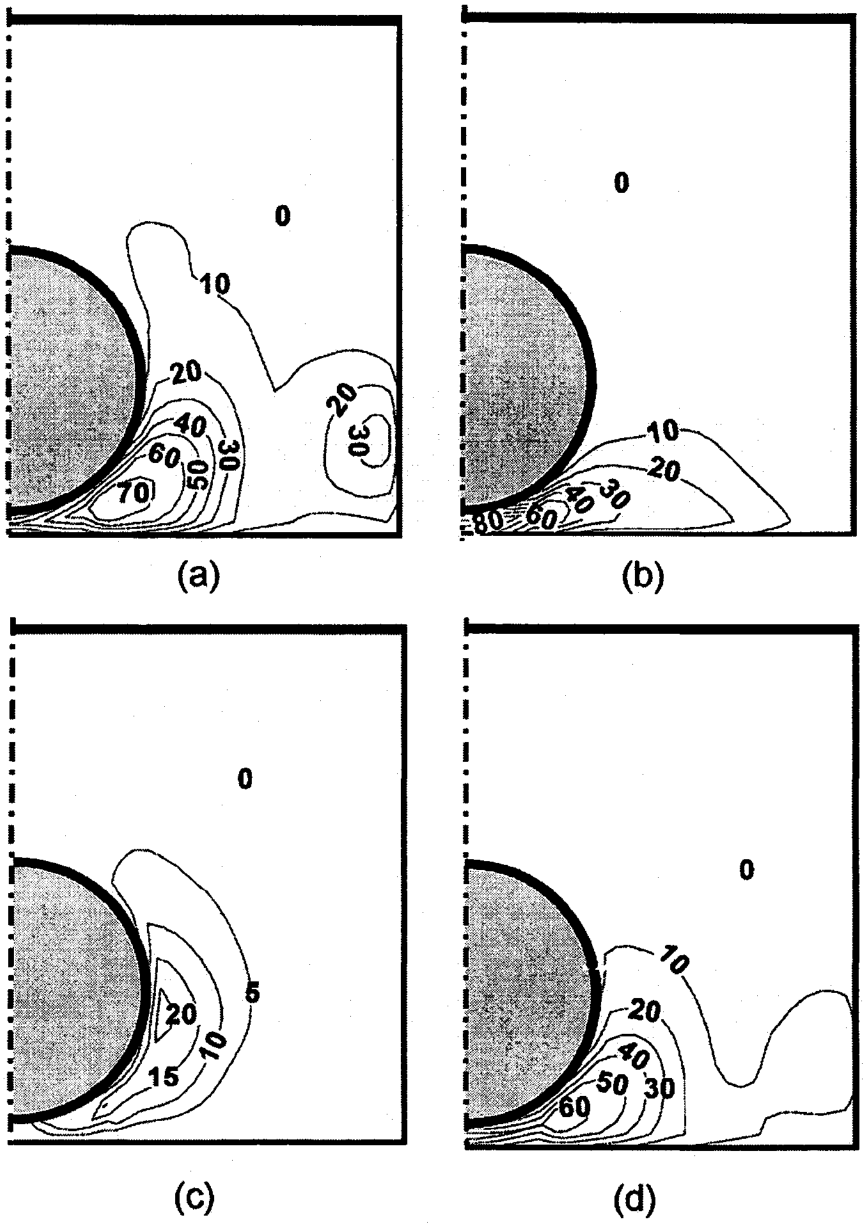

Figure 6 - 12 Predicted isocontours of the percent ratio of the coherent components to the totals : a) streamwise rms velocity ratio $\overline{u'_c}/\overline{u'}\times 100$; b) spanwise rms velocity ratio $\overline{w'_c}/\overline{w'}\times 100$; c) transverse rms velocity ratio $\overline{v'_c}/\overline{v'}\times 100$; and d) turbulent kinetic energy ratio $\bar{k}_c/\bar{k}\times 100$

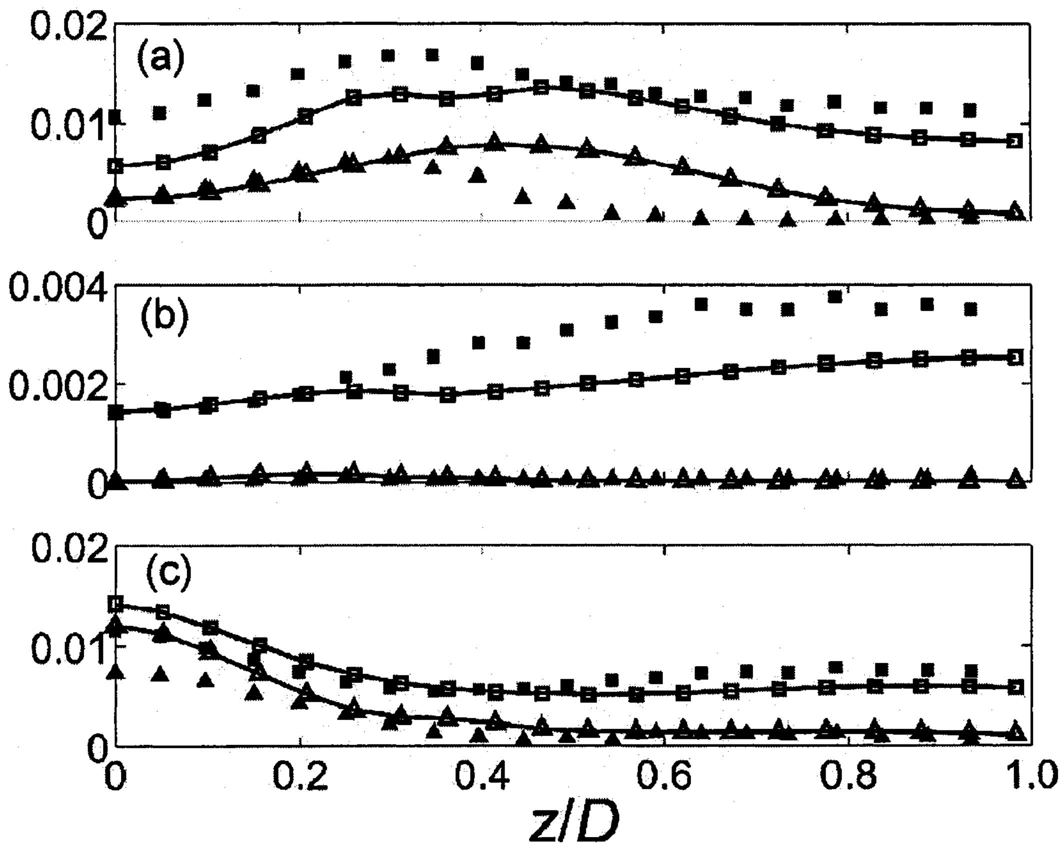

Figure 6 - 13 Comparison of present simulations (open symbols) with GT measurements (solid symbols) for total averages (□, ■) and coherent (Δ, ▲) parts on the equidistant plane : a) streamwise normal stress ; b) transverse normal stress ; c) spanwise normal stress ; the simulation results have been connected by solid lines as an aid to the eye

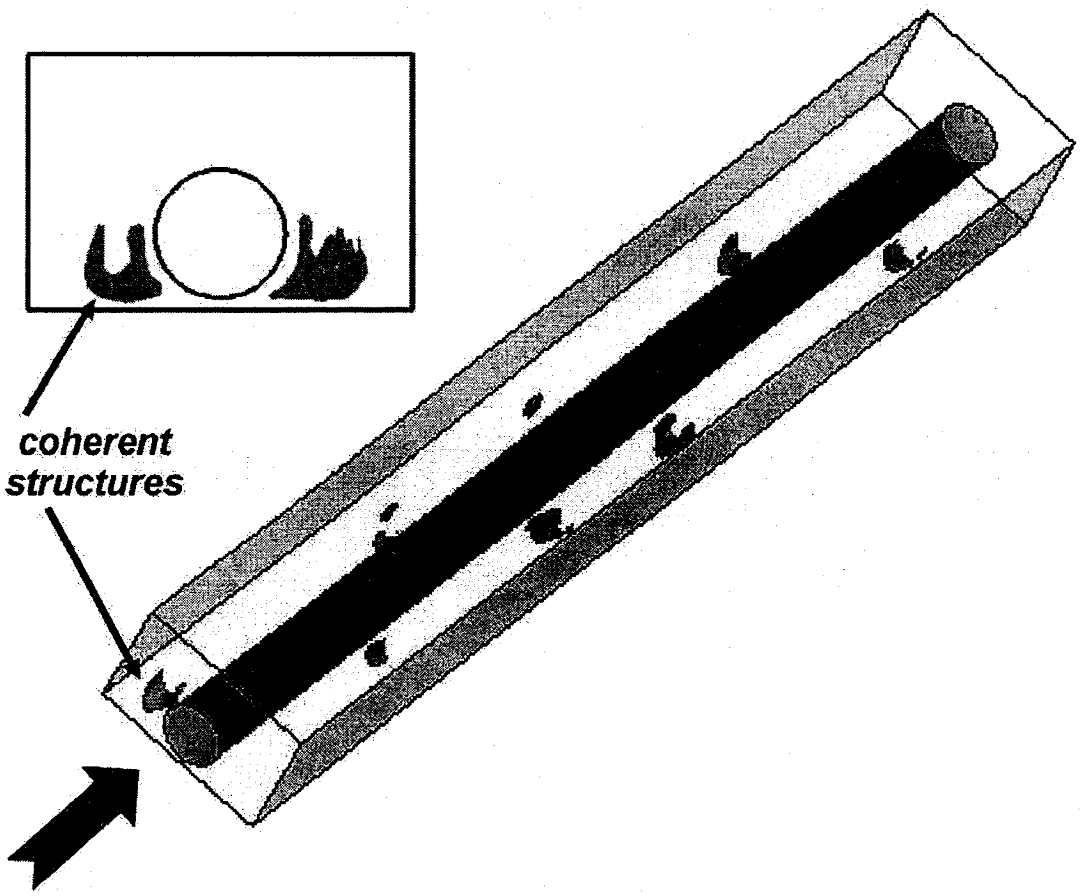

Figure 6 - 14 Coherent structures identified by the Q criterion ; the section shown is $20D$ long ; front view also shown for relative locations of coherent structures from the rod

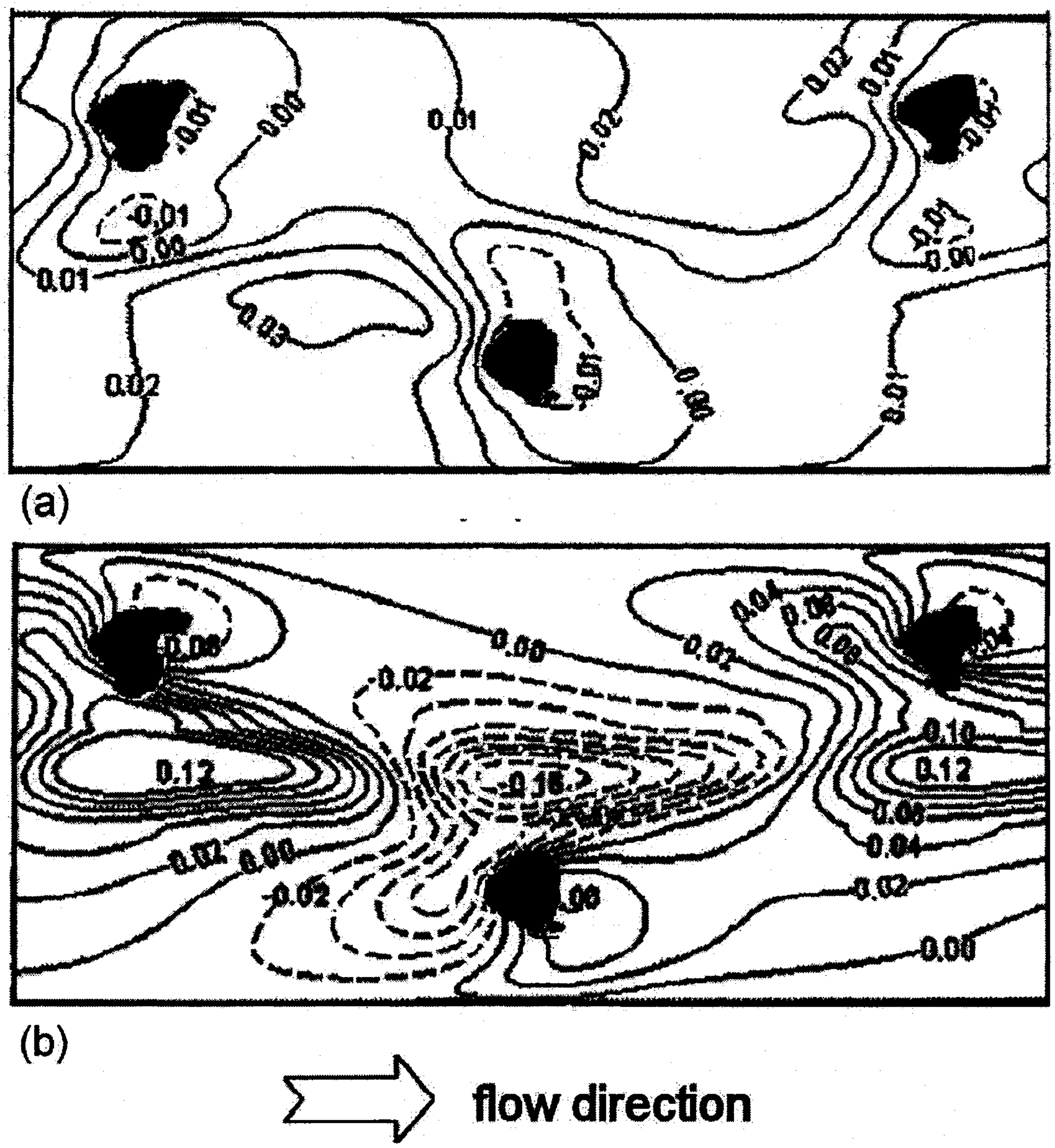

Figure 6 - 15 Predicted isocontours on the equidistant plane of : a) the dimensionless instantaneous static pressure $P/(1/2\rho U_b^2)$; b) the dimensionless instantaneous spanwise velocity W/U_b ; coherent structures identified by the Q criterion are also shown in all plots, all plots are 7.2D long and 3D high

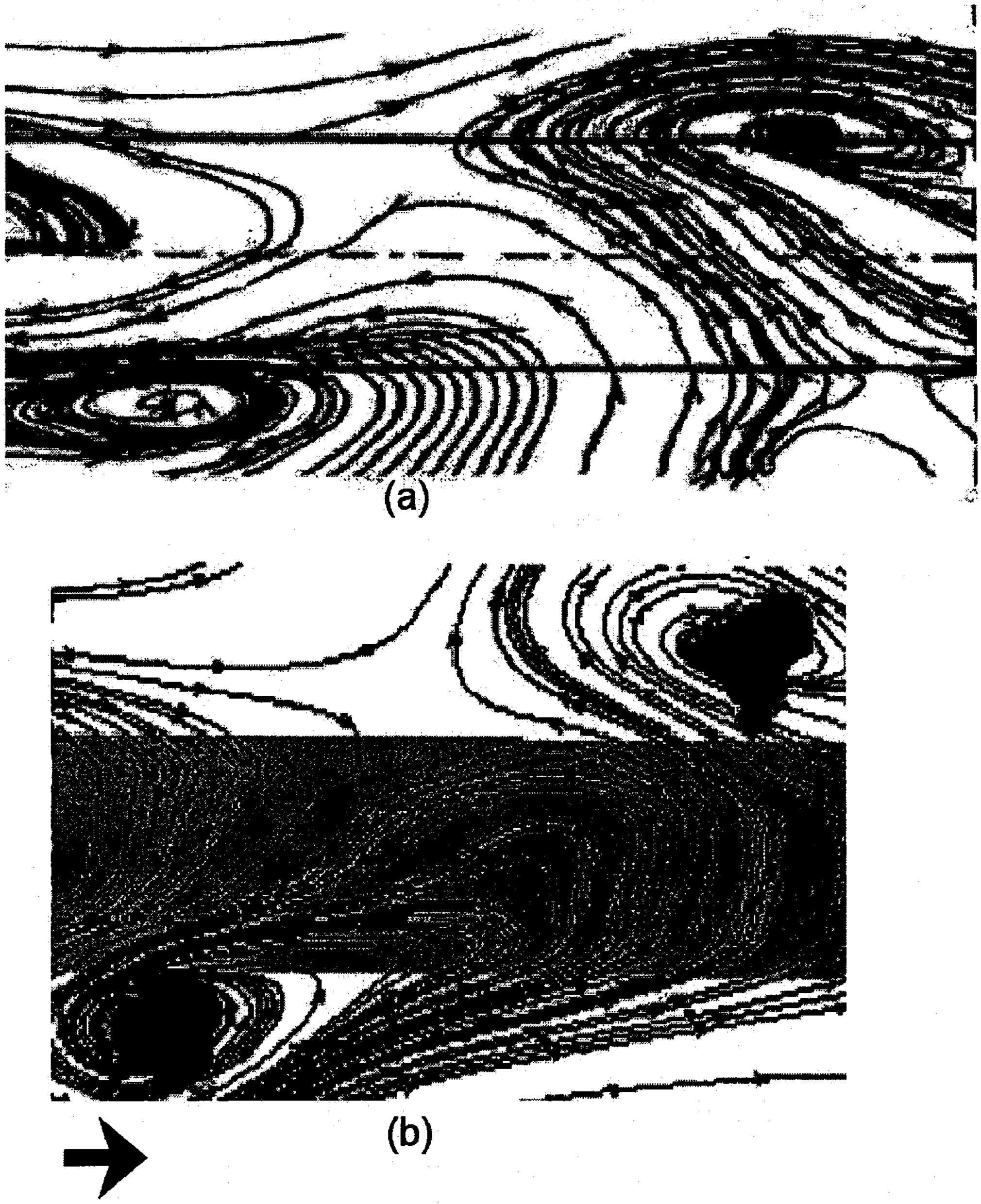

Figure 6 - 16 Experimental (a) and simulated (b) surface streamlines of velocity fields as seen by an observer moving with the average convective speed of the coherent structures

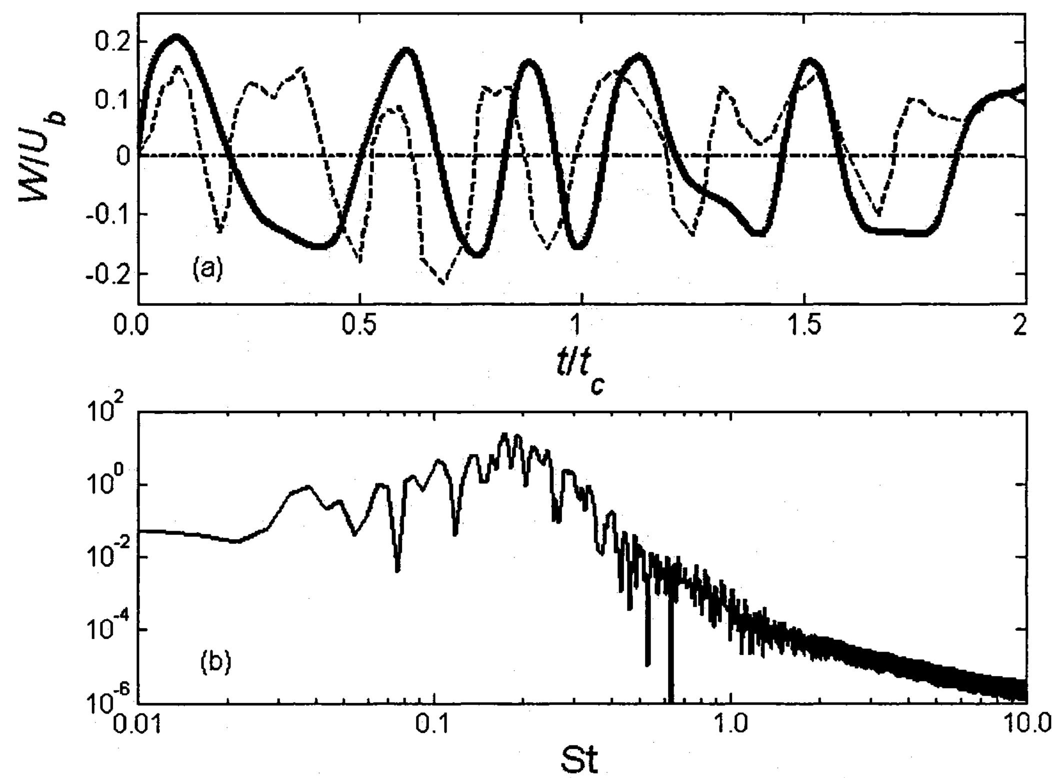

Figure 6 - 17 a) Representative time histories of the spanwise velocity in the centre of the gap : present simulations (——) and experimental results (----) ; b) the power spectrum, in arbitrary logarithmic scale, of the time history of the simulated spanwise velocity

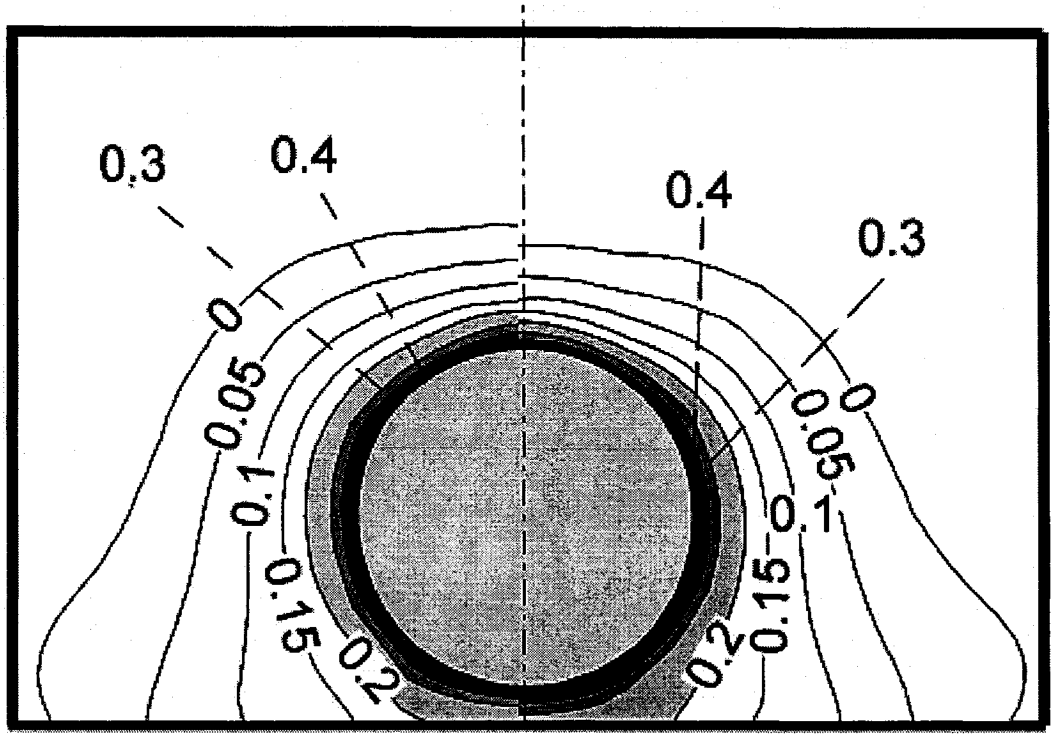

Figure 7 - 1 Predicted isocontours of the dimensionless time-averaged temperature difference $\overline{\Theta} = \left(\overline{T} - \overline{T}_b\right)/\left(\overline{T}_{\mathrm{rod,m}} - \overline{T}_b\right)$; the left-side plots correspond to the uniform rod temperature case and the right-side plots to the uniform rod heat flux case

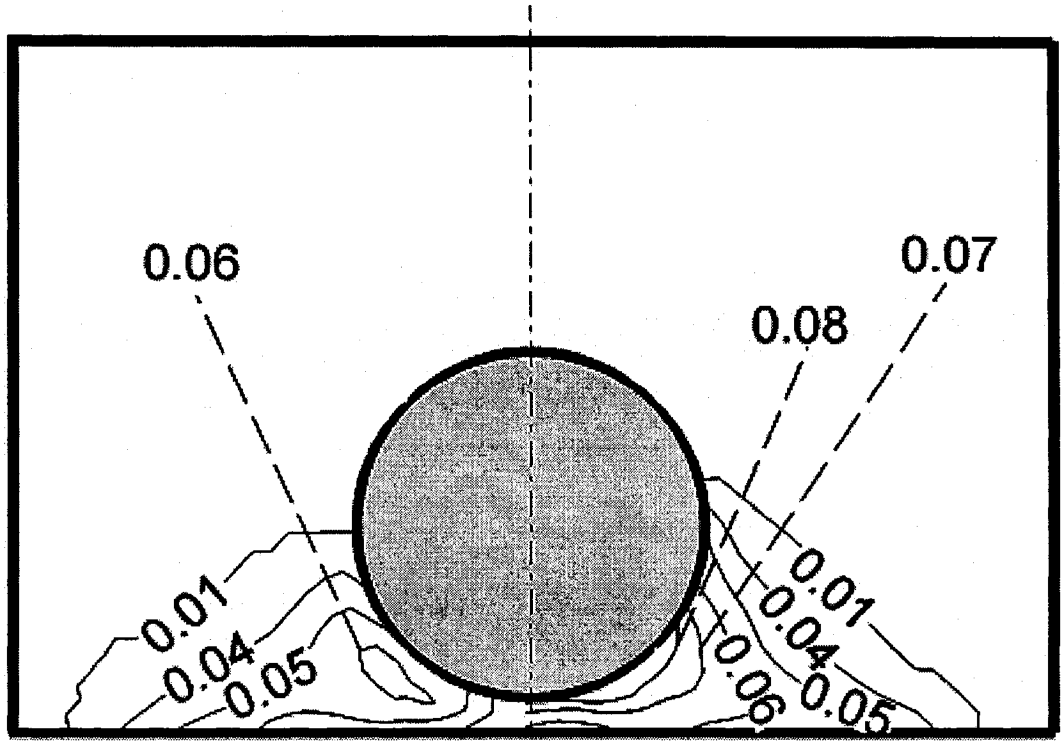

Figure 7 - 2 Predicted isocontours of the standard deviation of the normalized coherent temperature fluctuations $\sqrt{\overline{\vartheta_{co}^2}}/\left(\overline{T}_{\mathrm{rod,m}}-\overline{T}_b\right)$; the left-side plots correspond to the uniform rod temperature case and the right-side plots to the uniform rod heat flux case

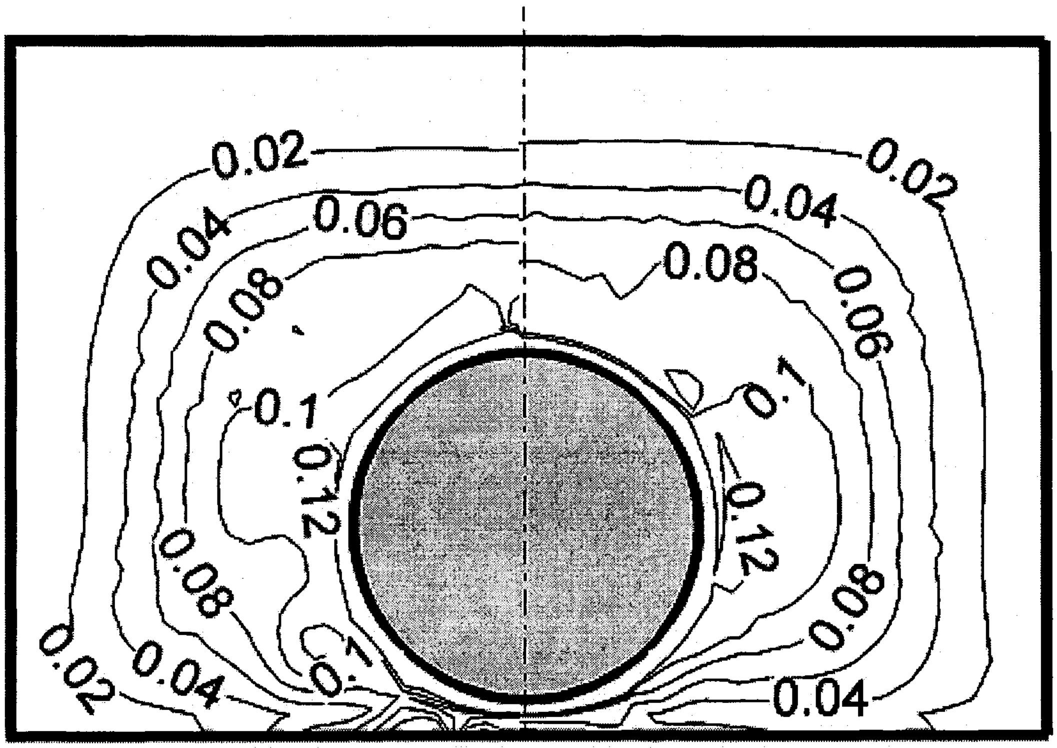

Figure 7 - 3 Predicted isocontours of the standard deviation of the normalized non-coherent temperature fluctuations $\sqrt{\overline{\vartheta_{nc}^2}}\Big/\left(\overline{T}_{\mathrm{rod,m}}-\overline{T}_b\right)$; the left-side plots correspond to the uniform rod temperature case and the right-side plots to the uniform rod heat flux case

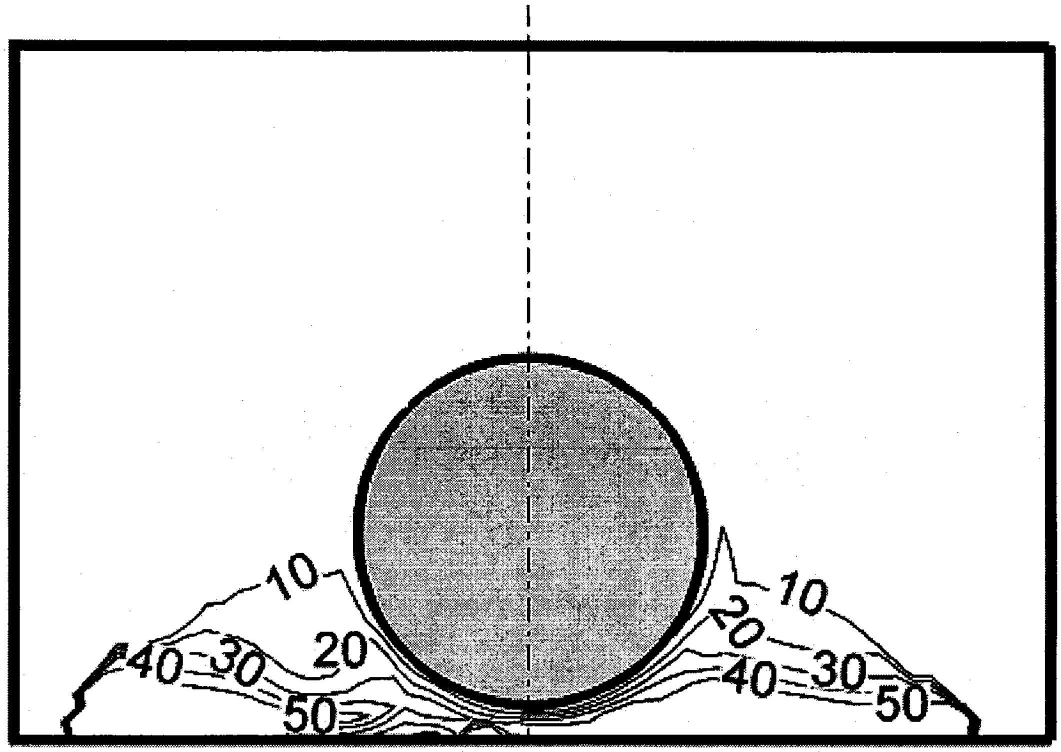

Figure 7 - 4 Predicted isocontours of the percent ratio of the variances of coherent and total temperature fluctuations $\overline{\vartheta_{co}^2} / \overline{\vartheta^2} \times 100$; the left-side plots correspond to the uniform rod temperature case and the right-side plots to the uniform rod heat flux case

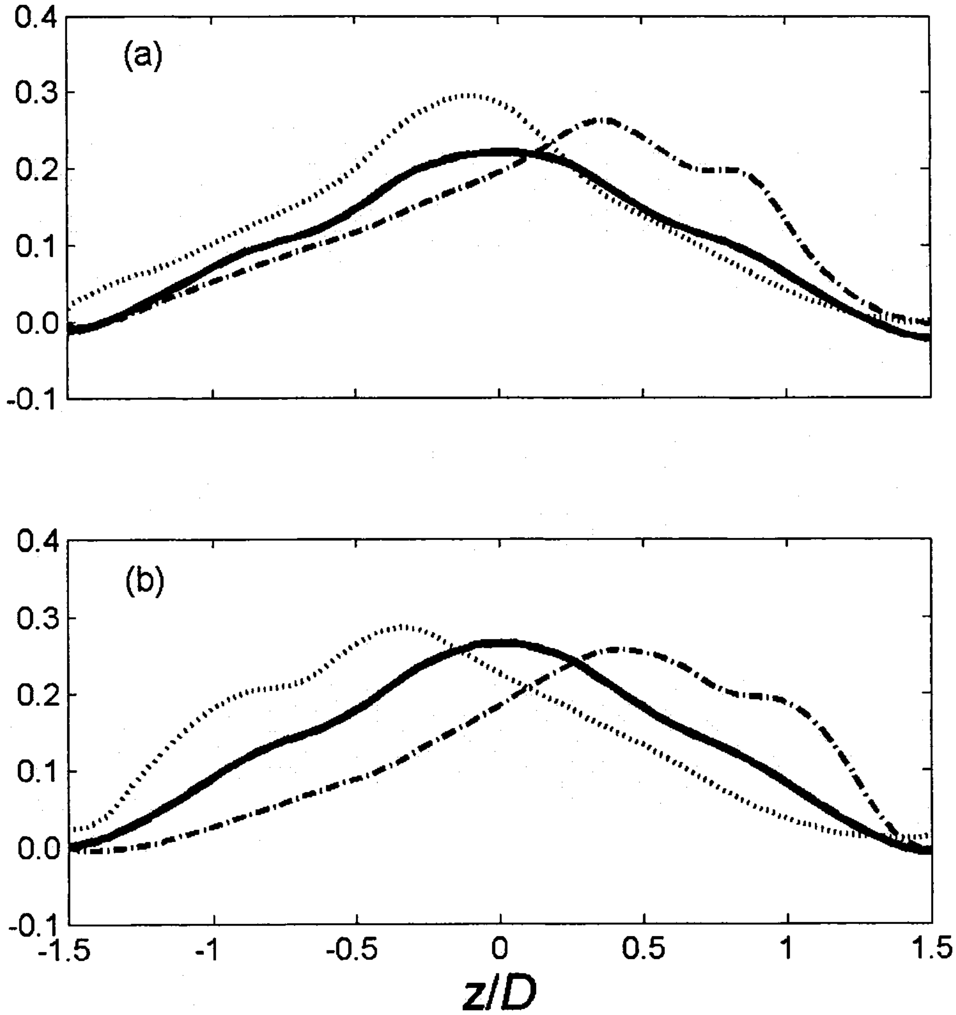

Figure 7 - 5 Spanwise variations of the time-averaged (————) and representative instantaneous (- - -, — — —) dimensionless temperature differences Θ on the bottom wall in the uniform rod temperature case (a) and uniform rod heat flux case (b)

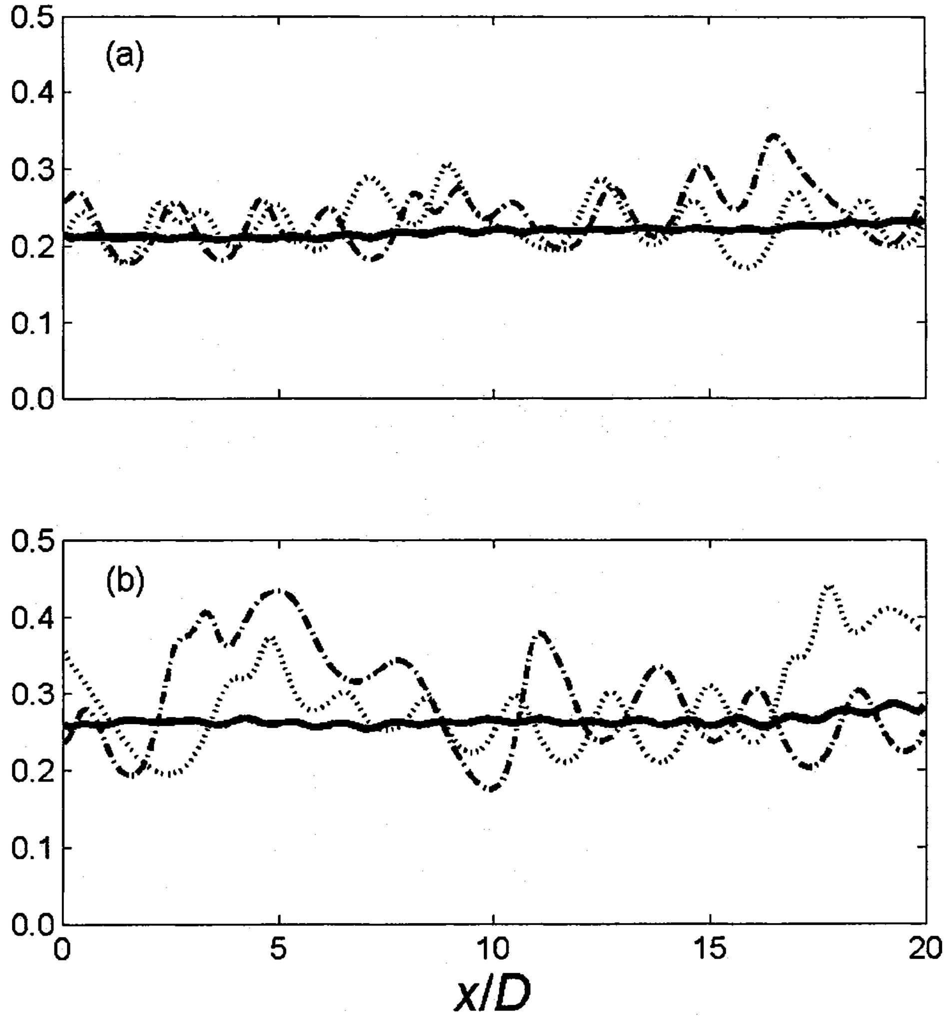

Figure 7 - 6 Streamwise variations of the time-averaged (————) and representative instantaneous (- - -, — — —) dimensionless temperature differences Θ on the bottom wall at $z/D = 0$ in the uniform rod temperature case (a) and uniform rod heat flux case (b)

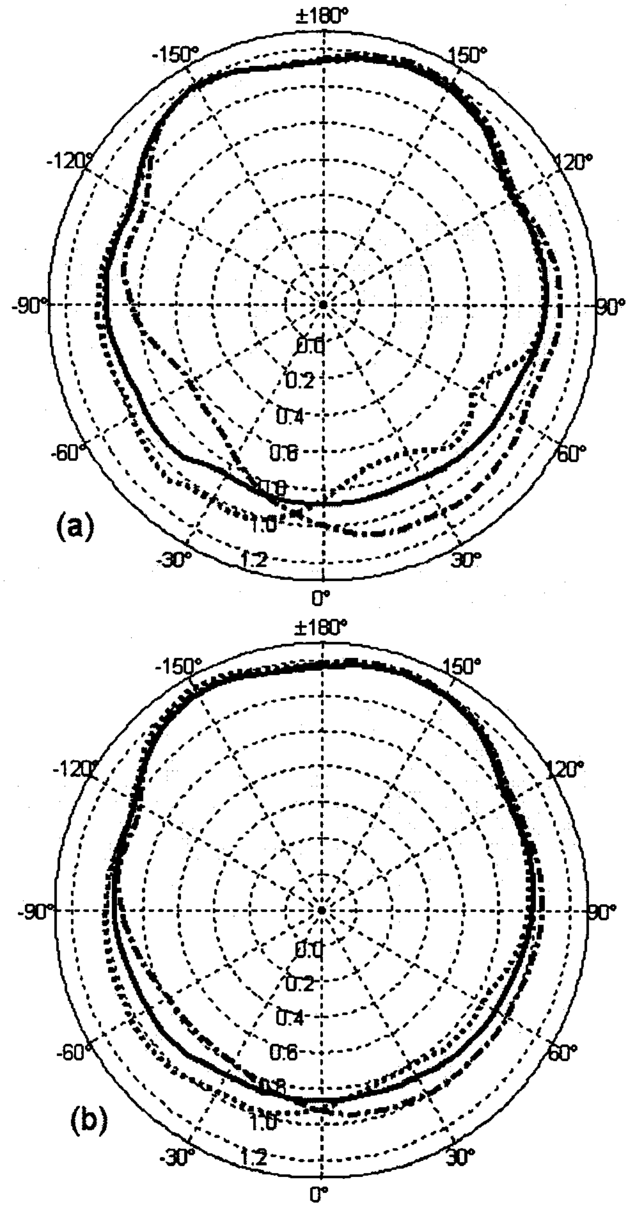

Figure 7 - 7 Circumferential variations of the time-averaged (———) and representative instantaneous (- - -, — — —) normalized Nusselt numbers $Nu/\overline{Nu}_{rod,m}$ around the rod in the uniform rod temperature case (a) and uniform rod heat flux case (b) ; the values have been normalized by the corresponding circumferential averages

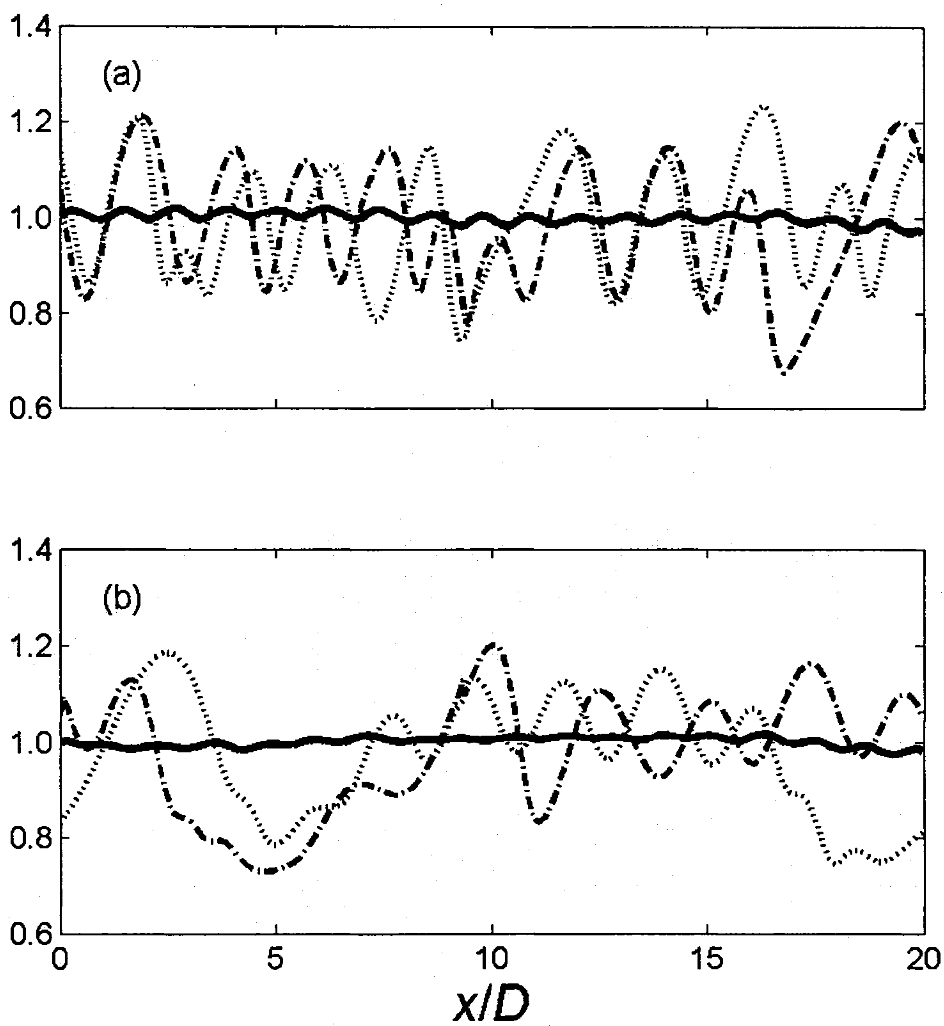

Figure 7 - 8 Streamwise variations of the time-averaged (————) and representative instantaneous (- - -, – – –) normalized Nusselt numbers $Nu/\overline{Nu}_m$ along the rod on the symmetry plane and facing the bottom wall in the uniform rod temperature case (a) and uniform rod heat flux case (b) ; the values have been normalized by the corresponding streamwise averages

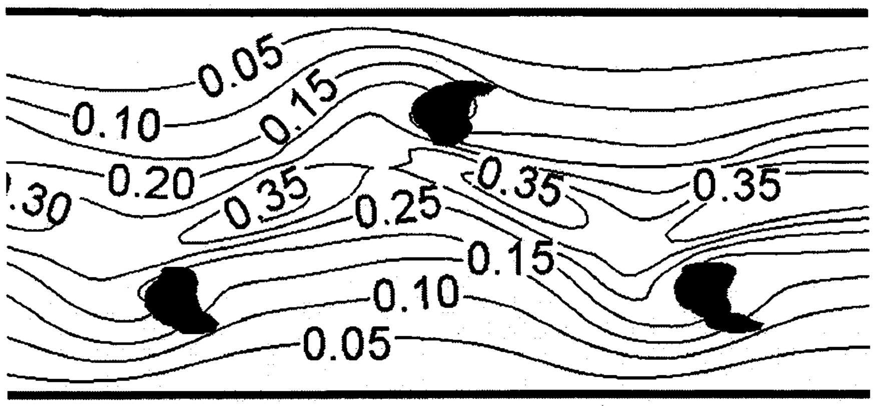

(a)

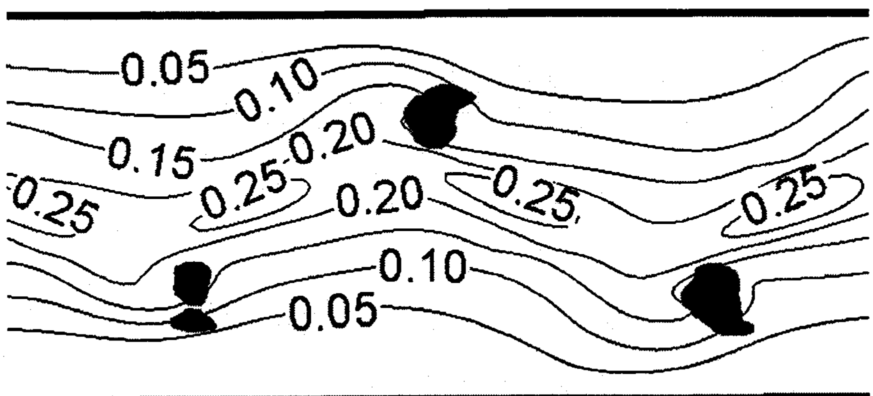

(b)

Figure 7 - 9 Predicted isocontours of the dimensionless instantaneous temperature difference Θ on the equidistant plane in the uniform rod temperature case (a) and uniform rod heat flux case (b) ; coherent structures identified by the Q criterion are also shown in both plots, which are 7.5D long and 3D high

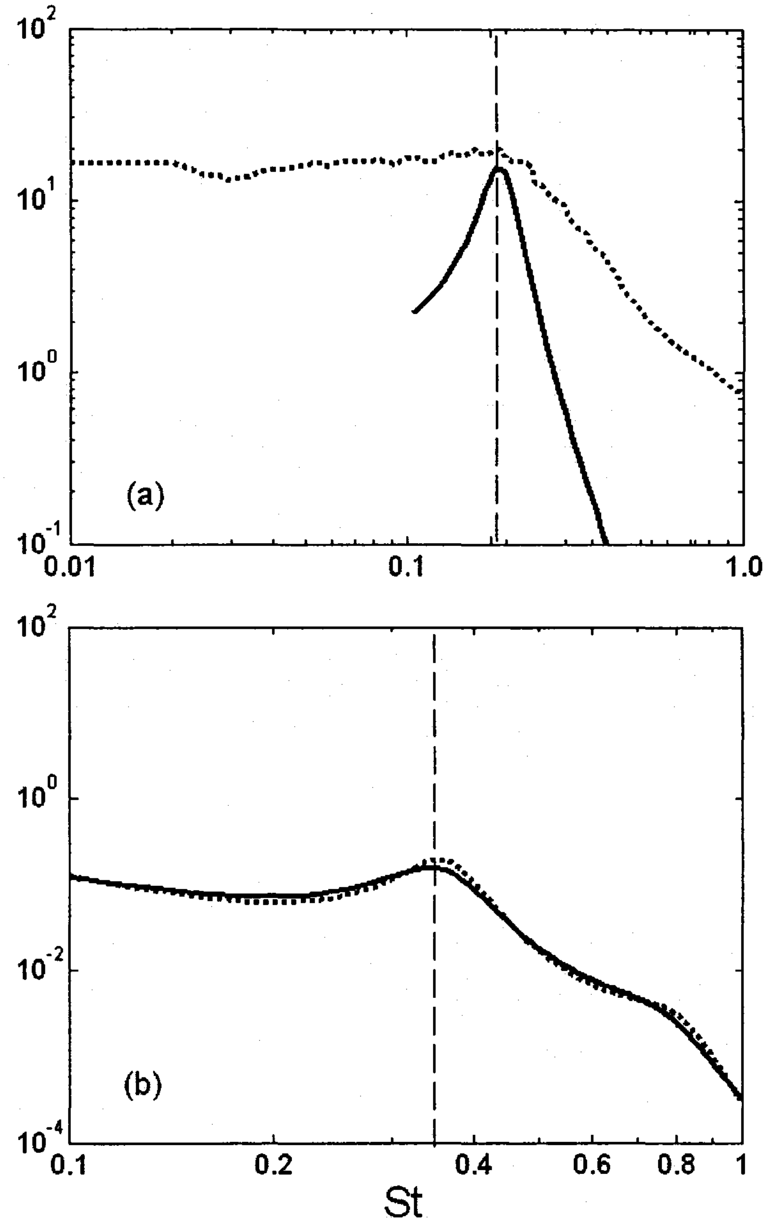

Figure 7 - 10 (a) Smoothened power spectra of the spanwise velocity in the centre of the gap in the present simulations (——) and as measured by Guellouz and Tavoularis (2000a) (. . . . .) ; (b) Smoothened power spectra of the resolved temperature in the centre of the gap in the constant rod temperature case (——) and the constant rod heat flux case (. . . . .)

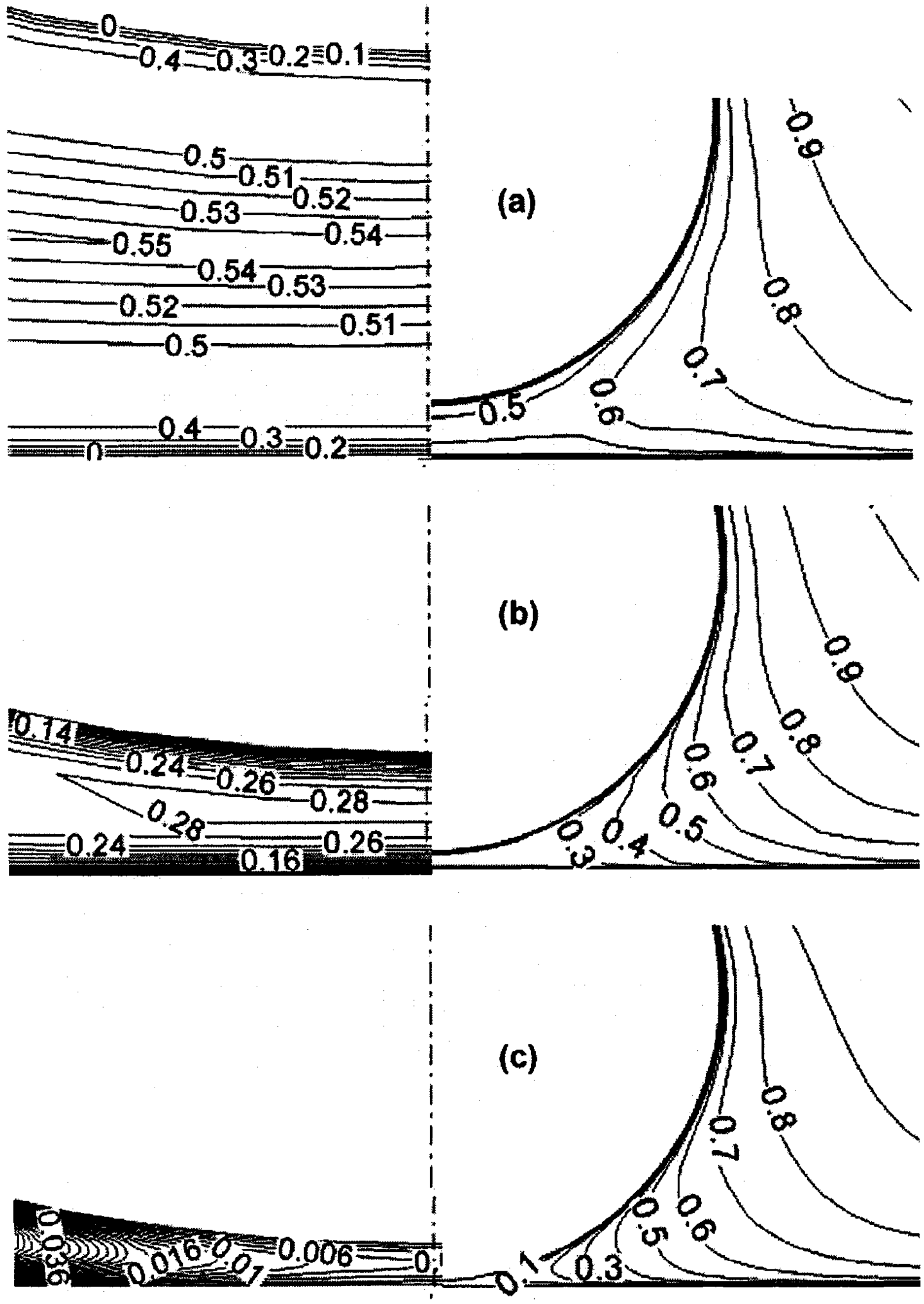

Figure 8 - 1 Isocontours of the dimensionless time-averaged streamwise velocity $\overline{U}/U_b$: (a) $\delta/D = 0.10$, (b) $\delta/D = 0.03$ and (c) $\delta/D = 0.01$; plots on the left are near-gap details of those on the right

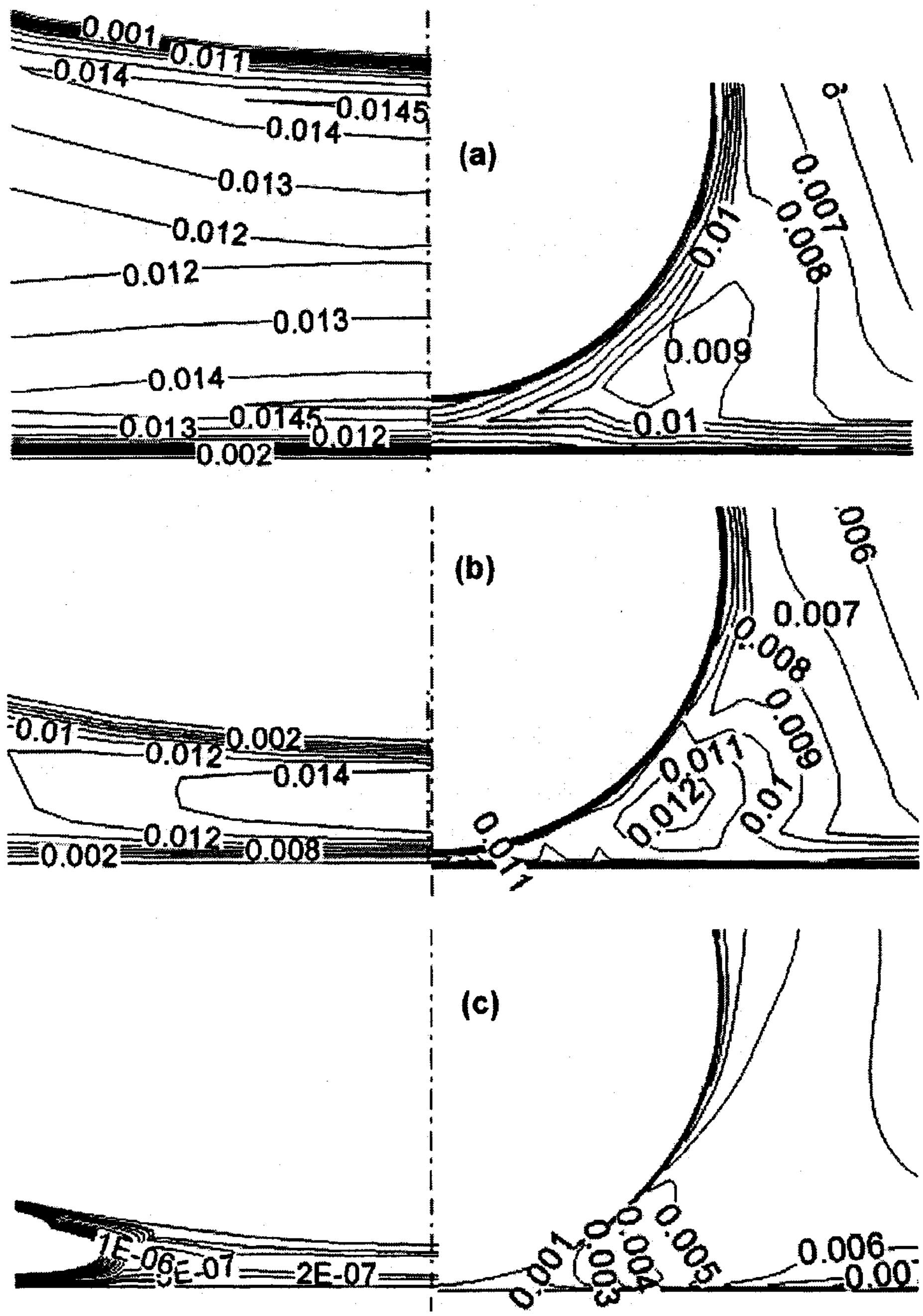

Figure 8 - 2 Isocontours of the dimensionless time-averaged total turbulent kinetic energy per unit mass $\bar{k}/U_b^2$: (a) $\delta/D = 0.10$, (b) $\delta/D = 0.03$ and (c) $\delta/D = 0.01$; plots on the left are near-gap details of those on the right

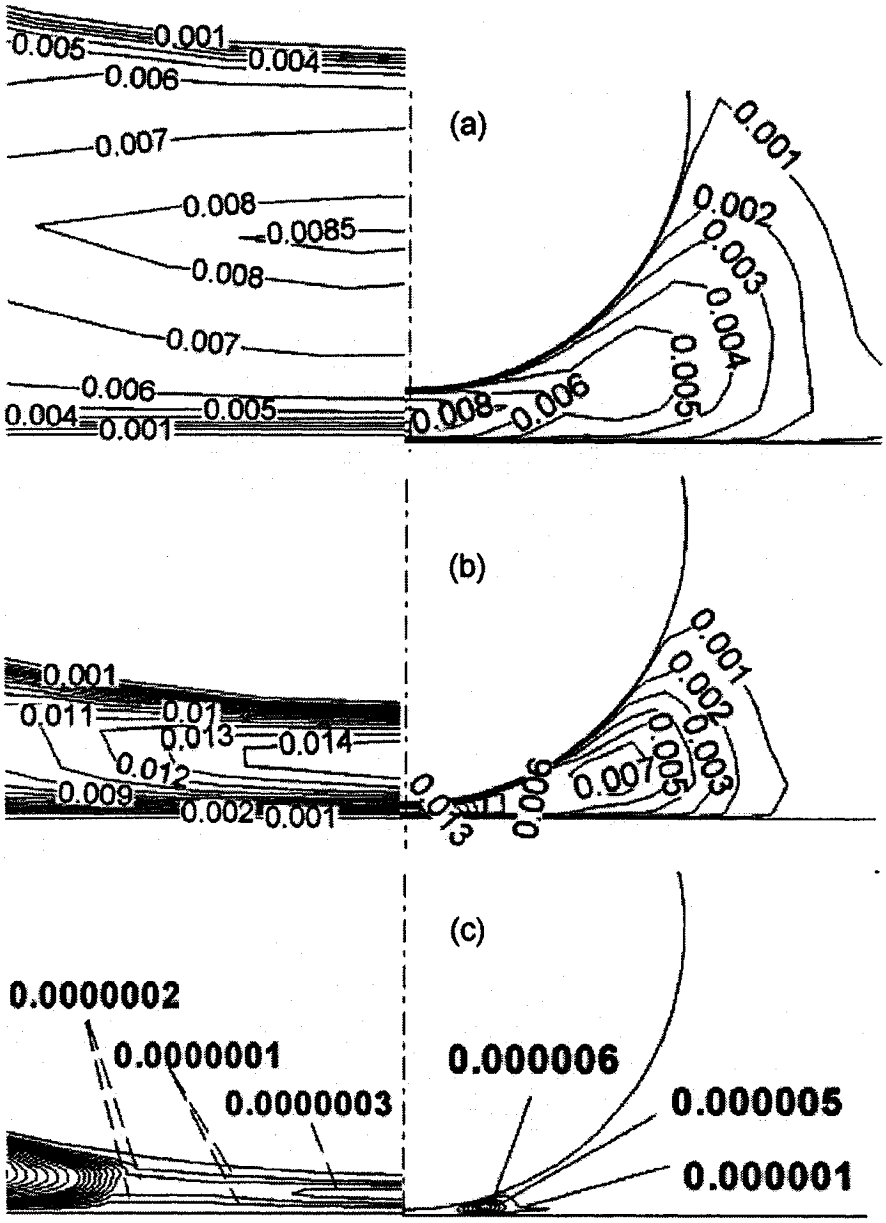

Figure 8 - 3 Isocontours of the dimensionless time-averaged coherent turbulent kinetic energy per unit mass $\bar{k}_c/U_b^2$: (a) $\delta/D = 0.10$, (b) $\delta/D = 0.03$ and (c) $\delta/D = 0.01$; plots on the left are near-gap details of those on the right

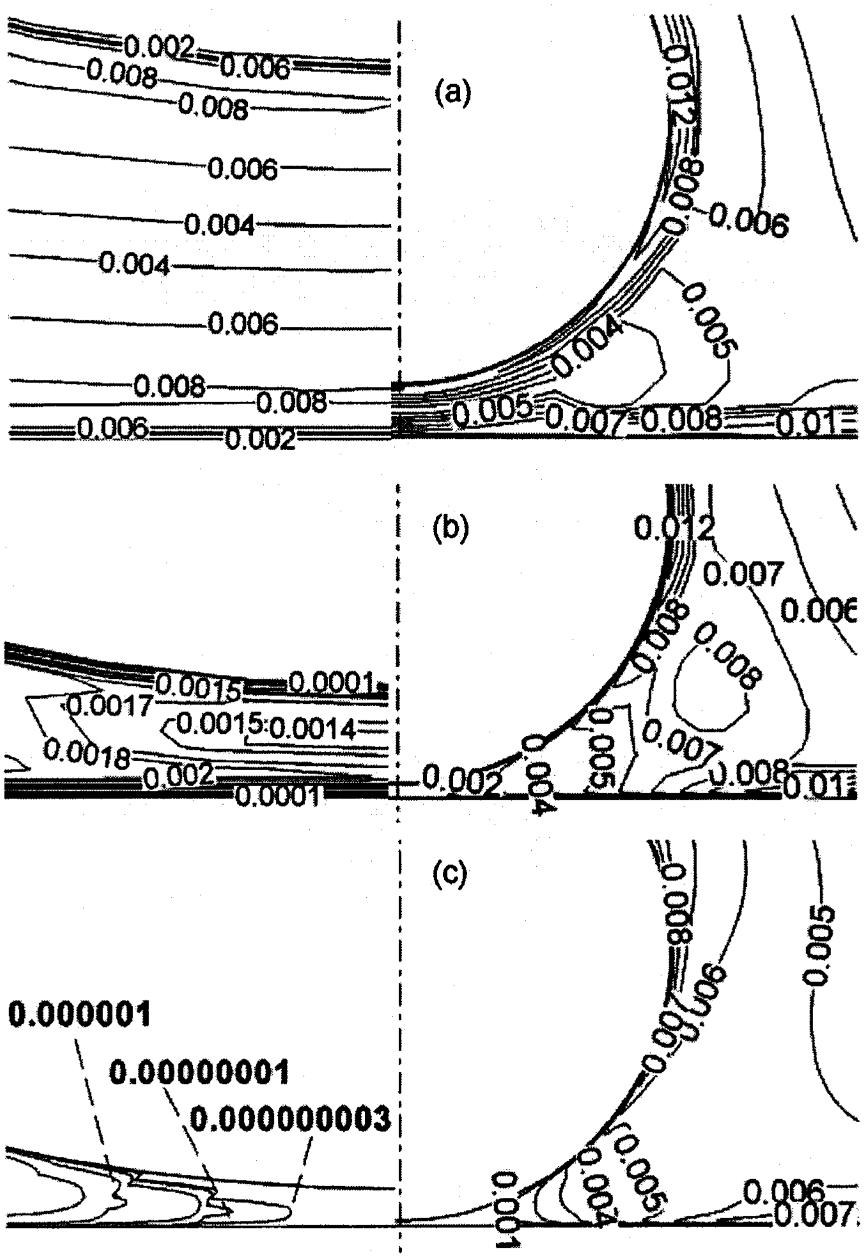

Figure 8 - 4 Isocontours of the dimensionless time-averaged non-coherent turbulent kinetic energy per unit mass $\bar{k}_{nc}/U_b^2$: (a) $\delta/D = 0.10$, (b) $\delta/D = 0.03$ and (c) $\delta/D = 0.01$; plots on the left are near-gap details of those on the right

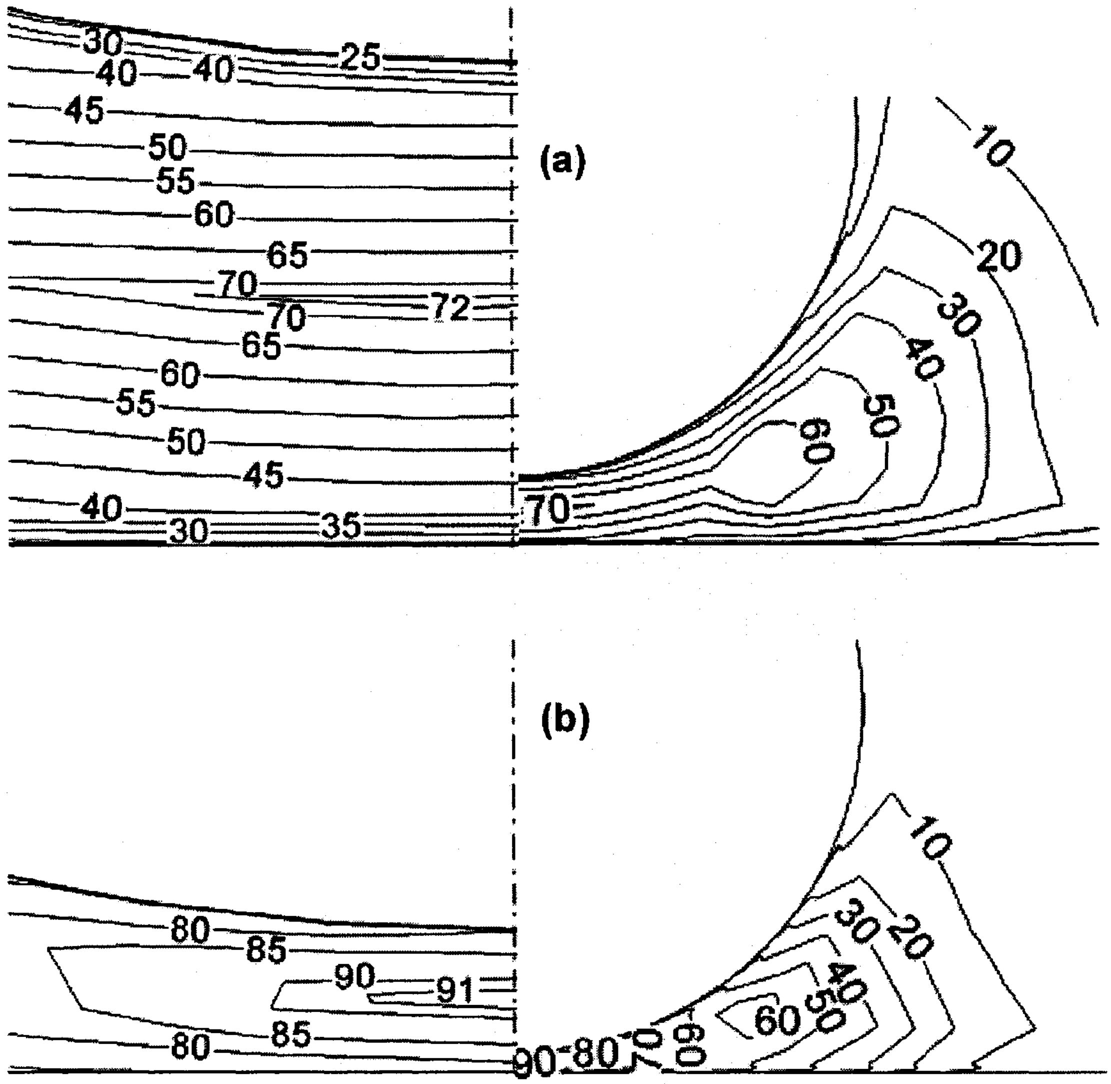

Figure 8 - 5 Isocontours of the ratio of coherent component and the total time-averaged turbulent kinetic energy per unit mass $\bar{k}_c/\bar{k}\ \times 100$: (a) $\delta/D = 0.10$ and (b) $\delta/D = 0.03$; plots on the left are near-gap details of those on the right

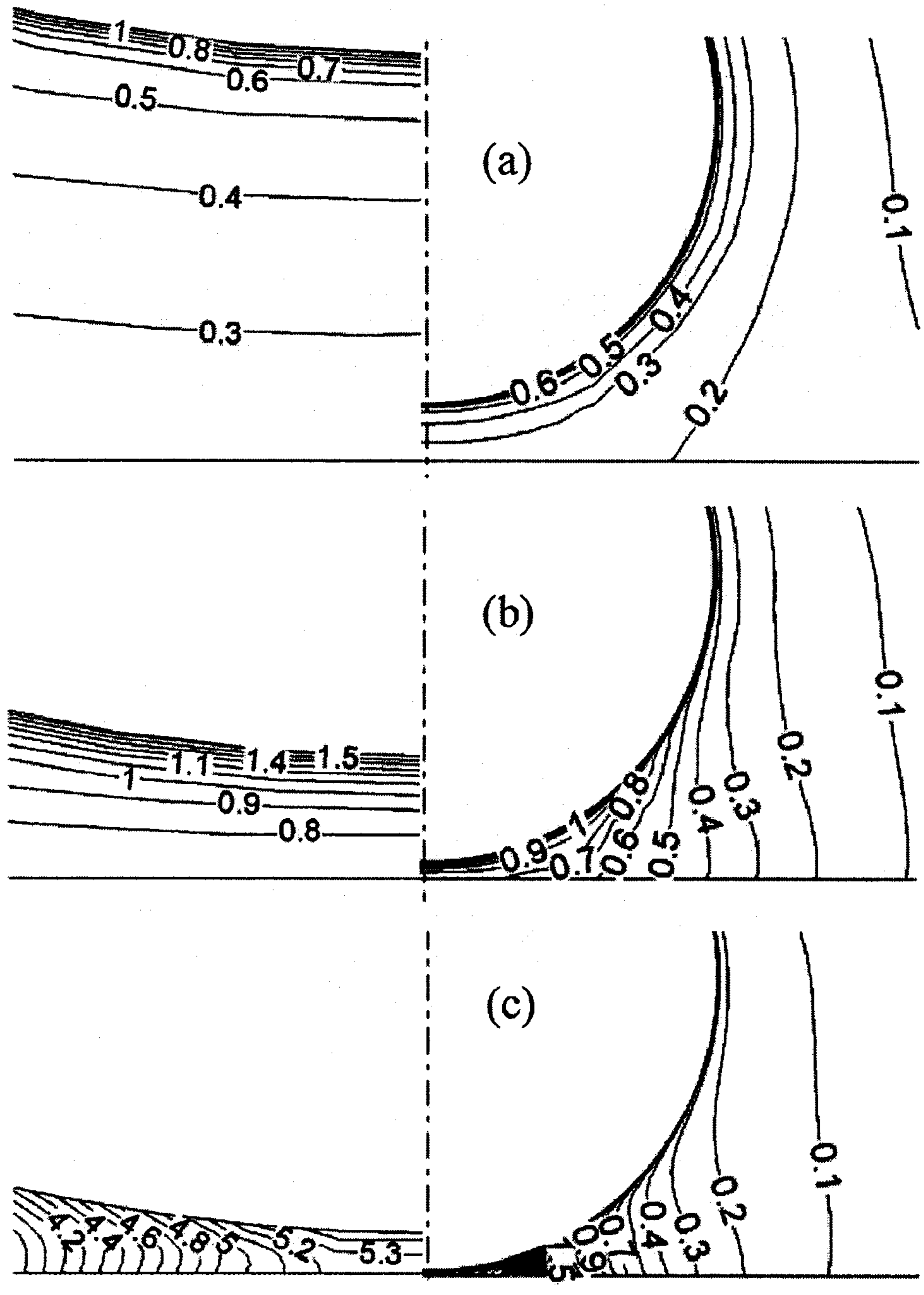

Figure 8 - 6 Isocontours of the time-averaged dimensionless temperature difference $\overline{\Theta}$: (a) $\delta/D = 0.10$, (b) $\delta/D = 0.03$ and (c) $\delta/D = 0.01$; plots on the left are near-gap details of those on the right

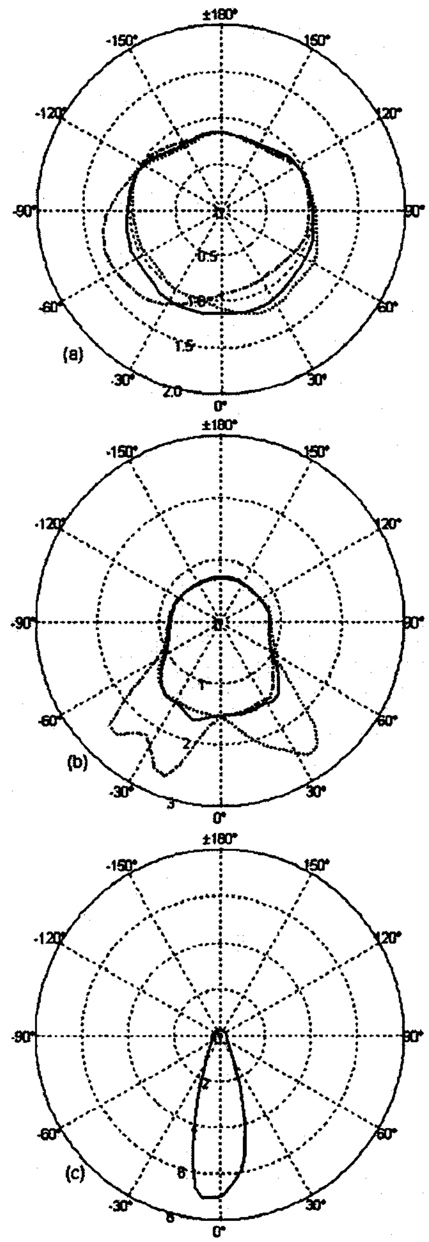

Figure 8 - 7 Circumferential variations of the time-averaged (————) and two representative instantaneous (— · —,·······) dimensionless temperature differences Θ : (a) $\delta/D = 0.10$, (b) $\delta/D = 0.03$ and (c) $\delta/D = 0.01$

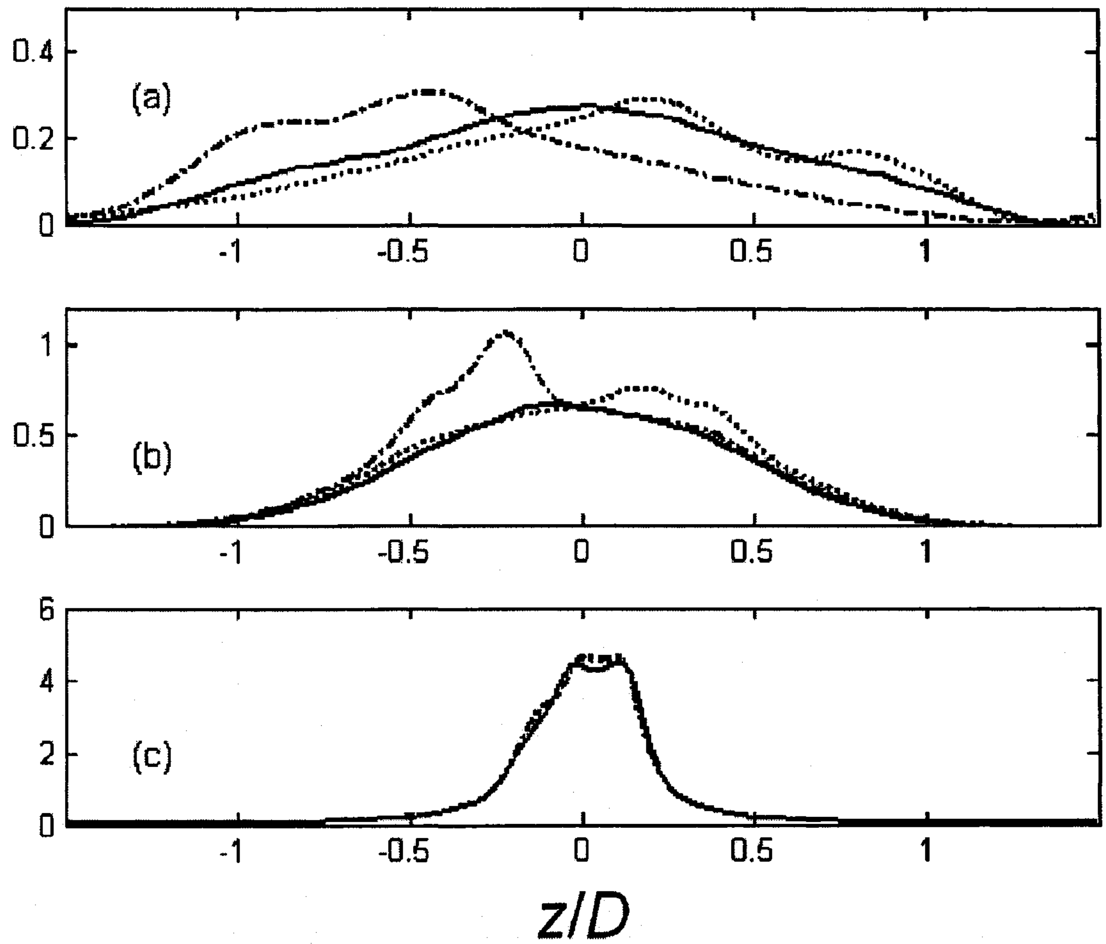

Figure 8 - 8 Spanwise variations of the time-averaged (————) and two representative instantaneous (— · —, ········) dimensionless temperature differences Θ : (a) $\delta/D = 0.10$, (b) $\delta/D = 0.03$ and (c) $\delta/D = 0.01$

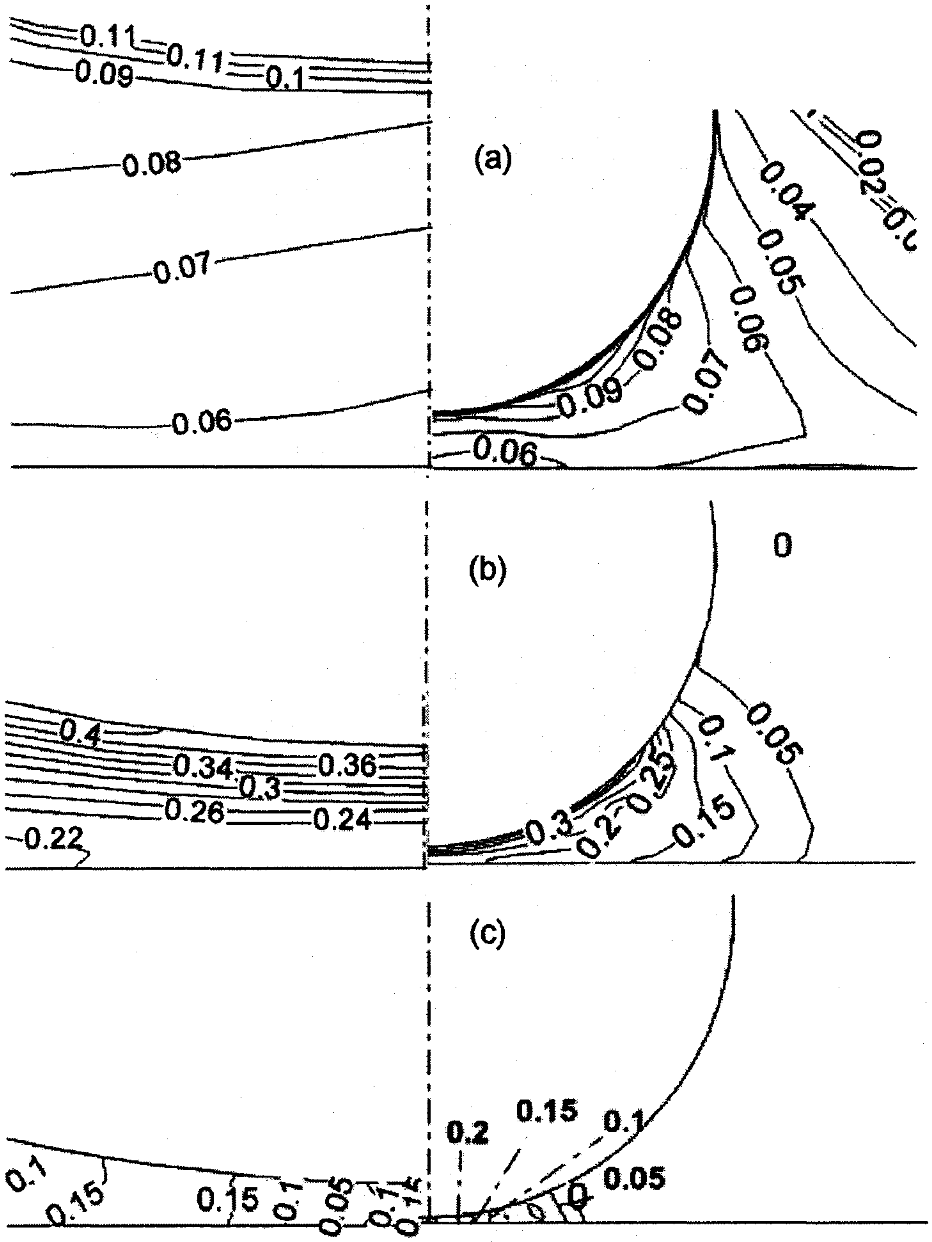

Figure 8 - 9 Isocontours of the normalized standard deviation of the coherent temperature fluctuations $\sqrt{\overline{\vartheta_c^2}} / \left(\overline{T}_{\text{rod,m}} - \overline{T}_b\right)$: (a) $\delta/D = 0.10$, (b) $\delta/D = 0.03$ and (c) $\delta/D = 0.01$; plots on the left are near-gap details of those on the right

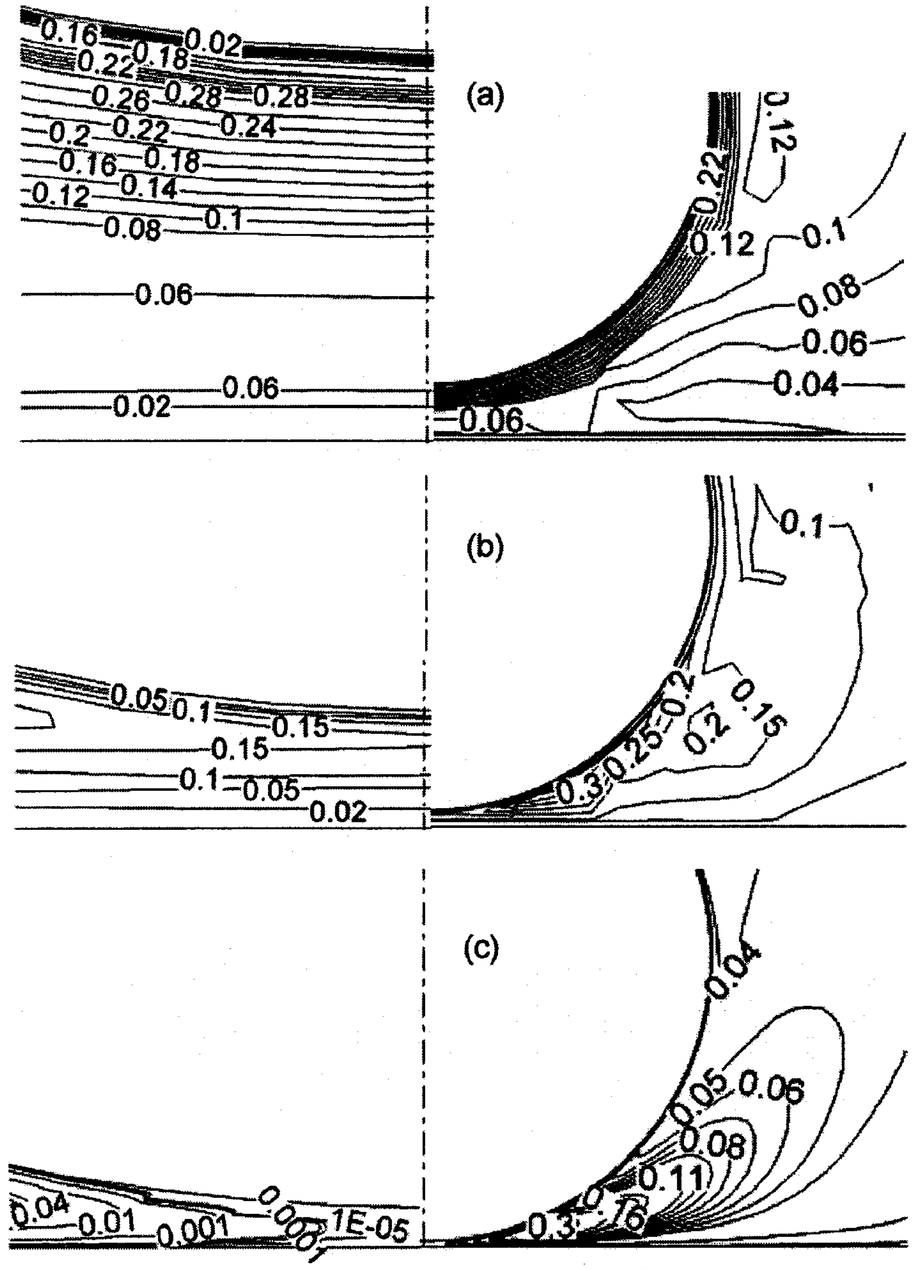

Figure 8 - 10 Isocontours of the normalized standard deviation of non-coherent temperature fluctuations $\sqrt{\vartheta_{nc}^2}/\left(\overline{T}_{\mathrm{rod,m}}-\overline{T}_b\right)$: (a) $\delta/D=0.10$, (b) $\delta/D=0.03$ and (c) $\delta/D=0.01$; plots on the left are near-gap details of those on the right

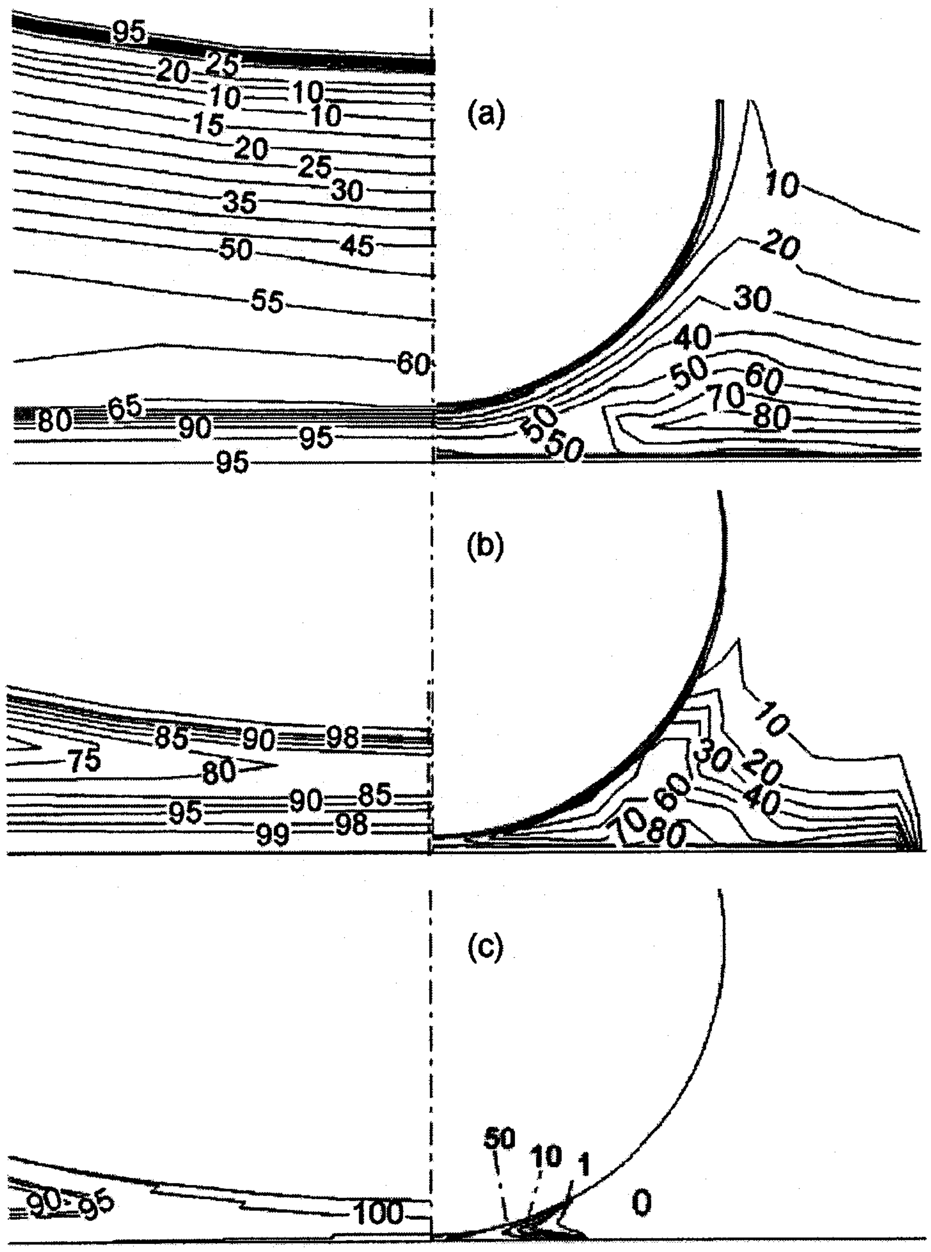

Figure 8 - 11 Isocontours of the percent ratio of the variances of coherent and total temperature fluctuations $\overline{\vartheta_c^2} / \overline{\vartheta^2} \times 100$: (a) $\delta/D = 0.10$, (b) $\delta/D = 0.03$ and (c) $\delta/D = 0.01$; plots on the left are near-gap details of those on the right

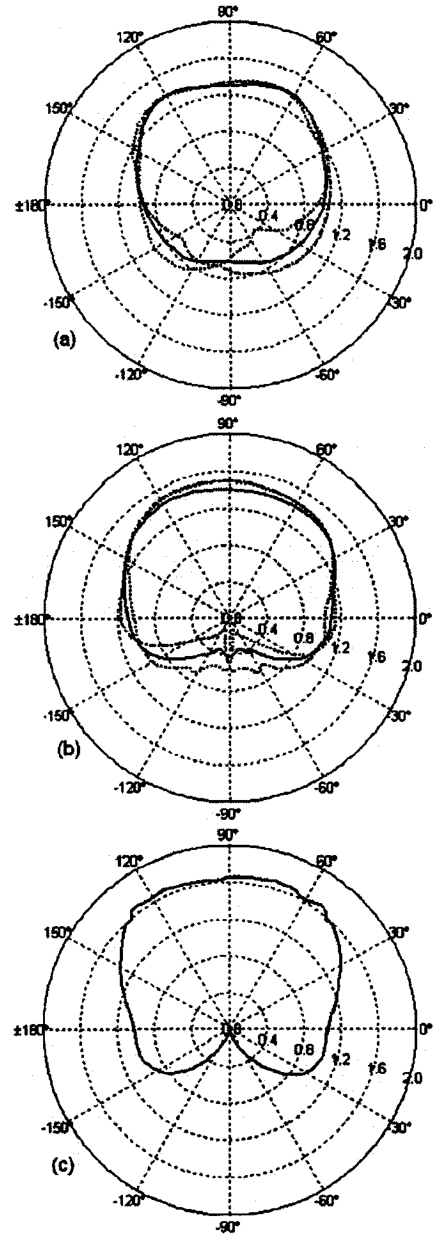

Figure 8 - 12 Circumferential variations of the time-averaged (————) and representative instantaneous (— · —, ·······) normalized skin friction coefficient around the rod ; (a) $\delta/D = 0.10$, (b) $\delta/D = 0.03$ and (c) $\delta/D = 0.01$; the values have been normalized by the corresponding circumferential averages, given in the text

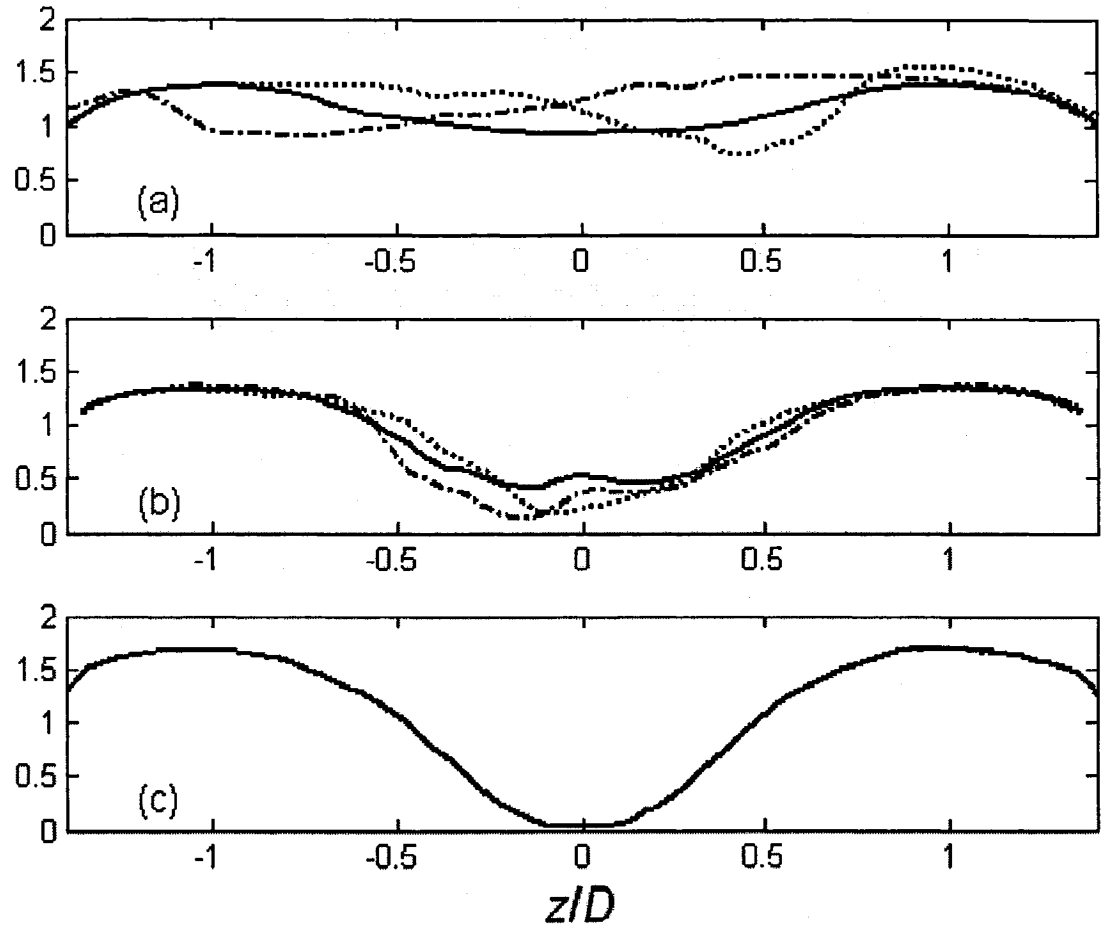

Figure 8 - 13 Variations of the time-averaged (————) and representative instantaneous (— · —, ········) skin friction coefficients across the span of the bottom wall ; (a) $\delta/D = 0.10$, (b) $\delta/D = 0.03$ and (c) $\delta/D = 0.01$; the values have been normalized by corresponding averages across the span, given in the text

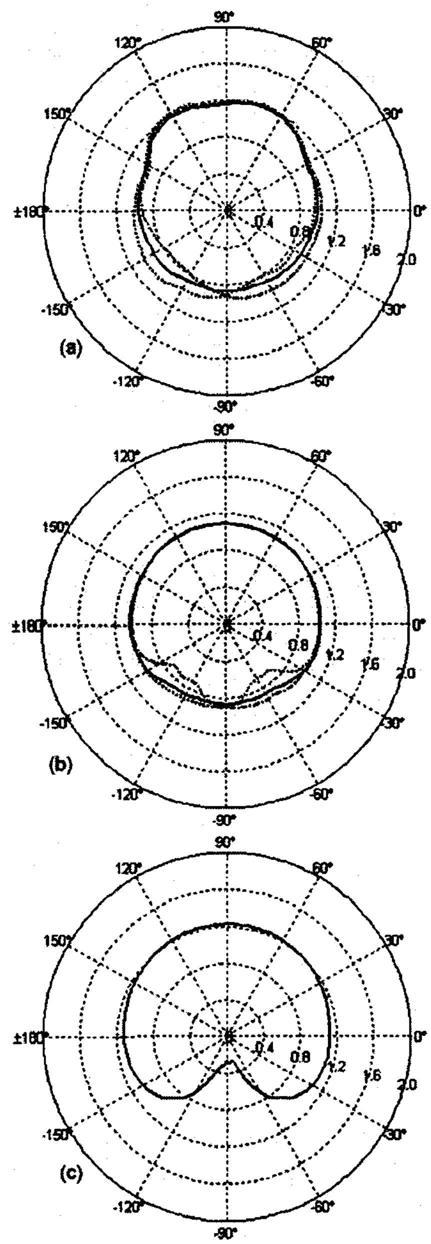

Figure 8 - 14 Circumferential variations of the time-averaged (————) and representative instantaneous (— · —, ·······) Nusselt number around the rod ; (a) $\delta/D = 0.10$, (b) $\delta/D = 0.03$ and (c) $\delta/D = 0.01$; the values have been normalized by the corresponding circumferential averages, given in the text

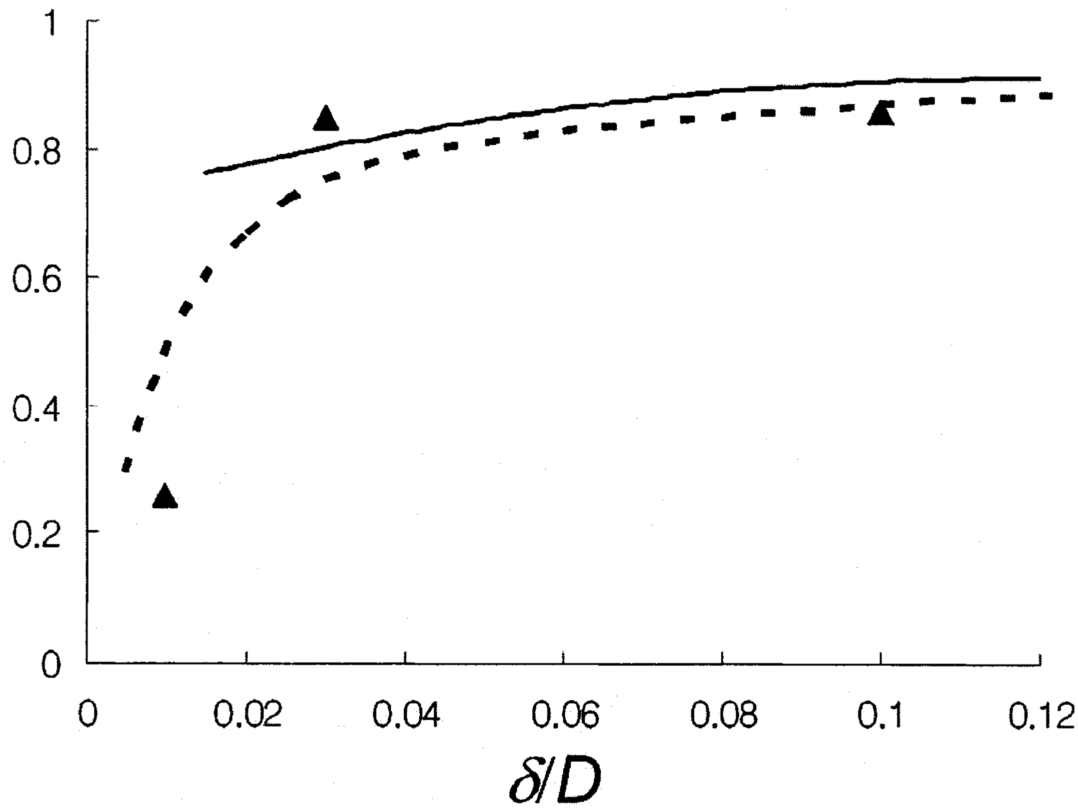

Figure 8 - 15 Variation of the minimum time-averaged Nusselt number on the rod, normalized by the circumferential average ; ▲ present simulations ; ——— curve fitted to Guellouz and Tavoularis' measurements (1992) ; – – – Guellouz's correlation (1998)

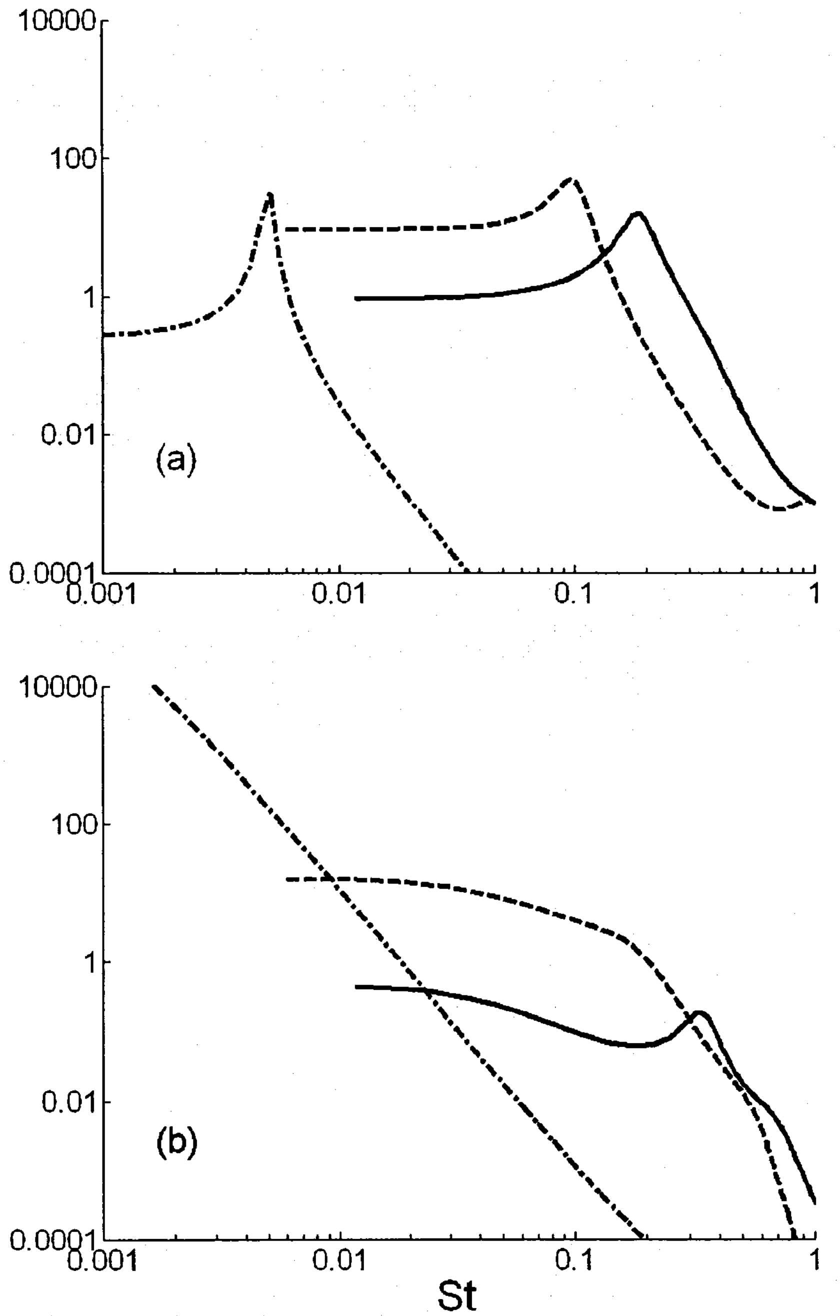

Figure 8 - 16 Power spectra of the spanwise velocity (a) and the temperature (b) in the center of the gap ; ——— $\delta/D = 0.10$; - - - $\delta/D = 0.03$; — · — $\delta/D = 0.01$

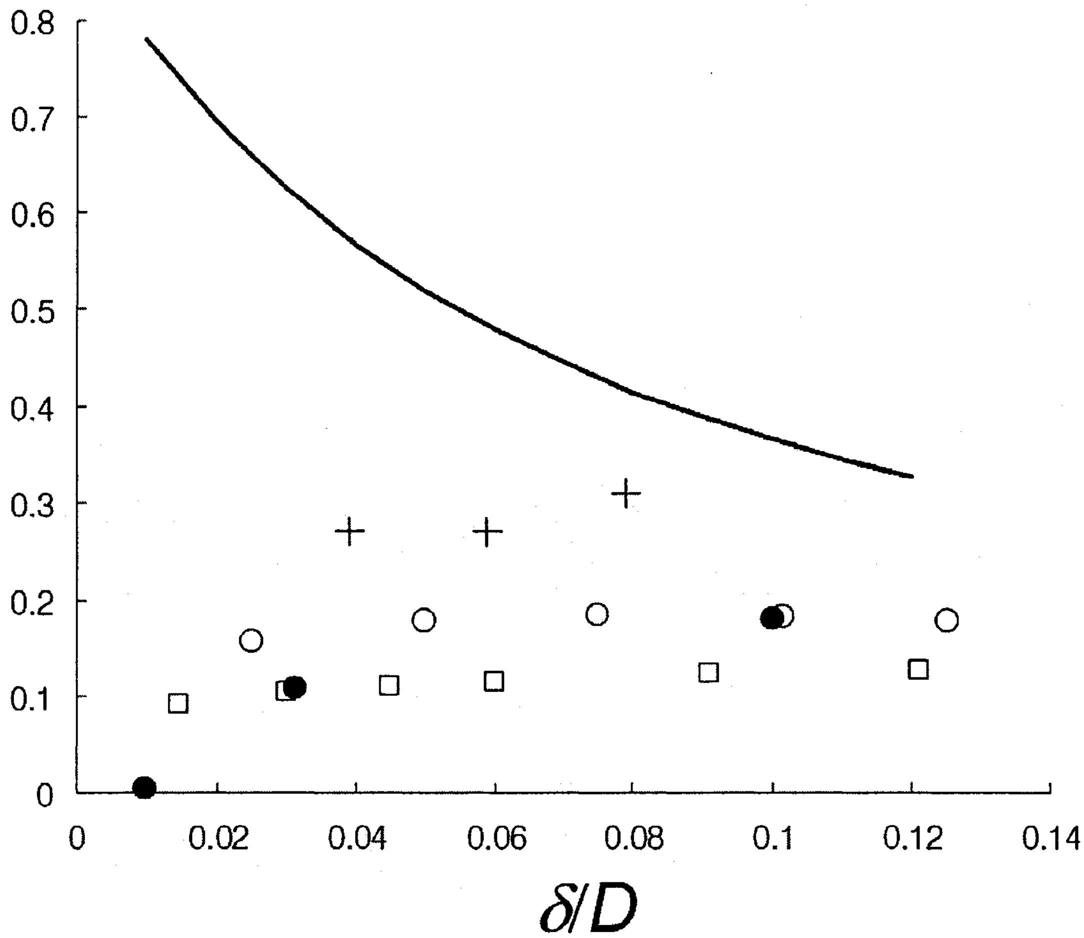

Figure 8 - 17 Variation of the peak Strouhal number in the gap centre with gap size; ● present simulations ; ○ Guellouz and Tavoularis' measurements (2000) ; □ Baratto, Sean and Tavoularis' measurements (2006) ; + Wu and Trupp's measurements (1994) ; ——— Möller's correlation (1991)

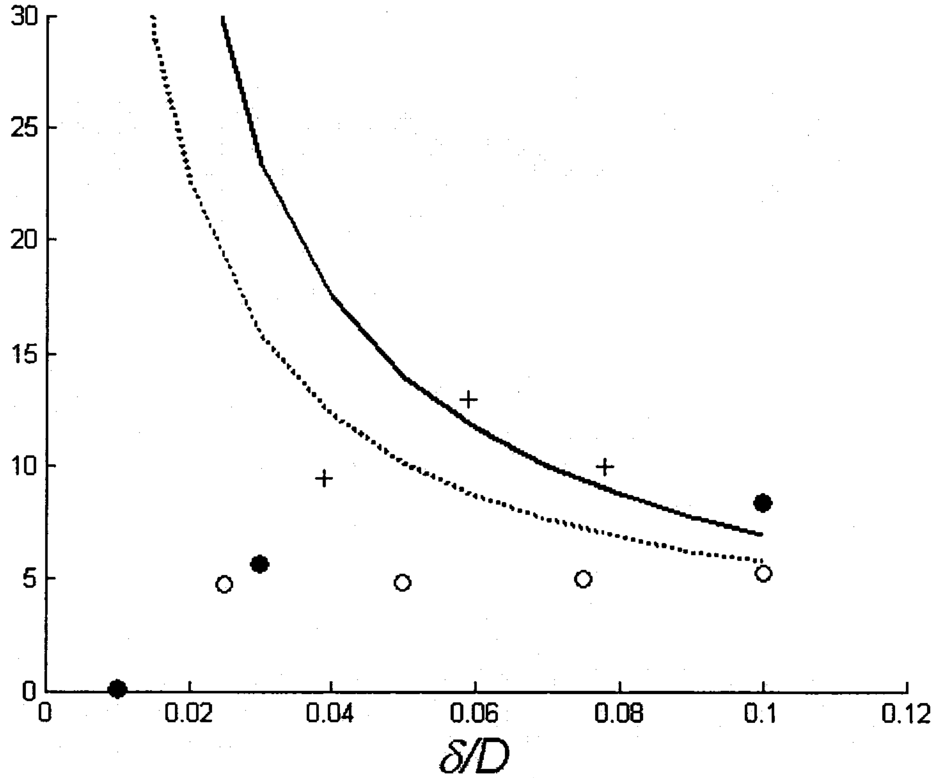

Figure 8 - 18 Variation of the mixing factor Y with gap size ; ● present simulations; ○ Guellouz and Tavoularis' measurements (2000a) ; + Wu and Trupp's measurements (1994) ; ——— Rehme's correlation (1992); ········ Rogers and Tahir's correlation (1975)

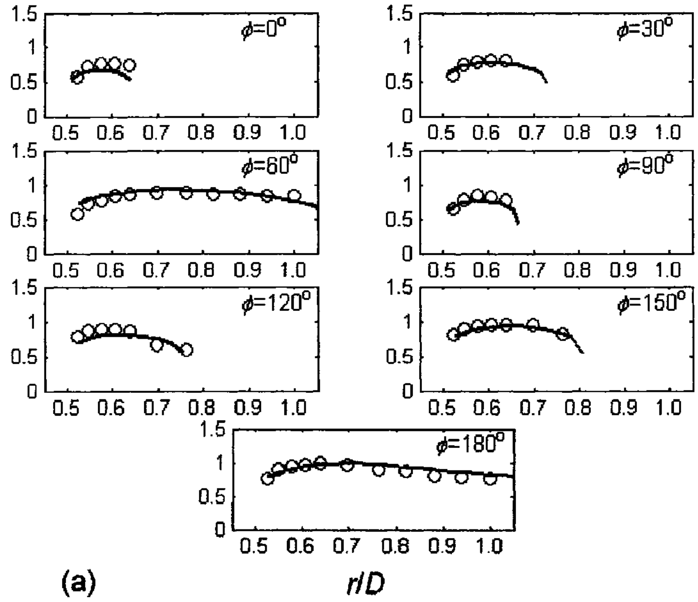

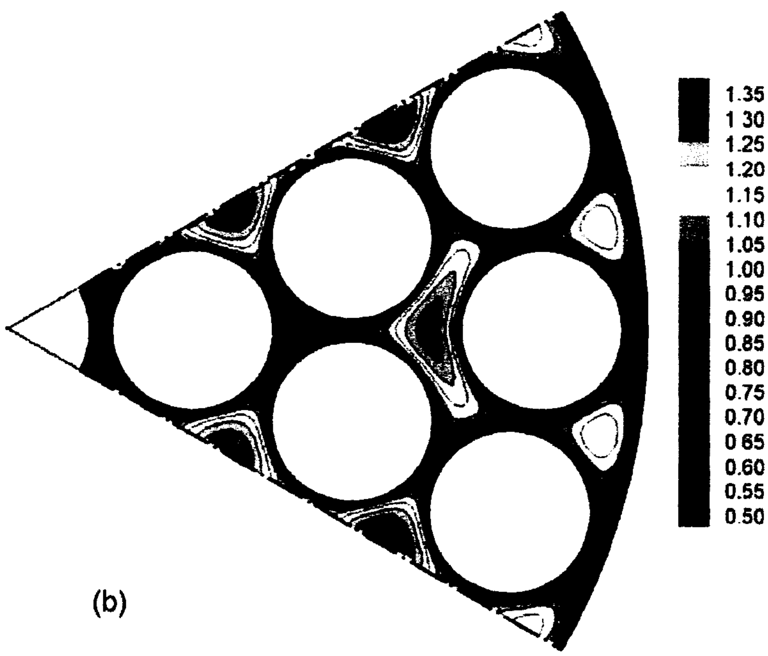

Figure 9 - 1 (a) Dimensionless time-averaged streamwise velocity $\overline{U}/\overline{U}_{max}$ around the middle outer rod ; —— simulations ; ○ OT experiments ; (b) predicted isocontours of $\overline{U}/U_b$

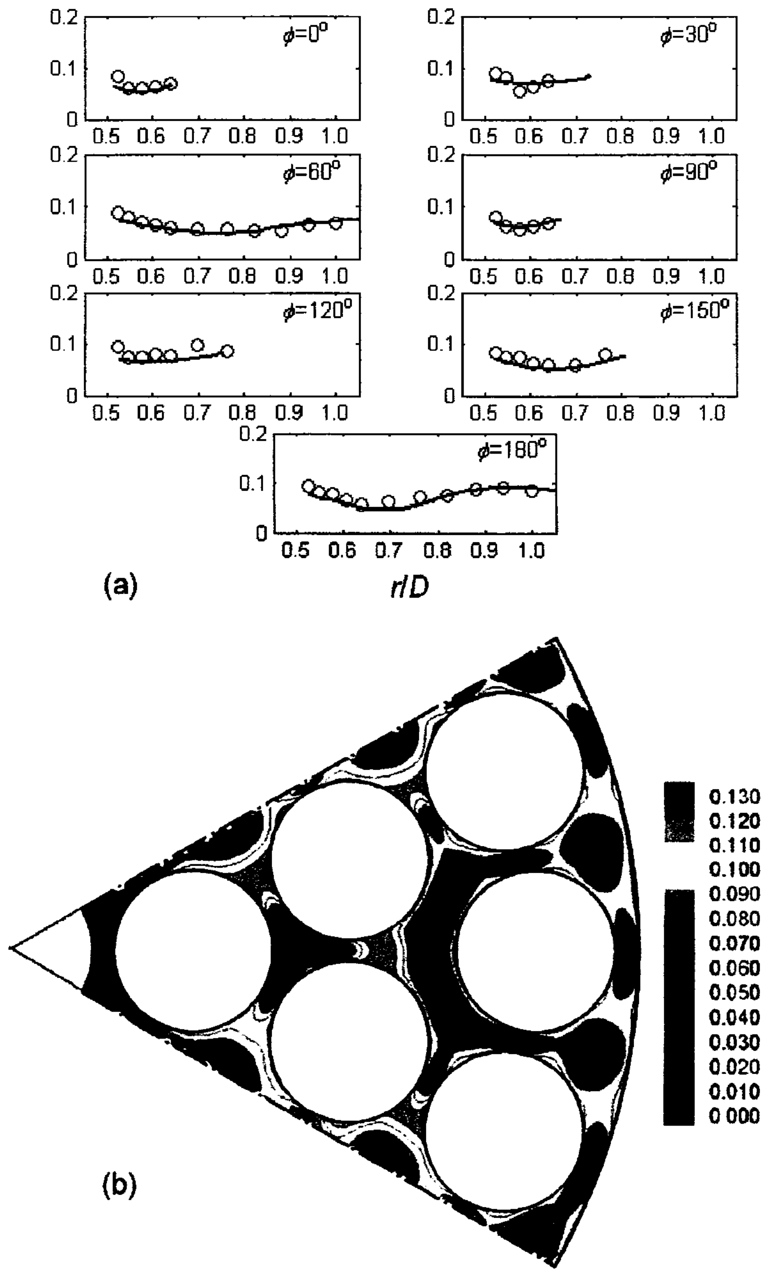

Figure 9 - 2 (a) Dimensionless standard deviation of axial velocity fluctuations $u'/\overline{U}_{max}$ around the middle outer rod ; —— simulations ; ○ OT experiments ; (b) predicted isocontours of u'/U_b

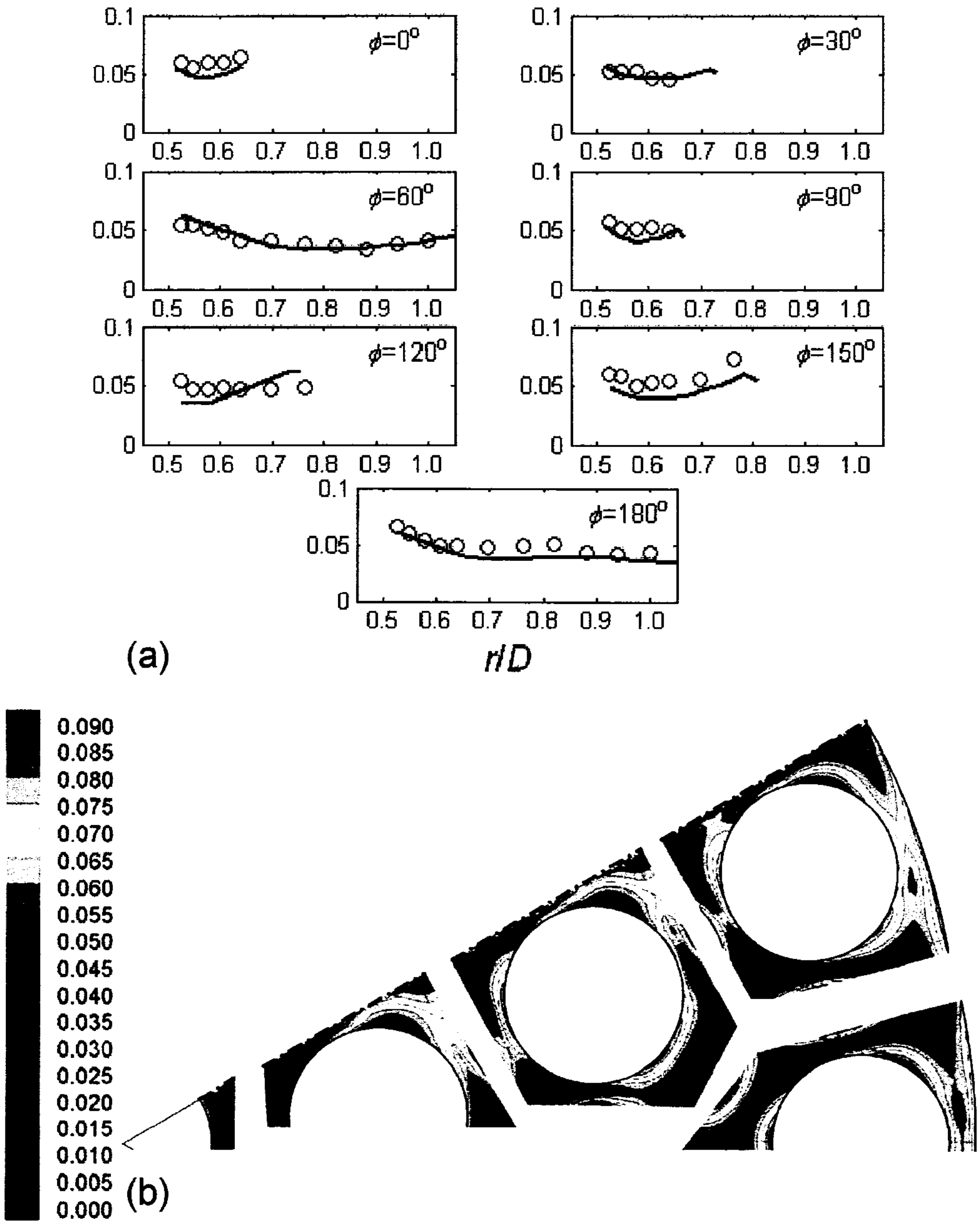

Figure 9 - 3 (a) Dimensionless standard deviation of azimuthal velocity fluctuations $u'_\phi/\overline{U}_{max}$ around the middle outer rod ; —— simulations ; ○ OT experiments ; (b) predicted isocontours of u'_ϕ/U_b in local coordinates

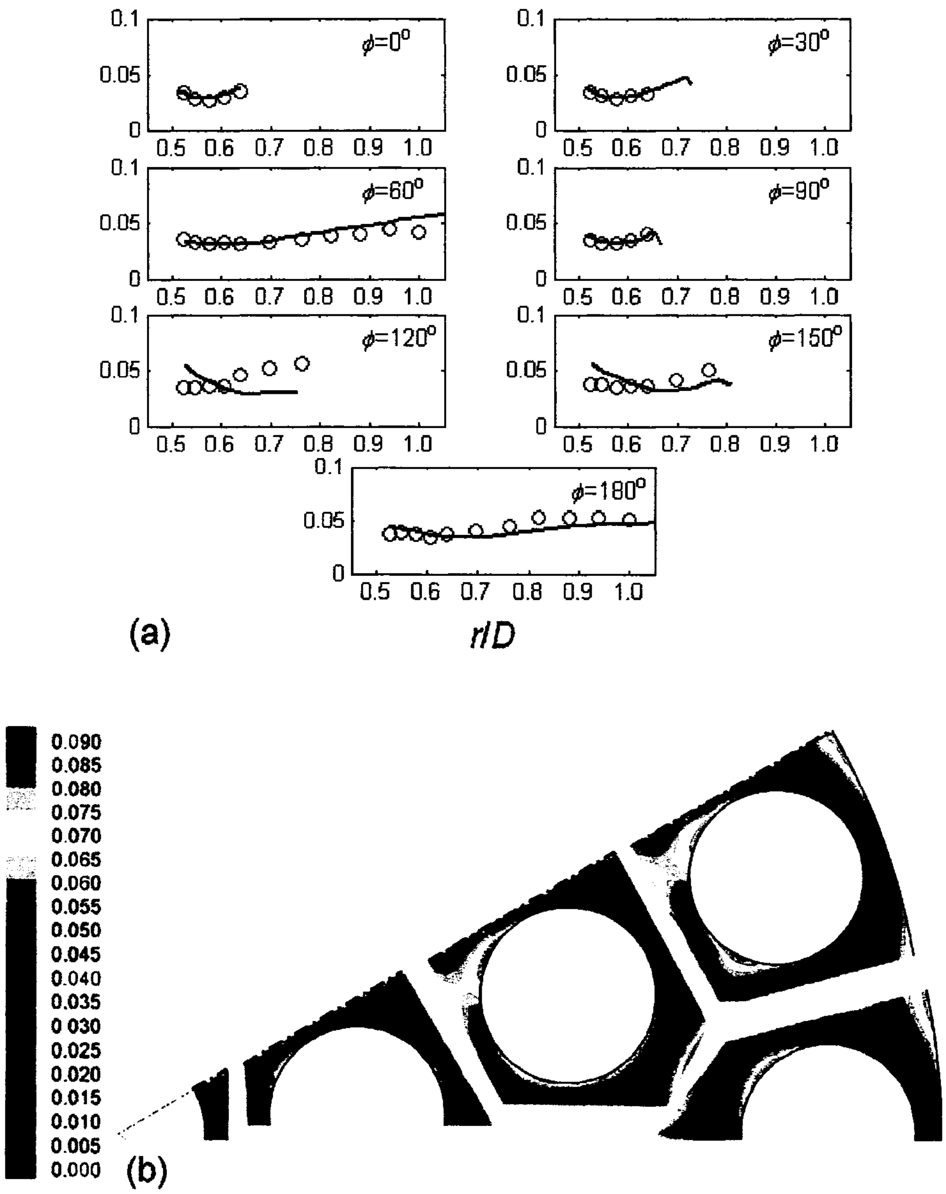

Figure 9 - 4 (a) Dimensionless standard deviation of radial velocity fluctuations $u'_r/\overline{U}_{\max}$ around the middle outer rod ; —— simulations ; ○ OT experiments ; (b) predicted isocontours of u'_r/U_b in local coordinates

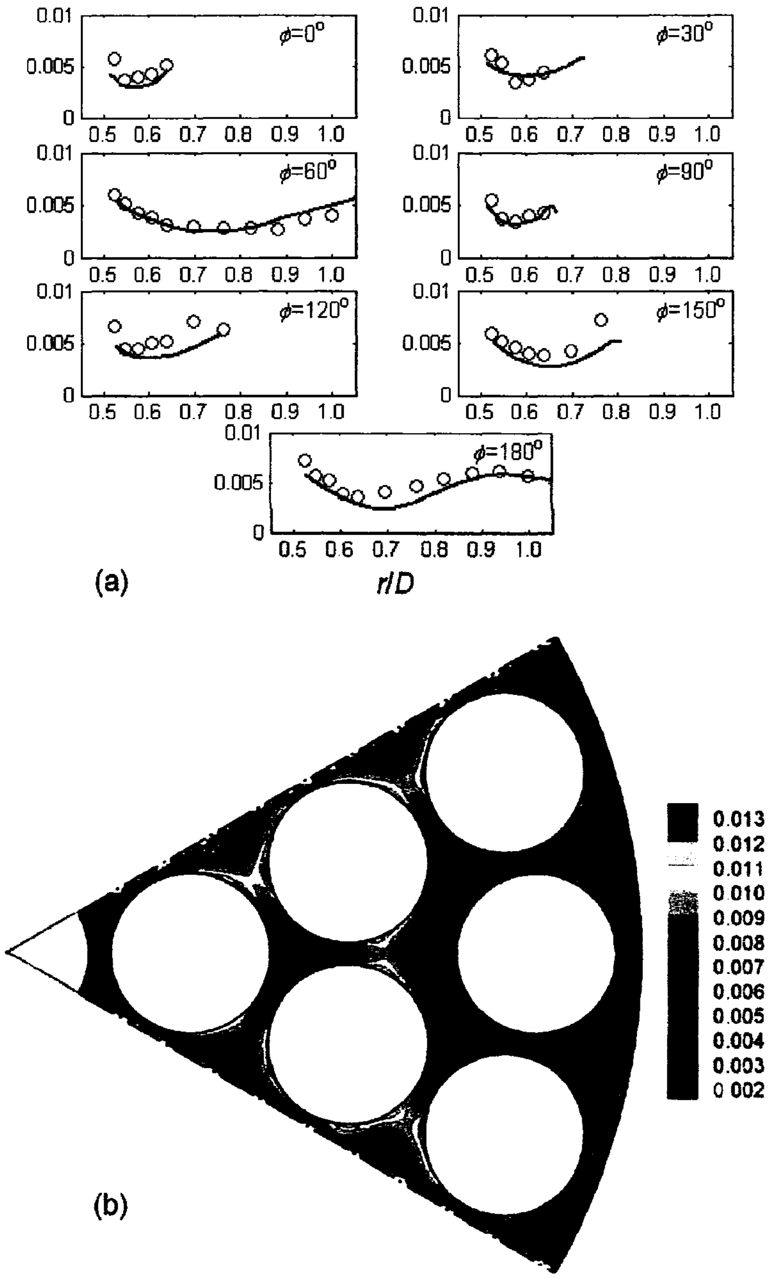

Figure 9 - 5 (a) Dimensionless time-averaged turbulent kinetic energy per unit mass $\bar{k}/\bar{U}_{\max}^{2}$ around the middle outer rod ; —— simulations ; ○ OT experiments ; (b) predicted isocontours of $\bar{k}/U_b^2$

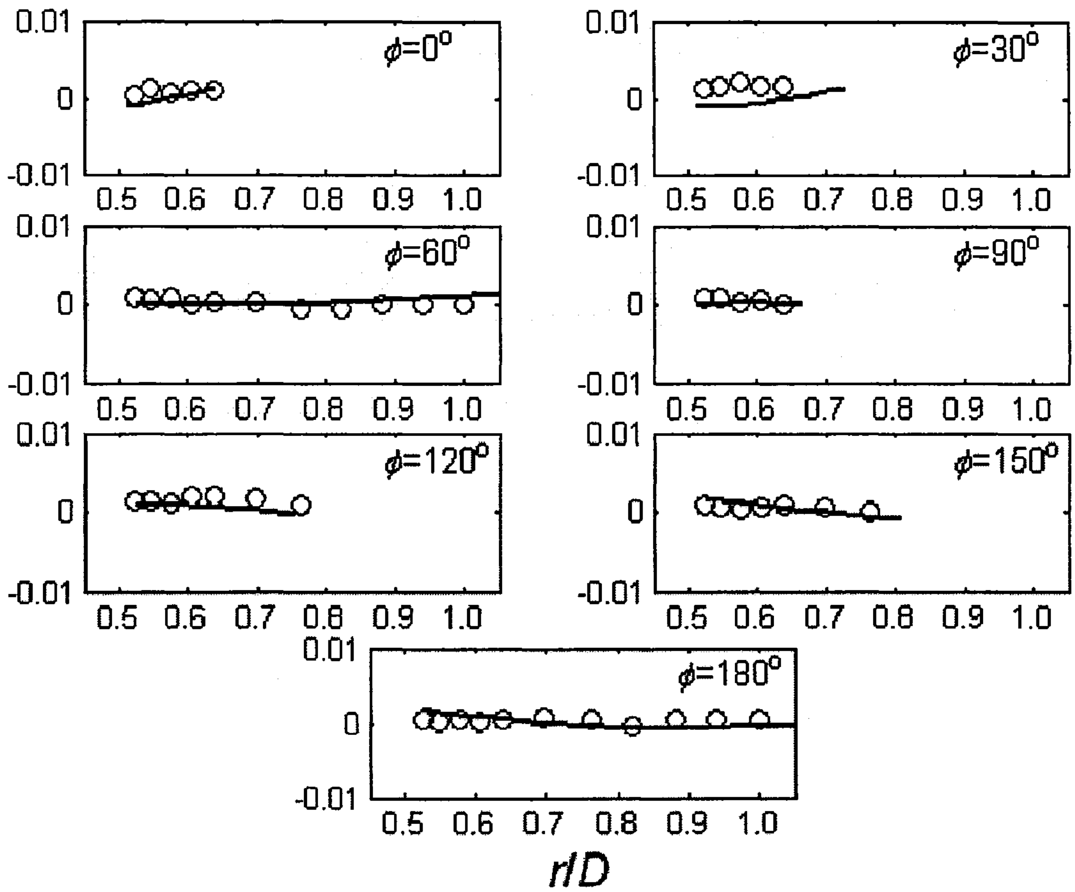

Figure 9 - 6 Dimensionless time-averaged turbulent shear stress $\overline{uu_\phi}/\overline{U}_{max}^2$ in the azimuthal direction around the middle outer rod ; —— simulations ; ○ OT experiments

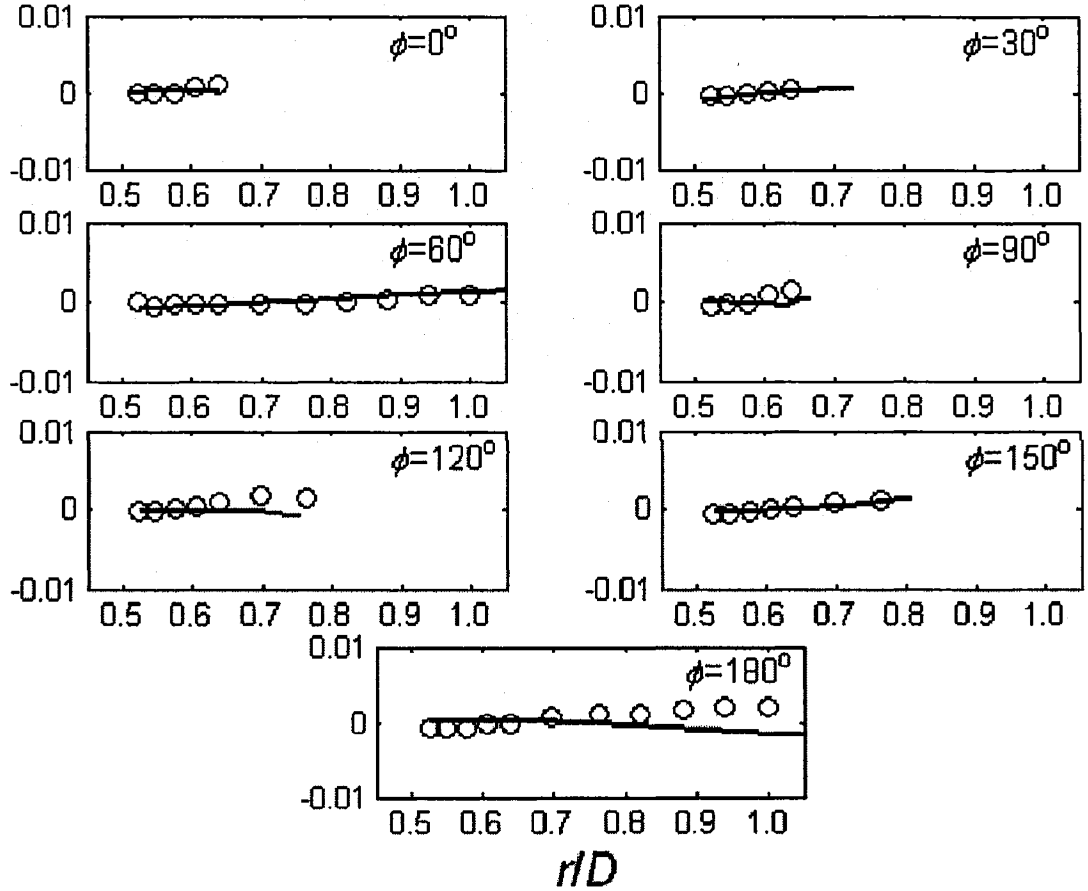

Figure 9 - 7 Dimensionless time-averaged turbulent shear stress $\overline{uu_r}/\overline{U}^2_{max}$ in the radial direction around the middle outer rod ; —— simulations ; ○ OT experiments

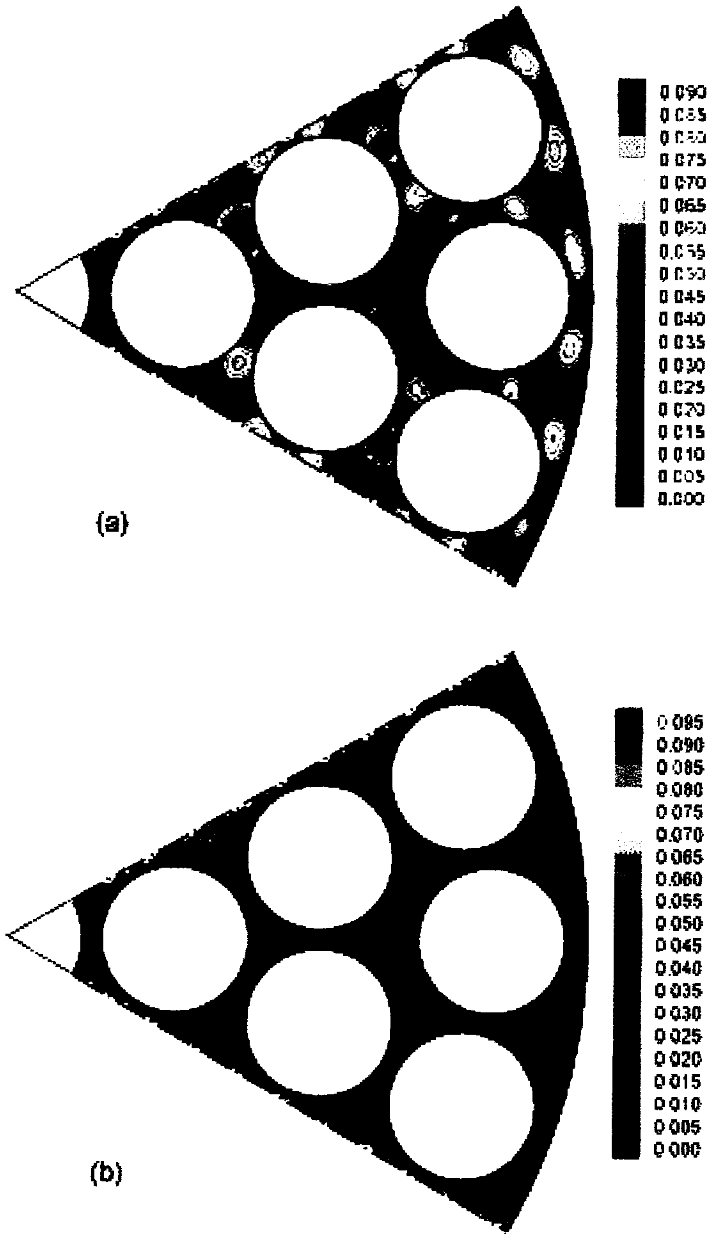

Figure 9 - 8 Dimensionless standard deviations of the predicted (a) coherent u'_c/U_b and (b) non-coherent u'_{nc}/U_b axial velocity fluctuations

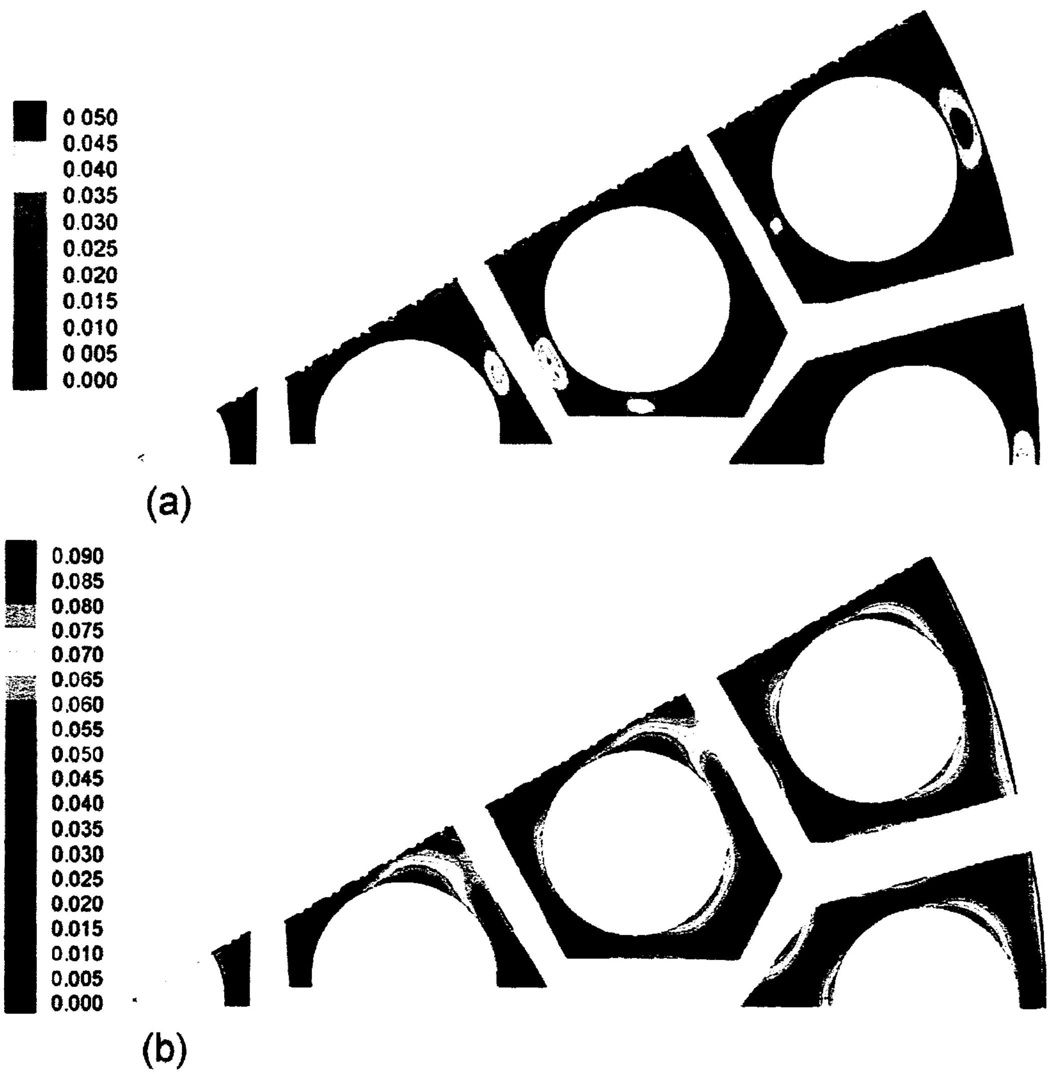

Figure 9 - 9 Dimensionless standard deviations of the predicted (a) coherent $u'_{\phi c}/U_b$ and (b) non-coherent $u'_{\phi nc}/U_b$ azimuthal velocity fluctuations in local coordinates

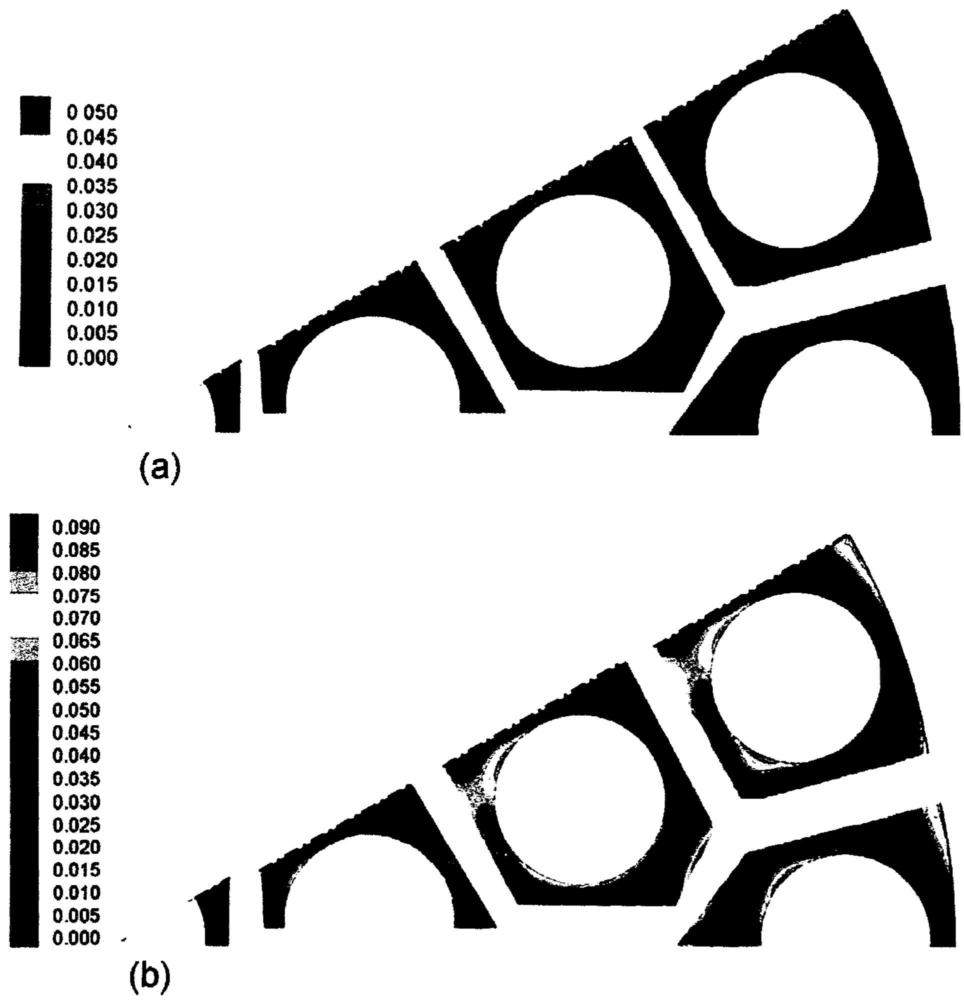

Figure 9 - 10 Dimensionless standard deviations of the predicted (a) coherent $u'_{r,c}/U_b$ and (b) non-coherent $u'_{r,nc}/U_b$ radial velocity fluctuations in local coordinates

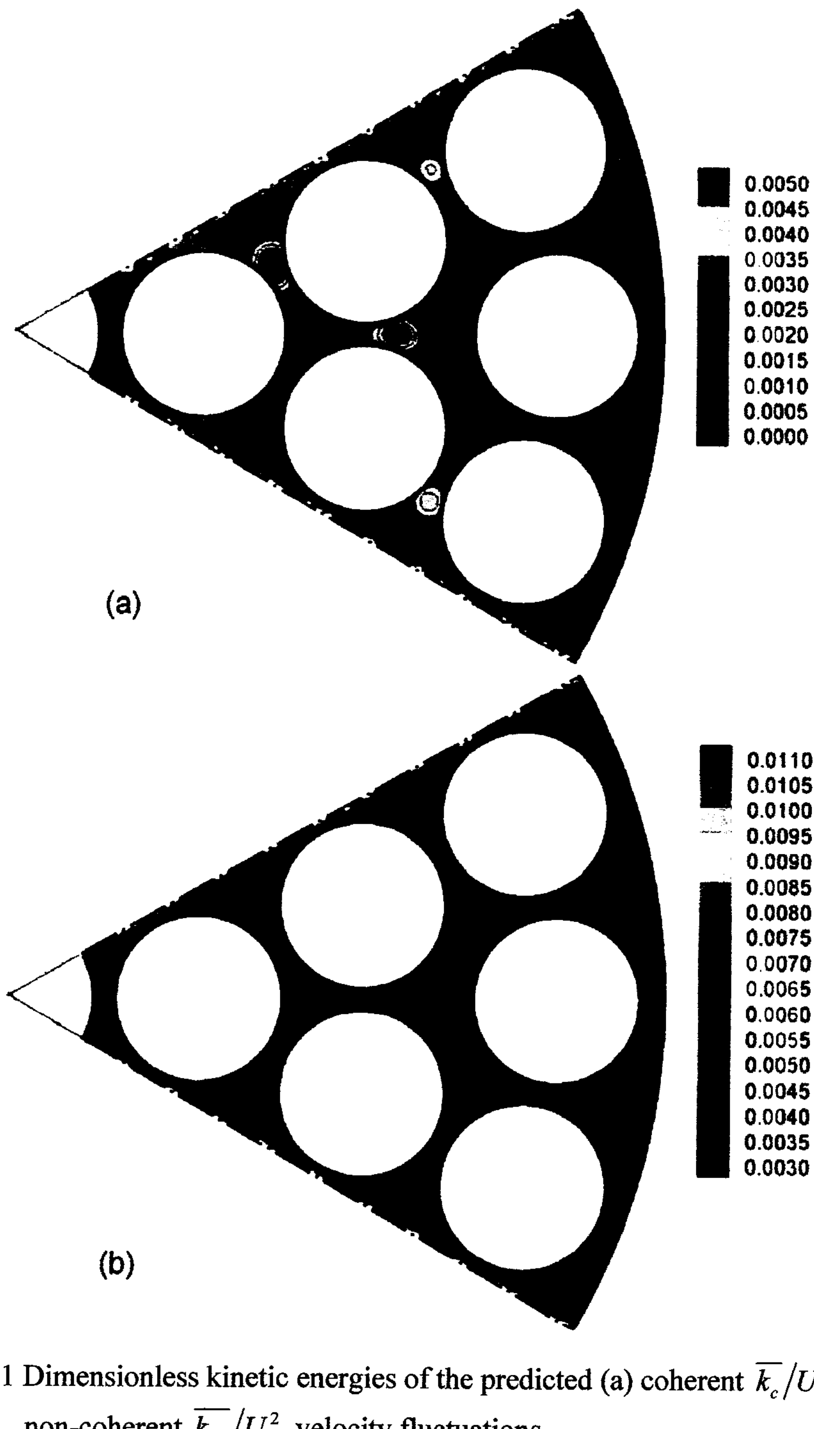

Figure 9 - 11 Dimensionless kinetic energies of the predicted (a) coherent $\overline{k_c}/U_b^2$ and (b) non-coherent $\overline{k_{nc}}/U_b^2$ velocity fluctuations

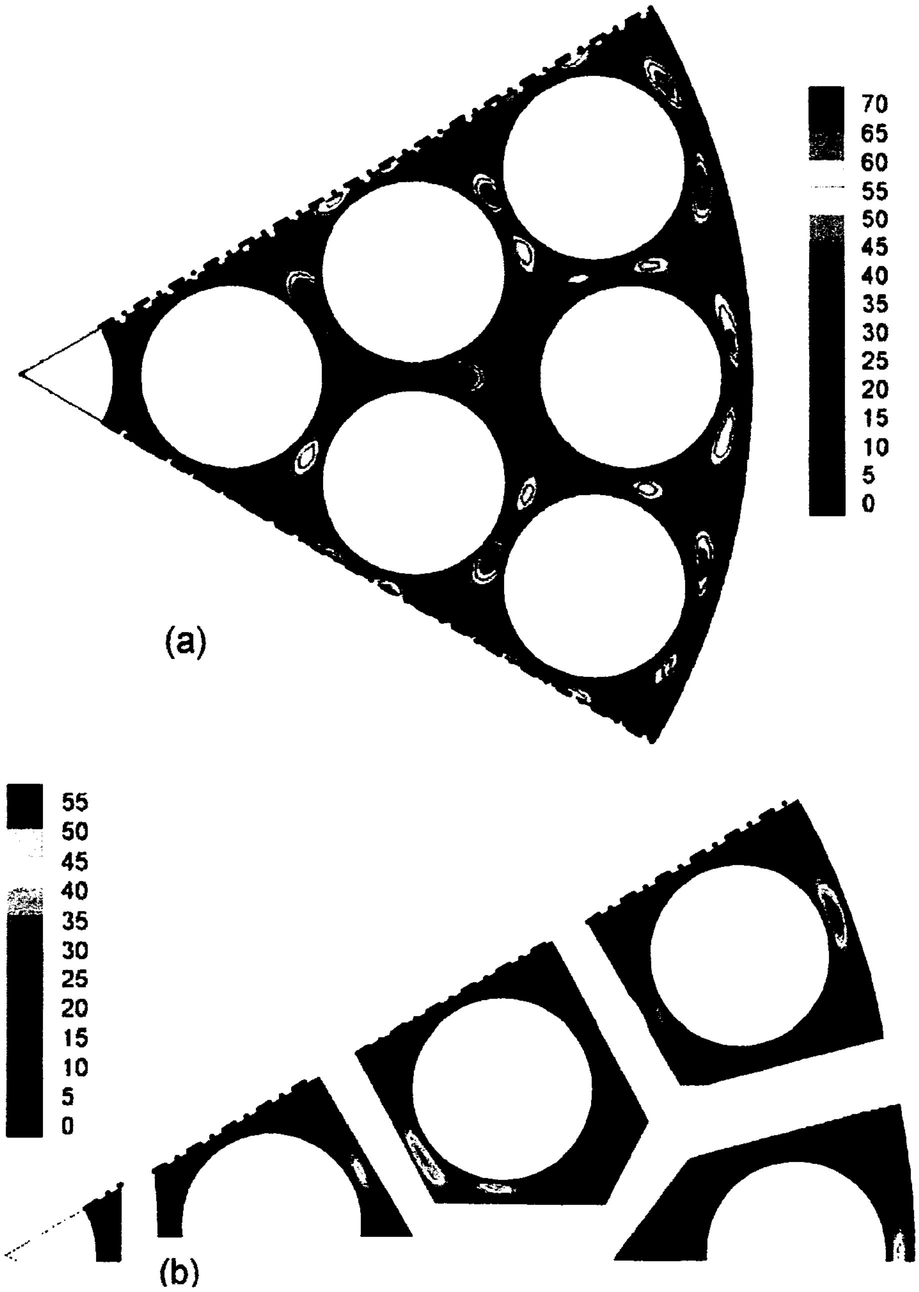

Figure 9 - 12 Predicted variance ratios of the coherent and total (a) axial velocity fluctuations $\overline{u_c^2}/\overline{u^2} \times 100$ and (b) azimuthal velocity fluctuations $\overline{u_{\phi,c}^2}/\overline{u_\phi^2} \times 100$ in local coordinates

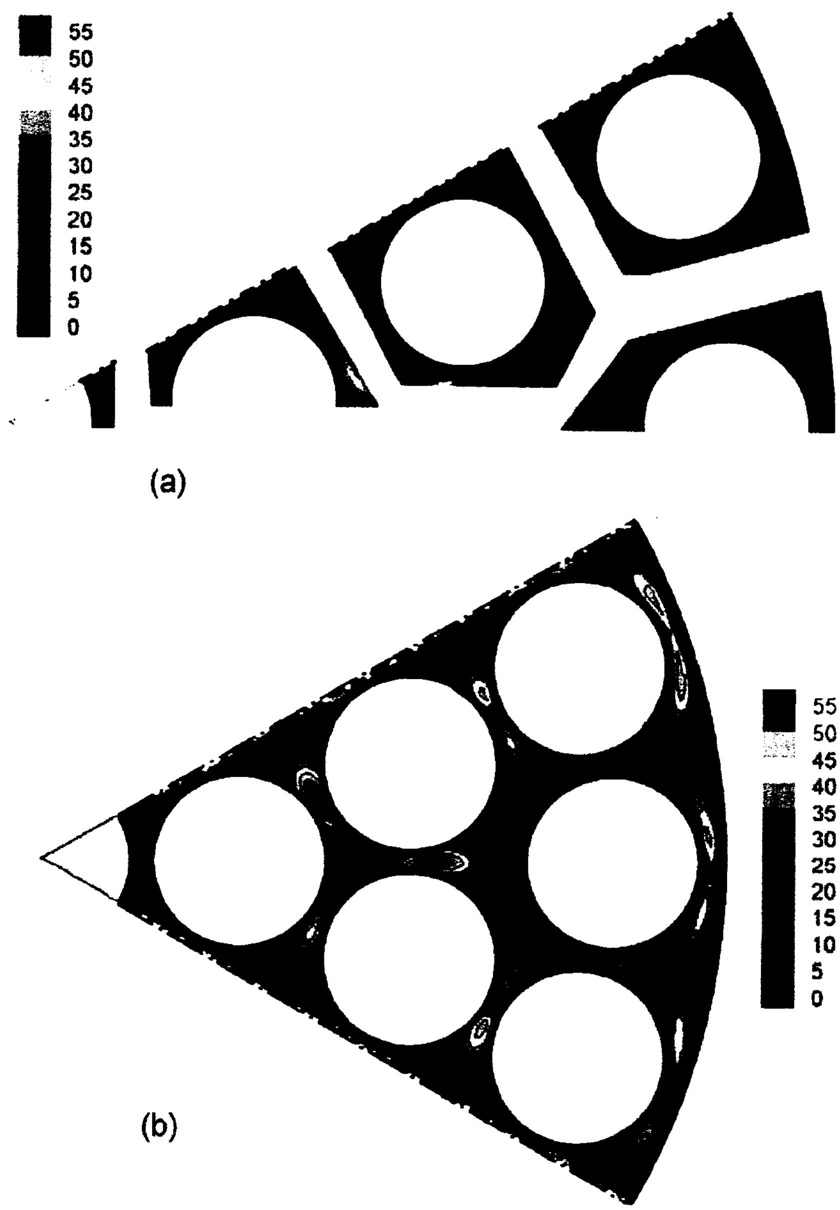

Figure 9 - 13 Predicted variance ratios of time-averaged coherent and total (a) radial velocity fluctuations $\overline{u_{r,c}^2}/\overline{u_r^2}\times 100$ in local coordinates and (b) kinetic energies $\overline{k_c}/\overline{k}\times 100$

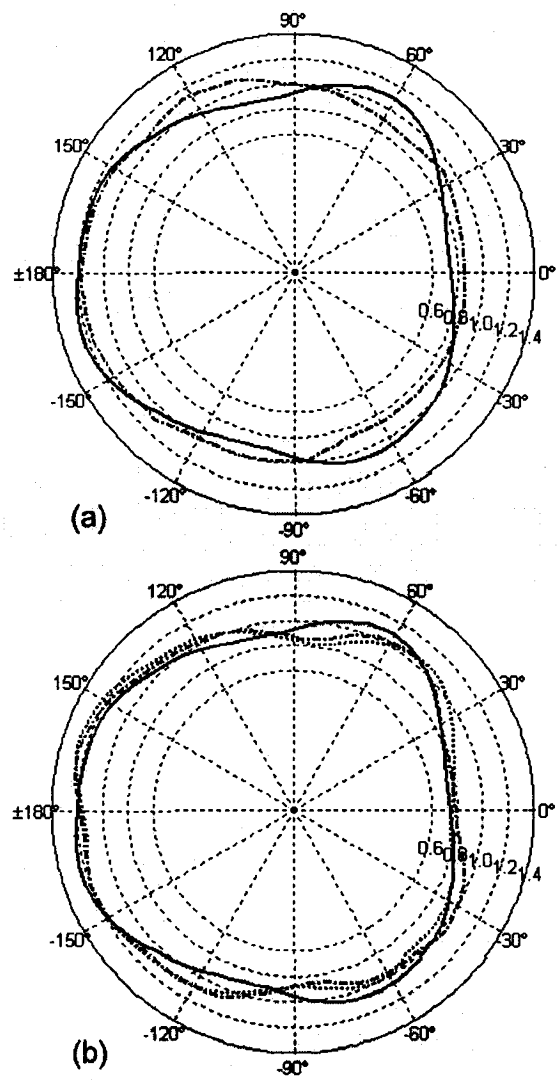

Figure 9 - 14 Circumferential variations around the middle outer rod of (a) the predicted time-averaged wall shear stress (————) and that measured by OT (– · –) ; (b) the predicted time-averaged wall shear stress (————) and representative instantaneous ones (- - -, – · –) ; the values have been normalized by the corresponding circumferential averages (0.63 Pa for both the simulations and the OT experiments)

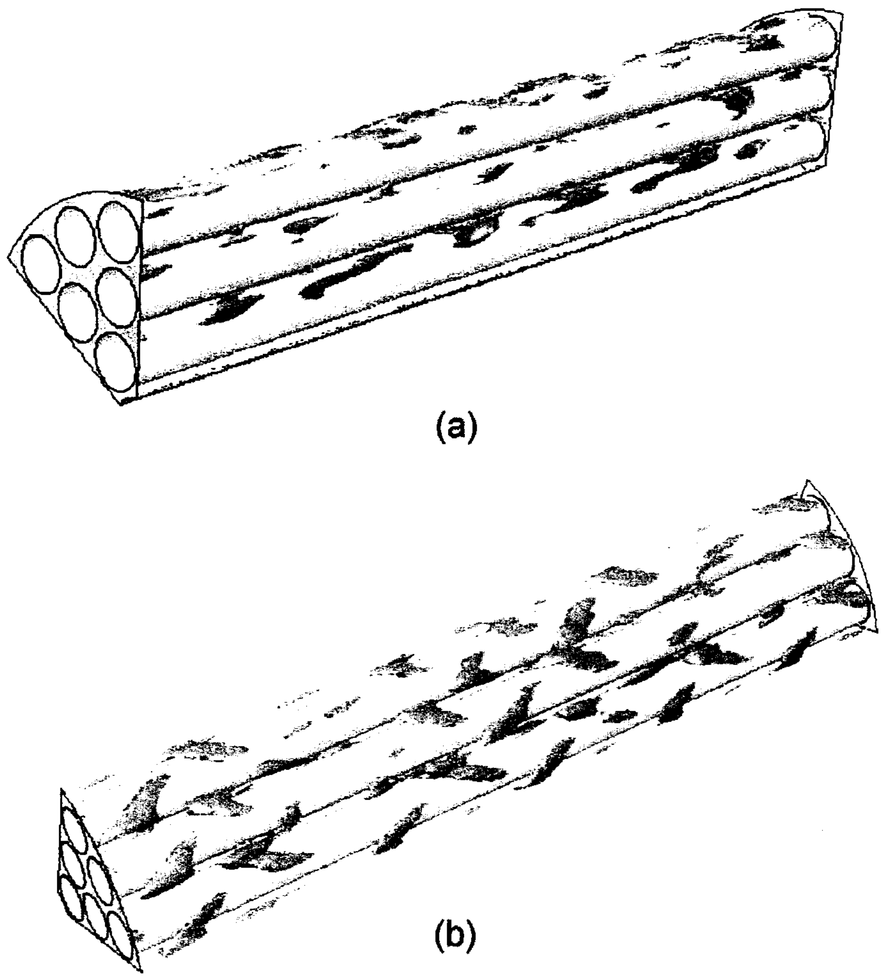

(a)

(b)

Figure 9 - 15 Two isometric views of coherent structures identified by the modified Q criterion : (a) square subchannels on a radial plane ; (b) wall subchannels between rods of the third ring and the wall of pressure tube

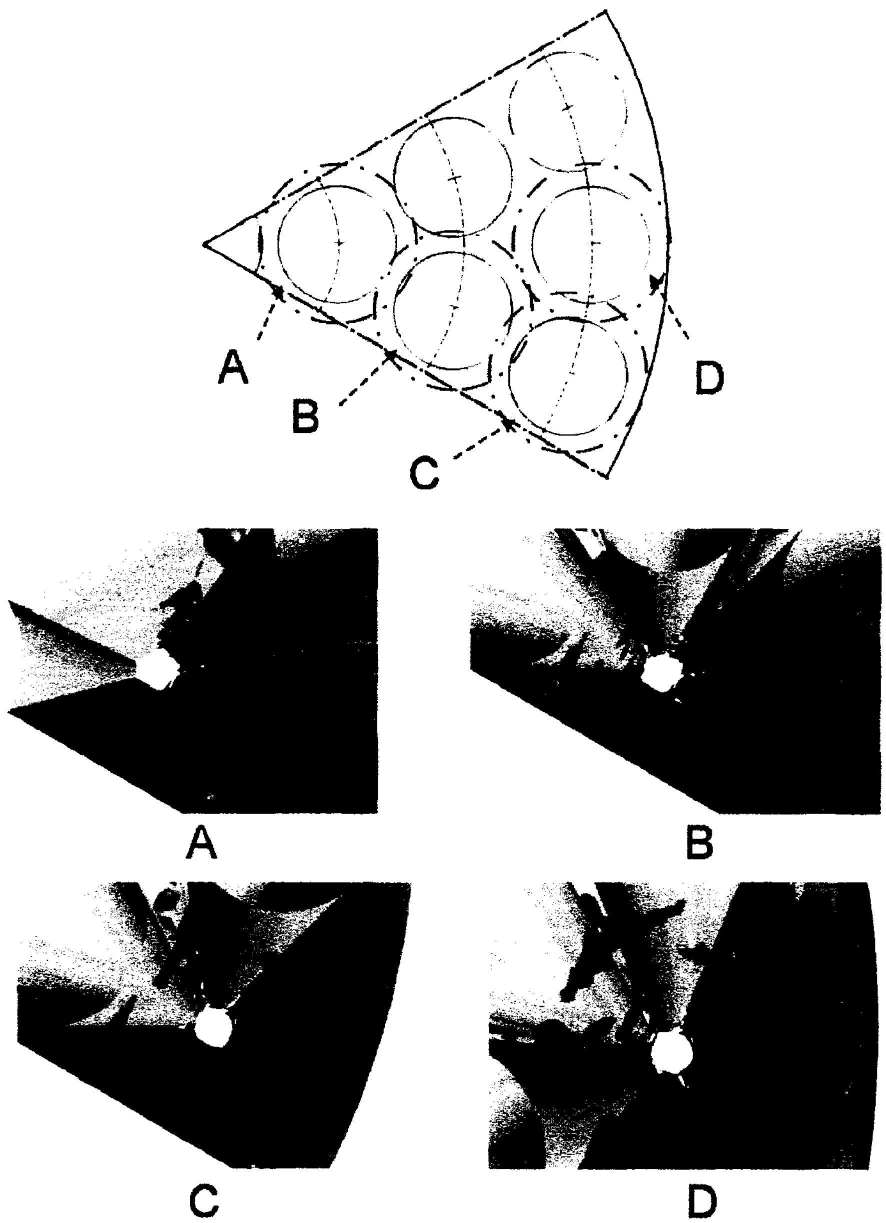

Figure 9 - 16 Inner views of the rod bundle showing coherent structures ; the rod in the center of each view has been made invisible, so that coherent structures in the surrounding subchannels can be seen

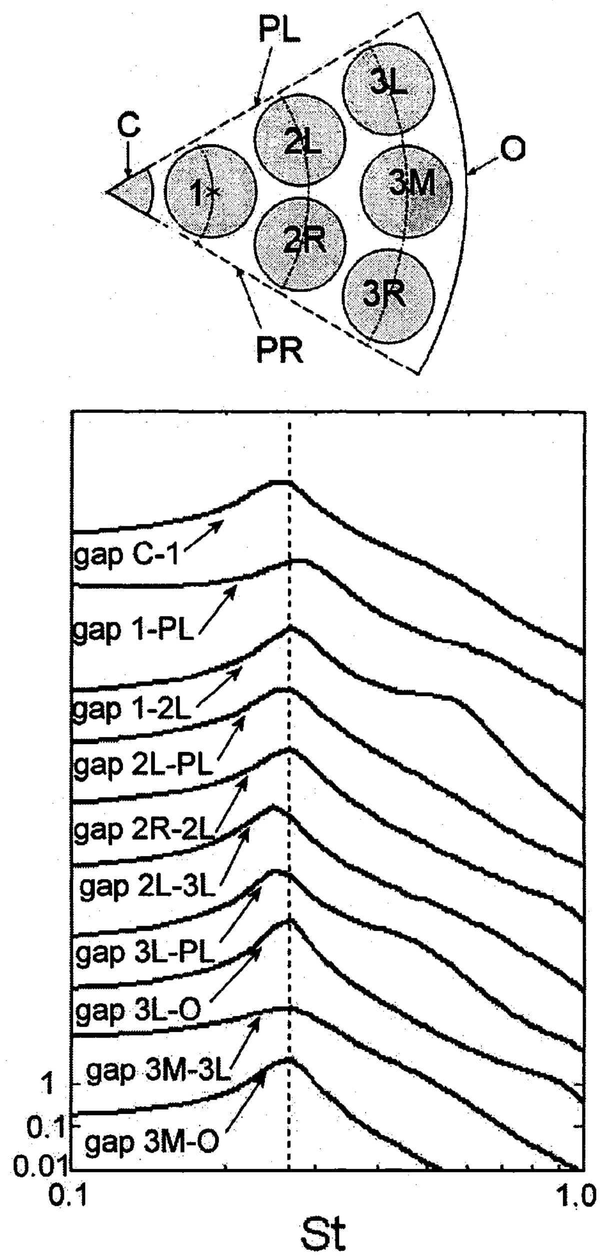

Figure 9 - 17 Smoothened power spectra of the azimuthal velocity in local coordinates in selected gap centers ; each spectrum has been shifted by a different distance along the logarithmic axis to prevent overlapping (arbitrary scale)

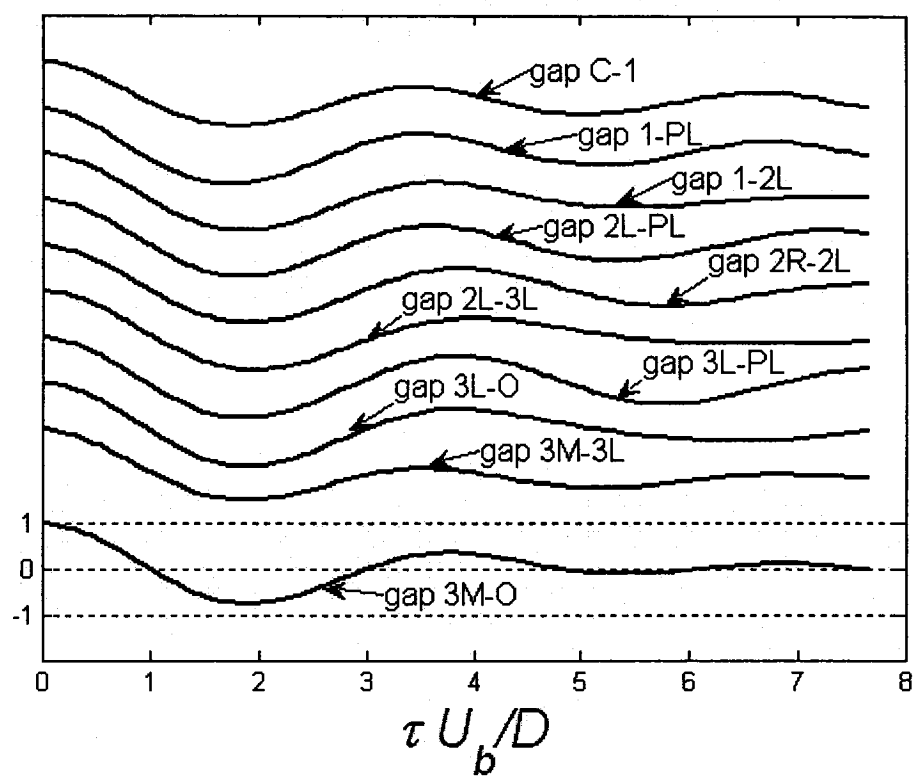

Figure 9 - 18 Auto-correlation coefficients of the azimuthal velocity in the centers of selected gaps ; each curve has been shifted by a different distance along its axis to prevent overlapping (see Fig. 9-17 for nomenclature)

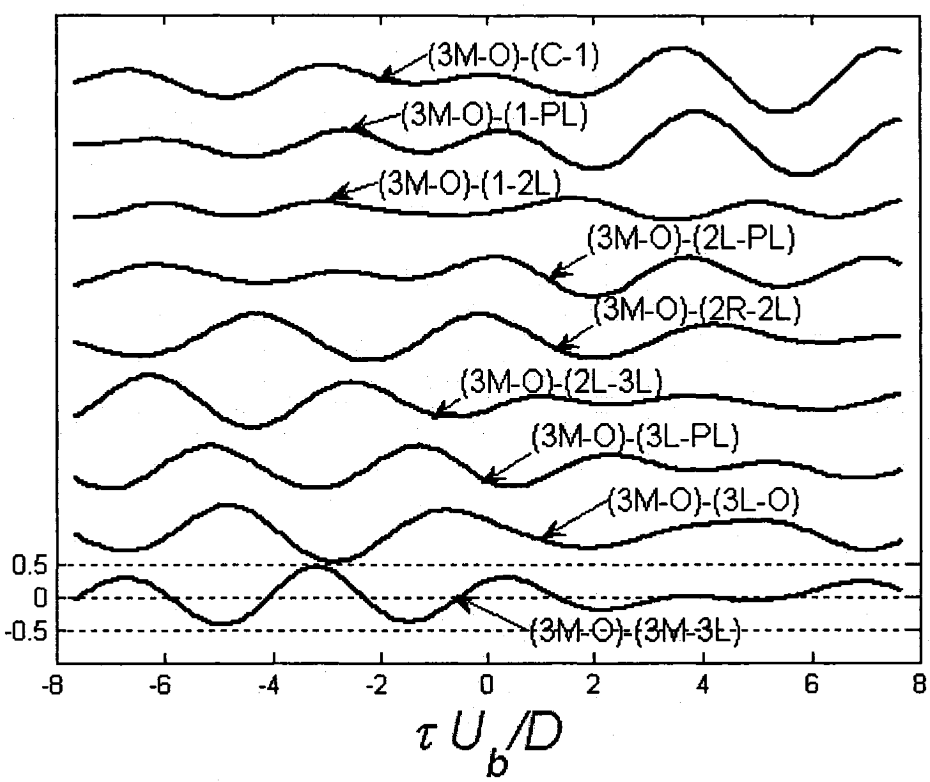

Figure 9 - 19 Cross-correlation coefficients between the azimuthal velocity fluctuations in the center of gap 3M-O and those in other selected gaps ; each curve has been shifted by a different distance along its axis to prevent overlapping (see Fig. 9-17 for nomenclature)

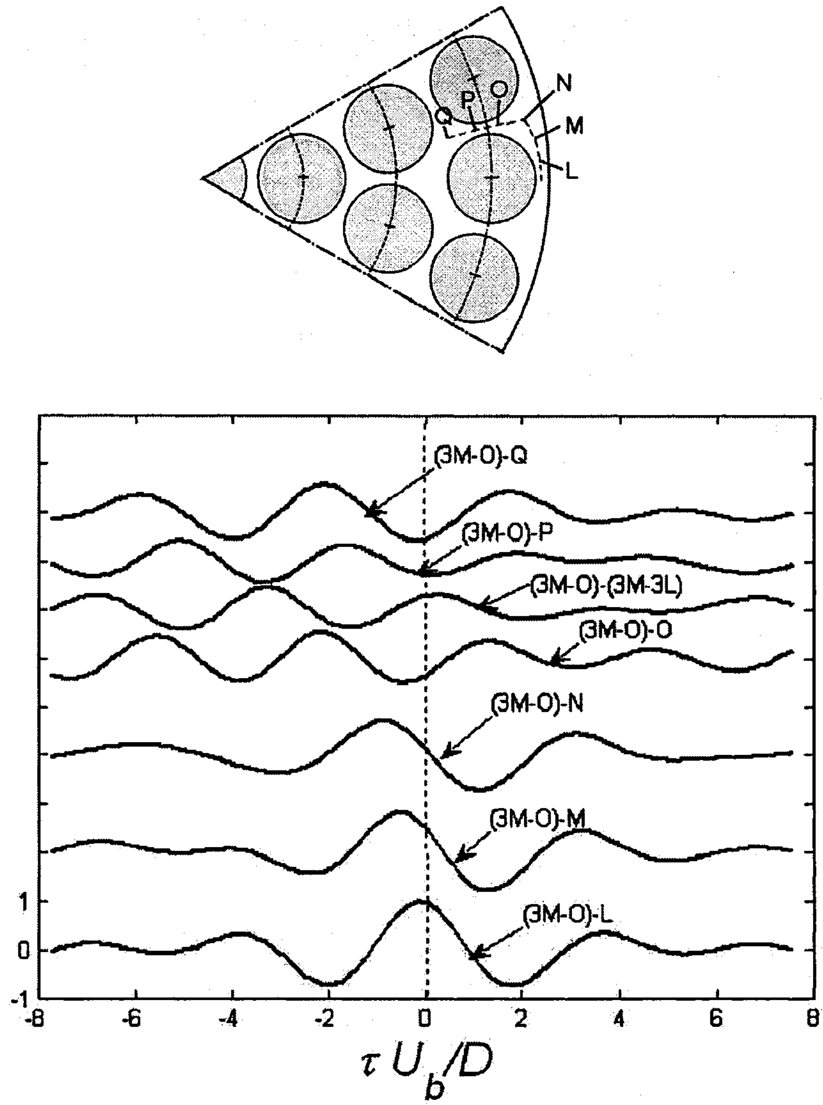

Figure 9 - 20 Cross-correlation coefficients between the azimuthal velocity fluctuations in the center of the gap 3M-O and the velocity fluctuations tangential to the maximum velocity line; each curve has been shifted by a different distance along its axis to prevent overlapping

Appendix A Developing flow in the single-rod duct

In these isothermal simulations, the length of flow domain was set at 54*D*, equal to that in the experimental study (Guellouz and Tavoularis, 2000a) and the inlet boundary condition for the velocity was set to uniform flow. To isolate other effects, the turbulence model and other boundary conditions were kept as same as those in the simulations described in Chapter 6, with the exception that, in order to accommodate the longer domain, the grid resolution was set somewhat coarser.

Figure A1 shows that, although the overall magnitude of predicted time-averaged velocity is somewhat smaller than the corresponding experimental one, the simulation reproduces the locations of two maxima of velocity in the two open subchannels, in agreement with the experimental findings (Guellouz and Tavoularis, 2000a). From this result, the difference between the simulations in Chapter 6 and the experimental distributions of mean velocity can be mainly attributed to the differences in boundary conditions.

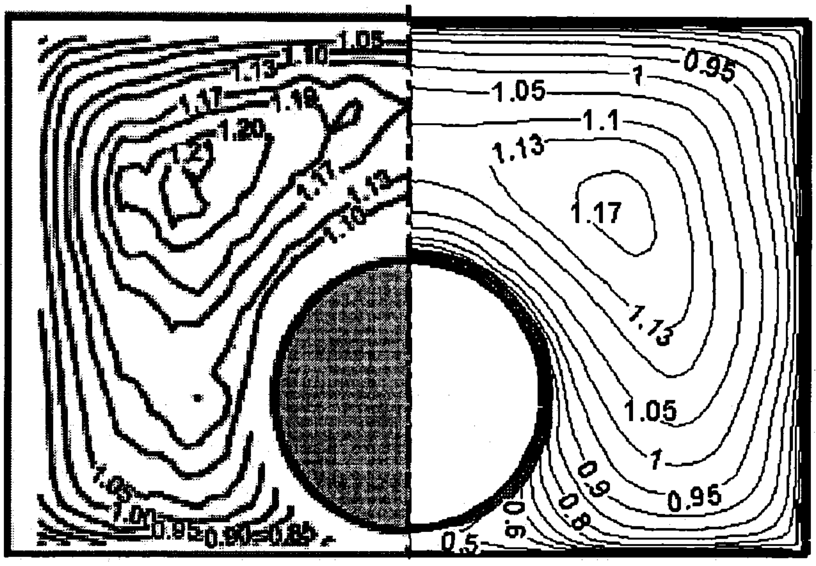

Figure A 1 Isocontours of the time-averaged dimensionless axial velocity in the GT experiments (left) and the developing flow simulations (right)